Universitat Politècnica de València
IU CMT – Clean Mobility & Thermofluids

ANALYSIS OF FUEL EFFECTS ON THE DIFFUSIVE FLAME STRUCTURE USING ADVANCED OPTICAL TECHNIQUES IN A SINGLE CYLINDER OPTICAL ENGINE.

Doctoral Thesis
Presented by:
Francisco José Tejada Magraner
Directed by:
Dr. Jose Vicente Pastor Soriano

Valencia, October 2023

DOCTORAL THESIS

ANALYSIS OF FUEL EFFECTS ON THE DIFFUSIVE FLAME STRUCTURE USING ADVANCED OPTICAL TECHNIQUES IN A SINGLE CYLINDER OPTICAL ENGINE.

Presented by:	D. Francisco José Tejada Magraner
Directed by:	Dr. José Vicente Pastor Soriano

Evaluation board:

President:	Dr. José Javier López Sánchez
Secretary:	Dr. María Arántzazu Gómez Esteban
Examiner:	Dr. Ezio Mancaruso

External examiners:

Dr. Michele Bardi
Dr. Ezio Mancaruso
Dr. Miriam Reyes Serrano

Valencia, October 2023

Abstract

The increase in CO_2 emissions in the transport sector has been continuous in recent years, mainly due to the carbonization of the sector, together with the increase in the vehicle fleet. This fact has adverse effects on environmental quality, being this gas is one of the main constituents of greenhouse gases, thus contributing to global warming.

To mitigate CO_2 emissions, a policy with strict regulations leading to decarbonizing the transport sector is necessary. In this regard, electrification of the transport sector is the main way to achieve such goals. Unfortunately, moving to full electrification of the sector in a relatively short time presents certain difficulties, such as high demand for renewable electricity, low battery capacity, and lack of refueling stations. Therefore, using synthetic fuels obtained from renewable energy sources is presented as a complementary option to help achieve CO_2 emission reduction targets because it can be implemented more quickly.

This doctoral thesis deals with characterizing two synthetic fuels, OME_1 and OME_X. First, a study was carried out to characterize both fuels high and low temperature flame structures under reference conditions of the *Engine Combustion Network* (ECN) in a high-pressure and high-temperature installation. Subsequently, measurements were performed on an optical engine, evaluating the effect of combining the use of OME_X/diesel blends and unconventional piston geometries on in-cylinder soot formation. Non-conventional piston geometries were used because, in diesel studies, soot reductions are achieved by improving the air-fuel mixing process. Therefore, it is intended to analyze whether this effect is also obtained in the presence of a synthetic fuel such as OME_X.

The facilities where the different studies have been carried out have optical accesses. Through them, different visualization techniques have been used based on laser and the radiation emitted by the flame.

In conclusion, it could be summarized that it has been seen that what is already known about the diesel combustion process can be applied to the combustion of OME_X, with the benefit that this is a fuel that does not present a soot precursor structure, making it suitable for real engine applications. Despite the incompatibilities of this fuel with the engine infrastructure, this is solved by using blends with diesel, which, in addition, by combining it with non-conventional piston geometries, significant reductions in in-cylinder soot formation are obtained.

Resumen

El aumento de las emisiones de CO_2 en el sector del transporte ha sido continuo en estos últimos años debido principalmente a la carbonización del sector junto al aumento de la flota de vehículos. Este hecho tiene efectos adversos en la calidad medioambiental, siendo este gas uno de los principales constituyentes de los gases de efecto invernadero, contribuyendo así al calentamiento global.

Para mitigar las emisiones de CO_2, es necesario una política con estrictas regulaciones que conduzcan a la descarbonización del sector del transporte. En este sentido, la electrificación del sector del transporte es la principal vía para conseguir tales objetivos. Lamentablemente, pasar a la electrificación total del sector en un periodo relativamente corto de tiempo presenta ciertas dificultades, como son la alta demanda de electricidad renovable, la baja capacidad de las baterías, y la falta de estaciones de repuesto. Por ello, el uso de combustibles sintéticos obtenidos a partir de fuentes de energía renovables se presenta como una opción complementaria para ayudar a alcanzar los objetivos de reducción de emisiones de CO_2, debido a que puede implementarse de forma más rápida.

En la presente tesis doctoral se aborda la caracterización de dos combustibles sintéticos, OME_1 y OME_X. Primeramente, se realizó un estudio para caracterizar la estructura de alta y baja temperatura de la llama de ambos combustibles bajo condiciones de referencia de la *Engine Combustion Network* (ECN) en una instalación de alta presión y temperatura. Posteriormente, se realizaron medidas en un motor óptico, evaluando el efecto que tiene la combinación del uso de mezclas de OME_X/diésel junto a geometrías de pistón no convencionales en la formación de hollín dentro del cilindro. El uso de geometrías de pistón no convencionales se usó debido a que en estudios usando diésel se consiguen reducciones de hollín al mejorar el proceso de mezcla aire-combustible. Por ello, se pretende analizar si ese efecto se obtiene igualmente en presencia de un combustible sintético como es el OME_X.

Las instalaciones en las que se han realizado los distintos estudios presentan accesos ópticos. A través de ellos se han usado distintas técnicas de visualización, tanto basadas en laser, como en la propia radiación emitida por la llama.

Como conclusiones, se podría resumir en que se ha visto que lo ya conocido sobre el proceso de combustión diésel puede ser aplicado a la combustión del OME_X, con el beneficio de que este es un combustible que no presenta estructura de precursores de hollín haciéndolo idóneo para aplicaciones reales de motor. A pesar de las incompatibilidades de este combustible con la infraestructura del motor, esta se soluciona usando mezclas con diésel, que, además, combinándolo con geometrías no convencionales de pistón se obtienen reducciones importantes de formación de hollín dentro del cilindro.

Resum

L'augment de les emissions de CO_2 en el sector del transport ha sigut continu en aquests últims anys degut principalment a la carbonització del sector al costat de l'augment de la flota de vehicles. Aquest fet té efectes adversos en la qualitat mediambiental, sent aquest gas un dels principals constituents dels gasos d'efecte hivernacle, contribuint així al calfament global.

Per a mitigar les emissions de CO_2, és necessari una política amb estrictes regulacions que conduïsquen a la descarbonització del sector del transport. En aquest sentit, l'electrificació del sector del transport és la principal via per a aconseguir tals objectius. Lamentablement, passar a l'electrificació total del sector en un període relativament curt de temps presenta unes certes dificultats, com són l'alta demanda d'electricitat renovable, la baixa capacitat de les bateries, i la falta d'estacions de suministre. Per això, l'ús de combustibles sintètics obtinguts a partir de fonts d'energia renovables es presenta com una opció complementària per a ajudar a aconseguir els objectius de reducció d'emissions de CO_2, pel fet que pot implementar-se de forma més ràpida.

En la present tesi doctoral s'aborda la caracterització de dos combustibles sintètics, OME_1 i OME_X. Primerament, es va realitzar un estudi per a caracteritzar l'estructura d'alta i baixa temperatura de la flama de tots dos combustibles sota condicions de referència de la *Engine Combustion Network* (ECN) en una instal·lació d'alta pressió i temperatura. Posteriorment, es van realitzar mesures en un motor òptic, avaluant l'efecte que té la combinació de l'ús de mescles de OME_X/dièsel al costat de geometries de pistó no convencionals en la formació de sutge dins del cilindre. L'ús de geometries de pistó no convencionals es va usar pel fet que en estudis usant dièsel s'aconsegueixen reduccions de sutge en millorar el procés de mescla aïre-combustible. Per això, es pretén analitzar si aqueix efecte s'obté igualment en presència d'un combustible sintètic com és el OME_X.

Les instal·lacions en les quals s'han realitzat els diferents estudis presenten accessos òptics. A través d'ells s'han usat diferents tècniques de visualització, tant basades en laser, com en la pròpia radiació emesa per la flama.

Com a conclusions, es podria resumir en què s'ha vist que el ja conegut sobre el procés de combustió dièsel pot ser aplicat a la combustió del OME_X, amb el benefici que aquest és un combustible que no presenta estructura de precursors de sutge fent-lo idoni per a aplicacions reals de motor. Malgrat les incompatibilitats d'aquest combustible amb la infraestructura del motor, aquesta se soluciona usant mescles amb dièsel, que, a més, combinant-ho amb geometries no convencionals de pistó s'obtenen reduccions importants de formació de sutge dins del cilindre.

The truth of a theory is in your mind, not in your eyes.

Albert Einstein

Acknowledgments

It has been four years since I started my PhD studies, and several people have been involved in this long journey to whom I would like to express my sincere gratitude.

First, I would like to thank CMT-Clean Mobility & Thermofluids Direction Board, José María Desantes and Jesús Benajes for allowing me to be part of this prestigious research center and for providing all the tools necessary to perform my investigation. I would like to thank all the administration staff, especially Amparo, Haby, and Elena. Also, I extend my gratitude to PUNCH-Torino group for the project associated with one of the experimental campaigns carried out in this thesis. Alberto Vasallo, Francesco Concetto, and Giacomo Belgiorno, it was a pleasure to participate in this investigation with you. I would like to thank the Universitat Politècnica de València for the financial support through the FPI UPV SUBP2 predoctoral contract.

I would like to express my gratitude to the Division of Combustion Physics from Lund University for allowing me to join their excellent team supervised by Mattias Richter. Thanks to Saeed, David, Sebastian, and Miaoxin, among others, for sharing their knowledge with me.

From now on, I would like to use my native language, both Spanish and Mallorquín (from I was born)

Quisiera agradecer a mi director de tesis, José Vicente Pastor Soriano, al que nos referimos como Xevi. Recuerdo la primera reunión que tuvimos acerca de lo que sería mi tesis doctoral y del aviso que ya me hiciste en ese momento: “Va a ser un camino duro”. En ese momento estaba tan abrumado por toda la información que me diste en esa media hora de reunión que ni me podía llegar a imaginar la verdad de esas palabras. Y sí, tenías toda la razón del mundo, estos cuatro años han sido muy duros. Habían días en los que creía que no sería capaz de seguir adelante y terminar el doctorado, pensando innumerables veces en si este camino que había escogido era el correcto. Como ya bien me conoces, yo no soy una persona que exprese sus sentimientos, me lo guardo y tiro adelante, a pesar de las innumerables veces que me has dicho “si alguna vez te sientes agobiado, levanta la mano y pide ayuda”. Aún sin verbalizar nada, siempre que he estado en esos momentos de flaqueza, aparecías por el despacho para charlar un rato conmigo, como si supieras en todo momento lo que pasaba por mi cabeza. De esas charlas hemos tenido unas cuantas en estos años y siempre acababan con un “ánimo chaval”.

He aprendido muchas cosas de ti como a ser perfeccionista, fijándose hasta en los pequeños detalles, como a ser crítico en el trabajo. Innumerables veces iba a tu despacho a hablar contigo sobre algunos resultados o ideas que se me habían podido ocurrir, orgulloso pensando que era fantástico lo que te iba a contar y desmontármelo todo con unas simples preguntas que me planteabas. Esto me hacía ver que tenía que pensar más las cosas y ser más riguroso con mi trabajo. En toda esta etapa siempre he tenido muy presente una frase que me dijeron en mi primer día del grado de Física: “Un buen Físico no es el que se sabe más ecuaciones de memoria sino el que es capaz de resolver cualquier problema que se le plantee. Al final del grado lo que se pretende es que aprendáis a pensar". Lo único que puedo decir es gracias por todo lo que me has enseñado y sobre todo por confiar en mí.

También me gustaría agradecer a Carlos Micó Reche, que aunque oficialmente no figure como director de Tesis, realmente siento como si hubieras sido uno. Lo que he dicho que he aprendido de Xevi puedo perfectamente extenderlo a ti, lo que no es raro habiendo sido también tu director de Tesis en su entonces. Siempre recordaré esos días al principio de mi doctorado en los que nos pasábamos días enteros intentando ajustar el láser para hacer las medidas de PLIF. Esa rigurosidad en el trabajo experimental que tienes al igual que en el análisis de los resultados me ha ayudado enormemente a crecer en mi formación como investigador, por lo que te lo agradezco plenamente. También me gustaría agradecerle a José María Garcia Oliver (Xemary) por todo el apoyo y conocimiento aportado durante estos años.

Quisiera agradecer a Omar Huerta, José Enrique del Rey y Daniel Lérida, como técnicos con los que más he tenido contacto y que han ayudado a que esta tesis siguiera adelante. En especial, me gustaría dedicar unas palabras a Omar. Gracias Omar, no solo por tu gran trabajo sino también por tu apoyo y por esos momentos de risa que le alegraban a cualquiera el día. Esta tesis aunque salga mi nombre, perfectamente se podría añadir el tuyo también. Toda la campaña experimental en la que se basa esta tesis ha estado operativa gracias a ti, y sé de primera mano que no ha sido fácil tenerla siempre a punto. Recuerdo por ejemplo cuando empezamos las medidas en el motor óptico y todos los problemas en los que nos vimos envueltos. Aún así, aunque montáramos y desmontáramos decenas de veces lo mismo, lo recuerdo con una sonrisa. He aprendido muchísimo de ti y te considero un gran amigo que ha sido un gran apoyo durante esta etapa.

Esta experiencia la he pasado junto a compañeros y amigos dentro del mismo centro de investigación, los cuales han sido un apoyo importantísimo. Quiero empezar con los "xiquets", un grupo de amigos que me acogió durante el primer año y que sin ellos no habría sido lo mismo. Ale, Rodri, Dai, Brayan, Arturo y Oscar, muchas gracias a todos por esos momentos tan divertidos que hemos pasado juntos. Como sabéis no siempre ha sido todo diversión, todos hemos pasado por momentos difíciles en que necesitábamos hablar con ese amigo/a, y para mi vosotros lo habéis sido.

Quiero extender las gracias también a Felipe, Alba y Leo, los que fueron mis predecesores y me ayudaron muchísimo sobretodo en mis inicios. En especial a Felipe, gracias por enseñar a este Físico ignorante de los motores todo tu conocimiento, además de haber sido un gran apoyo durante toda esta etapa. También quería agradecer a Usama, como amigo y compañero de despacho, thank you man. Hay muchísimia más gente a la que quiero agradecer como es a Andrés, Javi, Victor, Rami, Cassio, César y David, entre otros muchos más, pero tendría que hacer un documento igual de largo como ha sido la Tesis Doctoral, por lo que pido disculpas por no mencionarlos explícitamente.

Ahora me gustaría dedicar unas palabras a mi familia.

Papá y mamá, sinceramente siento que daros las gracias se queda muy corto. Lo habeis dado todo, tanto por Sofía como por mi. Si no hubiera sido por vosotros no habría llegado hasta donde estoy ahora y me siento muy orgulloso de teneros como padres. Solo espero que el día que me toque a mí, ser al menos la mitad de buenos que lo sois vosotros. Desde pequeño siempre me habéis inculcado que luche por mis sueños, que lo importante no es cuantas veces uno se caiga, sino que uno sea capaz de levantarse todas las veces que haga falta. Solo daros las gracias por haberme hecho ser la persona que soy a día de hoy. Os quiero. A mi hermana Sofía, a la que tengo siempre que la necesito. Gracias por tu apoyo y por tus tonterías que sacan la risa a cualquiera. Te quiero Sof.

A mi abuela Titi, muchas gracias por todo lo que has hecho por nosotros. Esas historias que nos cuentas siempre sobre tu juventud, como conociste al abuelo, y demás trastadas que hacias, siempre hacen sacarme una sonrisa y olvidar los problemas. A Puri, la que considero como una abuela. A pesar que desde pequeño siempre te estoy pinchando y molestando sigues aguantándome. Para mi, la palabra verano está siempre relacionada contigo. Muchas gracias por todo lo que has hecho por nosotros.

A Jose Pedro Magraner, o como le llamamos en la familia, Pepe. Sinceramente, mil gracias por todo tu apoyo. Siempre has estado muy pendiente tanto de Maria como de mi. Sin conocerme demasiado, tuviste plena confianza y apostaste por mi. Solo espero no haberte decepcionado. Mallorquins fent vida a València pareix que ve de familia. Una altra vegada, moltes gràcies per tot Pep.

También me gustaría dedicar unas palabra a los abuelos, que por desgracia ya no están aquí. Abuelo Tonio, nos dejaste justo al inicio de esta etapa. Siempre que te recuerdo, te veo con esa sonrisa que te caracterizaba. Creo que eras la persona más buena que he conocido nunca. Gracias tanto a ti como a Titi tengo muchos recuerdos buenos de mi infancia. Abuelo Paco y abuela Vito, vosotros nos dejasteis hace menos tiempo. Mi infancia en las vacaciones de navidad sois vosotros. Parece que mi pasión por los motores la he heredado de ti, abuelo. Ojalá pudiéramos seguir hablando de ello. De mi abuela Vito he aprendido a no conformarme nunca. Aún no he llegado al 10, como siempre me decías, pero seguiré luchando por ello. Aún así, se que te sentías orgullosa de mi.

També volia agraïr a sa meva segona familia, Mari, Toni, Meme, Xesc i Silvia, que me heu tractat com un fill, net i germà més. Vos estim.

Per acabar, m'agradaria agraïr a sa meva companyera de vida. Maria, pràcticament duc mes temps de sa meva vida amb tu que sense tu. Has tengut que passar moltes etapes de sa meva vida molt complicades, desde sa carrera universitaria, màster, i si no tenies suficient, doctorat. Encara i així, sempre has estat a n'es meu costat, recolzant-me, inclús en moments en que estava insoportable. Estic segur que de no ser per tu jo no estiria aquí on he arribat. Tu sempre has estat sa que m'ha animat i impulsat per seguir endavant. Se que per tu, no ha estat fàcil prendre segons quines decisions, per lo que t'ho agraeixo infinitament. T'estim moltissim, gràcies per fer-me millor persona.

Table of Contents

List of figures

List of tables

Nomenclature

$(A/F)_{st}$	Stoichiometric air-fuel ratio
2C	Two Color Pyrometry technique
aSOE	after start of energizing
aSOI	after start of injection
aTDC	after top dead centre
BEV	Battery electric vehicle
BSEC	Brake-specific energy consumption
BTE	Brake thermal efficiency
CAD	Crank angle degree
CDS	Controlled diffusive spray
CFD	Computational fluid dynamics
CH_2O	Formaldehyde molecule
CI	Compression ignition
CIV	Combustion image velocity
CN	Cetane number
CPF	Constant-pressure flow facility
CSN	Pistons used in this thesis (N = 1, 2, 3)
Deq	Equivalent diameter
DI	Direct injection
DME	Dimethyl ether

ECN	Engine Combustion Network
ECS	Engine control system
EGR	Exhaust gas recirculation
EM	Electromagnetic
EOI	End of injection
EU	European Union
FL	Flame length
FWHM	Full width at half maximum
GHG	Greenhouse gasses
GM	General Motors
HFI	High-flow injector
HPHT	High-pressure and high-temperature vessel
HSDI	High-speed direct-injection
HVO	Hydrotrated vegetable oil
ICE	Internal combustion engines
ICEV	Internal combustion engines vehicles
ID	Ignition delay
IMEP	Indicated mean effective pressure
KL	Integral value of soot extinction coefficient along the light path
LCA	Life cycle assessment
LFI	Low-flow injector

LHV	Low heat value
LII	Laser-induced incandescence
LL	Liquid length
LOL	Lift-off length
LTC	Low-temperature combustion
NEDC	New European Driving Cycle
NO_X	Nitrogen oxides
O_2	Oxygen molecule
OH	Hydroxyl radical
OH^*	Excited state of hydroxyl radical
OME_n	Oxymethylene ethers
PAH	Polycyclic aromatic hydrocarbon
P_{back}	Back pressure
PCV	Plano-Concave lens
PCX	Plano-Convex lens
P_{exh}	Exhaust pressure
PID	Proportional-Integral-Derivative controller
P_{inj}	Injection pressure
PLIF	Planar laser-induced fluorescence
PM	Particulate matter
PN	Particulate number

RCEM	Rapid compression expansion machine
RMZ	Radial mixing zone
RoHR	Rate of heat release
SA	Spray A-orifice
SD	Spray D-orifice
SOI	Start of injection
STD	Standard 8-hole conical nozzle
STP	Spray tip penetration
THC	Total hydrocarbons
T_{int}	Intake temperature
TTW	Tank-to-wheel
TWC	Three-way catalyst
UHC	Unburned hydrocarbons
UV	Ultraviolet
VW	Volkswagen
WTT	Well-to-tank
WTW	Well-to-wheel
Y_{O2}	Air mass fraction
YSI	Yield sooting index
Z_{st}	Stoichiometric mixture fraction

Chapter 1

Introduction

Content

1.1 Introduction

This first chapter aims to give the global context that has given rise to the completion of this doctoral thesis, as well as the meaning it has in the research group where it has been carried out. Finally, the chapter ends by listing the main objectives proposed to fulfill the thesis and briefly describing the structure of the different chapters that make up the document.

1.2 Context and Motivations

Climate change is currently occurring and will continue to worsen in the future despite the efforts to decrease emissions. Occurrences of severe weather and other climate-related hazards, such as floods and droughts, will become more common and severe in various areas, harming ecosystems, the economy, industries, and human health. As a result, it is crucial to adjust to the impacts of climate change, and these actions should be tailored to the specific conditions in different parts of Europe [1].

The transportation sector significantly impacts pollutant emissions, so much effort is being invested in reducing them. Within this sector, road vehicles, predominantly powered by internal combustion engines (ICE), produce two primary pollutant emissions: tailpipe and greenhouse gas (GHG) emissions (when considering the life cycle of CO_2).

Tailpipe emissions are pollutant emissions associated with the vehicle exhaust outlet. They are produced due to fuel combustion within the engine, making them emissions that occur during the vehicle operation. These emissions will depend on the fuel properties; thus, its chemical composition plays a crucial role in forming pollutants. The main pollutant emissions associated with diesel, as the reference fuel, are carbon monoxide (CO), nitrogen oxides (NOx), hydrocarbons (HC), and particulate matter (PM).

These emissions are considered local since they are located at the exhaust outlet. Thus, they are released directly into the immediate environment around the vehicle producing them. This has significant implications for air quality near roads and urban environments. This way, tailpipe emissions are strictly regulated by imposing limits to improve air quality and minimize environmental impact.

Since 1992, the EU has introduced increasingly stricter limits on light-duty and heavy-duty vehicle emissions through a series of ‘Euro’ standards. The latest and most stringent of these standards is Euro 6. Since the Euro standards were introduced, nitrogen oxides (NO_X) limit for diesel car engines has been reduced by 84% and particulates (PM) by 90%, while heavy-duty engines have been reduced by 95% and 97%, respectively [2].

A new Euro regulation, Euro VII, is being proposed to take effect in 2025. It aims to reduce approximately 56% of NO_X emissions and 39% of particle emissions by 2035 [3]. This framework highlights the significant need to advance combustion systems that meet the requirements of these regulations, leading to cleaner technologies in the transportation sector.

Regarding GHG emissions, mainly CO_2, they are highly detrimental to the atmosphere as they contribute to the greenhouse effect and climate change. Their formation occurs throughout the vehicle life cycle (also including the CO_2 emitted by the exhaust system) and the process of generating the energy source on which the vehicle operates. All these processes mentioned above are considered in the Life Cycle Assessment (LCA). This methodology evaluates the vehicle environmental impact throughout its life, from raw material extraction to final disposal.

Figure 1-1 highlights the LCA methodology. The methodology considers the entire vehicle life cycle from raw material processing (cradle) to the disposal phase (grave), called *cradle-to-grave*. It includes assembling, maintaining, and refueling during its complete life cycle and finally dismantling and recycling its components. Inside the *cradle-to-grave* cycle, *cradle-to-gate*, *well-to-tank* (WTT), *tank-to-wheel* (TTW), and *end-of-life* phases consider different processes. *Cradle-to-gate* is a partial product life cycle from raw material to the vehicle production factory gate phase only. The WTT phase focuses on the energy source to the tank storage, while the TTW focuses on the energy carrier as tank to the vehicle propulsion system during its operation. The combination of WTT and TTW is called well-to-wheel (WTW). It is usually used to analyze the energy conversion efficiency of the vehicle, total energy conversion, carbon footprint, and emission impacts.

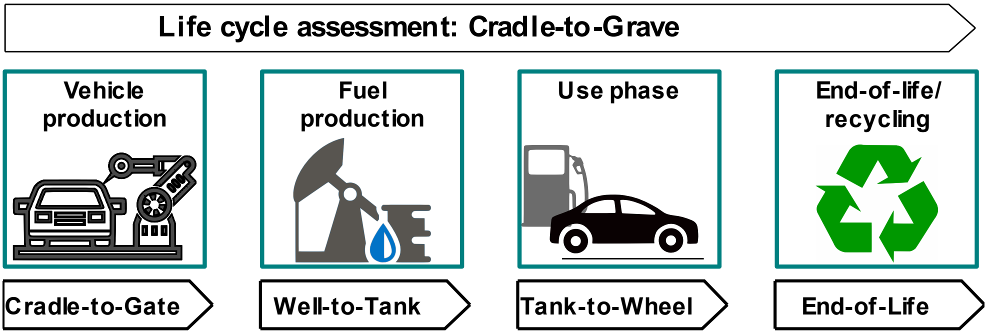

Figure 1-1 Life Cycle Assessment (LCA) of a vehicle.

Against tailpipe emissions, which are considered local emissions, CO_2 emissions are considered global emissions. This is because these emissions generated by a country or region can affect the climate and contribute to climate change anywhere in the world. Therefore, driven by the objective of reducing climate change as outlined in the Paris Agreement, regulations have emerged to address CO_2 emissions from vehicles.

The main objective of these regulations is to establish mandatory limits for the average CO_2 emissions of new vehicles sold in Europe. In this sense, the European Union aims to achieve climate neutrality by 2050 with a net-zero greenhouse gas emissions economy. This objective is at the core of the European Green Deal [3] and aligns with the EU's commitment to global climate action under the Paris Agreement. This strategy is primarily based on drastically reducing GHG emissions through using cleaner and more efficient technologies, promoting renewable energy sources, improving energy efficiency, and implementing sustainable practices.

In this regard, electrification as a vehicle propulsion system has emerged as the primary pathway to achieve these objectives. These vehicles eliminate tailpipe emissions (provided they are fully electric) as they lack an exhaust pipe, making it possible to eradicate local emissions. Therefore, to reach the net zero GHG emissions goals, eliminating internal combustion engines by 2035 was proposed, replacing them with battery electric vehicles (BEVs).

However, certain European countries opposed this elimination mainly due to significant shortcomings in vehicle electrification currently, such as the necessary infrastructure to supply the entire fleet of vehicles (over 300 million ICE vehicles in the EU according to the eFuel Alliance [4]), the limited range of vehicles due to battery capacity (especially in heavy-duty applications), and the lack of raw materials for battery manufacturing.

Furthermore, the origin of the electric power used in vehicles is crucial for achieving the objectives. If the electricity production comes from renewable energy sources, it will help reduce the carbon footprint. However, using this energy for electric vehicles will contribute significantly to CO_2 emissions if it is obtained from non-renewable sources. An example can be seen in Figure 1-2, where the comparison of electricity production (a) and the percentage of renewable energy sources used for that electricity (b) is shown for six different countries between 2018 and 2021 [5].

As seen in (a), China has experienced the most significant growth in electricity production, increasing by 9.7% between 2020 and 2021 and significantly surpassing production compared to other represented countries. However, in (b), it is evident that only 30% of that electricity is obtained from renewable sources in China, while countries like Sweden and Norway exceed 60%. This clearly shows that implementing electricity as a propulsion system for vehicles will depend on geographical location to have a favorable effect on reducing CO_2 emissions.

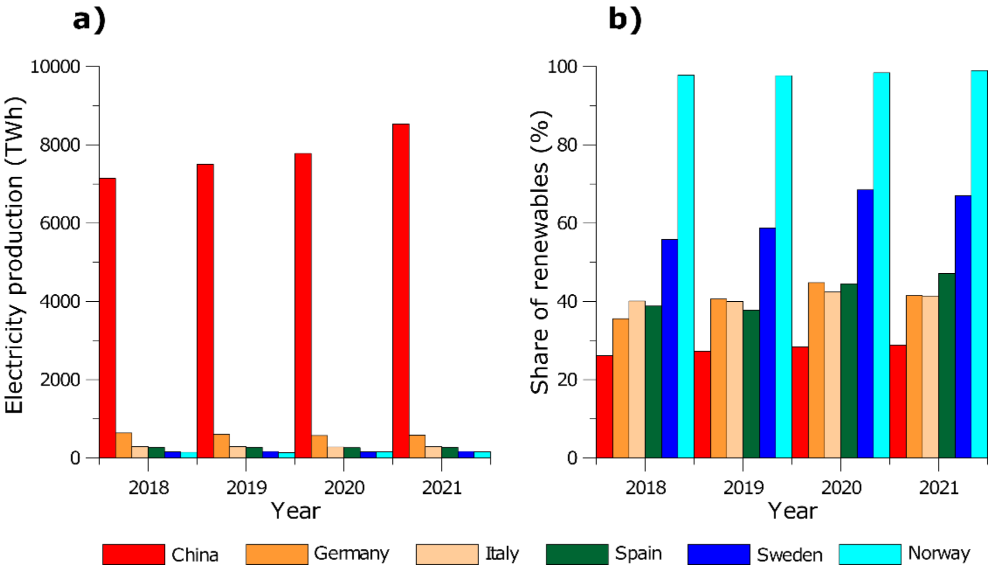

Figure 1-2 Electricity production (a) and share of renewable in electricity production (b) in China, Germany, Italy, Spain, Sweden, and Norway between 2018 to 2021. Source: [5].

In addition to considering the source of electricity, it is important to consider the significant impact of battery manufacturing and their range. The *Frontier Economic* company discussed the CO_2 emissions using LCA methodology comparing a compact class vehicle powered as conventional ICE and electric battery in Europe (as reference), Germany, and China [6]. The Volkswagen (VW) Golf as ICEV can cover a distance of 800 km without a problem with one tank (based on a tank size of 40 l and a consumption of 5 l/100 km). These ranges are not reached by the BEVs currently available. The Nissan Leaf, as a BEV with a battery capacity of 40 kWh and a consumption of 21 kWh/100 km, could not cover even a quarter of this distance. If the battery capacity (ignoring technical limitations) was scaled up to meet the required range, a battery with a capacity of around 170 kWh would be needed in the VW Golf example for a range of 800 km.

This would also have a negative impact in terms of CO_2 emissions. Figure 1-3 shows the contribution of CO_2 using the LCA methodology. The results show that although the *tank-to-wheel* (use phase) is zero for BEVs, there is a considerable increase in the *well-to-tank* (fuel production) and *cradle-to-gate* (vehicle production) phases. With the current electricity mix, producing this type of battery in China alone would cause almost as much CO_2 as the comparable vehicle with a combustion engine over its entire lifetime. Even when produced using supposedly “green” methods in the EU, the life cycle emissions are more than 35% higher than the ICEVs.

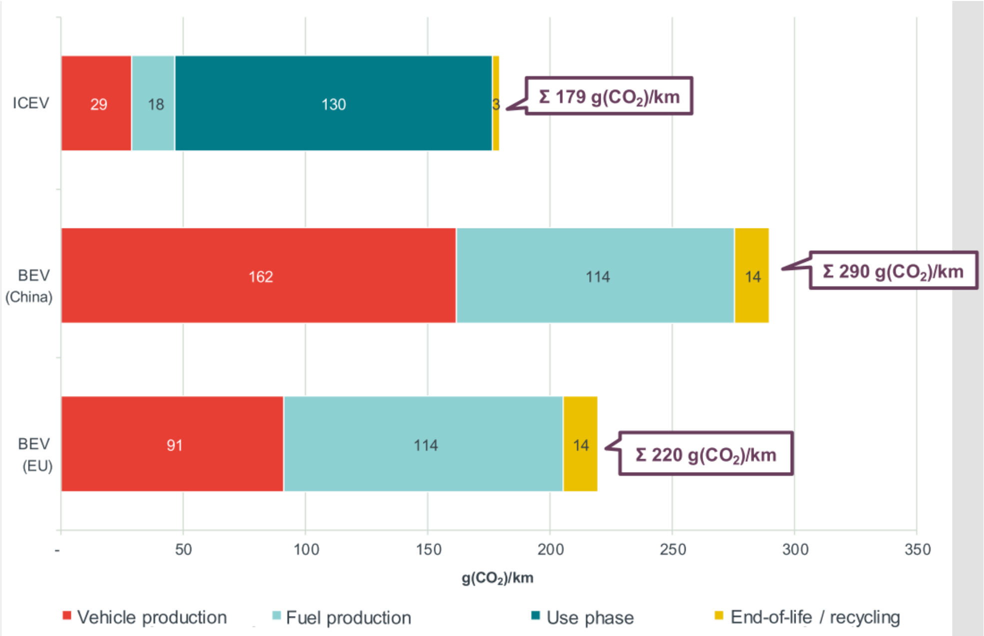

Figure 1-3 CO_2 emissions for ICEV (Germany), BEV (China) and BEV (EU) over the entire lifetime. Source: [6].

These countries that opposed eliminating internal combustion engines proposed using synthetic fuels, also known as electro-fuels (e-fuels). These fuels are generated from CO_2, H_2O, and electricity. As mentioned for electric vehicles, the origin of electricity will be crucial to determining whether the use of these synthetic fuels contributes positively or negatively to achieving the net zero GHG emissions plan objectives. With these fuels, it is possible to achieve a net balance in the CO_2 life cycle since the tailpipe emissions associated with them would be offset by capturing CO_2 from the atmosphere or CO_2 emission sources required for their production.

Currently, these fuels present certain challenges, such as high production costs and the need for large amounts of renewable electricity. Nonetheless, they are appealing because they can be used in new internal combustion engines, hybrid vehicles, and even the existing fleet, replacing fossil fuels entirely or partially. Introducing just 5% of e-fuels into conventional fuels could save 60 million tons of CO_2, equivalent to taking 40 million cars off the road for an entire year, according to studies conducted by the eFuel Alliance [4].

According to a study by Prognos AG, the Fraunhofer Institute UMSICHT, and DBFZ [7], production costs are expected to range from 0.70 to 1.33 euros per liter by 2050 (Figure 1-4). Thanks to the promising results with a small amount of e-fuel in the fuel mixture, it could avoid a significant increase in prices at gas stations.

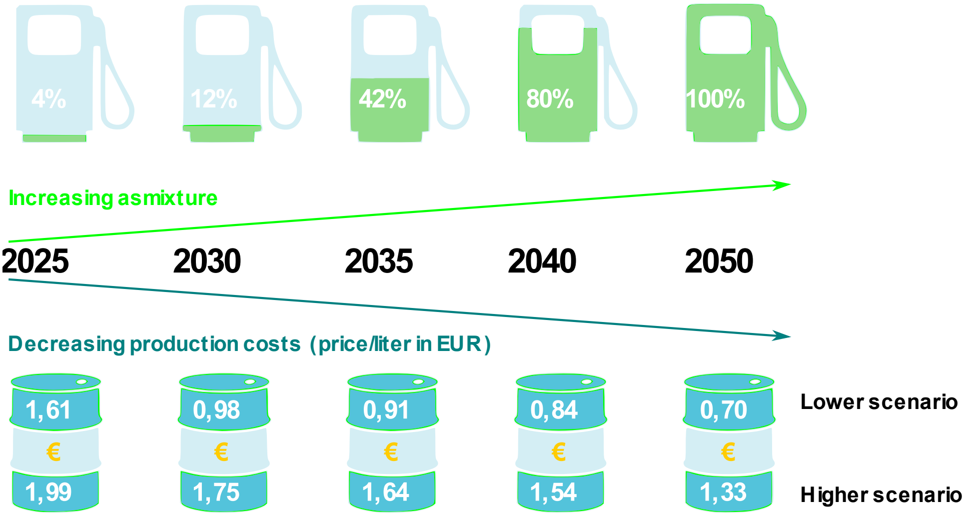

Figure 1-4 Increasing blending of e-fuels and simultaneously decreasing production costs ensure affordable consumer prices. Source: [7]

The *Frontier Economics* company made a similar comparison than in Figure 1-3. Using the same LCA methodology, they include an ICEV fueled with 70% of e-diesel as an e-fuel in Germany (Figure 1-5). The company reported that an ICEV fueled by a blend with e-fuel will generate around the same volume of CO_2 emissions as BEV (+2g(CO_2)/km), reducing 84g(CO_2)/km compared to using a conventional diesel.

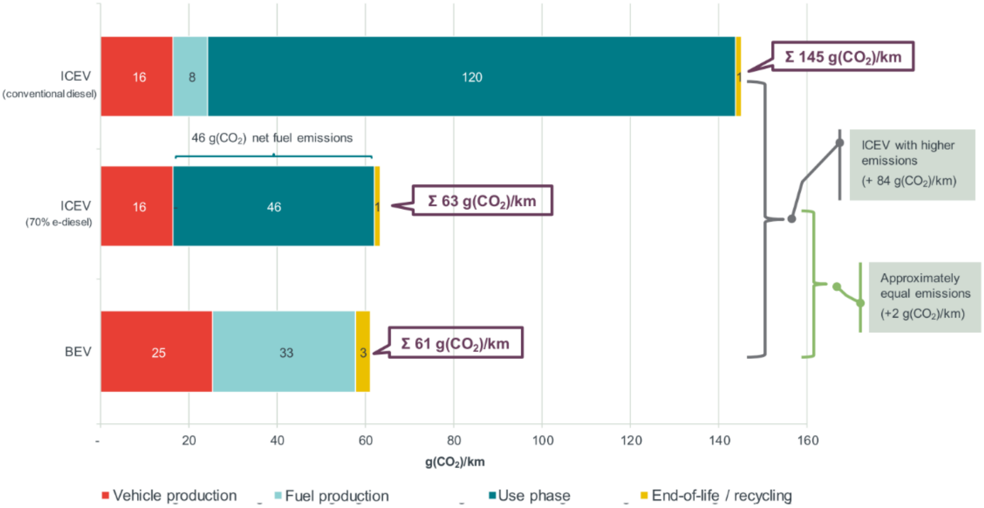

Figure 1-5 CO_2 emissions for ICEV (conventional diesel), ICEV (70% e-diesel), and BEV over the entire lifetime in Germany. Source: [6].

In this manner, e-fuels emerge as a viable option for producing carbon-neutral fuels, offering another complementary technology to vehicle electrification. Notably, they can be swiftly implemented, making them instrumental in achieving the goals set for 2050 while addressing the current shortcomings of electrification.

1.3 Background

As discussed in the previous section, the use of e-fuels can help achieve the goal of achieving a carbon-neutral footprint for the transportation sector by 2050. The study of such fuels, through the analysis of their physicochemical properties and their behavior under real engine conditions, is vital to achieve these objectives. One of the fuels that has shown great potential for engine applications is OME_X. This fuel, which will be discussed in more detail in Chapter 2 of this Doctoral Thesis, is an oxygenated fuel that can be obtained from renewable sources and offers significant benefits in reducing pollutant emissions.

Due to these promising results, the research group where I have carried out this thesis has focused on studying this fuel. A series of studies conducted on engines simulating real operating conditions demonstrated that this fuel complies with the current Euro VI regulations in terms of soot and NOx emissions [8]. However, this particular fuel presents some compatibility issues with the infrastructure of current engines, leading to the reduced lifespan of certain engine components. Using this e-fuel as an additive to a conventional fuel, such as diesel, has been proposed as a solution. Regarding emissions, it has been observed that these blends show significant reductions in soot compared to using diesel alone, highlighting the potential of this fuel as an additive to conventional fuel [9].

In addition to analyzing tailpipe emissions, Benajes et al. [10] conducted a series of numerical simulations of a vehicle based on experimental measurements from a heavy-duty multicylinder engine. They found that in the analysis of WTW emissions, OME_X can reduce the carbon footprint, primarily due to the fuel production method based on capturing CO_2 from the atmosphere and using renewable electricity.

These promising results led to a desire to understand and deepen the knowledge of its fuel combustion process. Therefore, conducting studies in facilities that provide optical access to the combustion chamber becomes crucial for further characterizing this fuel. Following these objectives, the thesis of García-Carrero [11] and Lewiski [12] focused on such characterization, using a High-Pressure High-Temperature (HPHT) facility and an optical engine, respectively. These theses served as predecessors to the current doctoral dissertation, and Chapter 2 will delve into them in more detail, while this chapter will briefly mention essential aspects to provide context for the importance of this Doctoral Thesis.

García-Carrero [11] thesis focused on a series of studies based on OME_X characterization in a high-pressure and high-temperature (HPHT) facility by determining a range of geometric and temporal parameters of the jet under both inert and reactive conditions. This analysis was carried out under reference conditions specified by the Engine Combustion Network (ECN) [13], which will be further discussed in the next chapter. The main reported results showed that this fuel appears not to form soot during the combustion process, which aligns perfectly with previous studies conducted on the engine.

The characterization of OME_X through the García-Carrero study had certain gaps, such as not studying the effect of this fuel under more realistic engine conditions where the injector is multi-hole, the engine dynamics influence the jet, and the existence of jet-wall interaction due to the presence of the piston. Additionally, as mentioned earlier, one of the current issues with OME_X is its incompatibility with the engine infrastructure. Therefore, it is necessary to analyze the combustion process of OME_X when mixed with diesel as well.

In order to address these gaps and further understand the behavior of OME_X in engine-like conditions, it becomes essential to conduct studies with more complex setups that can replicate the real-world challenges faced by the fuel in practical engine applications. By investigating the OME_X/diesel blend, researchers can gain insights into its compatibility with existing engine components and assess its potential as a viable alternative fuel option in the transportation sector.

In this context, the study conducted in Lewiski thesis [12] focused on the effect of using different blends of OME_X/diesel in a light-duty optical engine with optical access to the combustion chamber and evaluating various piston geometries. The thesis examined different percentages of OME_X/Diesel and the pure use of both OME_X and diesel, reporting reductions in soot formation in the cylinder when using different fuel blends. However, the clear effects of OME_X became evident when using a 50% OME_X mixture.

Furthermore, Lewiski analyzed the potential of an unconventional piston geometry in reducing soot formation when using pure diesel. The main results indicated that this piston geometry directly influenced the flame movement, allowing the flame to be redirected to optimal piston areas for soot oxidation. This effect contributed to a reduction in soot formation in the engine combustion process.

The findings from Lewiski thesis shed light on the potential benefits of OME_X/diesel blends in reducing soot emissions and optimizing combustion processes, providing valuable insights for the future development of more efficient and cleaner internal combustion engines.

The work carried out in the aforementioned theses demonstrates that OME_X is a strong candidate for the total or partial replacement of diesel, thereby aiding in achieving carbon neutrality goals by 2050. However, these studies highlight the need to further delve into the characterization of this fuel, addressing gaps that have not been covered yet and answering questions such as:

1. How is the flame structure of OME_X?
2. How does OME_X/diesel behave in larger displacement engines, where the swirl effect due to piston movement is much lower?

3. How does an unconventional piston geometry in larger-sized pistons, where the jet takes longer to impact the wall, affect the combustion process?
4. How does that piston geometry affect the combustion process when using OME_X?

These and some other questions are aimed to be addressed in the current thesis.

1.4 Objectives

The entire previous discussion highlights the importance of using e-fuels as clean fuels for Internal Combustion Engines (ICE) to achieve carbon neutrality goals by 2050. Among the wide range of e-fuels, OME_X stands out in the literature as a potential fuel for this objective. This is mainly due to its relative ease of direct application to the engine and its properties, which offer benefits in reducing pollutant emissions, allowing compliance with Euro regulations for vehicle circulation. However, further characterization of this fuel is necessary, with a more extensive database on combustion process characteristics considering real operating conditions that have not been fully explored in the literature.

In this way, the main objective of this doctoral thesis is to **improve the understanding of the combustion process of OME_X and OME_X/diesel blends under engine conditions and to identify the relevance of constructive and operational conditions on the mixing/combustion process and pollutant formation**.

This general objective is further specified in the following sub-objectives:

- To experimentally determine the flame structure of e-fuels, identifying the regions where ignition occurs at low temperature and the transition to high-temperature combustion. The aim is to verify if the combustion of e-fuels follows the known pattern of diffusion combustion with diesel-type fossil fuels.

  At this point, controlled experimental measurement conditions are used to isolate the spray to study the high-temperature and low-temperature regions of the flame using the Planar Laser-Induced Fluorescence technique (PLIF) combined with simultaneous intensified OH* high-speed imaging. This study continues the research conducted in García-Carrero thesis [11]. Therefore, it has been carried out in the same experimental setup under the same reference operating conditions specified by the Engine Combustion Network (ECN). This study contributes to increasing the characterization databases of two clean fuels with potential use in transport applications.

- Identify the relevance of some particular aspects of piston geometry on mixture formation, combustion development, and soot formation under engine conditions.

  This study tests two non-conventional piston designs in an internal medium-duty CI optical engine fueled with diesel. The tests were conducted under engine conditions, including simulated EGR conditions, to mimic more evident soot formation and oxidation effects. This way, the 2C-pyrometry technique using high-speed cameras and intensified OH^* high-speed imaging are applied. This study aims to expand on the research conducted in Lewiski thesis [12], thus examining the effect of that geometry in a larger-sized engine.

- To understand OME_X/diesel blends combustion behavior using non-conventional piston geometry under engine conditions.

  Despite the benefits of OME_X in reducing soot formation, this fuel presents a series of problems when used directly in the engine. For this, using a non-conventional piston geometry allows OME_X quantity reduction in the fuel with benefits in in-cylinder soot reduction. The same optical techniques used in the previous point are applied.

- To contribute to the research group methodological procedure for implementing the Planar Laser-Induced Fluorescence (PLIF) technique for OH detection.

  Although the PLIF technique has been used for many years and is well known in the field of combustion research, this thesis contributes to the first time it has been implemented for OH measurements in this research group. This leads to difficulties in implementation, both in experimental measurements, such as tunning the laser to the corresponding absorption band of the molecule, and image processing.

1.5 Approach and Content

This section aims to present the structure and working methodology followed in this doctoral thesis and a brief description of each document chapter. The thesis document consists of seven chapters, including the current Chapter 1.

Chapter 1 briefly discusses the global context that has motivated the study carried out in this thesis. Furthermore, the main objectives and the manuscript structure were introduced.

Chapter 2 presents a general description of the conventional diesel combustion process, focusing on the diesel flame structure presented by Dec [14] as a simple model to describe the flame structure in ideal conditions. Then, a more complex model reported by Musculus [15] is presented as a more detailed model to describe the flame structure in more realistic conditions. In addition, this chapter includes a bibliographic review of the different studies on the flame structure reported by the scientific community. Moreover, a general description of the in-cylinder air movement, specially generated by different bowl piston shapes, is discussed to understand how it affects the air-fuel mixture and soot formation/oxidation processes. Besides that, the section also describes the potential of replacing fossil fuels with e-fuels in compression ignition engines and their recent applications. In this way, the chapter covers the theoretical framework on which this thesis is based.

Chapter 3 delineates the tools and methodology employed in crafting the present thesis. It delves into a comprehensive explanation of the various optical facilities utilized for the experiments, elaborates on the test matrix, and provides an in-depth exploration of optical diagnostics techniques. Furthermore, this chapter scrutinizes the diverse fuels, piston geometries, and theoretical tools brought into play throughout the study.

The following chapters **Chapter 4** to **Chapter 6** pertain to the discussion of the thesis results.

In **Chapter 4,** the study of two synthetic fuels, OME_X and $OME_{1,}$ is presented. These fuels belonging to the e-fuel family look promising regarding soot reduction in ICE applications and achieving a neutral carbon footprint. For this, the results of the flame structure for both fuels, through the high-temperature reaction zone (traced by OH radical) and the low-temperature reaction zone (traced by CH_2O), are reported using the PLIF technique. In addition, OH^* high-speed images are simultaneously used to trace the high-temperature combustion process as a good marker of the Rate of Heat Release (RoHR).

Chapter 5 focused on the analysis of soot reduction by using two different real bowl piston shapes. Both pistons have protrusions, named radial lips in this thesis, on the periphery of the bowl, but with different geometry to analyze the effect on the combustion behavior. The fuel used is diesel as a reference fuel to characterize the evolution of soot inside the cylinder due to the piston effect. The optical analysis is carried out using three optical techniques: 2-Color pyrometry, OH^* chemiluminescence, and natural luminosity. The facility used in this study was a medium-duty optical diesel engine under engine-like conditions focusing on EGR methods, as a high-soot condition.

Finally, the last chapter of the results section, **Chapter 6**, aimed to analyze the combined effect of OME_X with the radial lips piston geometry in the combustion behavior using the same optical engine and techniques that the previous chapter. OME_X as an additive in diesel is helpful to avoid issues of this e-fuel with the engine infrastructure. Besides the benefits of OME_X in the blend, applying EGR methods increases the soot formation inside the cylinder when using conventional piston geometries. In this way, the results obtained using the radial lips piston geometry combined with several OME_X/diesel rates are reported in this chapter.

Chapter 7 serves as a condensed overview of the primary findings gleaned from this thesis. Moreover, it offers recommendations for prospective endeavors that, while not within the scope of this thesis, hold significant promise for enhancing the body of work.

Bibliography

[1] Air pollution — European Environment Agency n.d. https://www.eea.europa.eu/themes/air (accessed December 13, 2022).

[2] AECC website n.d. https://www.aecc.eu/ (accessed September 12, 2023).

[3] Climate European Comission. An Official Website of the European Union n.d. https://climate.ec.europa.eu/index_en (accessed July 10, 2023).

[4] eFuel Alliance e.V. 2022 n.d. https://www.efuel-alliance.eu/ (accessed July 14, 2023).

[5] Enerdata n.d. https://www.enerdata.net/ (accessed September 14, 2023).

[6] Kühn E, Ates A, Perner J, Steinfort T. THE OVERALL CO2 IMPACT FOR DRIVE TECHNOLOGIES IN INDIVIDUAL TRANSPORT TODAY AND IN THE FUTURE. Berlin: 2019.

[7] Hobohm J, Auf Der Maur A, Dambeck H, Kemmler A, Koziel S, Kreidelmeyer S, et al. STATUS AND PERSPECTIVES OF LIQUID ENERGY SOURCES IN THE ENERGY TRANSITION. 2018.

[8] García A, Gil A, Monsalve-Serrano J, Lago Sari R. OMEx-diesel blends as high reactivity fuel for ultra-low NOx and soot emissions in the dual-mode dual-fuel combustion strategy. Fuel 2020;275:117898. https://doi.org/10.1016/j.fuel.2020.117898.

[9] García A, Monsalve-Serrano J, Villalta D, Fogué-Robles Á. Evaluating OMEx combustion towards stoichiometric conditions in a compression ignition engine. Fuel 2021;303:121273. https://doi.org/10.1016/J.FUEL.2021.121273.

[10] Benajes J, García A, Monsalve-Serrano J, Martínez-Boggio S. Potential of using OMEx as substitute of diesel in the dual-fuel combustion mode to reduce the global CO2 emissions. Transportation Engineering 2020;1:100001. https://doi.org/10.1016/j.treng.2020.01.001.

[11] García Carrero AA. Experimental Study of the Fuel Effect on Diffusion Combustion and Soot Formation under Diesel Engine-Like Conditions. Universitat Politècnica de València, 2022. https://doi.org/10.4995/THESIS/10251/179997.

[12] Lewiski F. Analysis of the combustion process and soot formation in a single cylinder optical engine fueled with e-fuels and using different piston geometries. Universitat Politècnica de València, 2021. https://doi.org/10.4995/Thesis/10251/180351.

[13] Engine Combustion Network n.d. https://ecn.sandia.gov/ (accessed February 22, 2023).

[14] Dec JE. A conceptual model of DL diesel combustion based on laser-sheet imaging. SAE Transactions 1997:1319–48.

[15] Musculus MPB. Multiple Simultaneous Optical Diagnostic Imaging of Early-Injection Low-Temperature Combustion in a Heavy-Duty Diesel Engine, 2006. https://doi.org/10.4271/2006-01-0079.

Chapter 2

State of the Art

Content

2.1 Introduction

In the previous chapter, the current situation regarding pollutant emissions in the transportation sector has been shown, as well as the need to reduce them in order to meet the new legislation in force. For this, the challenges related to pollutant emissions from diesel engines have led the industry and research centers to investigate new solutions to minimize or eliminate them. One such alternative is in-cylinder pollutant reduction, which has been widely studied. In this way, non-fossil fuels are proposed as an option to address this issue. Using these fuels allows the transition to clean fuels, reducing the dependence on fossil-based fuels. In this way, this chapter starts reviewing the literature on the evolution of diesel flame structure and its combustion behavior. The understanding of the diesel combustion process has deepened, and the definition of the flame structure has improved thanks to the evolution of diagnostic techniques. This section will end by describing the current diesel flame structure, showing the recent studies reported by various authors. A good understanding of this description is crucial to characterize the behavior of the combustion process and pollutant formation. The following section introduces the OME_n family fuels. These e-fuels show great potential to be used in internal combustion engines, demonstrating excellent results in reducing pollutants. Therefore, a compilation of the most notable properties of these fuels will be presented, along with results obtained from various studies conducted in the literature.

2.2 Overview of Diesel Combustion Process.

2.2.1 Combustion Phases

The most classic way of studying the evolution of the combustion process in diesel engines is by comparing the temporal evolution of the fuel mass injected per time unit (injection rate - $\dot{m}_{inj}$) and the apparent Rate of Heat Release (aRoHR). The last calculation is based on applying the first law of thermodynamics to the volume enclosed in the cylinder at each instant, as explained by Heywood [1]. The pressure changes can relate directly to the amount of fuel chemical energy released due to combustion. Figure 2-1 shows an example of a comparison between both temporal evolutions obtained experimentally in a direct injection engine. The characteristic diesel combustion phases [1] are highlighted in the figure.

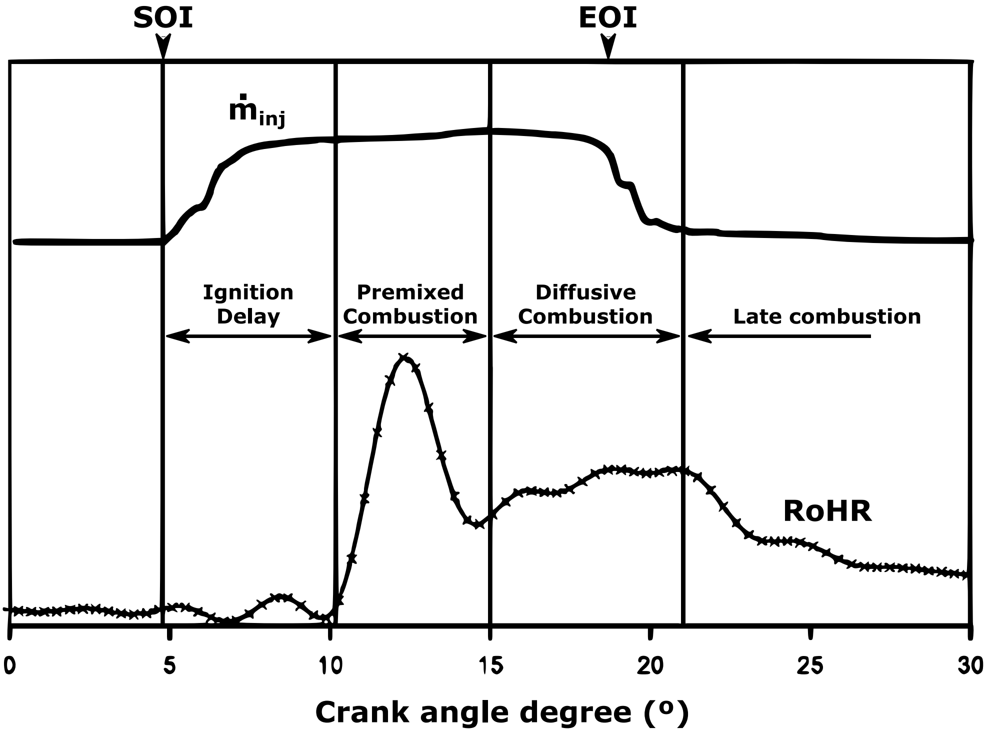

Figure 2-1. Definition of combustion stages from comparing fuel injection rates (upper curve) and heat release (lower curve).

The *Ignition Delay* phase corresponds to the first interval time after the start of the injection process (SOI), corresponding to when the injection rate increases above zero, is characterized by air-fuel mixing. This phase is governed by physical processes such as atomization, air entrainment, and evaporation. The air-fuel mixture in contact with the oxygen inside the combustion chamber makes the mixture unstable. This instability produces the appearance of low-intensity chemical pre-reactions, resulting in the breaking of the fuel molecules into shorter hydrocarbon chains as well as the formation of free radicals (highly reactive unstable intermediates). The pre-reactions culminate in the spontaneous autoignition of the mixture, which means the appearance of a highly exothermic reaction zone in the jet, defining the onset of combustion. This process is manifested in the graph above by a sudden increase in the heat release rate, thus completing the ignition delay phase.

Once appreciable heat release begins, three further phases are distinguished: *Premixed Combustion*, *Diffusive Combustion*, and *Late Combustion*.

During the *Premixed Combustion*, characterized as a transient phase, the release of chemical energy within the fuel flammability limits mixed with the air occurs rapidly. The rapid energy release comes from the combustion of the fuel-rich mixture, resulting in the first characteristic heat release peak (around 12˚ in Figure 2-1). The duration of this phase is typically defined from the beginning of combustion until the first minimum of the heat release curve.

The third phase, *Diffusive Combustion* phase, is controlled by the rate of the mixture accessible for burning. Several processes are involved, such as liquid fuel atomization, vaporization, air-fuel mixing, and chemical reactions within the spray. However, the air-fuel mixing process in a rich-mixture environment is the primary controlling factor for the burning rate. In addition, this mixing process is controlled by the spray momentum. As the injection process ends, the heat release rate decay is observed as the mixing process worsens due to the absence of the turbulent kinetic energy generated by the jet momentum.

Finally, the last diesel combustion phase, known as *Late Combustion*, appears during the expansion stroke. The RoHR persists, albeit at a diminishing pace, attributed to various factors. A portion of the fuel may remain unburned, while some of the fuel's energy remains in soot and combustion byproducts with a high fuel concentration, which can still be released. Additionally, the nonuniform composition of the cylinder charge and the mingling of burnt gases with air during this phase contribute to a more thorough combustion process and a decrease in dissociated product gases. Furthermore, as the temperature of the cylinder gases decreases during expansion, the kinetics of the final burnout processes slow down.

2.2.2 Autoignition

As mentioned previously, the air-fuel mixing formed during the *Ignition Delay* phase is unstable due to the interaction with the oxygen inside the combustion chamber and autoignites after a certain time has elapsed since the injection process. The reactions that lead to the release of heat appear initially in those locations of the fuel spray where an air-fuel mixture with sufficient temperature and composition for initiating the chemical reaction has been formed. This leads to the development of active intermediate species and the release of energy that will establish the oxidation reaction in the fuel spray. This heat release decisively influences the spray local thermodynamic conditions, simultaneously acting on the physical mixing process and developing chemical reactions. Therefore, the physical and chemical aspects of the combustion process are coupled from the beginning.

The autoignition phenomenon has been a subject of interest in characterizing the combustion process and flame structure. During the auto-ignition process, two stages can be highlighted: one associated with low temperature, which occurs before the *Premixed Combustion* phase, and the high-temperature stage, which appears with the drastic increase of the pressure in the combustion chamber, characteristic of the beginning of the *Premixed Combustion* phase. In 1998, Dec & Espey [2] analyzed this phenomenon in an optical engine employing imaging techniques to detect the chemiluminescence radiation. According to the measured spectra, they observed that the origin of the chemiluminescence radiation formed during the first stage of the autoignition phase is mainly due to the presence of formaldehyde (CH_2O) and CH radicals. These results were consistent with the spectral distribution obtained by Gaydon [3] in homogeneous mixtures of propane and air with rich dosing. Subsequently, Kosaka et al. [4] detected formaldehyde using *Laser Induced Fluorescence* (LIF) technique. The results were consistent with those of Dec and Espey, showing that this species appears to be a stable intermediate compound that only appears in the low-temperature autoignition process known as *cool flame*. On the other hand, Dec and Espey [2] observed that the appearance of OH radicals and soot characterizes the autoignition process associated with high-temperature reactions. Moreover, these OH radicals are not observed during the low-temperature stage and are, therefore, suitable to indicate the onset of high-temperature reactions [2,5,6].

At the end of the autoignition process, the process reaches conditions that favor the establishment of a self-sustained reaction. This results in the appearance of a stable diffusion flame front, which will maintain its basic structure throughout the rest of the combustion process as long as the injection process is maintained. The establishment of this reaction zone occurs during the end of the *Premixed Combustion* phase, marking the actual start of the *Diffusion Combustion* phase, and has been studied by Dec and Coy [6] using the OH LIF technique. This radical is a good marker to identify where the reaction between fuel and air occurs. The study indicates that the formation of the diffusion flame begins near the maximum RoHR during the premixed phase. Initially, this reaction zone is established around the jet front periphery and propagates upstream to a certain distance from the injector, known as the Lift-Off Length (LOL) distance.

2.2.3 Diffusion Combustion Phase. Diesel Flame Structure

In summary, once all the steps of the jet autoignition process are completed, the process enters the so-called *Diffusion Combustion* phase, extending until all the injected fuel is consumed. This phase is named based on the traditional classification of combustion processes (for example, as proposed by Glassman [7]), where combustion is classified as diffusion when the fuel and oxygen are not previously mixed (*Premixed Combustion*) but mixing and combustion occur simultaneously. During this phase, the flame front created in the previous stages consolidates, which can continue to self-sustain from the convective and diffusive supply of fuel and oxygen. The convective fuel supply is essential as it drives the mixing process through the momentum introduced by the jet. When the injection ends, the last substantial change in the flame structure occurs, transitioning to a combustion process dominated by the diffusion of oxygen and fuel, referenced as *Late Combustion* phase in Figure 2-1.

During the *Diffusive Combustion* phase, it is observed how the diffusion flame that began to form during the *Premixed Combustion* phase develops and reaches a quasi-steady state period maintained as long as the injection process does not end.

The knowledge of the diesel flame structure has been the subject of multiple studies, such as the conceptual model of it, which is clearly exposed in the works of Dec [8] and Flynn et al. [9]. Figure 2-2 shows the jet structure in one of its planes of symmetry, highlighting the optical diagnosis techniques used to construct this model. The model takes into account three different regions:

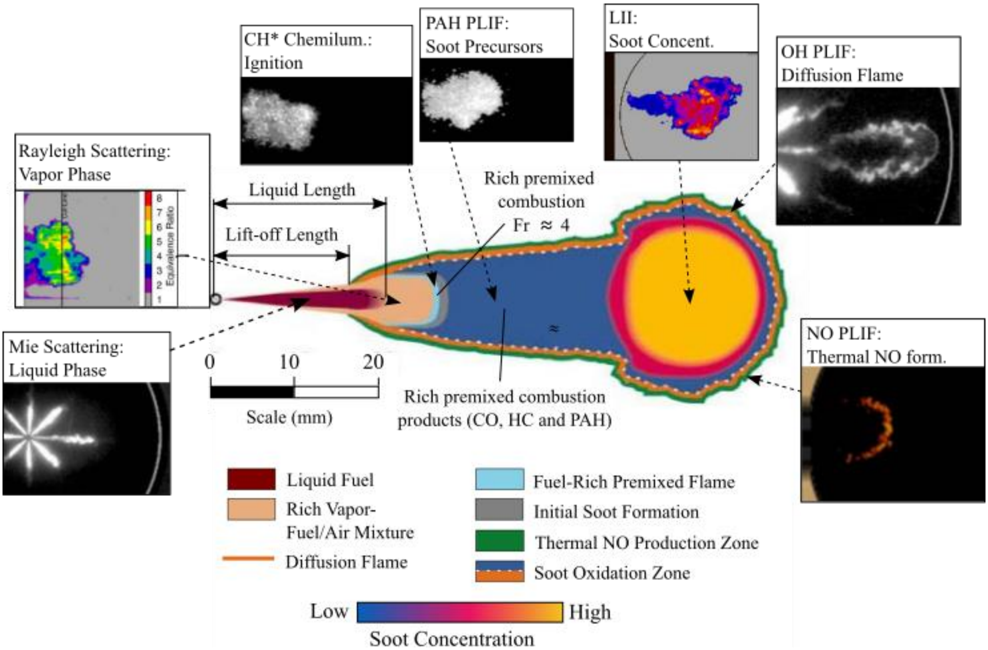

Figure 2-2. Schematic of the diesel flame structure during the quasi-stationary part of the diffusion combustion phase. Reprinted from [10].

The first zone, which corresponds to the immediate contact area with the injector nozzle, the flame has a non-reactive jet appearance since the reaction zone does not reach the injector due to the high velocities in this initial area. In fact, in this zone, atomization phenomena, air entrainment, and evaporation occur similarly to a non-reactive jet under evaporative conditions. This region appears from the nozzle to the liquid length (LL) position. As can be seen in Figure 2-2, this region has been detected by *Mie* and *Rayleigh Scattering* to characterize both liquid and vapor phases.

From the LOL position, the flame acquires a typical diffusion flame structure (second region), consisting of an inner zone occupied by soot and unburned fuel. Using soot *Laser-Induced Incandescence* (LII) and PAH *Planar Laser-Induced Fluorescence* (PLIF) techniques allows the characterization of this zone. Furthermore, this zone is surrounded by the reaction surface, where they are completely oxidized to CO_2 and H_2O upon finding the necessary oxygen proportion. Dec and Coy [6] study this reaction zone based on OH PLIF and show that it has the appearance of a surface with a very small thickness (less than 120 µm). According to measurements by Dec and Canaan [11] using NO PLIF, the outer part of this surface is where the nitrogen oxide formation zone is located since the necessary high temperature and oxygen availability conditions occur for the appearance of this species. In Figure 2-2, it can be observed that in this second region, the jet has a greater width than the area near the injector due to the expansion process induced by the high temperatures generated by the heat release, causing the jet silhouette to not be conical as in the non-reactive case. Additionally, a characteristic vortex of the non-stationary evolution of the flame is observed in the frontal part (analogous to the one that forms in a transient diesel jet under isothermal conditions [12,13]).

Just downstream of the LOL position, in the inner part of the flame near the spray axis, a third region of small thickness is established in which Dec hypothesizes the existence of a premixed reaction zone, which would consume all the oxygen enveloped by the non-reactive first zone of the jet so that the concentration of oxygen inside the diffusion flame zone is assumed to be zero. The products of this rich-dosed reaction (mainly CO and partially oxidized hydrocarbons) serve as a basis for forming soot inside the diffusion flame. The characterization of this region in the Dec model is based on the detection of CH^* chemiluminescence.

From the above macroscopic description of the quasi-stationary Diesel flame structure, the spatiotemporal evolution of a mass quantity (a package) of fuel injected through the nozzle as it passes through all these zones is described by Flynn et al. [9]. This evolution is represented in Figure 2-3 and detailed below, highlighting the air mass fraction (Y_{O2}), the dimensionless Heat Release (HR), the temperature (T/1000), and the soot and NO_X formation evolutions.

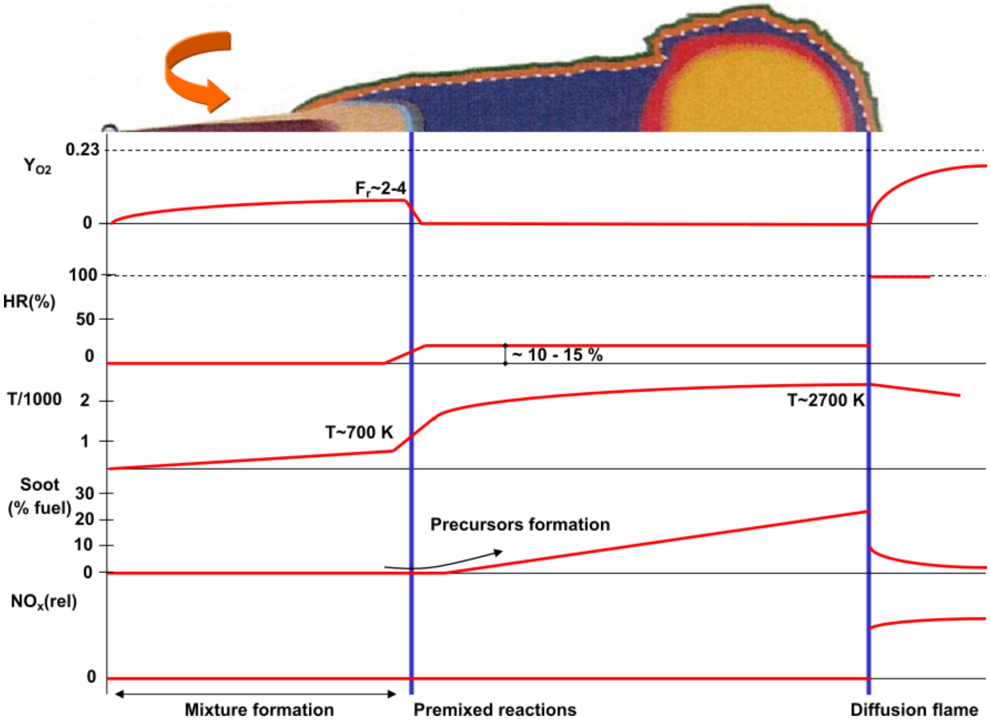

Figure 2-3. Conceptual model for conventional diesel flame structure during the quasi-stationary period. Source: [9]

Initially, the fuel package is atomized and mixed with air. As a consequence of droplet breakup and hot air entrainment, there is a rise in temperature, causing the liquid fuel to vaporize until it ultimately dissipates at a specific distance from the nozzle. From that distance, the vapor phase fuel continues to mix with air until it reaches the end of the first region described in Figure 2-2, where the premixed combustion zone is located. Upon reaching this point, the initial fuel mass has been diluted in the air to an equivalence ratio of approximately 4, heating up from the injection temperature to a value of approximately 700 K. As it passes through this premixed combustion zone, the previous mass burns, raising its temperature to approximately 1600 K. Since the local fuel-air mixture is rich, the enclosed oxygen is completely burned, resulting in a large proportion of partial oxidation products of the fuel. Among them, a large amount of carbon monoxide and short-chain unsaturated hydrocarbons (C_2H_2, C_2H_4, C_3H_3) are found, which are believed to be the species that lead to the polycyclic aromatic hydrocarbons (PAH) formation, constituting the true precursors of soot. According to estimates by Flynn et al. [9], around 10-15% of the chemical energy contained in the fuel is released in this combustion process. Next, the fuel package enters the diffusion flame zone, where it continues to mix and entrain gases. However, there is no contribution of free oxygen here, as the diffusion flame existing in the periphery and the premixed combustion zone it has just passed through prevent oxygen from penetrating into this zone (oxygen is only present in the form of products such as H_2O, CO, and CO_2). Due to the absence of oxygen, it is unlikely that heat will be released inside this zone.

On the other hand, approaching the diffusion flame front produces significant heating of the package, which, together with the composition rich in partial combustion products precursor to soot, causes this substance to appear inside the diffusion flame in the form of small particles at first that grow in size as they approach the flame front, next to which they reach their maximum size. Once the package eventually traverses the diffusion flame front, partial combustion byproducts undergo further combustion, facilitated by the oxygen diffusing from the outer region of the front. This process liberates the residual portion of the initial fuel chemical energy, accounting for approximately 85% of its total energy content. This achieves the maximum temperature at this front of the order of the adiabatic flame temperature. The formed soot is oxidized, mainly due to the high temperature and the presence of the OH radical, as indicated by Dec and Coy [6] results and more definitively confirmed by subsequent studies by Kosaka et al. [14] or Dec and Kelly-Zion [5]. All these works present simultaneous images of the spatial distribution of OH (as a marker of the reaction zone of the diffusion flame) and soot. The latter always appears surrounded by the OH radical, with very little overlap between the distributions of both substances. These radicals dominate in the highest temperature regions or where the air-fuel mixture is around the stoichiometric. Soot does not cross this reaction zone, which implies that this radical constitutes a fundamental mechanism of soot oxidation as long as conditions of high temperature persist, even when the injection process has already ended.

In low-temperature combustion processes, these OH regions are larger than in conventional high-temperature direct injection diesel engine processes as discussed by Musculus [15], a work that is an extension of Dec's conceptual model. This work involved the study of liquid penetration, ignition, and soot formation processes inside the cylinder of an optical engine using laser visualization techniques for low-load conditions, early injection, and low-temperature combustion (LTC), observing certain differences from conventional diesel combustion. Among these differences, Musculus concluded that OH is found throughout the cross-section of the spray, indicating a more complete mixing and leaner mixtures inside the spray in contrast to the thin sheet at the periphery of the diesel spray defined by Dec's model. This distribution of OH also helped to understand that the spatial distribution of NO formation had to be different as well. Although Musculus [15] did not measure NO spatial distribution in this study, he affirmed that NO had to form in the same relatively hot, oxygen-rich environments where OH exists under LTC conditions. Another contribution of Musculus work in these LTC conditions is that soot forms much further downstream, indicating that it only appears in fuel-rich head vortices where mixing is slower. However, due to the limited field of view during the experiments, details of the phenomena occurring close to the injector could not be analyzed.

In 2013, Musculus et al. [16] updated the conceptual model for LTC diesel engines, represented in Figure 2-4. This figure shows the combustion evolution, representing several CADs after the start of injection (ASI), where the right and left columns show experimental measurements, while the central columns show the conceptual model updated by Musculus et al. in LTC conditions. During the initial stage, the authors observe the formation of formaldehyde (CH_2O) through incomplete combustion, which serves as an indicator of unburned hydrocarbons (UHCs). These UHCs have the potential to generate soot precursors like PAH. However, in the subsequent stage, the presence of OH signifies complete combustion and the consumption of soot. Using the LIF technique, it becomes evident that the fuel located far from the injector undergoes complete combustion (OH LIF). In contrast, fuel near the injector fails to achieve complete combustion (CH_2O LIF). Consequently, they conclude that the region near the injector is a source of UHCs.

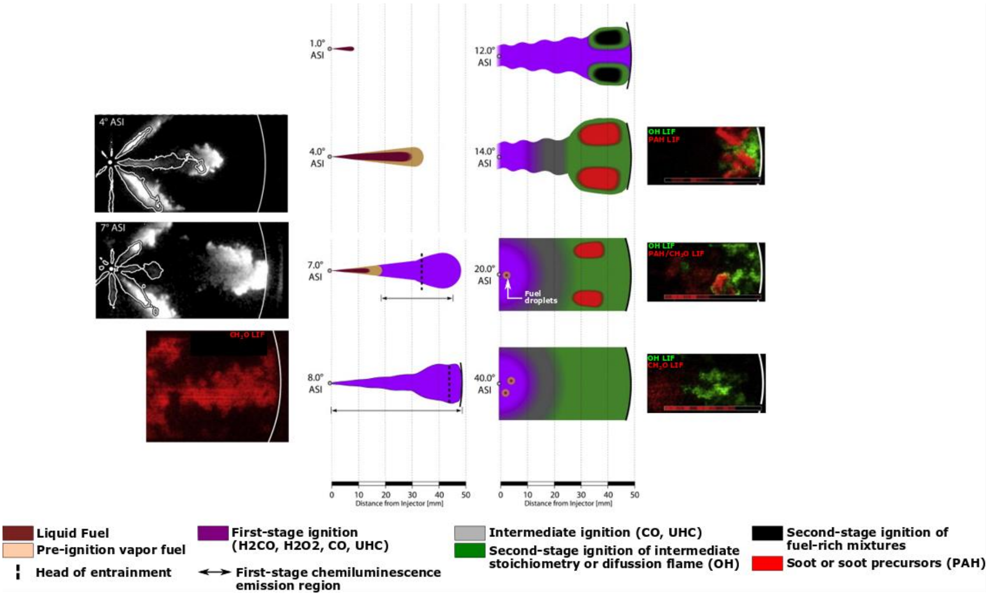

Figure 2-4 Conceptual model for low-load, single-injection, EGR-diluted, PPCI low-temperature heavy-duty DI diesel combustion (central columns) and experimental measurements (left and right columns). Modified from Musculus et al. [16]

Throughout a series of experimental works [17–19], Siebers and Higgins studied the phenomenon in detail for a diesel jet injected into a constant-volume chamber. These authors measured the LOL position using OH^* chemiluminescence [20]. A small area around the LOL position highlights the region where the *Premixed Combustion* phase appears in the conceptual model, indicating an area without soot formation. However, it appears downstream from that zone (Figure 2-2). The OH radical had previously been introduced as a marker of combustion zones in diffusion flames, allowing for measurements from its chemiluminescence that are more realistic of the flame onset than those obtained through natural soot luminosity.

The study of the LOL has allowed, in addition to understanding its behavior in relation to the basic variables of the combustion process, to deduce a series of implications regarding the formation of soot in the jet. A long lift-off length means that the spray has entrained a high amount of air, so lean mixtures can be achieved inside the spray, leading to low soot production. On the contrary, a short LOL will imply low air entrained by the spray, leading to richer mixtures and, consequently, a higher concentration of soot precursors, resulting in more soot production. This was observed by Siebers et al. [19], showing that it is possible to reach a point beyond which soot is no longer formed. This transition point is located at an equivalence ratio between 1.8 and 2.2 regardless of the rest of the conditions. This is similar to that obtained in the case of premixed flames of typical hydrocarbons, in which no soot is produced with relative dosages below a value of approximately 2 [1].

Additionally, the authors cite the study of Flynn et al. [9] (already referenced above), in which kinetic modeling results of the combustion process in hydrocarbon mixtures indicate that increasing the amount of oxygen in a mixture with a rich equivalence ratio decreases the amount of soot precursors formed. The modeling results show that this is because the carbon in the fuel tends to form carbon monoxide instead of soot precursors. The modeling also indicates that using oxygenated fuels reduces the formation of soot precursors, with a limit when the atomic oxygen/carbon ratio is on the order of 1.3, beyond which these precursors are not formed anymore. Siebers et al. indicate that the limit of air entrainment that eliminates the presence of soot (equivalence ratios between 1.8 and 2.2) would correspond to the atomic oxygen/carbon ratio just before the premixed flame being between 1.3 and 1.6. Therefore, according to these authors, there is a similar effect between the supply of oxygen before the premixed combustion zone through air entrainment and that obtained through the oxygen present in the fuel. However, a later study by Musculus et al. [21] in an optical engine with a number of surrogate fuels shows that the oxygen/carbon limit ratio is 0.55. This value, much smaller than the one obtained by Siebers et al. (between 1.8 and 2.2) with conventional diesel fuels, is justified by the authors mainly based on the difference in chemical structure between the fuels used (paraffinic) and the conventional diesel fuel (which also contains olefins and aromatics) and also possibly because the role of the oxygen provided by the fuel may not be exactly the same as that provided by entrainment.

Since its introduction in 1997, Dec's model has been a source of inspiration for numerous studies. The continuous advancement of experimental methodologies and testing facilities, including innovations like constant pressure vessels, has facilitated many research endeavors. These studies have contributed directly or indirectly to refining and enhancing the Dec model. Some research has followed a similar qualitative approach to Dec, yielding notable conceptual advancements in the field. Kosaka et al. [22] observed that the mechanisms involved in the combustion process change significantly once the quasi-steady diffusion combustion period is attained (Figure 2-5). Soot precursors continue forming in the jet's central fuel-rich part (purple), while a thick leaner region of OH radicals (yellow) flows towards the flame's centreline and is consumed before reaching the spray axis. Soot precursors at the spray axis transform into soot and move towards the spray head, where they grow and are displaced to the periphery by the head vortex's motion. Ultimately, the soot particles are transported upstream and re-entrained through the lean regions, where they are quickly oxidized. These observations are consistent with subsequent findings presented by Bruneaux [23]. The author employed a simultaneous combination of OH PLIF with PLIF at 355 nm to enable the localization of OH in relation to formaldehyde (low temperature ignition tracers), PAH (soot precursor), and soot. This method helped to identify an internal core consisting primarily of PAH, which was enveloped by a thick layer of hydroxyl radicals. This finding suggested the presence of a fuel-lean region in the periphery of the flame.

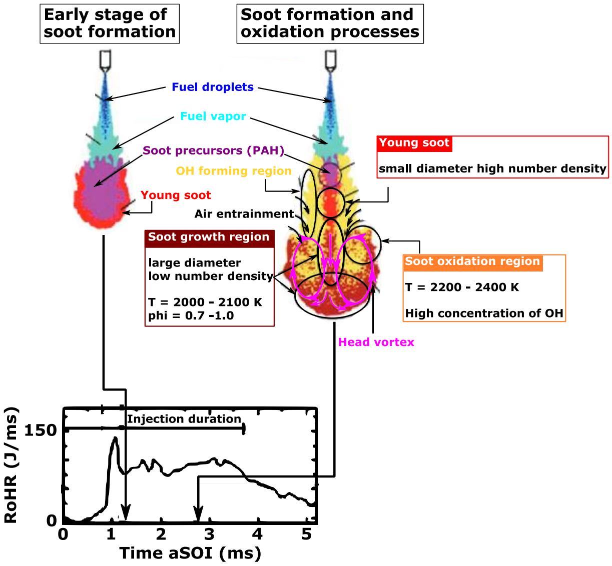

Figure 2-5. Conceptual model of soot formation and oxidation processes in a Diesel spray flame. Modified from: [22]*.*

More recently, Jing et al. [24] (Figure 2-6) used a different approach to visualize the structure of the flame to complement the previous conceptual models for spray combustion under different combustion modes. The authors utilized the natural luminosity and OH* chemiluminescence of the flame. They proposed the existence of a CH_2O/PAH and CH* layers (green) located between the fuel-lean (red) and soot (grey) regions. This study also highlighted the importance of these intermediate layers in controlling the soot formation process. On the one hand, within the LTC mode utilizing a wall configuration, OH^* is detected within the outer region of the flame, with its thickness diminishing progressively from the upstream to the downstream. However, it vanishes close to the wall. In the middle section, HCHO/CH emerges, beginning from the midpoint of the flame. Finally, soot is found within the inner part of the flame, positioned downstream. On the other hand, in the free-spray combustion mode, where no wall is present, the arrangement is depicted as follows: OH^* appears as the outermost layer, followed by HCHO/CH in the middle layer, and finally, soot is formed as the innermost layer. These three layers are observed sequentially from the outer to the inner regions. Notably, the soot region expands further in the centerline direction compared to the low-temperature combustion (LTC) mode.

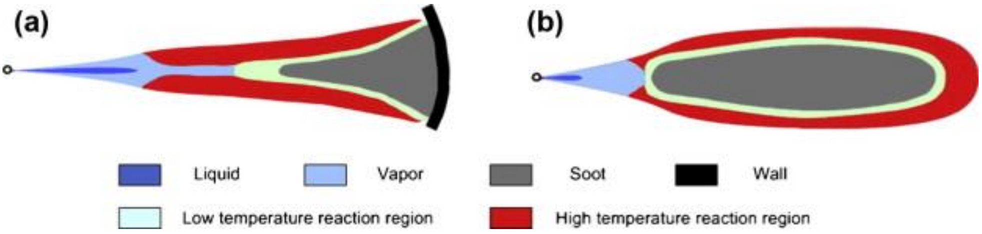

Figure 2-6. Low-temperature mode with a wall (a) and conventional combustion without wall (b) high-load quasi-steady diesel flame diagram based on OH^* and natural luminosity optical techniques. Source: [24]

2.3 Recent Studies in Diesel Flames

Sandia National Laboratories initiated the Engine Combustion Network (ECN) to advance combustion research for engine applications [25]. Over time, the ECN has expanded into an international collaboration in the engine combustion research field. The ECN recognizes the importance of both experimental and computational contributions and the need to consider experimental boundary conditions to ensure the consistency of results.

Guidelines for facility operation, diagnostic techniques, and postprocessing standards have been established to compare experimental results obtained in various setups directly. The initiative began representing a low-temperature combustion condition pertinent to engines utilizing moderate exhaust gas recirculation (EGR). The primary condition, referred to as Spray A, involves injecting n-dodecane into an ambient temperature of 900K, with an ambient density of 22.8 kg/m^3 and an oxygen percentage of 15%. A more comprehensive description of this reference condition can be found online on the website [25].

Various research institutes worldwide have demonstrated the ability to achieve the defined reference conditions using nominally identical injectors and n-dodecane as surrogate fuel, although with varying auxiliary equipment. The validation of these conditions relies on pressure and temperature measurements, as well as characteristic spray parameters, including liquid length, vapor penetration, and flame lift-off length [26–28]. Such validation provides credibility to subsequent studies investigating parametric variations by individual contributing institutes, facilitating the efficient expansion of the online data archive of the ECN.

In the series of collaborative ECN publications, the initial publication demonstrated the difficulties encountered in matching boundary conditions of different experimental facilities despite the reasonable agreement in spray penetration, ignition, and combustion [26]. Later on, the boundary conditions characterization was thoroughly assessed for more experimental facilities, and the sensitivity of variations was quantified [27]. The effort to overcome variability between facilities has emphasized the importance of standardizing diagnostic techniques and processing methods to consistently compare spray development, vaporization, and combustion [28]. In another collaborative publication, nozzle geometry and hydraulic behavior differences were disclosed, leading to corresponding downstream parameters from the injector orifice [29].

In recent years, extensive research has been conducted into soot formation, including experimental and numerical comparisons [30]. The systematic and organized approach of the ECN has also resulted in periodic workshops collaborating with several scientific institutions using the same operating conditions, leading to an important database of Spray A condition. For this reason, the first part of the results (Chapter 4) included in this thesis use the Spray A conditions as a reference.

2.3.1 Free Spray

Maes presented the findings on the flame structure of Spray A and the parametric variations from the constant volume combustion facilities at multiple research institutes (TU/e, IFPE$_n$, and Sandia). The results exhibited a consistent spatial distribution of the temporal evolution of the Spray A baseline, and the variations studied, as shown in

Figure 2-7 and Figure 2-8, respectively.

These figures combined the results obtained using several optical techniques as an RGB image at quasi-steady conditions. The white line represents the OH* contour (including the soot incandescent contribution). Furthermore, laser sheet size and direction are indicated with color-coded arrowhead, while the results of each experiment are color-coded, using green for the 355 nm PLIF (CH_2O and PAH), red for OH PLIF, and blue for soot volume fraction. The yellow signal refers to the overlap of OH and 355 PLIF measurements. Some authors reported a 355 nm PLIF signal close to the injector associated with the liquid zone scattering.

The comparison of Spray A as a baseline condition reported in Figure 2-7 shows the correspondence of these results for the different institutions. However, some differences reported by the institutions can be observed. As mentioned previously, the TU/e and IFPE$_n$ reported the interference by the scattering of the liquid zone upstream to the CH_2O. The second panel, representing the IFPE$_n$ results, shows a weak diffusive 355 nm PLIF signal downstream 50 mm from the injector (outside the laser sheet) due to the non-background luminosity correction in the images.

Considering the differences mentioned above, the researchers coincide in identifying regions of CH_2O formation downstream of the liquid length in fuel-rich areas with adequate entrainment of high-temperature ambient. Additionally, it is expected that CH_2O will be restricted to the spray core with limited oxygen availability. Soot formation has not occurred at the LOL position due to insufficient time and mixture temperature. However, notable soot luminosity is detected further downstream. The region between is anticipated to undergo partial fuel oxidation, leading to CH_2O formation, followed by the growth of PAHs as the process moves further downstream. The PAHs fluorescence intensity dominates the CH_2O signal, making it a strong interference for the CH_2O results in 355 nm PLIF measurements. However, because PAHs appear downstream of the CH_2O signal [31], the authors could identify the region of high signal intensity to the presence of these hydrocarbons. Moreover, the authors described the soot consumption, characterized by OH and OH* at the periphery, and the mixing and interaction with reactants while moving radially inward.

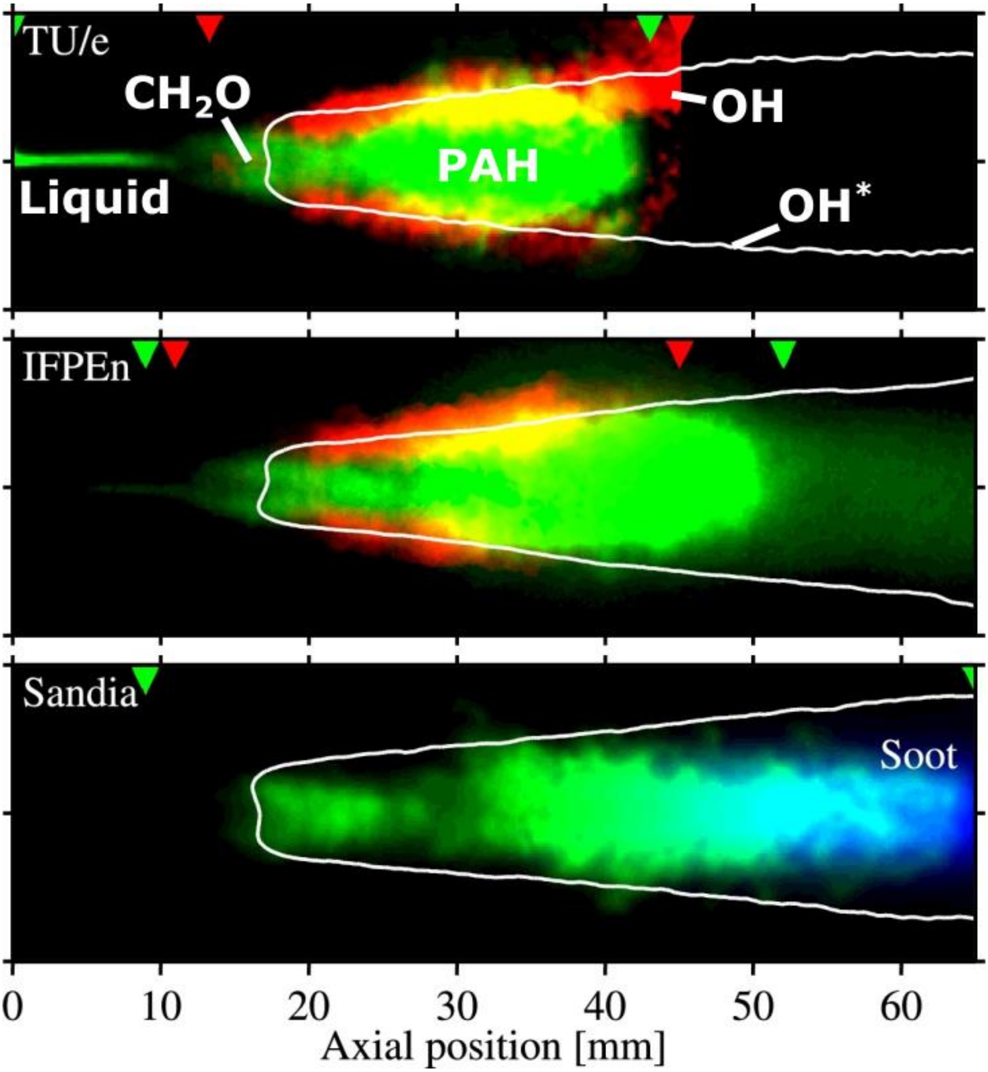

Figure 2-7. A combination of quasi-steady state results shows the spatial relation between OH PLIF (red), OH* (white line), 355 nm PLIF (green), and soot volume fraction (blue). Image modified from [32].

Later, the same authors studied parametric variations, as shown in Figure 2-8. Upon examining the range of O_2 concentrations, it is apparent that the areas containing CH_2O and PAH are distinct in the image with low oxygen content (13% O_2). As the oxygen concentration is raised, the region occupied by PAH grows in size and moves upstream, merging with the area where CH_2O fluorescence would be expected (highlighted with white brackets). The two areas are scarcely distinguishable in the lower image (21% O_2). Although visible, the CH_2O signal is relatively weak and is confined to a narrow zone near the spray axis, with a higher concentration at the point where OH emerges. According to reports, the liquid penetration of Spray A baseline can extend up to 12 mm downstream of the injector orifice [26–28]. Therefore, it is challenging to differentiate between the CH_2O structure and the light scattered by the liquid fuel.

Modifying the mixture reactivity by altering the temperature of the surrounding gas has a comparable impact. When the ambient temperature is extremely low (750 K, according to Sandia), the probability of soot precursors is minimal because centerline mixture fraction values at the LOL position (>40 mm) have already reached nearly stoichiometric conditions [31]. Farther downstream, an uneven pattern of CH_2O is detected, indicating isolated areas of fuel ignition in high-reactivity sections of the mixing layer at the jet periphery. In the center of the spray, the temperature is likely insufficient for first-stage ignition. At an ambient temperature of 800 K, the CH_2O distribution is located in the central area of the spray, and a small grouping of soot precursors is discernible farther downstream. However, Sandia reported that the intensity in this region is very low, so they tripled it to distinguish PAH more clearly, as shown by the white dashed rectangle in Figure 2-8. In the $IFPE_n$ results at 800 K, the OH and CH_2O signals are closer than in the other scenarios. As the temperature increases further, the fluorescence intensity of PAH rises relative to that of CH_2O, and it moves upstream until, at 1000 K, distinguishing between the two is almost impossible. Similar to the case with the highest oxygen concentration, CH_2O is confined to a limited area near the LOL. The connection between soot precursors and laser light sheet attenuation is further verified by comparing the regions of PAH fluorescence with those of OH PLIF above and below the spray axis in Figure 2-8. The conditions in which PAH fluorescence is dominant correspond to a large amount of attenuation in the OH PLIF results. Similarly, attenuation is less prominent when CH_2O structures are more prevalent. When both OH and CH_2O PLIF are employed, the attenuation in the OH signal can assist in identifying CH_2O.

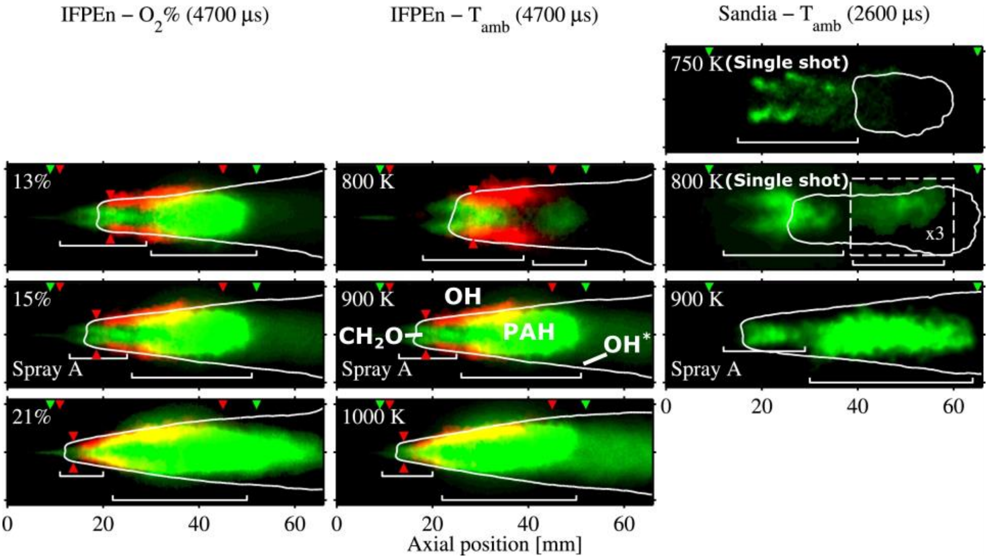

Figure 2-8. The effect of ambient oxygen concentration (left) and ambient temperature (middle, right) on the results of CH_2O and PAH fluorescence (green color channel), studied by $IFPE_n$ and Sandia. The red color channel is used for OH PLIF results when available, and the white contour depicts the OH^* outline. Figure reprinted from [32].

Heavy-duty diesel sprays and flame-wall interaction are other subjects to study. These areas have not been extensively studied due to the challenges involved, such as the difficulty in attaining high pressure in an optically accessible setup. Furthermore, optical diagnostic techniques may not be applicable in such ambient conditions, and the availability of appropriate numerical and kinetic models also becomes increasingly limited. To better understand events and features impacting heavy-duty CI engine operation, the ECN established reference conditions with two single-hole, heavy-duty diesel injectors (Spray C and Spray D) with relatively large orifices compared to the previous Spray A reference.

In this way, Maes [33] investigated spray formation and combustion processes using these heavy-duty diesel injectors. Maes found that a significant portion of the intensity detected in OH^* chemiluminescence images may originate from soot incandescence, especially further downstream of the LOL location. In these cases, OH^* chemiluminescence was not distinguishable in the downstream portion of the spray. The distribution of CH_2O from the larger orifice injector at ECN Spray A ambient conditions was similar in shape to that for the smaller injector nozzle but with larger dimensions, indicating that it scales with the orifice diameter. However, for the increased hole diameter, most of the CH_2O signal is likely to be obscured by PAH and soot luminosity during the quasi-steady state, regardless of the ambient conditions used in this study.

Additionally, fluorescence in the CH_2O wavelength range recorded at high-density conditions with increased oxygen percentages most likely contains significant contributions from PAHs, even shortly after ignition. Numerical simulations and analysis showed that the PAH structures encompass a large part of the CH_2O distributions.

2.3.2 Flame-Wall Interaction

In diesel engines with high-pressure diesel sprays, it is unavoidable for the spray flame to interact with the combustion chamber wall. The flame impingement with the piston wall affects the flame structure, and the combustion evolution. Typically, the piston bowl-rim is targeted in such engines, presenting various opportunities for optimizing the piston design [34–38]. In some cases, the piston shape is adjusted to redirect the sprays, aiming to promote engine efficiency and reduce emissions. However, the fixed spray orientation of high-pressure fuel injection equipment complicates the optimization process, particularly when combined with split injection strategies [15,39–41].

One piston design divides the flame into two regions of the combustion chamber: inside the piston bowl and the squish region (e.g., the designs discussed by Busch et al. [35]). In that case, the injection timing and strategy significantly influence the amount of fuel dispersed into specific regions.

Inert spray wall interaction studies at conditions relevant to CI engines indicate that, although there is no noticeable effect on the spray before impingement, mixing may be substantially affected in the contact region [42–45]. Specifically, Bruneaux [43] studied the effect of a flat wall in a high-pressure and high-temperature vessel. The author found that mixing is reduced compared to a free jet at the center impingement region, where the jet initially impinges on the wall. However, mixing increases again in the region where the spray moves along the wall and perpendicular to the spray axis. When wall distance and injection conditions are chosen such that the wall jet region surrounding the impingement region is dominant, the spray will exhibit overall mixing improvement compared to a free jet, while differences in upstream air entrainment are insignificant.

Several research groups have examined the impact of simplified jet-wall interaction on diesel-like combustion over the past few decades. Some results on soot production are inconclusive, possibly due to variations in spray, ambient conditions, and wall properties [23,46–48]. Pickett et al. demonstrated the potential to reduce or eliminate soot formation using flame-wall interaction, compared to a free jet, for two different injector orifices and two wall distances [60]. They also showed that a rectangular box, known as a "confined" configuration, resulted in a shorter LOL due to redirected combustion gases, which was aimed at simulating jet-jet interaction between adjacent sprays in an ICE. However, this configuration ultimately led to more soot formation due to shorter LOL and similar mixing, in line with previous soot studies [48]. Conversely, Wang et al. [48] found increased soot formation when a wall insert was placed a relatively short distance from the injector, suggesting that ambient conditions and properties may play a role. However, a conclusive understanding may still be lacking due to insufficient research on this topic [49].

Maes [33] investigated how a single fuel spray interacts with different types of solid walls under specific ambient conditions and simplified wall and shape designs. The different wall designs tested were a flat wall (W#), a 2D confined wall (W#C), and an axisymmetric confined wall (W#A) which can be seen in Figure 2-9. On the one hand, the W#C splits the spray between the piston bowl and the squish region. On the other hand, for the W#A, the fuel jet is aimed at the bowl instead of the piston bowl-rim, and the dispersed spray moves away from the spray axis and then redirects back toward the injector. The study also varied wall distances to investigate their influence on combustion and maintain realistic scaling with the tested injector orifices. Although this simulation does not directly relate to an ICE, it allows the spray to be simulated with a wedge-shaped mesh with a thickness similar to the cell size.

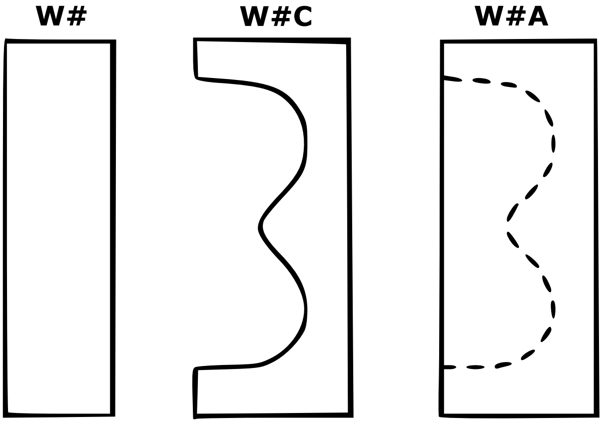

Figure 2-9. Schematic overview of the different wall designs used in Maes study. Source: [33].

The study first investigated flame-wall interaction using Spray A injector, three different wall shapes, and varying wall distances. Compared to a free jet, the interaction with the wall improved mixing, leading to a faster increase of aRoHR and a reduced burn-out duration. The largest changes were observed with a flat wall and the shortest wall distance. Additionally, soot formation was significantly reduced, as observed through natural luminosity and high-speed LII imaging. The results of experiments and numerical simulations with a larger injector supported the hypothesis of enhanced mixing with flame-wall interaction. However, it was also discovered that local heat loss from the experimental setup affected heat released by larger spray flames that interacted with the end wall. Experiments conducted with another injector (0.126 mm piezo injector) in the Sandia combustion vessel demonstrated that soot could be reduced by up to a factor of two through flame-wall interaction compared to free jet experiments. Finally, by examining multiple-injection strategies, the study showed that a closely coupled post-injection leads to the shortest and most abrupt burn-out, which is expected to impact engine-out emissions.

2.3.3 Flame-Wall Interaction in Engines

Studying flame-wall interaction under more realistic operating conditions is typically done using multi-hole injectors in real engines. The air-fuel mixture in such engines is influenced by engine dynamics, such as the swirl effect, which varies depending on the bore size. In larger engines with a greater bore size, where there is minimal swirl and reduced demand for air-fuel mixing, the combustion chamber typically exhibits a quiescent state, often characterized by a shallow piston cavity [50]. Under these conditions, the energy and momentum generated by the spray injection prove adequate for achieving appropriate fuel distribution and efficient air-fuel mixing [1]. These combustion systems operate at relatively low engine speeds and have high thermal efficiency. Heywood [1] classifies engines with piston bore sizes between 150 to 900 mm and engine speeds ranging from 120 to 2100 rpm as quiescent combustion systems.

Conversely, smaller engines require a faster air-fuel mixing rate and higher swirl ratio as engine speeds increase and piston bore size decreases. The intake port design promotes the swirl flow and is directly influenced by the bowl geometry. As a result, for swirl-assisted direct injection engines, the piston geometry typically involves narrow and deep (re-entrant) piston bowls [51].

Using a multi-hole injector, swirl-assisted DI engines have high efficiency and moderate injection pressures ranging from 1600 to 2000 bar. These engines typically have piston bore sizes ranging from 70 to 150 mm, suitable for both light-duty and heavy-duty vehicles.

Using an axisymmetric bowl-in-piston design, with the injector positioned at the center of the combustion chamber, is a prevalent choice in light and medium-duty vehicles. This configuration is typically employed in four-valve high-speed direct-injection (HSDI) diesel engines. A scheme of this geometry is highlighted in Figure 2-10. The combustion chamber refers to the volume between the squish region (blue) and the surface of the piston bowl (green). The bowl has a concave recess shape (see the zoom highlighted inside the square) that accommodates the radial spray, essential for swirl-assisted engines. This recess shape amplifies the swirl by compressing the air in the squish region into the bowl, resulting in a decrease in moment of inertia for the chamber charge and an increase in bore-scale angular velocity to conserve angular momentum [52]. Moreover, this bowl shape facilitates interaction with the spray. The most commonly used bowl geometry for light and medium-duty HSDI engines is the re-entrant piston (or ω shaped bowl).

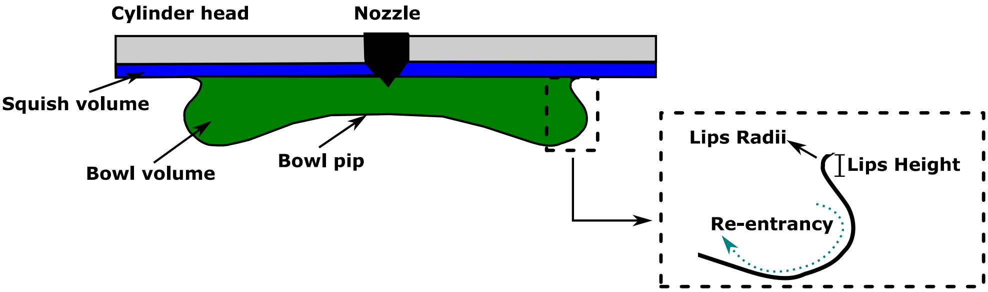

Figure 2-10. Areas of a four-valve HSDI diesel engine piston.

The re-entrance influences several factors: Firstly, it amplifies turbulence and enhances mixing rates within the bowl. Secondly, it sustains the kinetic energy of the fuel sprays by redirecting them toward the center of the cylinder. Lastly, it impacts the flow intensity from the squish area into the bowl. The bowl pip serves to redirect fuel jets, preventing the accumulation of fuel-rich mixtures in the central bowl area, all while preserving the desired compression ratio.

The interaction between the spray and the walls of the combustion chamber is typical in Diesel engines. Upon fuel spray injection into the piston bowl, the spray impacts the wall and spreads throughout the combustion chamber [53]. The spray-wall interaction area significantly impacts local air-fuel ratios in both the squish region and the bowl, ultimately affecting in-cylinder soot formation and engine thermal efficiency [35]. Generally, two main factors contribute to net soot emission: in-cylinder soot formation and in-cylinder soot oxidation, which occur at similar rates. Therefore, reducing engine-out soot emissions can be achieved by reducing soot formation or increasing soot oxidation efficiency. In order to achieve low soot formation, efficient soot oxidation, and high thermal efficiency, geometric parameters such as the piston bowl throat diameter, depth of the bowl, central pip area, and toroidal radius are extensively optimized [54].

Better air-fuel mixing and reduced soot formation can be achieved by distributing the spray evenly within the combustion chamber, which increases air entrainment [55–57]. In a typical re-entrant piston design, the bowl redirects the flame downwards and towards the center of the bowl. A small fraction of the spray is directed toward the squish region to utilize the available oxygen. The narrow throat of the bowl produces a strong squish and reverse squish flow, which improves fuel-air mixing.

The interaction between squish flow and swirl creates a strong mixing effect during the final phase of combustion, leading to improved late soot oxidation [58]. In a study by Zhu et al. [54] using computational fluid dynamics (CFD), the impact of using reentrant pistons with different toroidal radii on soot formation was analyzed. They reported that the highest concentration of soot for this type of bowl geometry is located at the periphery of the bowl, where strong flame/wall and flame-flame interactions occur, resulting in fuel-rich zones. Furthermore, the authors demonstrate the effect of varying geometric parameters of the bowl on soot formation and distribution, confirming that the piston bowl directly impacts soot formation in a diesel engine, emphasizing the importance of correctly developing the piston geometry for a specific engine. The optimum combustion chamber will differ depending on the engine size, swirl intensity, and number of injector orifices.

In recent years, various new piston designs have been developed for both high (light-duty) and low (heavy-duty) swirl-supported diesel engines. Different variations and optimizations are based on high-swirl engines re-entrant geometry. Zha et al. [52] provided a timeline review, showcasing the evolution and modifications of the re-entrant geometry over the years. Introducing a stepped or chamfered lip instead of the protruding lip marked a significant milestone in the new designs of re-entrant bowls. The literature suggests that better air-fuel mixing and more complete combustion can be achieved at the point where the spray is targeted when using the stepped lip geometry [59]. Figure 2-11 compares the conventional and stepped lip geometries.

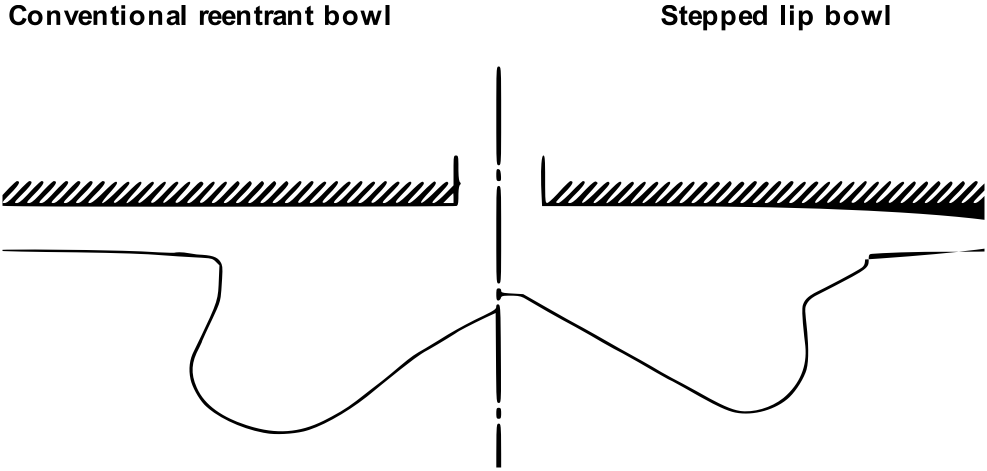

Figure 2-11 Comparison of conventional and stepped lip bowl geometries.

Several studies have also shown that the stepped lip can improve fuel consumption and reduce CO and soot emissions compared to the conventional re-entrant bowl shape [60–62]. Nelly et al. [63] investigated the performance of a two-stage chamber, a type of stepped lip bowl geometry, in a 2.2L 4-cylinder diesel engine and found that it improved fuel consumption at high engine loads while significantly reducing soot emissions by decreasing the local equivalence ratio. The “twin vortex” geometry, which also incorporates the stepped lip design, was developed and patented by Ricardo UK [64] and was tested in JCB off-highway Diesel engines, resulting in compliance with Tier 4 interim/Stage 3B legislation without the need for after-treatment systems, as well as improved fuel consumption [65]. Dockoon et al. [66] tested another variation of the stepped lip geometry, called the ULPC (ultra-low particulate emissions) piston, in light-duty and off-road applications and reported a reduction of over 60% in soot emissions and an improvement in the soot-NO_X trade-off.

In Figure 2-12, Busch et al. highlighted the differences between the conventional reentrant and stepped lip geometry regarding fuel splitting, jet impingement, and vortex dynamics. Around 50 % of the spray in the conventional bowl is redirected downward once the fuel collides with the lip. On the contrary, when employing the stepped lip bowl design, roughly 60% of vaporized fuel is directed toward the squish zone after contact with the piston step. Furthermore, in the case of the stepped lip bowl, the upwardly directed fuel impacts the cylinder head, diffusing both inward and outward. This recirculation process amplifies air utilization and promotes turbulent mixing during the latter part of the engine cycle. The upper toroidal vortex transports the mixture toward the cylinder center, away from the mixture in the outer squish region [35,67].

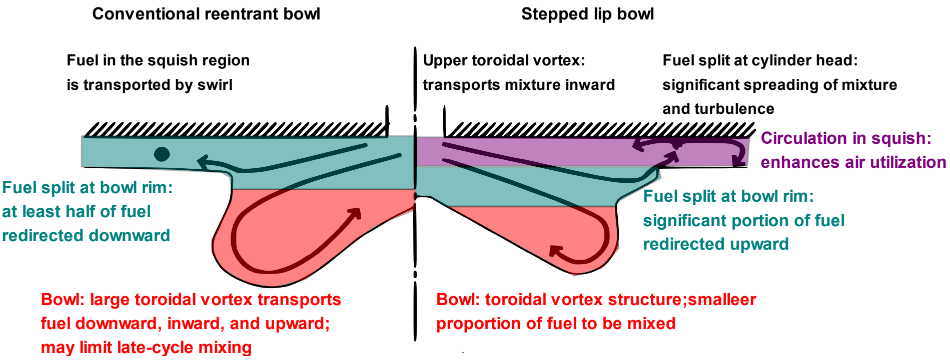

Figure 2-12. Comparison scheme between a conventional reentrant bowl and a stepped lip bowl. Modified from: [60].

A new type of piston called "wave piston" has been introduced by Volvo for low-swirl heavy-duty engines [68]. The piston features waves around the outer bowl circumference, as shown in Figure 2-13.

Figure 2-13 Wave piston bowl geometry designed by Volvo group [68].

Eismark et al. [69] studied the effectiveness of the wave piston for late-cycle oxidation. Their study used a high-pressure and high-temperature vessel and a single-cylinder engine to conduct the tests. The tests revealed a significant reduction of up to 80% in soot emissions and a substantial decrease in the soot-NO_X trade-off. The images captured during the vessel testing revealed enhancements in the soot oxidation process and a notable acceleration in soot burn-out. The protrusions effectively guide the flame towards the central region of the bowl, where an ample supply of fresh oxygen is available. However, following the flame's collision with the piston wall, the tangential movement of the flame led to undesirable flame-flame collisions at a 180º angle near the wall. This intense flame-flame interaction resulted in the dissipation of valuable kinetic energy from the spray, creating areas of stagnation where rich combustion products were mixed. In these stagnation zones, the oxidation rate of both fuel and soot experienced a reduction [69].

The purpose of the protrusions, as shown in Figure 2-14, is to promote a smoother flame-flame collision, resulting in a more efficient transfer of spray kinetic energy and fewer stagnation areas (identified by the letter P) within the combustion chamber. With a smoother collision between flames, more kinetic energy becomes available for generating crucial vortices.

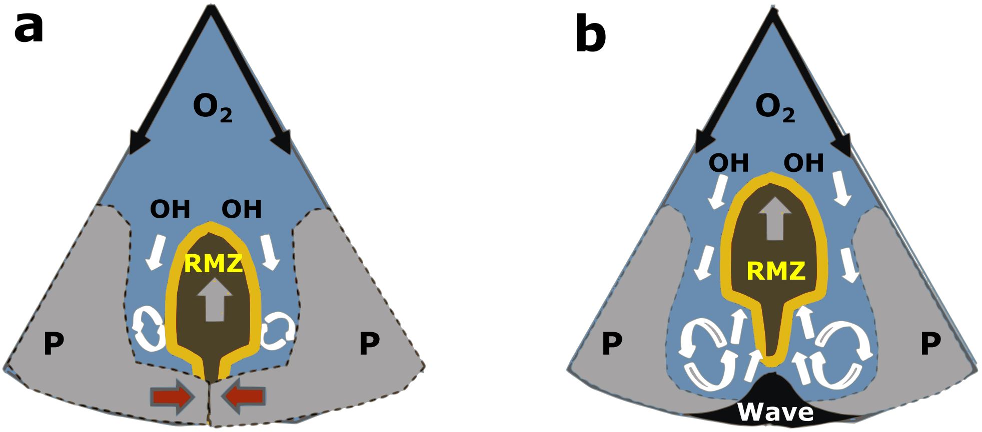

Figure 2-14. Scheme of the late-cycle mixing in low-swirl combustion. a) Sector of conventional piston bowl, b) Sector of piston bowl with wave-shaped protrusion. RMZ: radial mixing zone, P: combustion products, Wave: wave-shaped protrusion. Source: [69].

As shown in Figure 2-14, the wave piston generates a radial mixing zone (RMZ) that facilitates the movement of the flame and combustion products towards the center of the bowl where there is an abundant supply of oxygen, thereby enhancing the oxidation process. Even after the injection event has concluded, this active RMZ detaches from the piston wall and continues to move towards the center. An optical study conducted by Eismark et al. [70] captured this phenomenon using natural luminosity technique.

Lewiski thesis [71] reported several studies of the effect of these radial lips geometry compared to a conventional reentrant piston shape. The author studied the effect of the reentrant piston shape in a light-duty optical engine to mimic the actual operating conditions of a metal engine. Similar to the previous studies, Lewiski observed the common air motion patterns within this bowl geometry in swirl-supported engines. The flow from the squish region to the bowl, referred to as squish-bowl interaction, and the peripheral area exhibiting higher velocities were identified using the PIV technique, as depicted in Figure 2-15.

Then, the author characterized the flame movement and analyzed the in-cylinder soot formation using innovative piston bowl geometries, such as reentrant and hybrid pistons. The hybrid piston comprises two geometries: a sector with a stepped lip and a sector combining stepped lip and wave geometries. The differences in the flame movement induced by the different geometries were evaluated using the Combustion Image Velocity (CIV) technique. The results showed that the wave protrusions in the hybrid piston promoted the flame movement towards the bowl center, resulting in a higher velocity field on the side where both wave and stepped lip geometries coexist, as seen in Figure 2-16. However, both sides of the hybrid piston had a lower velocity field than the reentrant piston due to the effect of the stepped lip geometry, which splits the spray into two parts, reducing the kinetic energy available inside the bowl [71].

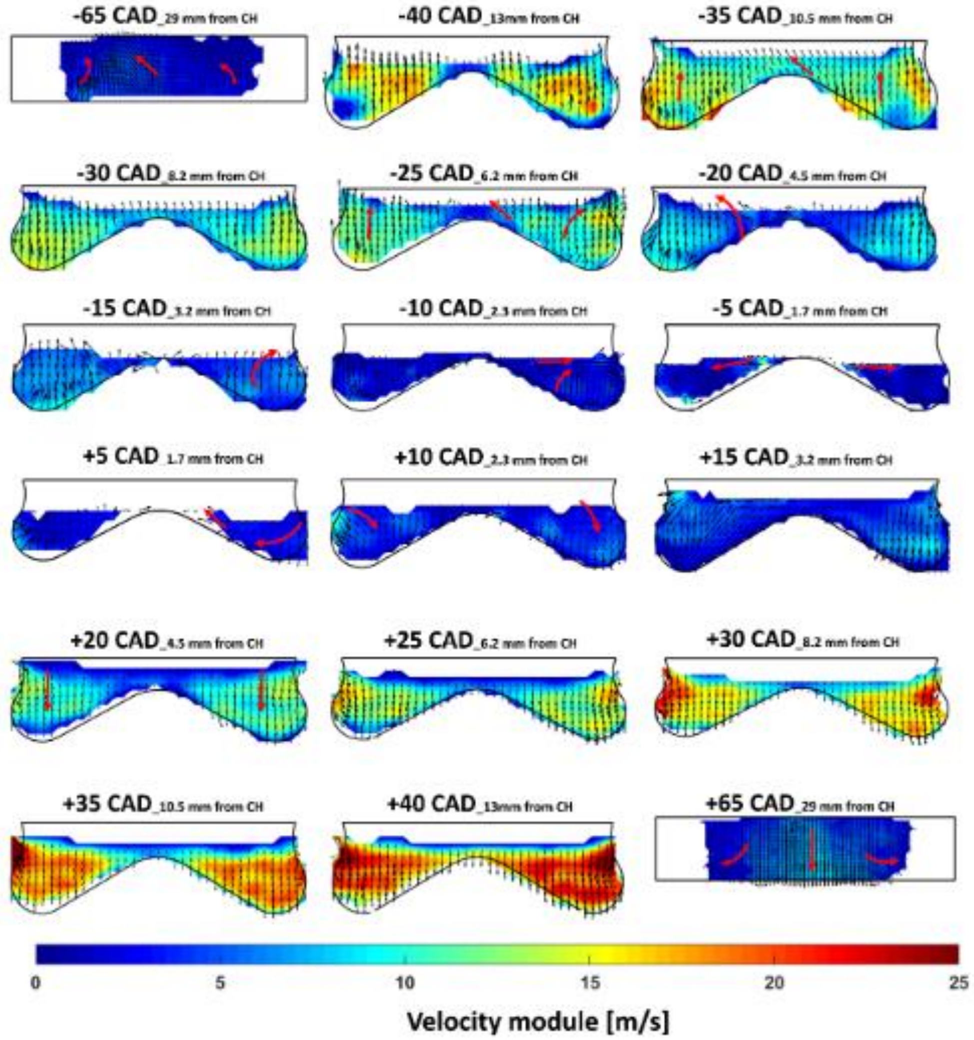

Figure 2-15 In-cylinder flow velocity evolution at motored conditions. Source: [71]

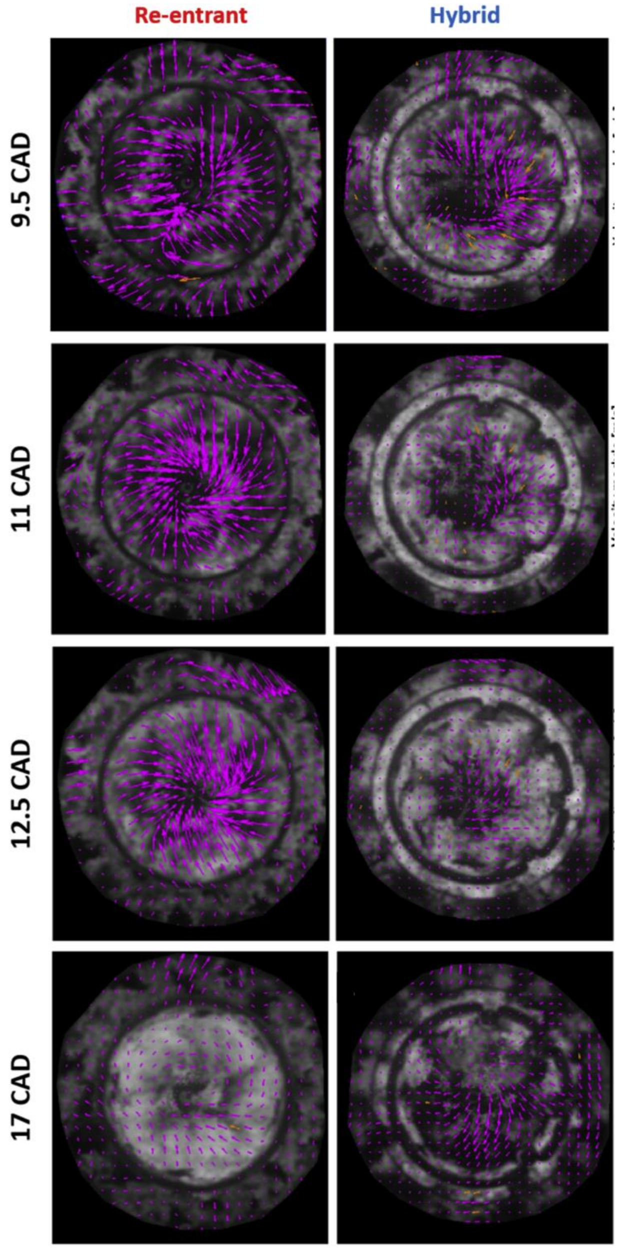

Figure 2-16. Velocity field analysis for different CADs comparing reentrant and hybrid pistons. Source: [71].

In terms of in-cylinder soot formation, Lewiski [71] reported a significant decrease in soot formation and a faster soot oxidation for both stepped lip and stepped lip-wave geometries compared to the reentrant bowl. Various engine operating conditions were evaluated to assess soot reduction, including modifications in the injection strategy and EGR conditions. However, the author highlighted that wave protrusions were particularly effective under the sweep of EGR conditions. During the discussion, Lewiski observed that, initially, the wave sector generated slightly more soot than the other. However, the oxidation process was faster. During the final stages of combustion, the waves sector had less area covered by the soot cloud than the no-waves sector.

The analysis of the combustion evolution and the in-cylinder soot evolution for larger engine sizes covering medium and heavy duty engines using these kind of pistons is a gap in the literature. For this reason, the second chapter of the results section of this thesis (Chapter 5) covers this issue. The analysis of this piston geometry is analyzed in a medium-duty optical engine under several engine-like conditions, including EGR-simulated conditions, to highlight the potential of the piston geometry in terms of in-cylinder soot formation/oxidation.

2.4 Oxymethylene Dimethyl Ethers as Alternative Fuel.

Utilizing oxygenated alternative fuels, such as Oxymethylene dimethyl ethers (OME_n), in diesel engines presents a promising solution to address environmental pollution [72] through the use of renewable energies. Its favorable physicochemical properties as well as good engine combustion and emission characteristics [73], push it to be considered a good alternative fuel option to replace traditional fossil fuels.

The synthesis of OMEn can be made following three different pathways, determined by the feedstocks utilized for the chain group: formaldehyde, trioxane, and para-formaldehyde [74]. The molecular structure of these fuels is $CH_3\text{-}O\text{-}(CH_2\text{-}O)_n\text{-}CH_3$, where n is the degree of polymerization [75]. The chain size directly affects its physical properties, which are crucial for ICE applications. The carbon atoms within OME_n are exclusively found as C-O bonds, suppressing the typical C-C bonds commonly observed in fossil fuels. This lack of C-C reduces the soot precursor formation, making it difficult to promote soot surface growth.

Secondly, OME_n have interesting properties such as good volatilization, low boiling point, and high oxygen content. These properties aid in improving the air-fuel in-cylinder mixture. Finally, the cetane number (CN) of OME_n is relatively high, resulting in a short ignition delay (ID), improving the combustion efficiency. Properties of OME_n, including the previously mentioned, for n from 1 to 6 are summarized in Table 2-1. The same table shows that the physicochemical properties of the different degrees of polymerization of OME_n differ from those of diesel, which can complicate the direct use of these fuels in engine applications. Therefore, the mixture of several OME_n with different degrees of polymerization, known as OME_X, is useful to achieve properties more similar to diesel.

Table 2-1. Properties of OME_1 to OME_6 [76–78].

Properties	OME_n					
	$n = 1$	$n = 2$	$n = 3$	$n = 4$	$n = 5$	$n = 6$
Cetane number (CN)	29	63	78	90	100	104
Flash point (ºC)	<0	16	20	77	103	169
Density at 20ºC (Kg/m^3)	860	960	1024	1067	1100	1130
Oxygen content (%)	42.1	45.3	47.1	48.2	49	49.6
Lower Heating Value (MJ/kg)	22.44	20.32	19.14	18.38	17.86	17.47
Viscosity at 25ºC (mm^2/s)	0.36	0.79	1.08	1.72	2.63	n.a.
Lubricity at 60ºC (µm)	759	n.a.	534	465	437	n.a.
Yield sooting index (YSI)	4.5	5.7	6.9	8.1	9.3	10.5

Despite the great advantages offered by this family of fuels, the low heating value (LHV) and their low lubricity present barriers in fuel consumption to achieve the same energy as diesel and problems with the engine infrastructure, respectively. Therefore, thanks to the good miscibility of these fuels with diesel, OME_n/diesel blends are proposed in the literature as a solution to overcome these difficulties presented by OME_n. Therefore, the characterization of the physicochemical properties of both OME_n and OME_n/diesel is necessary to improve the feasibility of these fuels in engine applications.

In 2019, Liu et al. [73] reviewed the application of OME_n in CI engines. This was further improved in [74], which focused on the spray characteristics of OME_n. Table 2-2 shows the physicochemical properties of OME_X and OME_X/diesel blends used in their studies. The degree of polymerization of OME_X is 3 ~ 8, and the mass fractions of OME_3 ~ OME_8 are 37.5%, 23.2%, 19.5%, 12.6%, 3.7%, and 1.8%, respectively. The OME_X volume fractions of OME_X/diesel blends are 10%, 20%, and 30%, marked here as P10, P20, and P30.

Table 2-2 Properties of OME_X and OME_X/diesel blends [79,80]. The data that is not available is noted as n.a.

Properties	Diesel	OME_{3-8}	P10	P20	P30
Cetane number (CN)	51.5	76	54	56.4	58.9
Boiling point (ºC)	310	180	n.a.	n.a.	n.a.
Density at 20ºC (Kg/m3)	822	1050	844.8	867.6	890.4
Oxygen content (%)	0	47.20	5.87	11.42	16.70
Hydrogen content (%)	13.49	8.78	12.90	12.35	11.82
Carbon content (%)	86.45	44.03	81.18	76.18	71.44
Lower Heating Value (MJ/kg)	42.6	17.8	39.6	36.7	33.9

The CN is a crucial indicator for assessing the ignition characteristics of fuels. As the cetane number rises, the fuel autoignition performance improves, resulting in a shorter ID, which benefits the engine cold start. Nevertheless, an excessively high CN can lead to uneven combustion and increased soot emissions. Typically, the diesel CN is not below 49 for CI engines, while OME_1 has a cetane number of only 29, rendering it unsuitable for CI engines. For OME_n polymerization greater than 2, the CN increases significantly, surpassing that of Euro V diesel fuel. This behavior suggests that OME_X/diesel blends can increase the fuel CN. Table 2-2 reveals that the OME_n/diesel blends CN increases as the OME_X quantity increases in the blend.

Given the growing severity of environmental issues, diesel engines must find ways to minimize particulate emissions promptly. One viable approach to address this problem is take the advantage of the oxygen content of these oxygenated fuels during the combustion process, as suggested in reference [81]. Researchers have undertaken various studies in recent years to reduce the particulate matter (PM) emissions in diesel engines through the utilization of oxygenated fuels like ethanol [82], biodiesel [83], DME [84], and OME_n. As discussed during this chapter, it is well known that polycyclic aromatic hydrocarbons (PAHs) are the primary precursors of soot formation. OME_n unique chemical structure, lacking C-C bonds, reduces the likelihood of soot precursor formation, thereby decreasing PM emissions. During the initial combustion stages, the CH_2-O- functional group in the OME_n molecule generates hydroperoxides, which break down into OH radicals in subsequent oxidation processes to oxidize soot precursors [85]. Table 2-2 shows that as the OME_X blending ratio increases up to P30, the oxygen content of OME_X/diesel blends increases from 0% to 16.7%. Liu et al. [79] conducted a study on the impact of OME_X/diesel blends on the engine emission performance of a heavy-duty Diesel engine. Their findings revealed significant reductions in soot, HC, and CO emissions using OME_X/diesel blends. A previous study [86] discovered that blending diesel fuel with 10%, 20%, and 30% OME_X reduces smoke emissions by 27.6%, 41.5%, and 47.6%, respectively, compared to pure diesel fuel.

The potential of OME_n to reduce soot is closely linked to its molecular structure, as mentioned previously. The sooting tendency (YSI) index has been used to identify molecules that are expected to have low soot-forming propensities [87]. In this way, Bartholet et al. [78] examined the impact of structural diversity on the physicochemical characteristics of OME_n. The authors observed that the YSI of OME_n gradually increased as the degree of polymerization (n) increased. They reported a significant reduction in YSI for OME_n compared to diesel. Thus, a decrease in YSI can be achieved by introducing OME_n in the fuel.

In 2017, Ottenwaelder et al. [88] reported a comparative analysis of the OME_1 and OME_X ($X = 3 - 5$) mixture formation process in a high-pressure facility, which revealed that the liquid penetration of OME_1 was lower than that of OME_X. In 2018, Srna et al. [89] analyzed the injection duration impact on the OME_n and n-dodecane Spray Tip Penetration (STP) in the air atmosphere using a rapid compression expansion machine (RCEM). The authors found that OME_n and n-dodecane STP (and cone angle) were similar before low-temperature ignition. Still, after ignition, the liquid penetration increased with the injection duration due to the momentum dissipation caused by the entrainment wave, as suggested by Musculus et al. [90]. This is a parameter important to consider when using OME_n fuel because the lower LHV of these fuels leads to injecting more fuel (increasing the injection pressure or the injection duration) to achieve the same energy released as diesel.

In another study, Honecker et al. [91] investigated the injection pressure, injection duration, ambient temperature, and ambient pressure effects on the OME_X ($X = 3 - 5$) spray cone angle, liquid penetration length, and gaseous penetration length in a high-pressure facility. They reported that the injection pressure did not significantly affect the liquid penetration length and gaseous penetration length, as the breaking droplet speed and the increase in spray speed balanced each other out at high injection pressure. The OME_X liquid penetration length gradually decreased with increasing ambient pressure. In addition, a slow increase in the gaseous penetration length at high ambient pressure was observed. The authors also reported that the spray cone angle was more sensitive to ambient temperature than ambient pressure, increasing the spray cone angle with the ambient temperature. These results agree with the behavior observed for sprays using conventional fuels.

As mentioned before, one of the properties important to take into account is the low LHV of OME_n compared to diesel. This issue leads to the need to increase the fuel quantity injected to achieve the same energy released. Fixing the same injection pressure for both fuels leads to a prolonged injection duration, which is challenging in optimizing the injection strategy. To address this issue, García et al. [92] studied the feasibility of using a high-flow injector (HFI) in an engine using GT Power software. The campaign involved a low-flow injector (LFI) with a nozzle diameter of 0.177 mm, a steady flow rate of 1300 cm^3/min, a high-flow injector with a nozzle diameter of 0.244 mm, and a steady flow rate of 2200 cm^3/min. Figure 2-17 shows that the high-flow injector had a higher flow rate and longer STP, significantly reducing the injection duration required for a given quantity of energy injected. The results reported a better mixing ability by OME_X ($X = 3 - 5$) compared to Diesel fuel. Still, an increased nozzle diameter led to lower mixing capability and reduced atomization quality, resulting in delayed combustion phasing and decreased combustion efficiency.

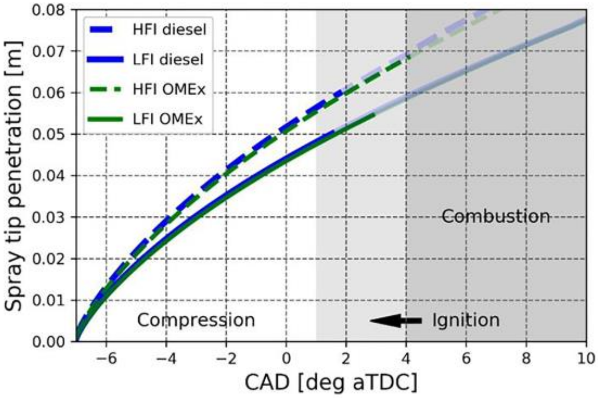

Figure 2-17 Spray Tip Penetration (STP) of different injectors and fuels. Source: [92]

In the literature, to overcome the problems associated with OME$_n$, this fuel is commonly used as an additive to blend with diesel. This mixture increases density and surface tension while the viscosity decreases. At the same time, it is important to remark that spray characteristics also change. Li et al. [93] were the first to investigate diesel fuel macroscopic and microscopic spray characteristics after blending with OME$_X$ ($X = 3 - 5$) using a high-speed image and particle/droplet image analysis technique in 2016. In this study, the blends used were 0%, 20%, 50%, and 100% of OME$_X$, labeled as P0, P20, P50, and P100, respectively. The effects of different blending ratios of OME$_X$, nozzle diameter, and injection pressure on the STP, the spray cone angle, and the spray projected area of the blends were investigated in a constant volume vessel under a nitrogen atmosphere of 4 MPa. Their findings suggest that fuel density was crucial during the initial spray stage. However, once the droplet was broken, viscosity and surface tension combined caused the STP curve slope to drop faster.

Ma et al. [94] conducted a study in 2017, employing high-speed imaging and PLII-LEM to examine the impact of volume fraction of OME$_X$ (0-30%) on OME$_X$/diesel ($X = 3 - 5$) combustion and spray characteristics within a constant volume vessel. According to their findings, adding a low-volume fraction of OME$_X$ did not significantly alter the liquid phase penetration, concluding it is unnecessary to modify the fuel injection strategy when blending OME$_X$ in low-volume fractions (up to 30%). Additionally, Huang et al. [95] investigated the influence of injection pressure on the spray penetration and cone angle of OME$_X$/diesel ($X = 3 - 4$) blends in a constant-volume combustion vessel. They observed a slight increase in spray penetration due to blending OME_X with diesel fuel.

In 2019, Liu et al. [96] investigated the spray characteristics of OME_X/diesel blends $(X = 3 - 6)$ under both evaporating and non-evaporating conditions, varying injection, and ambient pressures. The report indicated that under non-evaporating conditions, the STP of OME_X was higher than diesel fuel, owing to the high fuel density and resulting higher momentum. This view was also supported by the research of Li et al. [93], mentioned previously. However, due to OME_X high volatility, the STP was lower than diesel fuel under evaporating conditions.

As seen before, some physicochemical properties of OME_n differ from diesel. Researching pure OME_n is crucial to continue characterizing these fuels for ICE applications. In 2000, Ogawa et al. [97] conducted initial experiments to investigate the ultra-low emission and efficient combustion of OME_1 under stoichiometric combustion conditions. They employed exhaust gas recirculation (EGR) and a three-way catalyst (TWC) to achieve these objectives. Using a high-speed imaging technique, they observed the natural flame luminosity of OME_1 during the combustion process. The results indicated that introducing 30 vol% EGR could significantly reduce NO_X emissions without adversely affecting brake-specific energy consumption (BSEC) across a wide load range. However, carbon monoxide (CO) and total hydrocarbon (THC) emissions increased at high loads. To address this, using a TWC effectively reduced CO and THC emissions.

Considering that, in general $(n \geq 2)$, the OME_n CN is much higher than Diesel fuel, their combustion characteristics will also vary greatly. Therefore, Barro et al. [98] researched the combustion characteristics of OME_X (80% OME_3 and 20% OME_4) on a heavy-duty single-cylinder engine. The results showed that the high OME_X CN caused its ID to be shorter than diesel. In addition, the proportion of premixed combustion was reduced, while the diffusion combustion was faster. Thus, OME_X brake thermal efficiency (BTE) was higher than diesel without considering the gas exchange cycle. Furthermore, the influence of EGR on combustion characteristics was considered in their subsequent study. On this basis, Barro et al. [99] studied the impact of OME_X on diesel emissions. Compared with diesel, the THC and CO emissions of OME_X increased significantly in globally stoichiometric operation, and the proportion of methane in THC was relatively high. NO_X emission was highly sensitive to EGR. The authors reported that after burning OME_X, the particle size was mainly concentrated below 20 nm, and the injection pressure had little effect on the particle size distribution. Pélerin et al. [100] studied the impact of OME_1 and OME_X $(X = 3 - 6)$ on engine combustion and emissions characteristics. The results showed that although the injection duration of OME_1 and OME_X was longer, the combustion duration was shorter than Diesel fuel. In addition, without the use of EGR, due to the high oxygen content of OME_n, the emissions of CO and volatile organic compounds (VOC) were significantly lower than diesel. Moreover, soot mass and particle number (PN) were one order of magnitude lower. However, due to the more CH_2O– units in OME_X, the CH_2O emission was significantly higher than Diesel and OME_1. At low load conditions, the NO_X emission of OME_n was higher than diesel fuel, but it was the opposite at high load conditions due to the different high-temperature residence times.

As mentioned at the beginning of this section, this fuel family has some incompatibilities with the engine infrastructure. The swelling corrosion effect of OME_n on rubber and plastics significantly hinders its application in current diesel engines [101]. To identify a suitable sealing material for OME_n, Pélerin et al. [100] conducted a comparative study on the weight changes of seven different elastomers before and after immersing them in OME_1 and OME_X $(X = 3 - 6)$. Their research revealed that ethylene propylene diene rubber exhibited minimal weight change after 100 hours of immersion in OME_n, indicating its potential use as a sealing material for OME_n engines.

As seen previously, the research on OME_n is focused on mixtures with different polymerization degrees due to the possibility of achieving physicochemical properties closer to diesel. García-Carrero [102] conducted several studies in her thesis analyzing both OME_1 and OME_X $(X = 3 - 6)$ for two reference ECN conditions (Spray A and Spray D) in a high-pressure and high-temperature vessel. These conditions use two different nozzles which main difference is the size of the orifice, which is about double for the case of Spray D (medium and heavy-duty applications). Regarding ignition and combustion development, the injector modification has no significant effects when comparing both fuels. This fact is not observed for dodecane and Hydrotreated Vegetable Oil (HVO), fuels also evaluated by the author. Due to the difference in momentum flux between both sprays, Spray D causes a faster penetration than Spray A and a longer liquid length (LL). It was found that the ID for OME_1/Spray D was 9% lower than for Spray A, whose behavior for other fuels, including OME_X, is inverse, with a higher ID for the case of Spray D. In the case of LOL, the trend is similar to that obtained in the ID, except for OME_1, in which the LOL of Spray D is higher than that of Spray A, as well as for other fuels. Figure 2-18 compares HVO (left) and OME_1 (right) of the different parameters mentioned.

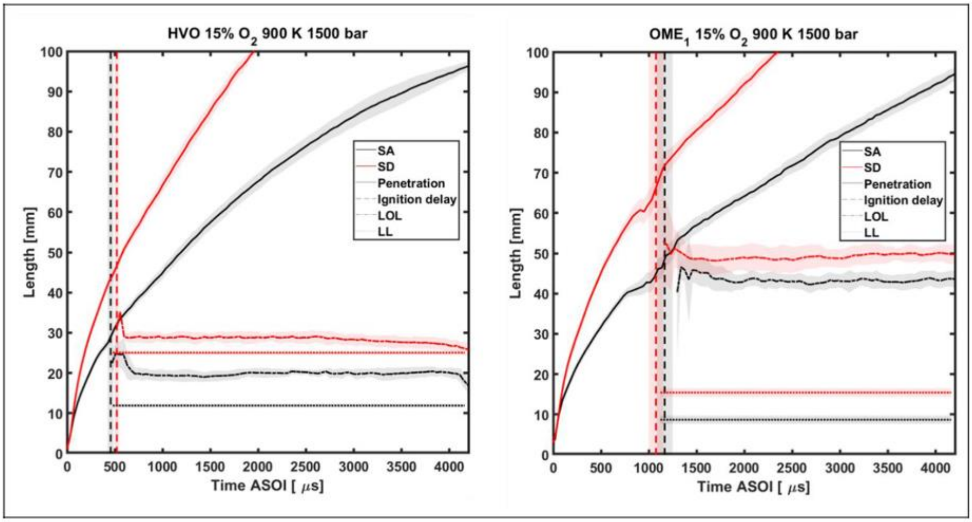

Figure 2-18 Comparison of the effect of nozzle diameter for HVO (left) and OME_1 *(right) on the characteristic spray parameters. Source:* [103]

García-Carrero observed that the combustion for OME_1 using Spray A is closer to premixed combustion than diffusive combustion, while for Spray D, it is a kind of transition. This is related to the low value of the equivalence ratio at the LOL position. In addition, no soot signs were detected for the oxygenated fuels (OME_1 and OME_X), consistent with the low equivalence ratio at the obtained LOL and the lack of C-C bonds.

As seen in this section, several OME_X compositions are used for different studies. The influence of OME_n chain length on engine combustion and emission characteristics presents a challenging aspect to comprehend. To address this, Dworschak et al. [104] conducted a study on a single-cylinder engine, analyzing the combustion and emission characteristics, as well as the particle size distribution of OME_n with varying chain lengths. Figure 2-19 illustrates that as the OME_n chain length increased, the combustion speed slowed down, resulting in decreased peak values of heat release rate and in-cylinder pressure. However, the combustion duration did not exhibit any dependence on the chain length. The study also revealed that NO_X emissions decreased with increasing chain length, primarily due to the reduction in combustion temperature resulting from a decrease in the peak value of the RoHR.

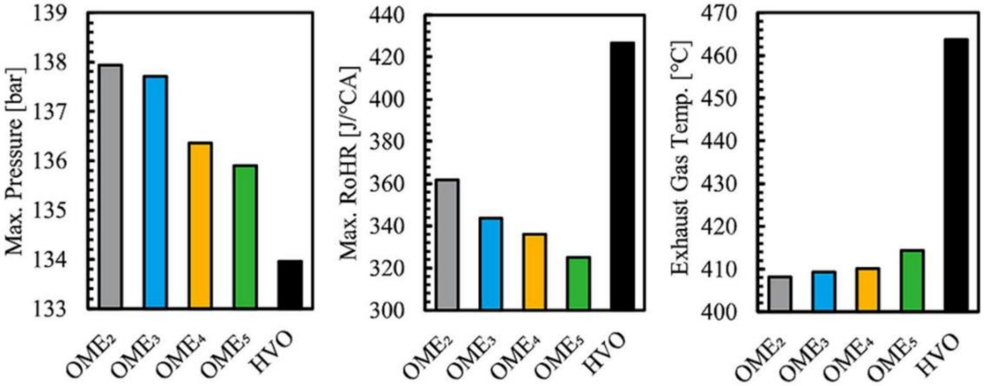

Figure 2-19. Max. cylinder pressure (left), max. RoHR (middle) and exhaust gas temperature (right). IMEP = 13 bar, 1200 rpm, no EGR, AFR = 1.8. Source: [104].

Conversely, carbon dioxide (CO_2) and CH_2O emissions increased. Furthermore, as the chain length increased, the thermal efficiency decreased by 1.95%, which aligns with the findings of Omari et al. [105]. At moderate load conditions, the particle size distribution exhibited no significant change with increasing chain length. Still, the concentration of particles increased substantially, potentially attributed to the decrease in combustion temperature. The geometric mean diameter of OME_n particles was found to be 35-40 nm, similar to that of the reference fuel. However, the particulate matter (PM) emission remained well below the regulatory limits.

In 1999, Dibble et al. [106,107] first studied the effects of OME_1/diesel blends on emissions characteristics in a Cummins B5.9 six-cylinder engine. They addressed the special precautions necessary for handling and storing these blends in fuel tanks due to the high volatility of OME_1. During the experiment, OME_1/diesel blends were prepared with 5%, 10%, 20%, and 30% volume fractions. Under steady conditions, measurements were taken for THC (total hydrocarbon), CO, NO_X, and PM emissions. The findings indicated that blending 30% OME_1 with diesel fuel resulted in a 35% reduction in PM emissions, while NO_X emissions decreased by 7-10% compared to diesel fuel. However, the blending of OME_1 led to increased THC and CO emissions. In a similar experiment, Gardner et al. [108] observed a 5-10% increase in brake-specific fuel consumption (BSFC) due to the lower LHV of OME_1.

Pellegrini et al. [109,110] studied the effects of OME_X/diesel blends ($X = 3 - 5$) on the combustion behavior and emission characteristics in CI engines. They specifically focused on comparing the particulate size distribution and PAH emissions of different fuels. The researchers discovered that, compared to diesel fuel, the high CN of OME_X led to a shorter ignition delay (ID) of the pilot injection. In contrast, the ID of the main injection remained unaffected due to the influence of the pilot injection [111]. However, since the lower heating value (LHV) of OME_X was lower than that of diesel fuel, the combustion phase in the expansion stroke and CA50 (crank angle at 50% mass fraction burned) were prolonged, decreasing thermal efficiency. Additionally, both THC and CO emissions decreased due to a reduction in the aromatic content of the fuel after blending with OME_X. The researchers observed that with an OME_X blending ratio of 50% and an EGR (exhaust gas recirculation) ratio of 35%, soot emissions were reduced by 84%, while NO_X emissions slightly increased. The authors attributed this effect to the intramolecular oxygen present in OME_X, which acted as an oxidizing agent, leading to significant soot oxidation during the final combustion phase.

To investigate the potential of oxygenated fuels as a means to reduce emissions from older vehicles instead of replacing them, Pellegrini et al. [112] conducted a study on regulated and non-regulated emissions from an engine using an electric single-roller chassis dynamometer, following the New European Driving Cycle (NEDC). The findings indicated a significant reduction in particulate matter (PM) emissions after blending 10% OME_X, while carbon dioxide (CO_2) and nitrogen oxide (NO_X) emissions increased. Additionally, there was a slight decrease in carbon monoxide (CO) and hydrocarbon (HC) emissions. The researchers suggested that the addition of OME_X resulted in a shorter ignition delay (ID) and prolonged residence time of the fuel in a high-temperature environment, facilitating the complete oxidation reaction of HC and CO [113].

Zhu et al. [114] conducted experiments on a single-cylinder CI (compression ignition) engine to investigate the effects of injection timing and blending ratios of OME_1/diesel blends on engine combustion and emission characteristics. The findings demonstrated that advancing the injection timing and increasing the OME_1 blending ratio improved engine thermal efficiency. Smoke and carbon monoxide (CO) emissions were notably reduced, aligning with previous studies [114,115]. However, there was an increase in hydrocarbon (HC) emissions with the OME_1 blending ratio. Nitrogen oxide (NO_X) emissions showed less sensitivity to changes in the blending ratio but significantly decreased with a delay in injection timing. Furthermore, as the injection timing advanced and the blending ratio increased, there was a significant decrease in the number of ultrafine particles and nanoparticles emitted.

In previous studies, it has been observed that NO_X emissions tend to increase when using OME_X/diesel blends slightly. Consequently, in order to simultaneously reduce particulate matter (PM) and NO_X emissions, the use of exhaust gas recirculation (EGR) becomes necessary. To explore the effects of EGR ratio on combustion and engine emission characteristics with OME_X/diesel blends ($X = 3 - 6$), Liu et al. [79] conducted experiments. The results demonstrated that the peak value of the rate of heat release (RoHR) decreased with increasing OME_X blending ratio, primarily due to the low calorific value and short mixing time of OME_X. However, the combustion rate notably increased during the late combustion period. When the EGR ratio was zero, the NO_X emissions from OME_X/diesel blends showed a slight improvement compared to diesel fuel, attributed to the high CN of OME_X, which shortened the ID period and reduced the premixed combustion ratio [116]. Additionally, the NO_X emissions further decreased with an increase in the EGR ratio. Iannuzzi et al. [117] also arrived at a similar conclusion. Therefore, EGR can significantly enhance the trade-off relationship between soot and NO_X emissions when utilizing OME_X/diesel blends.

Research has indicated that using OME_X/diesel blends significantly reduces soot emissions. In a study by Iannuzzi et al. [118], OH^* chemiluminescence and two-dimensional 2-Color Pyrometry (2C) techniques were employed to examine the processes of soot formation and oxidation following the combustion of OME_n/diesel and OME_X/diesel blends. The results revealed that no detectable soot was observed when burning pure OME_2 fuel, indicating that pure fuel combustion hardly produced any soot. Furthermore, findings from Ma et al. [94] demonstrated that both flame luminance and flame area decreased with an increase in the OME_X blending ratio. The reduction in soot emissions was attributed to the high oxygen content in the OME_n molecule and its molecular structure, which lacks C-C bonds that inhibit the formation of soot precursors. Additionally, Tan et al. [119] reported that the oxygen content in the molecule was not the sole factor influencing soot formation. The free radicals generated during the pyrolysis process of OME_n exhibited strong smoke-suppressing capabilities and significantly reduced soot emissions.

Lewiski [71] conducted a study in a 1.6L single-cylinder optical engine, analyzing several OME_X/diesel blends using high-speed spectroscopy imaging. The author reported the absence of soot during combustion using pure OME_X, confirming what was seen in previously mentioned studies. With an increase of diesel in the blend, the radiation associated with thermal radiation from soot also increased. Using 10% diesel was sufficient for the visible flame radiation to increase by an order of magnitude. Compared to the case of pure diesel, the values of soot remained very low for the cases of lower diesel concentration, showing up to 20% of diesel in the blend does not contribute to significant excess soot formation. In the case of 50% OME_X, a substantial reduction in soot was obtained compared to the pure Diesel case. However, the author noted that the late soot oxidation is extended due to the low LHV value of OME_X and, therefore, the longer injection duration required to achieve the same energy release as pure diesel.

These studies showed the importance of studying these fuels in engine-like conditions. The literature needs to include more relevant studies in larger engine sizes to improve the characterization of these e-fuels. Moreover, studies such as Lewiski showed that a substantial quantity of OME_X is needed to reduce notably the in-cylinder soot formation. This issue makes it necessary to find strategies to keep low soot values without increasing the OME_X quantity. For this reason, the last result chapter of this thesis (Chapter 6) aims to analyze the combined effect of piston geometry and OME_X/diesel blends in a medium-duty optical engine under engine-like conditions.

2.5 Summary and Conclusions

This chapter provides a summary of what is known about the Diesel combustion process under engine conditions. The characteristic phases of diesel combustion and the autoignition stage have been described as critical in pollutant emissions. This section has ended by showing how various authors have contributed to the characterization of the diesel flame structure up to the present day.

The ECN has been introduced as an organization operating under certain reference conditions, making studies carried out in different experimental facilities comparable and providing a database for experimental and CFD studies. Under this framework, various authors have contributed to characterizing the diesel spray for various operating conditions, such as ambient temperature and injection pressure.

In addition to the description of the free spray, a condition for a more accurate analysis of the combustion phenomenon, studies have also been conducted on how the spray-wall interaction affects the combustion process and flame structure. It has been observed that wall geometry significantly influences the combustion process. Therefore, various authors have studied modifications to the piston geometry to see how it affects the combustion process and soot formation. This geometry has evolved over the years to the radial-lips geometry, which significantly reduces soot, primarily by avoiding direct flame-flame interaction and redirecting the flame to areas of the piston where fresh oxygen is present and can oxidize the soot present in the flame.

To conclude, a compilation of the physicochemical characteristics of OME_n fuels has been discussed. These properties, along with its oxygenated molecular structure and lack of C-C bonds, make it a good candidate for use in engine applications as a substitute for diesel fuel. Therefore, the scientific community has been exploring these fuel combustion processes and flame structures compared to diesel. It has been observed that there are no soot precursors present in OME_n, and therefore, no soot is produced during the combustion process. The literature shows that a mixture of several OME_n, known as OME_X, can achieve properties closer to diesel.

However, despite OME_n advantages, some disadvantages, such as lower low heating value (LHV) and lubricity, make its direct use difficult. Hence, studies have mainly focused on using OME_X and diesel mixtures to overcome these fuels drawbacks while taking advantage of their potential for reducing soot. In general, results are promising when using blends of OME_X and diesel. However, it should be noted that the presence of diesel in the blend produces soot during the combustion process, which can be significant depending on the engine operating condition, such as the use of EGR strategies, currently mandatory in CI engines, to comply with NO_X emission legislation.

The discussion carried out in this chapter shows the importance of continuing to study OME_n fuels to be a good candidate for use in engine applications. This thesis aims to contribute to characterizing these fuels regarding combustion behavior and in-cylinder soot evolution by implementing several optical techniques. Consequently, the results section is divided into three chapters, aiming to address the gaps identified in this literature survey:

The first one (Chapter 4) studies the flame structure of OME_X and OME_1 under Spray A and Spray D ECN conditions, taking as a reference the case Spray A (dodecane fuel). The analysis is carried out in free spray conditions in a HPHT facility using OH and 355 nm PLIF techniques. The study contributes to enlarging the database carried out in the García thesis [102].

The second (Chapter 5) analyzes the effect of using unconventional piston geometries in a medium-duty optical engine in engine-like conditions. In Lewiski thesis [71], the use of this unconventional piston geometry showed a good impact on soot reductions in light-duty engines. However, it is important to study the spray/wall behavior when the distance is larger and the swirl effect is low.

The third (Chapter 6) analyzes the combustion behavior using several OME_X/Diesel blends. The literature shows the potential of using these blends in pollutant emissions reduction in the current engine fleet. However, the study carried out in Lewiski thesis [71] reported an important contribution of soot when low proportions of OME_X are used in a light-duty optical engine. In this way, this last result chapter aims to analyze the in-cylinder soot evolution in a larger optical engine (the same as Chapter 5). Furthermore, the inclusion of unconventional piston geometry with OME_X/diesel blends is studied in order to achieve low soot emissions.

Before addressing these issues in the results analysis, the next chapter (Chapter 3) will present the experimental facilities and tools used for the studies.

Bibliography

[1] Heywood J. Internal Combustion Engine Fundamentals. 2nd ed. New York: McGraw-Hill Education; 2018.

[2] Dec JE, Espey C. Chemiluminescence Imaging of Autoignition in a DI Diesel Engine. SAE Technical Paper 982685, 1998. https://doi.org/10.4271/982685.

[3] Gaydon AG. The Spectroscopy of Flames. Dordrecht: Springer Netherlands; 1974. https://doi.org/10.1007/978-94-009-5720-6.

[4] Kosaka H, Drewes VH, Catalfamo L, Aradi AA, Iida N, Kamimoto T. Two-dimensional imaging of formaldehyde formed during the ignition process of a diesel fuel spray. SAE Technical Papers 2000. https://doi.org/10.4271/2000-01-0236.

[5] Dec JE, Kelly-Zion PL. The Effects of Injection Timing and Diluent Addition on Late-Combustion Soot Burnout in a DI Diesel Engine Based on Simultaneous 2-D Imaging of OH and Soot. SAE Technical Papers, SAE International; 2000. https://doi.org/10.4271/2000-01-0238.

[6] Dec JE, Coy EB. OH radical imaging in a di diesel engine and the structure of the early diffusion flame. SAE Technical Papers 1996. https://doi.org/10.4271/960831.

[7] Glassman Irvin. Combustion. 3rd ed. San Diego: Academic Press; 1996.

[8] Dec JE. A conceptual model of DL diesel combustion based on laser-sheet imaging. SAE Transactions 1997:1319–48.

[9] Flynn PF, Durrett RP, Hunter GL, Zur Loye AO, Akinyemi OC, Dec JE, et al. Diesel combustion: An integrated view combining laser diagnostics, chemical kinetics, and empirical validation. SAE Technical Paper 1999-01-0509, 1999. https://doi.org/10.4271/1999-01-0509.

[10] Micó Reche C. DEVELOPMENT OF MEASUREMENT AND VISUALIZATION TECHNIQUES FOR CHARACTERIZATION OF MIXING AND COMBUSTION PROCESSES WITH SURROGATE

FUELS. Universitat Politècnica de València, 2015. https://doi.org/10.4995/Thesis/10251/58991.

[11] Dec JE, Canaan RE. PLIF Imaging of NO Formation in a DI Diesel Engine. SAE Technical Paper 980147, 1998. https://doi.org/10.4271/980147.

[12] Correas Jiménez D. Estudio teorico-experimental del chorro libre diesel isotermo. Universitat Politècnica de Valencia, 1998.

[13] Arrègle J. Análisis de la estructura y dinámica interna de chorros Diesel. Universitat Politècnica de Valància, 1998.

[14] Kosaka H, Nishigaki T, Kamimoto T, Sano T, Matsutani A, Harada S. Simultaneous 2-D Imaging of OH Radicals and Soot in a Diesel Flame by Laser Sheet Techniques. SAE transactions, 1996, p. 1184–95. https://doi.org/10.4271/960834.

[15] Musculus MPB. Multiple Simultaneous Optical Diagnostic Imaging of Early-Injection Low-Temperature Combustion in a Heavy-Duty Diesel Engine, 2006. https://doi.org/10.4271/2006-01-0079.

[16] Musculus MPB, Miles PC, Pickett LM. Conceptual models for partially premixed low-temperature diesel combustion. Prog Energy Combust Sci 2013;39:246–83. https://doi.org/10.1016/j.pecs.2012.09.001.

[17] Siebers DL, Hyggins BS. Effects of Injector Conditions on the Flame Lift-off Length of DI Diesel Spray. Springer-Verlag; 2002.

[18] Siebers DL, Higgins B. Flame Lift-Off on Direct-Injection Diesel Sprays Under Quiescent Conditions. SAE transactions, 2001, p. 400–21. https://doi.org/10.4271/2001-01-0530.

[19] Siebers DL, Higgins B, Pickett L. Flame Lift-Off on Direct-Injection Diesel Fuel Jets: Oxygen Concentration Effects. SAE transactions, 2002, p. 1490–509. https://doi.org/10.4271/2002-01-0890.

[20] Higgins B, Siebers DL. Measurement of the Flame Lift-Off Location on DI Diesel Sprays Using OH Chemiluminescence. SAE Technical Papers, 2001. https://doi.org/10.4271/2001-01-0918.

[21] Musculus MP, Dec JE, Tree DR. Effects of Fuel Parameters and Diffusion Flame Lift-Off on Soot Formation in a Heavy-Duty DI Diesel Engine. SAE transactions, 2002, p. 1467–89. https://doi.org/10.4271/2002-01-0889.

[22] Kosaka H, Aizawa T, Kamimoto T. Two-dimensional imaging of ignition and soot formation processes in a diesel flame. International Journal of Engine Research 2005;6:21–42. https://doi.org/10.1243/146808705X7347.

[23] Bruneaux G. Combustion structure of free and wall-impinging diesel jets by simultaneous laser-induced fluorescence of formaldehyde, poly-aromatic hydrocarbons, and hydroxides. International Journal of Engine Research 2008;9:249–65. https://doi.org/10.1243/14680874JER00108.

[24] Jing W, Roberts WL, Fang T. Spray combustion of Jet-A and diesel fuels in a constant volume combustion chamber. Energy Convers Manag 2015;89:525–40. https://doi.org/10.1016/j.enconman.2014.10.010.

[25] Engine Combustion Network n.d. https://ecn.sandia.gov/ (accessed February 22, 2023).

[26] Pickett LM, Genzale CL, Bruneaux G, Malbec L-M, Hermant L, Christiansen C, et al. Comparison of Diesel Spray Combustion in Different High-Temperature, High-Pressure Facilities. SAE Int J Engines 2010;3:2010-01–2106. https://doi.org/10.4271/2010-01-2106.

[27] Meijer M, Somers B, Johnson J, Naber J, Lee S-Y, Malbec LM, et al. ENGINE COMBUSTION NETWORK (ECN): CHARACTERIZATION AND COMPARISON OF BOUNDARY CONDITIONS FOR DIFFERENT COMBUSTION VESSELS. Atomization and Sprays 2012;22:777–806. https://doi.org/10.1615/AtomizSpr.2012006083.

[28] Bardi M, Payri R, Malbec LM, Bruneaux G, Pickett LM, Manin J, et al. Engine Combustion Network: Comparison of Spray Development, Vaporization, and Combustion in Different Combustion Vessels. Atomization and Sprays 2012;22:807–42. https://doi.org/10.1615/ATOMIZSPR.2013005837.

[29] Kastengren AL, Tilocco FZ, Powell CF, Manin J, Pickett LM, Payri R, et al. Engine Combustion Network (ECN): Measurements of Nozzle Geometry and Hydraulic Behavior. Atomization and Sprays 2012;22:1011–52. https://doi.org/10.1615/ATOMIZSPR.2013006309.

[30] Skeen SA, Manin J, Picket LM, Cenker E, Bruneaux G, Kondo K, et al. A Progress Review on Soot Experiments and Modeling in the Engine Combustion Network (ECN). SAE Int J Engines 2016:883–98.

[31] Pickett LM, Manin J, Genzale CL, Siebers DL, Musculus MPB, Idicheria CA. Relationship Between Diesel Fuel Spray Vapor Penetration/Dispersion and Local Fuel Mixture Fraction. SAE Int J Engines 2011;4:2011-01–0686. https://doi.org/10.4271/2011-01-0686.

[32] Maes N, Meijer M, Dam N, Somers B, Baya Toda H, Bruneaux G, et al. Characterization of Spray A flame structure for parametric variations in ECN constant-volume vessels using chemiluminescence and laser-induced fluorescence. Combust Flame 2016;174:138–51. https://doi.org/10.1016/j.combustflame.2016.09.005.

[33] Maes N. The life of a spray. 2019.

[34] Genzale CL, Reitz RD, Musculus MPB. Effects of Piston Bowl Geometry on Mixture Development and Late-Injection Low-Temperature Combustion in a Heavy-Duty Diesel Engine. SAE Int J Engines 2008;1:2008-01–1330. https://doi.org/10.4271/2008-01-1330.

[35] Busch S, Zha K, Perini F, Reitz R, Kurtz E, Warey A, et al. Bowl Geometry Effects on Turbulent Flow Structure in a Direct Injection Diesel Engine. SAE Technical Paper, 2018. https://doi.org/10.4271/2018-01-1794.

[36] Perini F, Zha K, Busch S, Kurtz E, Peterson RC, Warey A, et al. Piston geometry effects in a light-duty, swirl-supported diesel engine: Flow structure characterization. International Journal Engine Research 2018;19:1079–98. https://doi.org/10.1177/1468087417742572.

[37] Shiwaku T, Yasaki S, Nishida K, Ogata Y, Suzuki M, Umehara T. Split Injection Spray Development, Mixture Formation, and Combustion Processes in a Diesel Engine Piston Cavity: Rig Test and Real Engine

Results. SAE Technical Paper, 2018. https://doi.org/10.4271/2018-01-1698.

[38] Chen Y, Li X, Li X, Zhao W, Liu F. The wall-flow-guided and interferential interactions of the lateral swirl combustion system for improving the fuel/air mixing and combustion performance in DI diesel engines. Energy 2019;166:690–700. https://doi.org/10.1016/j.energy.2018.10.107.

[39] Han Z, Uludogan A, Hampson GJ, Reitz RD. Mechanism of Soot and NOx Emission Reduction Using Multiple-injection in a Diesel Engine. SAE Technical Paper, 1996. https://doi.org/10.4271/960633.

[40] Badami M, Mallamo F, Millo F, Rossi EE. Influence of Multiple Injection Strategies on Emissions, Combustion Noise and BSFC of a DI Common Rail Diesel Engine. SAE Technical Paper, 2002. https://doi.org/10.4271/2002-01-0503.

[41] O'Connor J, Musculus M. Post Injections for Soot Reduction in Diesel Engines: A Review of Current Understanding. SAE International Journal Engines 2013:400–21. https://doi.org/10.4271/2013-01-0917.

[42] Meingast U, Staudt M, Reichelt L, Renz U, Sommerhoff F-A. Analysis of Spray/Wall Interaction Under Diesel Engine Conditions. SAE Technical Paper, 2000. https://doi.org/10.4271/2000-01-0272.

[43] Bruneaux G. Mixing Process in High Pressure Diesel Jets by Normalized Laser Induced Exciplex Fluorescence Part II: Wall Impinging Versus Free Jet. SAE Technical Paper, 2005. https://doi.org/10.4271/2005-01-2097.

[44] Magnusson A, Andersson S, Jedrzejowski S. Spray-Wall Interaction: Diesel Fuels Impinging on a Tempered Wall. SAE Technical Paper, 2006. https://doi.org/10.4271/2006-01-1116.

[45] Ruth D, O'Connor J. Development and Verification of Reduced-Order Model for Diesel Spray Penetration and Spreading during Wall Impingement. SAE Technical Paper, 2017. https://doi.org/10.4271/2017-01-0814.

[46] Pickett LM, López JJ. Jet-Wall Interaction Effects on Diesel Combustion and Soot Formation. SAE Technical Paper, 2005. https://doi.org/10.4271/2005-01-0921.

[47] Gao J, Moon S, Zhang Y, Nishida K, Matsumoto Y. Flame structure of wall-impinging diesel fuel sprays injected by group-hole nozzles. Combust Flame 2009;156:1263–77. https://doi.org/10.1016/j.combustflame.2009.01.014.

[48] Wang X, Huang Z, Zhang W, Kuti OA, Nishida K. Effects of ultra-high injection pressure and micro-hole nozzle on flame structure and soot formation of impinging diesel spray. Appl Energy 2011;88:1620–8. https://doi.org/10.1016/j.apenergy.2010.11.035.

[49] Dreizler A, Böhm B. Advanced laser diagnostics for an improved understanding of premixed flame-wall interactions. Proceedings of the Combustion Institute 2015;35:37–64. https://doi.org/10.1016/j.proci.2014.08.014.

[50] Cartellieri WP, Herzog PL. Swirl Supported or Quiescent Combustion for 1990’s Heavy-Duty DI Diesel Engines - An Analysis. SAE Technical Papers, 1988. https://doi.org/10.4271/880342.

[51] Mollenhauer K, Tschöke H. Handbook of Diesel Engines. Berlin, Heidelberg: Springer Berlin Heidelberg; 2010. https://doi.org/10.1007/978-3-540-89083-6.

[52] Zha K, Busch S, Warey A, Peterson RC, Kurtz E. A Study of Piston Geometry Effects on Late-Stage Combustion in a Light-Duty Optical Diesel Engine Using Combustion Image Velocimetry. SAE Int J Engines 2018;11:2018-01–0230. https://doi.org/10.4271/2018-01-0230.

[53] Pickett LM, Siebers DL, Idicheria CA. Relationship Between Ignition Processes and the Lift-Off Length of Diesel Fuel Jets. JSTOR, 2005. https://doi.org/10.4271/2005-01-3843.

[54] Zhu Y, Zhao H, Melas DA, Ladommatos N. Computational Study of the Effects of the Re-entrant Lip Shape and Toroidal Radii of Piston Bowl on a HSDI Diesel Engine’s Performance and Emissions. SAE Technical Papers, 2004. https://doi.org/10.4271/2004-01-0118.

[55] Lee J, Lee S, Kim J, Kim D. Bowl Shape Design Optimization for Engine-Out PM Reduction in Heavy Duty Diesel Engine. SAE Technical Papers, 2015. https://doi.org/10.4271/2015-01-0789.

[56] Wickman DD, Senecal PK, Reitz RD. Diesel Engine Combustion Chamber Geometry Optimization Using Genetic Algorithms and Multi-Dimensional Spray and Combustion Modeling. SAE Technical Papers, 2001. https://doi.org/10.4271/2001-01-0547.

[57] Bianchi GM, Pelloni P, Corcione FE, Mattarelli E, Bertoni FL. Numerical Study of the Combustion Chamber Shape for Common Rail H.S.D.I. Diesel Engines. SAE Technical Paper, 2000. https://doi.org/10.4271/2000-01-1179.

[58] Kurtz EM, Styron J. An Assessment of Two Piston Bowl Concepts in a Medium-Duty Diesel Engine. SAE Int J Engines 2012;5:2012-01–0423. https://doi.org/10.4271/2012-01-0423.

[59] Leach F, Ismail R, Davy M, Weall A, Cooper B. The effect of a stepped lip piston design on performance and emissions from a high-speed diesel engine. Appl Energy 2018;215:679–89. https://doi.org/10.1016/j.apenergy.2018.02.076.

[60] Busch S, Zha K, Perini F, Reitz R. Piston Bowl Geometry Impacts on Late-Cycle Flow and Mixing in a Small-Bore Diesel Engine. 2017.

[61] Dahlstrom J, Andersson O, Tuner M, Persson H. Experimental Comparison of Heat Losses in Stepped-Bowl and Re-Entrant Combustion Chambers in a Light Duty Diesel Engine. SAE Technical Papers, 2016. https://doi.org/10.4271/2016-01-0732.

[62] Dolak JG, Shi Y, Reitz RD. A Computational Investigation of Stepped-Bowl Piston Geometry for a Light Duty Engine Operating at Low Load. SAE Technical Papers, 2010. https://doi.org/10.4271/2010-01-1263.

[63] Neely GD, Sasaki S, Sono H. Investigation of Alternative Combustion Crossing Stoichiometric Air Fuel Ratio for Clean Diesels. SAE Technical Paper, 2007. https://doi.org/10.4271/2007-01-1840.

[64] Cornwell R, Conicella F. Direct injection diesel engines. US 8,770,168 B2, 2014.

[65] Smith A. Ricardo low emissions combustion technology helps JCB create the off-highway industry's cleanest engine. Ricardo Press Release 2010:4–6.

[66] Yoo D, Kim D, Jung W, Kim N, Lee D. Optimization of Diesel Combustion System for Reducing PM to Meet Tier4-Final Emission Regulation without Diesel Particulate Filter. SAE Technical Papers, 2013. https://doi.org/10.4271/2013-01-2538.

[67] Busch S, Zha K, Kurtz E, Warey A, Peterson R. Experimental and Numerical Studies of Bowl Geometry Impacts on Thermal Efficiency in a Light-Duty Diesel Engine. SAE Technical Papers, 2018, p. 1–12. https://doi.org/10.4271/2018-01-0228.

[68] Eismark J, Balthasar M. Device for Reducing Emissions in a Vehicle Combustion Engine. US 8,499,735 B2, 2013.

[69] Eismark J, Christensen M, Andersson M, Karlsson A, Denbratt I. Role of fuel properties and piston shape in influencing soot oxidation in heavy-duty low swirl diesel engine combustion. Fuel 2019;254:115568. https://doi.org/10.1016/j.fuel.2019.05.151.

[70] Eismark J, Andersson M, Christensen M, Karlsson A, Denbratt I. Role of Piston Bowl Shape to Enhance Late-Cycle Soot Oxidation in Low-Swirl Diesel Combustion. SAE Int J Engines 2019;12:03-12-03–0017. https://doi.org/10.4271/03-12-03-0017.

[71] Vargas Lewiski F de. Analysis of the combustion process and soot formation in a single cylinder optical engine fueled with e-fuels and using different piston geometries. Universitat Politècnica de València, 2021. https://doi.org/10.4995/Thesis/10251/180351.

[72] Hua Y, Liu S, Li R, Mei L. Experimental study of regulated and unregulated emissions from a diesel engine using coal-based fuels. Fuel 2020. https://doi.org/10.1016/j.fuel.2020.118658.

[73] Liu H, Wang Z, Li Y, Zheng Y, He T, Wang J. Recent progress in the application in compression ignition engines and the synthesis technologies of polyoxymethylene dimethyl ethers. Appl Energy 2019;233–234:599–611. https://doi.org/10.1016/j.apenergy.2018.10.064.

[74] Liu J, Wang L, Wang P, Sun P, Liu H, Meng Z, et al. An overview of polyoxymethylene dimethyl ethers as alternative fuel for compression ignition engines. Fuel 2022;318:123582. https://doi.org/10.1016/j.fuel.2022.123582.

[75] Zhao Q, Wang H, Qin Z, Wu Z, Wu J, Fan W, et al. Synthesis of polyoxymethylene dimethyl ethers from methanol and trioxymethylene with molecular sieves as catalysts. Journal of Fuel Chemistry and Technology 2011;39:918–23. https://doi.org/10.1016/S1872-5813(12)60003-6.

[76] Arellano-Treviño MA, Bartholet D, To AT, Bartling AW, Baddour FG, Alleman TL, et al. Synthesis of Butyl-Exchanged Polyoxymethylene Ethers as Renewable Diesel Blendstocks with Improved Fuel Properties. ACS Sustain Chem Eng 2021;9:6266–73. https://doi.org/10.1021/acssuschemeng.0c09216.

[77] Chen Y, Ma J, Han B, Zhang P, Hua H, Chen H, et al. Emissions of automobiles fueled with alternative fuels based on engine technology: A review. Journal of Traffic and Transportation Engineering (English Edition) 2018;5:318–34. https://doi.org/10.1016/j.jtte.2018.05.001.

[78] Bartholet DL, Arellano-Treviño MA, Chan FL, Lucas S, Zhu J, St. John PC, et al. Property predictions demonstrate that structural diversity can improve the performance of polyoxymethylene ethers as potential bio-based diesel fuels. Fuel 2021;295:120509. https://doi.org/10.1016/j.fuel.2021.120509.

[79] Liu J, Wang H, Li Y, Zheng Z, Xue Z, Shang H, et al. Effects of diesel/PODE (polyoxymethylene dimethyl ethers) blends on combustion and emission characteristics in a heavy duty diesel engine. Fuel 2016;177:206–16. https://doi.org/10.1016/j.fuel.2016.03.019.

[80] Liu H, Wang Z, Zhang J, Wang J, Shuai S. Study on combustion and emission characteristics of Polyoxymethylene Dimethyl Ethers/diesel blends in light-duty and heavy-duty diesel engines. Appl Energy 2017;185:1393–402. https://doi.org/10.1016/j.apenergy.2015.10.183.

[81] Wei J, Zeng Y, Pan M, Zhuang Y, Qiu L, Zhou T, et al. Morphology analysis of soot particles from a modern diesel engine fueled with

different types of oxygenated fuels. Fuel 2020;267:117248. https://doi.org/10.1016/j.fuel.2020.117248.

[82] Nour M, Attia AMA, Nada SA. Improvement of CI engine combustion and performance running on ternary blends of higher alcohol (Pentanol and Octanol)/hydrous ethanol/diesel. Fuel 2019;251:10–22. https://doi.org/10.1016/j.fuel.2019.04.026.

[83] Zheng Z, Wang X, Zhong X, Hu B, Liu H, Yao M. Experimental study on the combustion and emissions fueling biodiesel/n-butanol, biodiesel/ethanol and biodiesel/2,5-dimethylfuran on a diesel engine. Energy 2016;115:539–49. https://doi.org/10.1016/j.energy.2016.09.054.

[84] Theinnoi K, Suksompong P, Temwutthikun W. Engine Performance of Dual Fuel Operation with In-cylinder Injected Diesel Fuels and In-Port Injected DME. Energy Procedia 2017;142:461–7. https://doi.org/10.1016/j.egypro.2017.12.072.

[85] Burger J, Siegert M, Ströfer E, Hasse H. Poly(oxymethylene) dimethyl ethers as components of tailored diesel fuel: Properties, synthesis and purification concepts. Fuel 2010;89:3315–9. https://doi.org/10.1016/j.fuel.2010.05.014.

[86] Liu J, Sun P, Huang H, Meng J, Yao X. Experimental investigation on performance, combustion and emission characteristics of a common-rail diesel engine fueled with polyoxymethylene dimethyl ethers-diesel blends. Appl Energy 2017;202:527–36. https://doi.org/10.1016/j.apenergy.2017.05.166.

[87] Montgomery MJ, Das DD, McEnally CS, Pfefferle LD. Analyzing the robustness of the yield sooting index as a measure of sooting tendency. Proceedings of the Combustion Institute 2019;37:911–8. https://doi.org/10.1016/j.proci.2018.06.105.

[88] Ottenwaelder T, Pischinger S. Effects of Biofuels on the Mixture Formation and Ignition Process in Diesel-Like Jets, 2017. https://doi.org/10.4271/2017-01-2332.

[89] Srna A, Barro C, Herrmann K, Möri F, Hutter R, Boulouchos K. POMDME as an Alternative Pilot Fuel for Dual-Fuel Engines: Optical

Study in a RCEM and Application in an Automotive Size Dual-Fuel Diesel Engine, 2018. https://doi.org/10.4271/2018-01-1734.

[90] Musculus MPB, Kattke K. Entrainment Waves in Diesel Jets. SAE Int J Engines 2009;2:2009-01–1355. https://doi.org/10.4271/2009-01-1355.

[91] Honecker C, Neumann M, Glueck S, Schoenen M, Pischinger S. Optical Spray Investigations on OME3-5 in a Constant Volume High Pressure Chamber, 2019. https://doi.org/10.4271/2019-24-0234.

[92] García A, Monsalve-Serrano J, José Sanchís E, Fogué-Robles Á. Exploration of suitable injector configuration for dual-mode dual-fuel engine with diesel and OMEx as high reactivity fuels. Fuel 2020;280:118670. https://doi.org/10.1016/j.fuel.2020.118670.

[93] Li D, Gao Y, Liu S, Ma Z, Wei Y. Effect of polyoxymethylene dimethyl ethers addition on spray and atomization characteristics using a common rail diesel injection system. Fuel 2016;186:235–47. https://doi.org/10.1016/j.fuel.2016.08.082.

[94] Ma X, Ma Y, Sun S, Shuai S-J, Wang Z, Wang J-X. PLII-LEM and OH* Chemiluminescence Study on Soot Formation in Spray Combustion of PODEn-Diesel Blend Fuels in a Constant Volume Vessel, 2017. https://doi.org/10.4271/2017-01-2329.

[95] Huang H, Teng W, Li Z, Liu Q, Wang Q, Pan M. Improvement of emission characteristics and maximum pressure rise rate of diesel engines fueled with n-butanol/PODE3-4/diesel blends at high injection pressure. Energy Convers Manag 2017;152:45–56. https://doi.org/10.1016/j.enconman.2017.09.038.

[96] Liu J, Feng L, Wang H, Zheng Z, Chen B, Zhang D, et al. Spray characteristics of gasoline/PODE and diesel/PODE blends in a constant volume chamber. Appl Therm Eng 2019;159:113850. https://doi.org/10.1016/j.applthermaleng.2019.113850.

[97] Ogawa H, Nabi N, Minami M, Miyamoto N, Bong-Seock K. Ultra Low Emissions and High Performance Diesel Combustion with a Combination of High EGR, Three-Way Catalyst, and a Highly Oxygenated Fuel, Dimethoxy Methane (DMM). SAE transactions, 2000, p. 1019–27. https://doi.org/10.4271/2000-01-1819.

[98] Barro C, Parravicini M, Boulouchos K. Neat polyoxymethylene dimethyl ether in a diesel engine; part 1: Detailed combustion analysis. Fuel 2019;256:115892. https://doi.org/10.1016/j.fuel.2019.115892.

[99] Barro C, Parravicini M, Boulouchos K, Liati A. Neat polyoxymethylene dimethyl ether in a diesel engine; part 2: Exhaust emission analysis. Fuel 2018;234:1414–21. https://doi.org/10.1016/j.fuel.2018.07.108.

[100] Pélerin D, Gaukel K, Härtl M, Jacob E, Wachtmeister G. Potentials to simplify the engine system using the alternative diesel fuels oxymethylene ether OME1 and OME3−6 on a heavy-duty engine. Fuel 2020;259:116231. https://doi.org/10.1016/j.fuel.2019.116231.

[101] Härtl M, Seidenspinner P, Jacob E, Wachtmeister G. Oxygenate screening on a heavy-duty diesel engine and emission characteristics of highly oxygenated oxymethylene ether fuel OME1. Fuel 2015;153:328–35. https://doi.org/10.1016/j.fuel.2015.03.012.

[102] García Carrero AA. Experimental Study of the Fuel Effect on Diffusion Combustion and Soot Formation under Diesel Engine-Like Conditions. Universitat Politècnica de València, 2022. https://doi.org/10.4995/THESIS/10251/179997.

[103] Pastor J V., García-Oliver JM, Micó C, García-Carrero AA. An experimental study with renewable fuels using ECN Spray A and D nozzles. International Journal of Engine Research 2021. https://doi.org/10.1177/14680874211031200.

[104] Dworschak P, Berger V, Härtl M, Wachtmeister G. Neat Oxymethylene Ethers: Combustion Performance and Emissions of OME2, OME3, OME4 and OME5 in a Single-Cylinder Diesel Engine, 2020. https://doi.org/10.4271/2020-01-0805.

[105] Omari A, Heuser B, Pischinger S, Rüdinger C. Potential of long-chain oxymethylene ether and oxymethylene ether-diesel blends for ultra-low emission engines. Appl Energy 2019;239:1242–9. https://doi.org/10.1016/j.apenergy.2019.02.035.

[106] Cheng AS, Dibble RW. Emissions Performance of Oxygenate-in-Diesel Blends and Fischer-Tropsch Diesel in a Compression Ignition Engine, 1999. https://doi.org/10.4271/1999-01-3606.

[107] Vertin KD, Ohi JM, Naegeli DW, Childress KH, Hagen GP, McCarthy CI, et al. Methylal and Methylal-Diesel Blended Fuels for Use in Compression-Ignition Engines, 1999. https://doi.org/10.4271/1999-01-1508.

[108] Gardner TP, Low SS, Kenney TE. Evaluation of Some Alternative Diesel Fuels for Low Emissions and Improved Fuel Economy. SAE Transactions, 2001, p. 24–78. https://doi.org/10.4271/2001-01-0149.

[109] Pellegrini L, Marchionna M, Patrini R, Beatrice C, Del Giacomo N, Guido C. Combustion Behaviour and Emission Performance of Neat and Blended Polyoxymethylene Dimethyl Ethers in a Light-Duty Diesel Engine, 2012. https://doi.org/10.4271/2012-01-1053.

[110] Pellegrini L, Patrini R, Marchionna M. Effect of POMDME Blend on PAH Emissions and Particulate Size Distribution from an In-Use Light-Duty Diesel Engine, 2014. https://doi.org/10.4271/2014-01-1951.

[111] Beatrice C, Bertoli C, Del Giacomo N, Migliaccio M na. Experimental Investigation on High-Quality Diesel Fuels Effects in a Light Duty CR Diesel Engine. SAE Transactions, 2000, p. 1517–24. https://doi.org/10.4271/2000-01-1911.

[112] Pellegrini L, Marchionna M, Patrini R, Florio S. Emission Performance of Neat and Blended Polyoxymethylene Dimethyl Ethers in an Old Light-Duty Diesel Car, 2013. https://doi.org/10.4271/2013-01-1035.

[113] Faiz A, Weaver CS, Walsh MP. Air Pollution from Motor Vehicles: Standards and Technologies for Controlling Emissions. World Bank Publications; 1996.

[114] Zhu R, Miao H, Wang X, Huang Z. Effects of fuel constituents and injection timing on combustion and emission characteristics of a compression-ignition engine fueled with diesel-DMM blends. Proceedings of the Combustion Institute 2013;34:3013–20. https://doi.org/10.1016/j.proci.2012.06.174.

[115] Ren Y, Huang ZH, Jiang DM, Liu LX, Zeng K, Liu B, et al. Engine performance and emission characteristics of a compression ignition engine fuelled with diesel/dimethoxymethane blends. Proceedings of the Institution of Mechanical Engineers, Part D: Journal of Automobile

Engineering 2005;219:905–14. https://doi.org/10.1243/095440705X28367.

[116] Li T, Okabe Y, Izumi H, Shudo T, Ogawa H. Dependence of Ultra-High EGR Low Temperature Diesel Combustion on Fuel Properties, 2006. https://doi.org/10.4271/2006-01-3387.

[117] Iannuzzi SE, Barro C, Boulouchos K, Burger J. POMDME-diesel blends: Evaluation of performance and exhaust emissions in a single cylinder heavy-duty diesel engine. Fuel 2017;203:57–67. https://doi.org/10.1016/j.fuel.2017.04.089.

[118] Iannuzzi SE, Barro C, Boulouchos K, Burger J. Combustion behavior and soot formation/oxidation of oxygenated fuels in a cylindrical constant volume chamber. Fuel 2016;167:49–59. https://doi.org/10.1016/j.fuel.2015.11.060.

[119] Tan YR, Botero ML, Sheng Y, Dreyer JAH, Xu R, Yang W, et al. Sooting characteristics of polyoxymethylene dimethyl ether blends with diesel in a diffusion flame. Fuel 2018;224:499–506. https://doi.org/10.1016/j.fuel.2018.03.051.

Chapter 3

Tools and Methodology

Content

3.1 Introduction

This chapter aims to introduce the tools and methodology used in this thesis. We will begin by discussing the optical techniques used. In this section, the physical phenomenon on which these techniques are based will be briefly described, and the explanation will focus in greater detail on the specific application used in the studies of this thesis. The following section will focus on explaining the different experimental facilities in which the studies detailed in the following chapters have been carried out. Finally, we will focus on the study parameters on which the thesis is based: fuels and piston geometries, as has been mentioned throughout the previous chapters.

3.2 Optical Techniques for the Analysis of the Combustion Process

As seen in Chapter 2, the use of optical techniques for the study of combustion phenomena and the description of flame structure is essential. Over the years, experimental methodology and technology improvements have made it possible to study this phenomenon with increasing precision.

The use of optics in this field is vital since they are considered non-intrusive techniques, which means that the phenomenon, in this case, the combustion process, can be analyzed without the event being affected by the analysis technique. There is a wide variety of optical techniques used in the field of combustion, and each one has its usefulness, depending on what needs to be studied.

It is important, perhaps, to separate these techniques into two main categories: those based on the radiation emitted by the flame itself, naturally, and those based on forcing that radiation, which would not be emitted solely by combustion. The first category would include any technique that does not require electromagnetic radiation (EM) as an external source to force radiation during the combustion process. However, in the second category, all techniques based on using a laser source would be introduced, known as laser spectroscopy techniques. In this case, the laser source is used to force specific radiation emission (depending on the technique used) in the study area. These techniques are usually used to detect species formed within the flame, obtaining, for example, temperature, composition, concentration, etc.

In this thesis, optical techniques belonging to both categories have been used: Chemiluminescence and Natural Flame Radiation belong to the first group, while Planar Laser-Induced Fluorescence (PLIF) belong to the second group. All of them will be described in detail below.

3.2.1 Planar Laser Induced Fluorescence

Actually, the phenomenon is known as Laser-Induced Fluorescence (LIF) since the planar aspect refers only to a variation in the geometry of the laser beam, going from a circular beam (direct output from the laser source) to a laser sheet through the use of a series of optical elements that allow this transformation, which will be discussed later. This geometric transformation of the laser beam has its advantages, which will also be discussed later. To begin with, let's talk about the physical phenomenon of this process without going into too much detail since countless books and studies use techniques based on this phenomenon. The development of the discussion is based on Hua Zhao description in [1].

Laser-induced fluorescence (LIF) is the emission of light (photons) by an atom (or molecule) that has been excited by a laser beam. Initially, the atom (or molecule) is in a lower electronic state (corresponding to a lower energy level) before being excited and transitioning to a higher electronic level (and therefore higher energy). This is consistent with the principle of lowest energy state as a general principle in quantum mechanics, which defines that any quantum system tends towards a lower energy state as long as the system does not interact with external perturbations. In this case, the source that perturbs the system is the laser source introducing energy to the molecule (system). This phenomenon is also known as energy absorption. Quantum mechanics indeed defines energy levels as discrete levels, so it is necessary for the energy absorbed by the system to be equal to the energy gap required to excite the molecule to one of the higher energy levels. In fact, to induce the LIF phenomenon, it is essential to introduce the energy necessary to overcome this gap from a lower electronic level to a higher one and thus move to what is known as the molecule excited state. This energy, by the laser, is made by the interaction of the energy of the photons with the molecule (light/matter interaction). Quantum mechanics shows that the photon energy is inversely proportional to its wavelength, so the wavelength of the laser will be key to achieving electronic excitation.

Each atom (or molecule) has a characteristic diagram of energy levels, which could be used as a fingerprint analogy for individuals. Therefore, the LIF signal can be related to specific properties, such as the concentration of absorbing species. The fluorescence phenomenon is a function of the population of the upper (excited) energy level. The mathematical development is not carried out because many sources of information detail the procedure perfectly. This development results in a mathematical expression of the fluorescence signal proportional to the number of molecules in the excited level (3-1).

$$F = h\upsilon N_2 A_{21} \frac{\Omega}{4\pi} lAN_t \frac{B_{12}}{B_{21} + B_{12}} \frac{1}{1 + \frac{I_{sat}^{v}}{I_v}} \tag{3-1}$$

$$I_{sat}^{v} = \frac{(A_{21} + Q_{21})c}{B_{21} + B_{12}} \tag{3-2}$$

Where h is Planck constant, υ is the frequency of fluorescence emission, Ω is the solid angle collection, A is the area of the laser beam, l is the axial extension of the beam from where the fluorescence is observed, I_v is the spectral intensity of the laser, N_2 is the population in the excited level, N_t is the sum of the population of both energy levels, A_{21}, B_{21}, B_{12} and Q_{21} are the Einstein coefficients associated with spontaneous emission, stimulated emission, stimulated absorption, and quenching, respectively. Finally, I_{sat}^{v} is the saturation intensity defined by (3-2).

The fluorescence signal equation (3-1) can be simplified by assuming two cases, referring to low and high laser intensity.

In the case of low-intensity ($I_v \ll I_{sat}^{v}$), the previous equation simplifies to equation (3-3):

$$F = \frac{h\upsilon}{c} \frac{\Omega}{4\pi} lAN_t B_{12} I_v \frac{A_{21}}{A_{21} + Q_{21}} \tag{3-3}$$

It is known as the linear fluorescence equation because fluorescence has a linear behavior with laser intensity. This regime causes the detection of species to be significantly reduced because the term $A_{21} \ll Q_{21}$ at atmospheric or higher pressure. Therefore, in this regime, it is necessary to evaluate the quenching rate constant to make quantitative measurements of the species of interest. The difficulty arises because this quenching rate is sensitive to pressure, composition, and temperature, making it difficult to measure quantitative LIF in combustion environments at atmospheric or high pressure.

In the case of high-intensity ($I_v \gg I_{sat}^v$), fluorescence is independent of irradiance, and the quenching effect can be ignored. However, being in this regime is not easy as parts of the beam, such as the edges, do not achieve saturation, in addition to achieving saturation during the entire duration of the laser pulse. Furthermore, if the beam geometry is modified to a planar beam for PLIF, which is commonly used in ICE applications, it is even more difficult to achieve saturation.

The fluorescence signal tends to shift towards the red compared to the incident radiation from the laser (Stokes shift), making it ideal for avoiding interferences from spuriously scattered laser light or Mie scattering [2].

In this thesis, the PLIF technique has been used in the low-intensity regime because of the difficulty in achieving the high-intensity condition mentioned before. A lens system shown in Figure 3-1 is composed of three cylindrical lenses. The first is a Plano-Concave lens (PCV) with a focal length (f) equal to -12.7 mm. This lens transforms the original laser spot to a broad plane, which means that the X-coordinate is not modified, keeping the circular spot original size, while the Y-coordinate is stretched. Then, a Plano-Convex lens (PCX) with f=100 mm collimates the laser light so the Y-coordinate does not increase. This lens fixes the laser plane's height, improving the energy laser distribution. Finally, another PCX with f=500mm focuses the incident laser beam in the X-coordinate, keeping its height (Y-coordinates is fixed). This third lens concentrates the laser energy in a narrow laser sheet. This modification in the geometry allows obtaining a two-dimensional map of the species of interest in the measurement zone, thus providing good spatial resolution (due to the narrow laser sheet geometry) and temporal resolution due to the short duration of the laser pulse (around 10 ns).

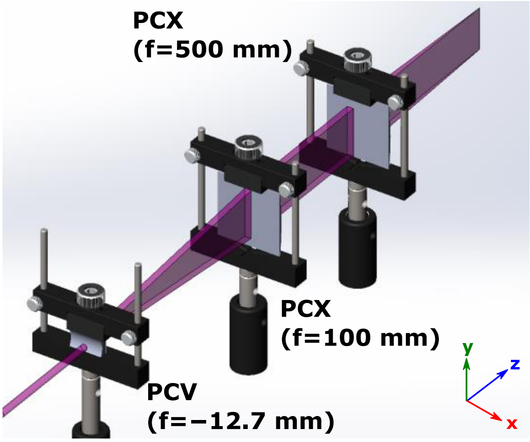

Figure 3-1 Lens system for the geometrical transform of the laser spot. It is composed by three cylindrical lenses.

This technique has been used to detect two species occurring naturally during the combustion process and provide important information about this process. On the one hand, formaldehyde (CH_2O) is known as an intermediate generated during the autoignition process initial phase, as mentioned in Chapter 2. As autoignition evolves towards the high-temperature regime, CH_2O is rapidly consumed, transitioning to high-temperature ignition. Therefore, these species are excellent natural tracers of the initial phase of the autoignition process. It is also known as a tracer of low-temperature reactions or "cool flame". The fluorescence excitation spectrum of CH_2O has a peak at 354.82 nm, corresponding to the 4_0^1 line of the $\tilde{A}^1A_2 - \tilde{X}^1A_1$ band [3]. In this way, the third harmonic (355 nm) of a Nd:YAG laser (Laser Continuum Surelite II) was used to excite these molecules. The emission spectrum, slightly shifted to the red, starts at about 360 nm. Most CH_2O fluorescence is found in the range of 390 to 460 nm [1]. In order to reduce the signal-to-noise ratio, a background image is subtracted from PLIF images. In this case, the background image refers to measurements without the laser, removing any contribution from chemiluminescence radiation in the 355 nm PLIF images. This procedure is discussed in detail in the Methodology section of Chapter 4.

The other species studied is the OH radical. This radical is in equilibrium as a product in the high-temperature regions of the flame, making it ideal as a tracer of the high-temperature reaction zones. With this in mind, the relationship between both CH_2O and OH species can be seen. When the

OH radical appears, and hence the high-temperature reactions, the CH_2O in that zone coexisting with the OH begins to be consumed due to the high-temperature reactions. The setup employs a Nd:YAG (Powerlite DLS System 8010) pumped dye laser (Vista Dye Laser) feed with Rhodamine 590. The output is doubled (Vista FX Frequency) to excite the OH radical at 283.46 nm, which corresponds to the P1(4) band of the (1,0) vibrational band of $A^2\Sigma - X^2\Pi$ transition. Although the Q branch is often detected because of its high line strength, at high pressures, it may be preferable to detect weaker branches, such as the P branch, to reduce the absorption effect caused by the flame. [4]. The fluorescence emission associated with this specie is around 310 nm. The excitation wavelength selection was obtained by knowing the excitation spectrum of OH (LIFBASE [5]), represented in Figure 3-2, and by calibrating the laser wavelength using a Bunsen burner flame. Usually, on-resonant and off-resonant measurements of OH PLIF are used [6,7]. On-resonant measurements refer to those associated with a peak of the OH transition of high-intensity fluorescence. In contrast, off-resonant measurements refer to the selection of a wavelength at which there is no such transition, and therefore, no fluorescence signal from OH is detected. In this way, the off-resonant measurement can be extracted from the on-resonant measurement, thus reducing the signal-to-noise ratio. As mentioned for 355 nm PLIF, a detailed example of this procedure appears in Chapter 4. Considering this, the highest intensity peak obtained in the calibration used as an on-resonant was associated with 283.46 nm (red line). The 283.38 nm was used as the off-resonant measurement (green line).

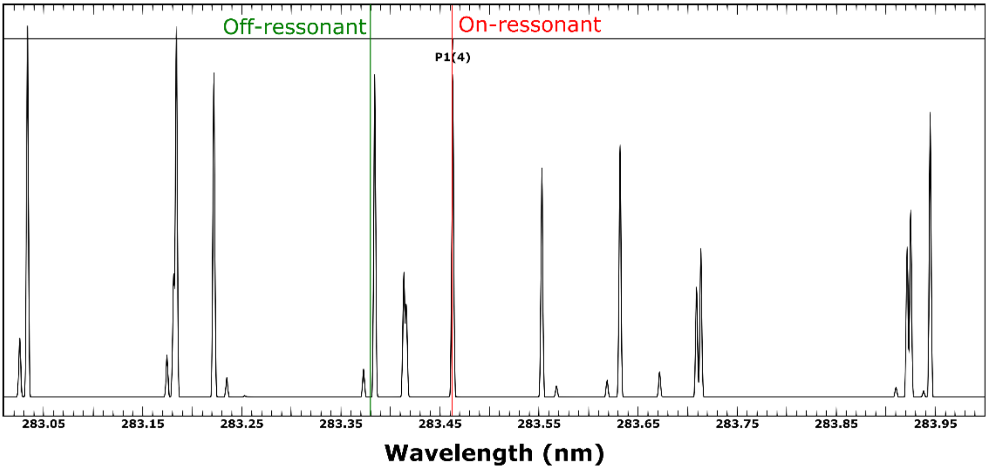

Figure 3-2 OH excitation spectrum simulated with LIFBASE software [5].

3.2.2 Two Color Pyrometry

The Diesel flame emits visible broadband radiation (natural flame radiation) that is primarily dominated by soot incandescence. Soot particles within the flame and surrounding gas have nearly identical temperatures, causing the particles to emit thermal radiation akin to a body at high temperatures. This thermal radiation is much more intense than emissions from other species via the chemiluminescence phenomenon. Consequently, images taken during Diesel combustion using visible-wavelength cameras primarily show soot radiation [8]. The Two-Color Pyrometry (2C) technique is an optical thermometry method that leverages the presence of radiating soot within the flame. This soot radiation intensity (I_{soot}) is directly proportional to the radiation emitted by a black body at the same temperature (T).

The 2C method is founded on the principle that the radiation emitted by a sooting flame, with uniform temperature and soot distribution, relies on the wavelength, temperature, and amount of soot within the flame. Assuming the flame emits radiation akin to a blackbody, the intensity of soot radiation at a particular wavelength can be mathematically expressed using Planck's law, as depicted in equation (3-4).

$$I_b(T,\lambda) = \frac{C_1}{\lambda^5\left[e^{\frac{C_2}{\lambda T}} - 1\right]} \tag{3-4}$$

Where I_b is the radiance emitted by the blackbody. $C_1 = 3.7418 \times 10^{-16}\, Wm^2$ the first Planck constant, $C_2 = 1.4388 \times 10^{-2}$mk is the second Planck constant, and λ is the wavelength. However, the soot is a grey body with an emissivity ε below 1. Thus, the emission of the flame can be expressed as the equation (3-5).

$$I(T,\lambda) = \varepsilon I_b(T,\lambda) \tag{3-5}$$

The emissivity ε is the fraction of blackbody radiation emitted by a surface at wavelength λ. In this sense, $I(T,\lambda)$ is the emissivity of a nonblackbody and $I_b(T,\lambda)$ is the emissivity of a blackbody, where both are at the same temperature (T) and wavelength λ. For the two-color technique, an apparent temperature T_a is considered in the calculation, which is defined as the blackbody temperature that emits the same radiation intensity as a nonblackbody at temperature T. Taking into the definition of T_a, it is possible to assume that $I_b(T_a, \lambda) = I(T, \lambda)$. Combining this assumption with equations (3-4) and (3-5) makes it possible to express the equation (3-6).

$$\varepsilon(\lambda) = \frac{e^{\left(\frac{C_2}{\lambda T}\right)} - 1}{e^{\left(\frac{C_2}{\lambda T_a}\right)} - 1} \qquad (3\text{-}6)$$

In practice, $\varepsilon(\lambda)$ is estimated for soot particles using the empirical correlation developed by Hottel and Broughton [9]:

$$\varepsilon(\lambda) = 1 - e^{-\left(KL/_{\lambda^{\alpha}}\right)} \qquad (3\text{-}7)$$

K and L are the absorption coefficient (proportional to the number density of soot particles) and the geometric thickness of the flame along the optical axis of the detection system, respectively. The product KL represents the dependence of emissivity with the amount of soot and includes the total contribution of the soot along the optical path, regardless of its distribution or geometrical size [10]. Zhao [11] concluded that for the visible wavelength range, the parameter α, which depends on the soot properties, can be used as a constant value of 1.39 for most fuels.

Combining equations (3-6) and (3-7), an expression for the KL parameter is obtained *(3-8)*

$$KL = -\lambda^{\alpha} ln\left[1 - \left(\frac{e^{\left(\frac{C_2}{\lambda T}\right)} - 1}{e^{\left(\frac{C_2}{\lambda T_a}\right)} - 1}\right)\right] \qquad (3\text{-}8)$$

The unknown product KL can be eliminated by rewriting the above equation for two specific wavelengths, λ_1 and λ_2.

$$\left[1-\left(\frac{e^{\left(\frac{C_2}{\lambda_1 T}\right)}-1}{e^{\left(\frac{C_2}{\lambda_1 T_{a1}}\right)}-1}\right)\right]^{\lambda_1^{\alpha_1}}=\left[1-\left(\frac{e^{\left(\frac{C_2}{\lambda_2 T}\right)}-1}{e^{\left(\frac{C_2}{\lambda_2 T_{a2}}\right)}-1}\right)\right]^{\lambda_2^{\alpha_2}} \tag{3-9}$$

As the 2C system will initially generate a specific digital level for each camera of the system (camera λ_1 and camera λ_2) which corresponds to the radiation from the flame at the two wavelengths, the system can be calibrated by getting the apparent temperatures T_{a1} and T_{a2} correspondent to the digital level from the camera λ_1 and camera λ_2, respectively. A calibration curve representing the digital level against blackbody temperature can be obtained for each wavelength. When the calibration is generated, the instantaneous digital levels can be converted to the apparent temperatures. In the case of this current thesis, a tungsten-ribbon calibration lamp (Osram Wi17G) is used as a blackbody source. The procedure followed was already applied in other studies [10,12]. The lamp is powered by an electrical assembly consisting of a voltage source and a variable resistor. The latter allows controlling the electrical power supply with a precision of 0.1 A, strictly covering the operating range of the lamp. Three different electric currents, 9.1 A, 11.7 A, and 13.0 A, were applied to the tungsten lamp to get its spectral calibration. The radiance levels of these three different lamp intensities are expected in a Diesel flame. This calibration allowed to know the radiance emitted by the lamp through a specific area of 25 mm in diameter located at the lamp center.

For the correct calibration, the radiance for the three currents must be the same as the two lambdas used in the experimental campaign, 560 and 660 nm. The curves of radiance vs. wavelength of the Osram Wi17G are reported in Figure 3-3.

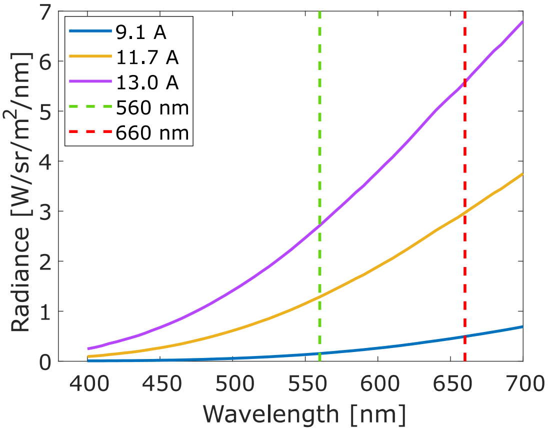

Figure 3-3 Curves of the calibration lamp. The vertical lines mark the wavelengths used to apply the 2C method.

The calibration process is performed exactly in the same optical system used to obtain the images in the optical engine, keeping the same distance from the lamp to the optical system and the flame to the optical system. Twenty images of the lamp filament were taken for each calibrated point (9.1 A, 11.7 A, and 13.0 A). An example of the filament image captured by the camera for the three currents is shown in Figure 3-4. The digital level of the pixels inside the area of 25 mm in diameter is averaged and compared with the calibration values of the lamp. From this procedure, the calibration curve for each wavelength can be obtained. It is important to consider that camera parameters, such as shutter speed, aperture, etc., affect the pixels digital level, so each configuration has its respective calibration curve.

Figure 3-4 Lamp filament images for different electrical currents.

In order to obtain KL evolution, a perfect matching (pixel by pixel) overlap between two images recorded by both cameras is needed. To achieve this, different spatial correction tools are applied using MATLAB software. These tools take both images, one is spatially fixed, and translation, rotation, and scaling matrices are applied to obtain a spatial transformation matrix to use in the other image. The left image in Figure 3-5 shows the two raw images from both cameras (red and green colors) before applying the spatial transform matrix. In contrast, the right image shows the overlap after using the spatial transformation matrix, where the perfect pixel matching is represented in yellow. It is important to remark that the spatial matrix transformation is calculated for each repetition.

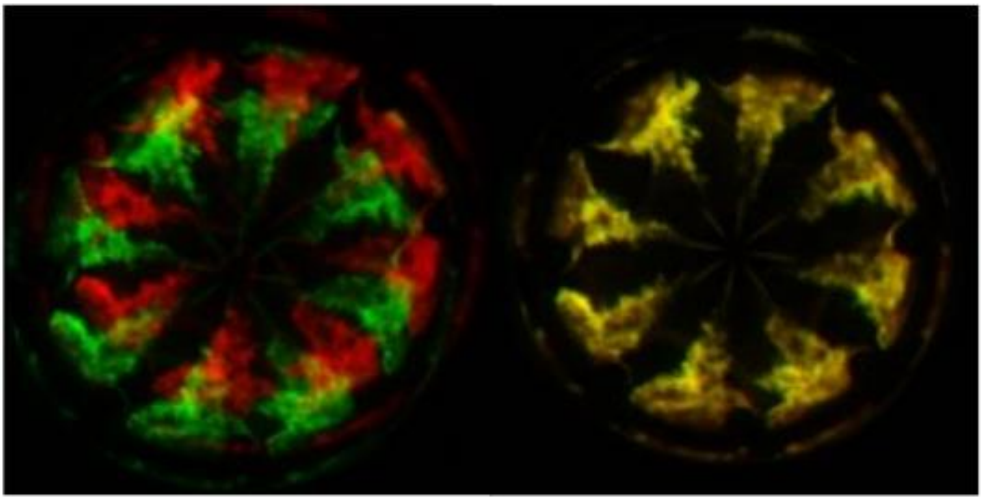

Figure 3-5 2-Color pyrometry algorithm to obtain KL values. The left image corresponds to the image from both cameras (red and green colors). In addition, the overlap image after applying the spatial transform matrix is shown in the right image. The color yellow highlights the perfect pixel matching.

Furthermore, the code could not find a good spatial match in some image regions. In this way, these regions could induce errors in the KL calculation attributed to different sources of uncertainties [13]. When some of these regions lead to a radiation intensity out of a physical solution, the code assigns a value of 3, which is the maximum value, for the KL analysis.

3.2.3 OH^* Chemiluminescence

The process of chemiluminescence is the spontaneous emission of light due to a previous excitation of chemical reactions, as its name suggests. This chemical reaction is capable of exciting the molecule to an excited state of energy, which after a certain characteristic time (of the molecule), releases the excess energy returning to its initial electronic state in the form of light (photon). Therefore, chemiluminescence production involves two primary stages: formation (R 1) and radiative transitions (R 2) of excited-state radicals. It is worth noting that not all excited-state radicals participate in the chemiluminescence generation process. For instance, as depicted in reaction (R 3), certain radicals may interact with other species, leading to nonradiative transitions [14].

$$A + B \rightarrow R^* + others \qquad \text{(R 1)}$$

$$R^* \rightarrow R + hv \qquad \text{(R 2)}$$

$$R^* + M \rightarrow R + M \qquad \text{(R 3)}$$

Where A, B, and R are different ground-state radicals; R^* is an excited-state radical, and M is a third body species.

In combustion environments, the emission of ultraviolet radiation at approximately 308 nm is attributed to the transitions of OH ($A^2\Sigma^+ - X^2\Pi$) from its electronically excited state (known as OH^*) to its ground state. The species involved in reactions (R 1), (R 2), and (R 3) are denoted by the letters A, B, and R, respectively, and correspond to H, O, and OH. The chemiluminescence of OH^* has been the subject of extensive research. Studies have revealed that OH^* is primarily formed through reaction (R 1) at temperatures below 2800 K, while at temperatures above 2800 K, the production of OH^* is mainly via the reverse reaction in (R 3). Combustion-generated OH^* chemiluminescent emissions are frequently utilized to locate high-temperature reaction zones and serve as a tracer of the RoHR. The OH^* band between 280 and 350 nm, with its emission peak at 308 nm, has the highest intensity in the UV region and is practically isolated from all other emission bands generated during the combustion process [15].

3.3 Experimental Facilities

As mentioned in Chapter 1, this thesis was carried out through three experimental campaigns. The first one is based on the analysis of the combustion process and flame structure of OME_X and OME_1. For this purpose, the detection of OH^* was carried out through its chemiluminescence as a tracer of high-temperature reactions, along with the detection of two chemical species considered as tracers of low- and high-temperature of the flame, CH_2O and OH, respectively, through the implementation of the PLIF technique. This study was conducted under ECN conditions for two different nozzle geometries. To avoid disturbances in the flame and combustion process, this study was conducted in a high-pressure and high-temperature (HPHT) vessel, along with the use of single-hole nozzles that allow for free jet conditions, meaning that the jet is not disturbed by jet-jet or jet-wall interactions.

On the other hand, this thesis other two experimental campaigns were carried out in a single-cylinder optical compression ignition engine. This setup evaluated the combustion process and soot formation/oxidation under more realistic conditions than the previous setup (jet-wall interaction, multi-hole injector, and engine dynamics) using different piston geometries and OME_X/Diesel fuel blends. For this purpose, two high-speed imaging techniques were implemented simultaneously: OH^* chemiluminescence for the analysis of the high-temperature zones of the flame inside the combustion chamber, indicating the soot oxidation zones, and two-color pyrometry for the registration of soot concentration.

Therefore, this section will describe the experimental facilities used in this thesis: the high-pressure and high-temperature (HPHT) vessel and the single-cylinder optical compression ignition engine.

3.3.1 High-Pressure High-Temperature Vessel

The High Pressure and High Temperature (HPHT) facility simulates the thermodynamic conditions similar to that of a diesel engine during injection. It is classified as a constant-pressure flow (CPF) facility. The chamber of the vessel features three windows: two opposite each other and measuring 128 mm in diameter, and the last one perpendicular to the other two, measuring 181 mm in diameter. Independent control of ambient gas temperature, gas composition, oxygen concentration, and pressure can be achieved to obtain desired parameter values. Figure 3-6 presents a schematic diagram of the vessel control system. The test chamber can work as an open circuit with air or a closed loop circuit with a mixture of air and nitrogen to reduce oxygen concentration. In the open circuit, the valves are set to filter, compress, and store air in high-pressure reservoirs. To reduce air humidity in the test chamber, a high-pressure industrial dryer is used, followed by the introduction of dry air through a 30 kW electric heating system. The hot gases exit the vessel and are cooled before being released into the atmosphere. Gas flow is controlled by a manually operated valve downstream of the chamber, which, when combined with circuit valves, enables the closed loop mode for simulating exhaust gas recirculation (EGR) by adding nitrogen and continuously monitoring oxygen concentration. The test rig control system measures and regulates chamber temperature and pressure, with heaters controlled by a Proportional-Integral-Derivative (PID) controller that maintains a fixed temperature set point. A PID system regulates chamber pressure through a flow control valve that increases air pressure. At the same time, heaters are protected by ensuring a minimum gas flow value, maximum output temperature, and minimum coolant flow. The combustion chamber, o-ring seals, and thermos regulator unit are cooled by a separate cooling unit that drives ethylene glycol coolant from the reservoir to the HPHT vessel via a pump, sending it to a chiller before returning it to the reservoir at a temperature of around 17ºC. During experimentation, a second circuit is employed to regulate and maintain a constant temperature for the injector. The injection frequency is low (0.25 Hz), so the fuel temperature is equivalent to that of the nozzle tip. To regulate the temperature of the injector, an aluminum cap is installed to act as a conductor between the coolant chamber surrounding the injector and the nozzle tip, thereby ensuring that both the fuel and nozzle tip temperature are under control [16].

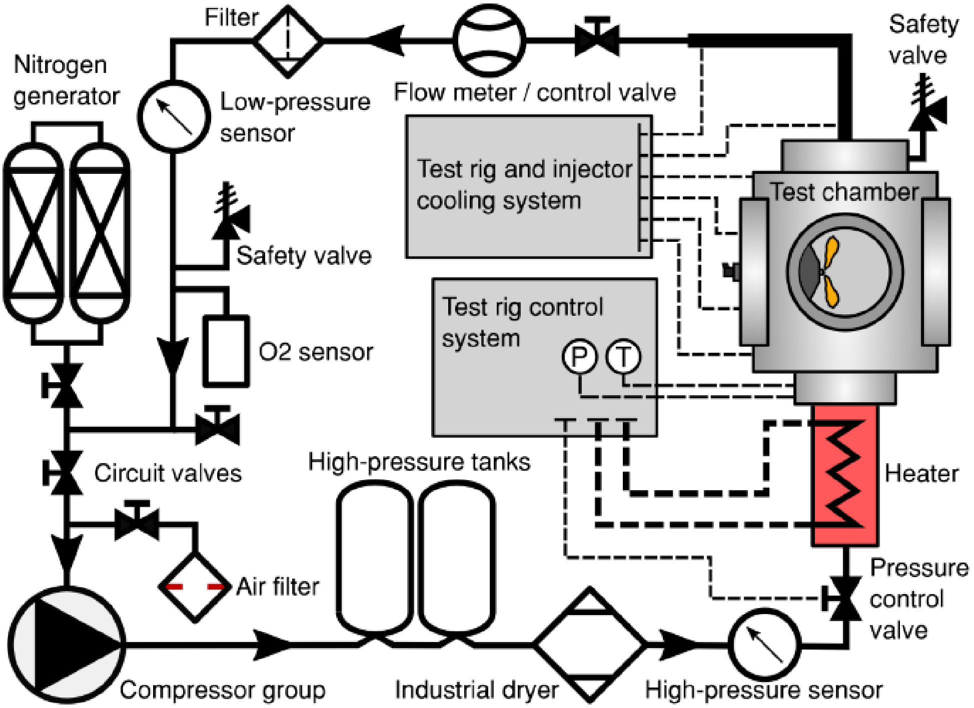

Figure 3-6. Schematic diagram of High Pressure and High Temperature (HPHT) installation. Source: [17].

The HPHT facility can reach temperatures of up to 1100 K and 15 MPa pressure, and its test section has a volume of approximately 15 liters. A thick insulation layer minimizes heat transfer between the inner and outer walls. The inner wall controls the temperature inside the chamber, while the outer wall helps withstand structural loads. To improve the temperature distribution, the heated gas exits through four steel tubes and enters the combustion chamber through a swirl diffuser. Table 3-1 summarizes the key characteristics of the HPHT facility, while a detailed description and characterization of the vessel can be found in [17,18].

Table 3-1 Main characteristics of the High Pressure and High Temperature facility.

Facility type	CPF
Chamber diameter	200 mm
Chamber height	250 mm
Maximum pressure	15 MPa
Maximum temperature	1100 K
Main heater power	30 kW
Gas velocity	<0.3 m/s

A conventional common-rail system equipped with a pressure sensor and a solenoid-activated injector was used. Additionally, a diaphragm pump was used to supply the fuel due to its polymerized tetrafluoroethylene construction, which is better suited for low-lubricity hydrocarbons than more conventional fuel pumps. The system could reach pressures of up to 230 MPa, with an injection frequency of 0.25 Hz.

This thesis used two single-hole nozzles from the ECN [19] associated to Spray A and Spray D reference conditions. These injectors are denoted as SA (Spray A-orifice) and SD (Spray D-orifice) in this thesis. It is important to highlight that SA is considered as a light-duty engine reference, while SD is considered for medium and heavy-duty engines.

Table 3-2 summarizes their key characteristics, including the K-factor, which is a standard characteristic parameter that represents the conicity of the nozzle based on the difference between its inlet and outlet diameters.

Table 3-2 SA and SD characteristics [19].

	SA	**SD**
Number of holes	1	1
Nozzle Diameter	89.4	190.3
Nozzle k-factor (-)	1.5	1.5
Discharge coefficient	0.86	0.86
Hole angular orientation	axial	axial

3.3.2 Optical Engine

The tests were conducted on a Bowditch optical engine model based on a DURAMAX 3.3 L medium-duty CI General Motors (GM) platform, as shown in Figure 3-7. This engine uses the conventional overhead valve design with push rods for valve operation. In this facility, a specific box was installed just on the cylinder side to allocate the camshaft, as the distance between the head and block is increased due to the optical access design. As a result, there are no lateral optical accesses to the combustion chamber, and combustion can be imaged only through the optical piston. However, this adaptation allows for a higher compression ratio than in typical optical engines. Moreover, the optical engine utilizes the same cylinder head as the conventional engine, featuring four valves and a centered solenoid injector per cylinder. Table 3-3 summarizes the optical engine main geometric parameters.

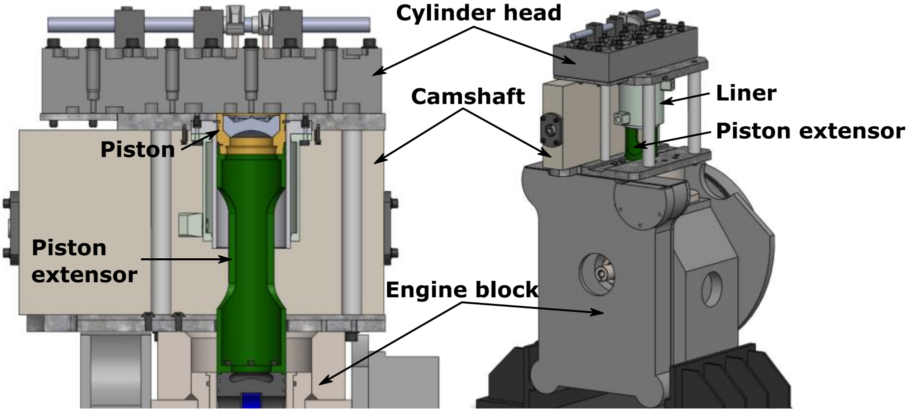

Figure 3-7 Optical engine.

To reduce air leakages (also known as blow-by), specialized piston rings made of a synthetic material called Rulon® J are utilized, which expands as the temperature increases.

Table 3-3 Optical engine characteristics.

Parameter	Value
Engine characteristics	4 stroke, direct injection
Number of cylinders [-]	1
Number of valves [-]	4
Stroke [mm]	99
Bore [mm]	103
Displacement [L]	~ 0.8
Effective compression ratio	13.3

The DRIVVEN Engine Control System (ECS) manages the injection system. This research engine controller is based on the PXI platform from National Instruments and features an open-source LabVIEW software project. It functions as a steady-state engine control application and also serves as a template for advanced control applications. With this device, it is possible to control both piezoelectric or solenoid direct injectors and port fuel injectors, including the ability to set parameters such as injection duration, injection timing, and the number of injections per cycle. Additionally, the number of cycles at firing conditions, working in skip fire mode, can be defined, which is crucial for preserving optical parts in optical engines. The injection system employs a conventional high-pressure fuel pump with a common rail and a pressure control valve mounted in the pressure rail, combined with a PID control, maintaining constant pressure as desired. The system is capable of achieving injection pressures up to 2000 bar.

The studies carried out in this facility utilized two different nozzles: a standard 8-hole conical nozzle (STD); and a Controlled Diffusive Spray (CDS) 8-hole nozzle, named also Counterbore. An example of both designs can be observed in Figure 3-8. The concept of the CDS nozzle aims to enhance the flexibility of distributing the spray in the combustion chamber. A shorter spray penetration and wider spray cone angle are achieved, resulting in a combustion reaction closer to the center of the piston bowl rather than at the bowl's walls, as it would be with a more conventional nozzle (STD) [20]. The CDS effect is achieved by counterboring the holes of the nozzle. Numerical [21] and experimental [22,23] studies comparing STD and counterbore nozzles, among others, can be found in the literature. For example, Payri et al. [22] reported an appreciable decrease in pollutant emissions, especially in particulate matter and hydrocarbon emissions, due to the improvement of fuel-air mixing promoted by the counterbore nozzle geometry.

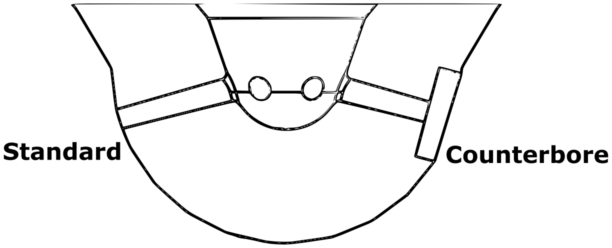

Figure 3-8 Comparison of standard (left) and counterbore (right) nozzle orifices. Reprinted with permission [22].

When operating under skip fire conditions, a single cylinder in an optical engine generates very little heat, making it challenging to warm up the coolant and lubricant fluids to the required working temperature. To address this issue, the optical engine features an independent cooling system designed to maintain low liner temperatures and preserve the piston rings. The system consists of a spiral pipe between the inner liner (in contact with the piston rings) and the outer liner. The coolant, ethylene glycol, enters one side of the spiral pipe, circulates around the liner, and exits the other side. The refrigeration machine, controlled by a PID regulator, ensures the coolant remains between 15°C and 25°C. This approach ensures consistent temperature conditions for the cylinder walls across all operating points.

The lubrication system comprises two circuits, both of which ensure the adequate lubrication of the engine metallic parts, including the crankshaft and valve train. In the first circuit, an external pump delivers oil to the engine, serving as a coolant fluid. With the aim to decrease the oil temperature, oil flows to a second circuit with a heat exchanger. Throughout all tests conducted in this thesis, the oil temperature (60°C) and pressure (3 bar) remain constant.

It is crucial to emphasize that the intake and exhaust system described below is exclusive to single-cylinder engine test cells, where the intake and exhaust system are external, enabling efficient and highly flexible acquisition of desired intake air conditions.

Figure 3-9 illustrates the air supply system, which includes a screw compressor capable of supplying intake air at up to 30 bar pressures and a maximum flow rate of 400 kg/h for each test condition. The intake air is first directed to a filter to remove particles that may cause damage to the engine components during combustion. A dryer and heat exchanger are used to prepare the intake air, followed by entry into a 500-liter settling chamber to equalize the flow and reduce pressure waves. An air heater, regulated by a PID control, is positioned just before the intake port to achieve the required air temperature for various engine conditions.

Similar to the intake system, the exhaust system is also external and removes the exhaust gases produced during the combustion process. A settling chamber is present in the exhaust system to prevent pressure pulses. Additionally, an exhaust backpressure valve regulates the exhaust pressure and simulates conditions comparable to the turbine backpressure of a conventional turbocharged compression ignition engine. The exhaust pressure is consistently maintained at 0.2 bar above the intake pressure.

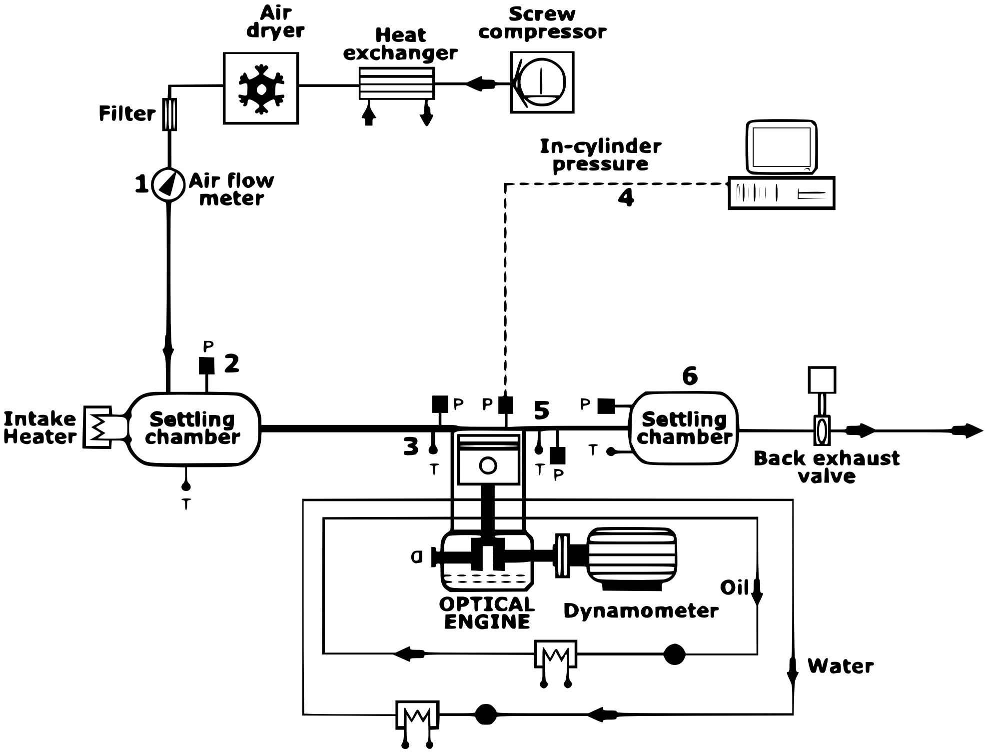

Figure 3-9 Single-cylinder test cell schematic diagram.

The following describes the sensors and equipment used to conduct the experimental campaigns presented in this thesis. The principles and uncertainties of these devices are discussed to provide information about the reliability of the measurements.

Although the optical engine is motored by the dynamometer and operates at skip-fire conditions, the torque and speed measurements are critical to operating the engine safely. The dynamometer actuates as a motor when it drives the engine (no combustion operation) or as a generator when it is driven by the engine (during combustion operation). The torque measurement is performed by torque flanges as well as load cells which are coupled to the dynamometer. It provides the highest sensibility to load variations employing a strain gauge inside a specific metal shape. A calibration curve has to be provided to the acquisition system, where the output voltage from the load cell is related to a calibrated weight. The current thesis uses a Schenck dynamometer equipped with a load cell to perform the tests. The main characteristics of the dynamometer can be visualized in Table 3-4.

Table 3-4 Dynamometer characteristics.

Type	dynamometer
Manufacturer	Schenk
Nominal Power [kW]	2200
Nominal Torque [Nm]	562
Max. Speed [rpm]	9000
Min. Speed [rpm]	250

For the engine speed measurements, different sensors can be employed. Hall and inductive effect sensors placed near a gearwheel generally provide engine speed measurements. However, for the heat release analysis, the toothed wheel has limitations due to the low number of pulse per stroke (60-2). In this way, an additional optical encoder AVL 364, with a resolution of 0.5 CAD, was installed on the crankshaft of the optical engine. The presence of three output signals (A, B, and C) are typical in this kind of encoder. The signal A is related to the pulses generated per stroke. B is a phased A, which allows to determine the direction of rotation. Finally, signal C is the trigger used to reference the piston position concerning the start of acquisition.

The average pressure and temperature measurements are used to monitor and control different systems and subsystems of the optical engines and get quantitative information on essential engine parameters where the signal dynamics are low. In the test cell, the average pressure was measured using a PMA P40 model piezoresistive pressure transducer.

The measurement range is from 0 to 10 bar with 25 mbar accuracy. The average pressure sensor is installed in different parts of the optical engine, such as intake and exhaust systems, cooling circuits, and lubricant circuits. Regarding temperature measurements, they are performed by using K-type thermocouples and thermo-resistive sensors. The thermocouples have a measurement range from 0 to 1400°C and an accuracy of 2.5°C. The water and oil temperatures were measured with the thermo resistive sensors, where temperatures from -200 to +850°C and an accuracy of 0.3°C can be registered.

Most combustion analyses in ICE can be performed thanks to instantaneous pressure measurements. These kinds of measurements are highly complex and require special instrumentations, where the signal from the transducer must be with low thermal shock and support high-pressure values. A Kistler 6124A glow-plug piezoelectric transducer [3] was mounted in the cylinder head for the in-cylinder pressure measurements, where the pressure and temperature conditions are severe. Piezoelectric sensors measure relative pressure and are appropriate for both high temperatures and high pressure. The transducer allows measurement range from 0 to 300 bar, with an operating temperature range from -40 to 400°C. The accuracy is 1.25 bar. In addition, no additional cooling system is required by this sensor, simplifying installation on the cylinder head. A Kistler 5015 charge amplifier conditioned the signal from the sensor before being acquired by the acquisition system. Besides the average pressure values, the instantaneous one was also registered for the intake and exhaust pressure measurements. For this purpose, a Kistler 4045A10 piezoresistive sensor [4] was mounted in both intake and exhaust manifolds just before the ports. This sensor provides a measurement range from 0 to 10 bar, allowing a maximum temperature of 120°C. Piezoresistive sensors measure absolute pressure and can be used when the temperature and pressure conditions are not excessively high.

The measurement of air mass flow is crucial for ICE studies since, from this parameter is possible to calculate derived parameters such as equivalence ratio or volumetric efficiency. In addition, for the thermodynamic characterization of optical engines, the correct mass flow measurement is mandatory for this thesis. For the air mass flow rate measurement, a Sensyflow from Sensycom company is employed. This device uses a hot wire anemometer to perform the measurements, where the measuring range is from 0 to 400 Kg/h and the accuracy of 1% over the measured value [5].

In order to obtain information about heat release in CI engines, it is necessary to utilize thermodynamic diagnostics. To accomplish this, the Dewesoft X software [24] was employed, offering a variety of data acquisition and analysis tools for various industries, including the automotive sector. Among its many features, the software combustion analysis module enables users to diagnose and optimize engine performance by analyzing pressure and temperature measurements during combustion.

During an engine combustion cycle, Dewesoft X software collects and analyzes real-time data from pressure and temperature sensors. The software provides various analysis tools to diagnose engine problems, such as incomplete combustion or skip fires. For instance, it can calculate peak pressure, maximum temperature, and the rate of heat release (RoHR) during each combustion cycle. These metrics help identify weak or delayed combustion, leading to reduced engine performance or increased emissions.

As mentioned previously, different piston geometries will be used due to their importance in the air/fuel mixing process and their involvement in the flame dynamics within the combustion chamber, which is key to reducing soot formation within the cylinder.

Several studies mentioned in Chapter 2 have shown that the geometry of radial lips on the edge of the bowl has benefits in reducing soot formation inside the cylinder, mainly by avoiding direct flame-to-flame interaction once they hit the bowl wall while also guiding the flame towards the center of the bowl where there is fresh oxygen available to oxidize the soot present in the flame. This has been observed mainly in light-duty engines, such as in the study by Lewiski [25], so more studies are needed in larger engines where the swirl effect is less pronounced. Due to the great potential observed for radial lips, the analysis of the impact of modifying the geometry of these protrusions is of great interest to continue characterizing and improving the design of this geometry.

In this way, this thesis has considered four piston geometries: two conventional geometries and two non-conventional, including protrusions on the bowl wall. These geometries have been evaluated in optical engine studies, so these pistons are made of quartz to allow visual access to the combustion chamber from the bottom of the bowl. These geometries are distributed among three different pistons whose geometries can be seen in Figure 3-10. Throughout the thesis, each piston will be called Combustion System N (CSN), where N is the piston number (N = 1, 2, 3). The first piston (CS1) combines open bowl and radial lips, which are protrusions on the edge of the bowl. The second piston (CS2) combines two different geometries: one part of the bowl has a open bowl geometry (representing the typical geometry used under real conditions), and the other part of the bowl is a combination of open bowl and radial lips, which are somewhat more abrupt than those of the first piston (CS1). In this piston, each part will be referred to as CS2-

NoLips and CS2-Lips, respectively. This hybrid piston has the advantage of being able to analyze the same combustion event with two different geometries. However, the effect of one geometry can interfere with the other. For this reason, the effective area used for the analysis of each geometry has a gap between them, highlighted in Figure 3-10 as red for CS2-Lips and blue for CS2-NoLips. Finally, the third piston (CS3) has a reentrant geometry, a replica of the actual piston used in the engine metal version. It is commonly used in light and medium-duty engines. Thus, this geometry is a reference for comparison with non-conventional geometries.

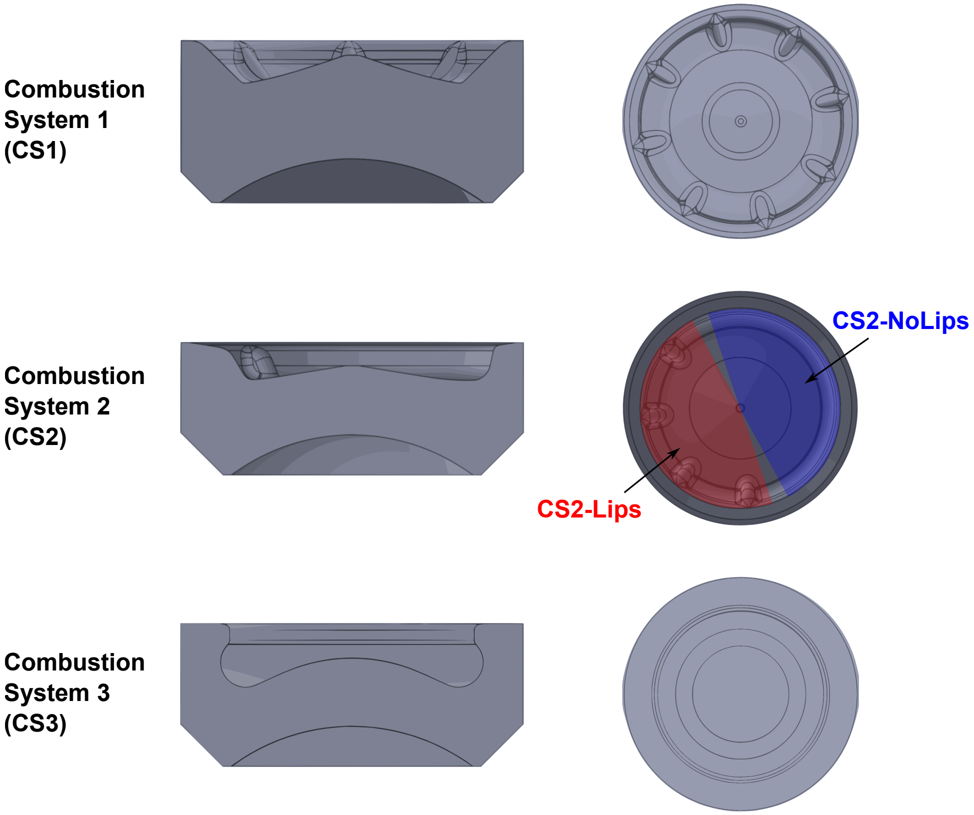

Figure 3-10 Piston sketches. CS1 has a geometry with symmetric protrusions on the edge of the bowl. CS2 contains two geometries: one part with only reentrant geometry (CS2-NoLips) marked in blue and a geometry that combines both reentrant and protrusion geometries (CS2-Lips) marked in red. CS3 has a purely reentrant geometry.

Regarding CS3, the quartz piston mimics the metal version used in the actual engine. CS1 and CS2 were built from the geometry in the metal version provided by PUNCH Torino company (as a partner of a part of this study). Furthermore, the manufacture of the CS2, including two different geometries in the same bowl, was proposed by our institute group. The company carried out a series of simulations to optimize the protrusion geometry on the bowl edge. Furthermore, this company provides measurements in the metal version of the engine to adjust the engine operating conditions in the optical version.

CS1 was a previous version of CS2, in which the modification of the geometry of the protrusion enhanced the reduction of soot. Each bowl is inserted into a metal holder to fix it to the engine structure and protect the quartz bowl from possible impacts that lead to damage (see Figure 3-11). Once the transparent bowl is inserted, the holders of CS1 and CS2 protrude above the top surface of the bowl. This gap acts as stepped lip geometry. However, this geometry is not present in CS3. In this case, the holder and transparent bowl are at the same height.

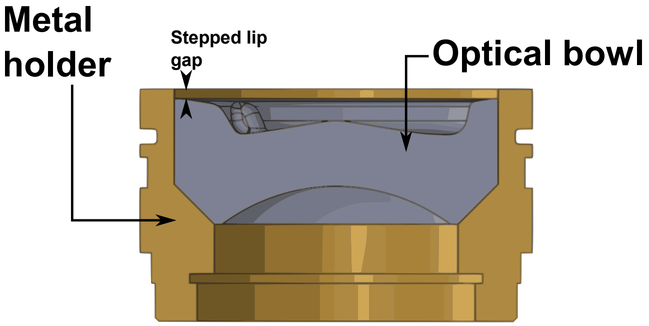

Figure 3-11 Quartz bowl (gray) and metal holder (gold).

3.4 Fuels

This research work utilized four different fuels: two fossil fuels, Dodecane and Diesel, and two synthetic fuels belonging to the OME_n family, OME_1, and a mixture of various OME_n (referred to as OME_X in this thesis). The study in HPHT vessel was conducted under ECN conditions, so Dodecane was used as a standard surrogate for diesel fuel. This is mainly due to their similar physicochemical properties and easy implementation of Dodecane in CFD models due to its well-defined chemical structure ($C_{12}H_{26}$).

For these reasons, Dodecane is often used as a model compound to represent Diesel fuel. In the same setup, both OME_1 and OME_X were also used. These fuels belong to the oxymethylene ether family, whose general molecular structure is CH_3-O-$(CH_2$-$O)_n$-CH_3. The first is a single-component fuel corresponding to the family shortest carbon chain ($n = 1$). However, the latter is a multi-component fuel, which is a mixture of single components with different chain lengths.

Finally, diesel was used as a reference fuel for the studies conducted in the optical engine to compare and analyze the effect of piston geometry and the impact of using OME_X as a blend. The diesel used is a low-sulfur and biodiesel-free diesel. The composition of the OME_X used in this thesis and the properties of all the fuels mentioned above are reflected in Table 3-5 and Table 3-6, respectively.

Table 3-5 Composition of OME_X fuel used in this thesis.

Molecule	**Content (wt%)**
OME_1	0.01
OME_2	<0.01
OME_3	57.9
OME_4	28.87
OME_5	10.08
OME_6	1.91

Table 3-6 Fuel properties

Characteristics	**Diesel**	**Dodecane**	**OME_1**	**OME_X**
Density $[kg/m^3]$ $(T = 15°C)$	842.0	751.2	866.7	1057.1
Viscosity $[mm^2/s]$ $(T = 40°C)$	2.93	1.44	0.36	1.08
Cetane number [-]	55.7	74.0	28.0	68.6
Lubricity [µm]	386	563	747	320
Flash point [°C]	-	83	<40	65
Lower heating value $[MJ/kg]$	42.44	44.20	19.25	19.21
Initial boiling point [°C]	155.1	214.0	37.4	144.9
Final boiling point [°C]	363.1	218.0	38.0	242.4
Total contamination $[mg/kg]$	<24	-	<1	<1
Carbon content [% m/m]	86.2	84.0	48.4	44.2
Hydrogen content [% m/m]	13.8	16.0	10.4	8.8
Oxygen content [% m/m]	0	0	42.1	45.0
$(A/F)_{st}$ at 21% of O_2	14.39	14.92	7.22	5.89
$(A/F)_{st}$ at 15% of O_2	19.98	20.72	10.03	8.18

3.5 Summary and Conclusions

In this chapter of the thesis, the tools and facilities used for the different studies that will be presented in the following chapters have been highlighted.

The various optical techniques used as analysis tools have been explained, describing their principles and their application to the study. Then, the experimental facilities used in this thesis are detailed: high-pressure and high-temperature (HPHT) installation and optical engine.

The former has provided a more controlled study, thanks to the ability to control the thermodynamic parameters within it with great precision while having free jet conditions, no engine dynamics, or wall collision. The study carried out in this facility comprises the Spray A and Spray D conditions of the ECN. In this way, the main characteristics of the facility and these conditions have been discussed.

The second installation has provided a study closer to engine-like conditions. In this case, the engine dynamics affect the combustion process and the flame-wall interaction due to the presence of the piston. The optical engine main characteristics, along with the injection, lubrication, cooling systems, and piston geometries used in this facility, have been mentioned. Regarding the pistons used, the geometry of each of them has been explained. In total, four different geometries have been used in three pistons.

Subsequently, we moved on to the key elements of this thesis: the study of OME_n fuels. Conventional fuels used as reference (Dodecane and diesel) and e-fuels, also called oxygenated fuels (OME_X and OME_1), have been used. Their most relevant physicochemical properties have been mentioned.

Bibliography

[1] Zhao H. Laser Diagnostics and Optical Measurement Techniques in Internal Combustion Engines. Warrendale, PA: SAE International; 2012. https://doi.org/10.4271/R-406.

[2] Eckbreth AC. Laser diagnostics for combustion temperature and species. vol. 3. Second. Great Britain: Taylor & Francis Books; 1996.

[3] Donkerbroek AJ, Van Vliet AP, Somers LMT, Frijters PJM, Klein-Douwel RJH, Dam NJ, et al. Time-and space-resolved quantitative LIF measurements of formaldehyde in a heavy-duty diesel engine. Combust Flame 2010;157:155–66.

[4] Escofet Martin D. Laser diagnostics for high pressure combustion. University of California, 2017.

[5] Luque J, Crosley DR. LIFBASE: Database and Spectral Simulation Program 1999.

[6] Donkerbroek AJ, van Vliet AP, Somers LMT, Dam NJ, ter Meulen JJ. Relation between hydroxyl and formaldehyde in a direct-injection heavy-duty diesel engine. Combust Flame 2011;158:564–72. https://doi.org/https://doi.org/10.1016/j.combustflame.2010.09.024.

[7] Maes N. The life of a spray. Technische Universiteit Eindhoven, 2019.

[8] García Oliver JM. Aportaciones al estudio del proceso de combustión turbulenta de chorros en motores diesel de inyección directa. Universitat Politècnica de València, 2004. https://doi.org/10.4995/Thesis/10251/55164.

[9] Hottel HC, Broughton FP. Determination of True Temperature and Total Radiation from Luminous Gas Flames. Industrial & Engineering Chemistry Analytical Edition 1932;4:166–75. https://doi.org/10.1021/ac50078a004.

[10] Pastor J V., García-Oliver JM, García A, Micó C, Möller S. Application of optical diagnostics to the quantification of soot in n-alkane flames under diesel conditions. Combust Flame 2016;164:212–23. https://doi.org/10.1016/j.combustflame.2015.11.018.

[11] Zhao H, Ladommatos N. Optical diagnostics for soot and temperature measurement in diesel engines. Prog Energy Combust Sci 1998;24:221–55. https://doi.org/10.1016/S0360-1285(97)00033-6.

[12] Xuan T, Pastor J V., García-Oliver JM, García A, He Z, Wang Q, et al. In-flame soot quantification of diesel sprays under sooting/non-sooting critical conditions in an optical engine. Appl Therm Eng 2019;149:1–10. https://doi.org/10.1016/j.applthermaleng.2018.11.112.

[13] Musculus MPB, Singh S, Reitz RD. Gradient effects on two-color soot optical pyrometry in a heavy-duty DI diesel engine. Combust Flame 2008;153:216–27. https://doi.org/10.1016/j.combustflame.2007.10.023.

[14] Liu Y, Tan J, Wan M, Zhang L, Yao X. Quantitative Measurement of OH* and CH* Chemiluminescence in Jet Diffusion Flames. ACS Omega 2020. https://doi.org/10.1021/acsomega.0c01093.

[15] Zhang T, Yu G, Guo Q, Wang F. Experimental Study on the Characteristics of Impinging Reaction Region with OH* Chemiluminescence in Opposed Impinging Diffusion Flames. Energy & Fuels 2013. https://doi.org/10.1021/ef401204g.

[16] Payri R, García-Oliver JM, Bardi M, Manin J. Fuel temperature influence on diesel sprays in inert and reacting conditions. Appl Therm Eng 2012;35:185–95. https://doi.org/10.1016/j.applthermaleng.2011.10.027.

[17] Viera Sotillo AA. Effect of multiple injection strategies on the Diesel spray formation and combustion using optical diagnostics. Universitat Politècnica de València, 2019. https://doi.org/10.4995/Thesis/10251/123954.

[18] Payri R, Gimeno J, Cardona S, Ayyapureddi S. Experimental study of the influence of the fuel and boundary conditions over the soot formation in multi-hole diesel injectors using high-speed color diffused back-illumination technique. Appl Therm Eng 2019;158:113746. https://doi.org/10.1016/j.applthermaleng.2019.113746.

[19] Engine Combustion Network n.d. https://ecn.sandia.gov/ (accessed February 22, 2023).

[20] Serizawa K, Ueda D, Mikami N, Tomida Y, Weber J. Realizing Robust Combustion with High Response Diesel Injector with Controlled Diffusive Spray Nozzle and Closed Loop Injection Control. SAE Technical Papers 2017;2017-March. https://doi.org/10.4271/2017-01-0845.

[21] Tu PW, Xu H, Srivastava DK, Dean K, Jing D, Cao L, et al. Numerical Investigation of GDI Injector Nozzle Geometry on Spray Characteristics. SAE Technical Papers 2015;2015-Septe. https://doi.org/10.4271/2015-01-1906.

[22] Payri R, De La Morena J, Monsalve-Serrano J, Pesce FC, Vassallo A. Impact of counter-bore nozzle on the combustion process and exhaust emissions for light-duty diesel engine application. International Journal of Engine Research 2018;20:46–57. https://doi.org/10.1177/1468087418819250.

[23] Payri R, Hardy G, Gimeno J, Bautista A. Analysis of counterbore effect in five diesel common rail injectors. Exp Therm Fluid Sci 2019;107:69–78. https://doi.org/10.1016/J.EXPTHERMFLUSCI.2019.05.008.

[24] DewesoftX 2020.

[25] Lewiski F. Analysis of the combustion process and soot formation in a single cylinder optical engine fueled with e-fuels and using different piston geometries. Universitat Politècnica de València, 2021. https://doi.org/10.4995/Thesis/10251/180351.

Chapter 4

Flame Structure Characterization for OME_X and OME_1

Content

4.1 Introduction

The primary objective of this thesis first results chapter is to analyze the combustion process and flame structure of OME_1 and OME_X fuels. These e-fuels have gained significant scientific interest due to their excellent properties in terms of reducing soot formation in internal combustion engines (ICE), as discussed in previous chapters.

Similar to diesel, understanding the physicochemical characterization and combustion process of OME_n fuels is crucial for comprehending the associated emissions. Before this thesis, García-Carrero [1] developed a database for OME_1 and OME_X, including fundamental combustion process parameters such as lift of length (LOL), flame penetration (FL), ignition delay (ID), and liquid penetration (LL), among others under Spray A and Spray D reference ECN conditions. All this information was shared and can be consulted in [2]. However, the flame structure, characterized by the low and high-temperature zones, had not been previously analyzed. Therefore, this chapter examines both zones using CH_2O PLIF and OH PLIF as tracers of low- and high-temperature zones, respectively, using the same ECN conditions. Additionally, measurements of OH^* are included, which serve as a tracer of high-temperature reactions and as a reference in previous studies.

In this way, this chapter starts comparing the flame structure of the Spray A reference case with the other results contributed by other authors. This provides a strong basis for continuing to use the same methodology for the e-fuels that are intended to be studied in this chapter of the thesis. Then, the flame structure of OME_1 and OME_X is discussed through the analysis of OH, CH_2O, and OH^* under Spray A and Spray D conditions. This Chapter of the thesis is a combination of two scientific publications resulting from the results acquired during the course of this doctoral thesis [3,4].

4.2 Operating Conditions

The study was conducted in a high-pressure and high-temperature (HPHT) facility under Spray A and Spray D conditions. The description of the facility as well as Spray A-orifice and Spray D-orifice, named as SA and SD, respectively in this thesis, has been described in Chapter 3.

Four operating conditions were used in this study, highlighted in Table 4-1. The Spray A conditions is used as a reference case (dodecane and SA). Then, the fuel is modified using the same ambient conditions of Spray A and Spray D.

Table 4-1 Summary of operating conditions.

Test name	Spray A	OME_1-Spray A	OME_1-Spray D	OME_X-Spray A	OME_X-Spray D
Fuel	Dodecane	OME_1	OME_1	OME_X	OME_X
Nozzle orifice	SA	SA	SD	SA	SD
Gas temperature [K]	900	900	900	900	900
Gas density $[kg/m^3]$	22.8	22.8	22.8	22.8	22.8
Oxygen (%vol)	15	15	15	15	15
Injection pressure [MPa]	150	150	150	150	150

To establish a reference point for the start of injection, the time after the start of injection (aSOI) has been taken into account. This time considers the delay between the injection trigger pulse and the actual start of injection, influenced by both fuel properties and injector characteristics. García-Carrero [1] characterized this delay for these fuels and conditions. The values are presented in Table 4-2. This thesis does not evaluate the case of Dodecane under Spray D condition.

Table 4-2. Injection delay for each fuel and nozzle.

	Dodecane	**OME_X**	**OME_1**
Spray A	265 µs	265 µs	265 µs
Spray D	-	384 µs	530 µs

4.3 Optical Arrangement

In this study, various optical techniques were used to conduct experiments. The techniques included hydroxyl radical (OH) planar laser-induced fluorescence (PLIF) and excited state hydroxyl (OH^*) chemiluminescence imaging. OH is an ideal tracer for high-temperature oxidation reactions under near stoichiometric conditions [5], while formaldehyde (CH_2O) PLIF was used to trace low-temperature reactions under lean-mixture conditions, which are typical of the early stages of diffusive combustion [6]. The optical setup used in the experiments is shown in Figure 4-1 and described in detail in the following paragraphs.

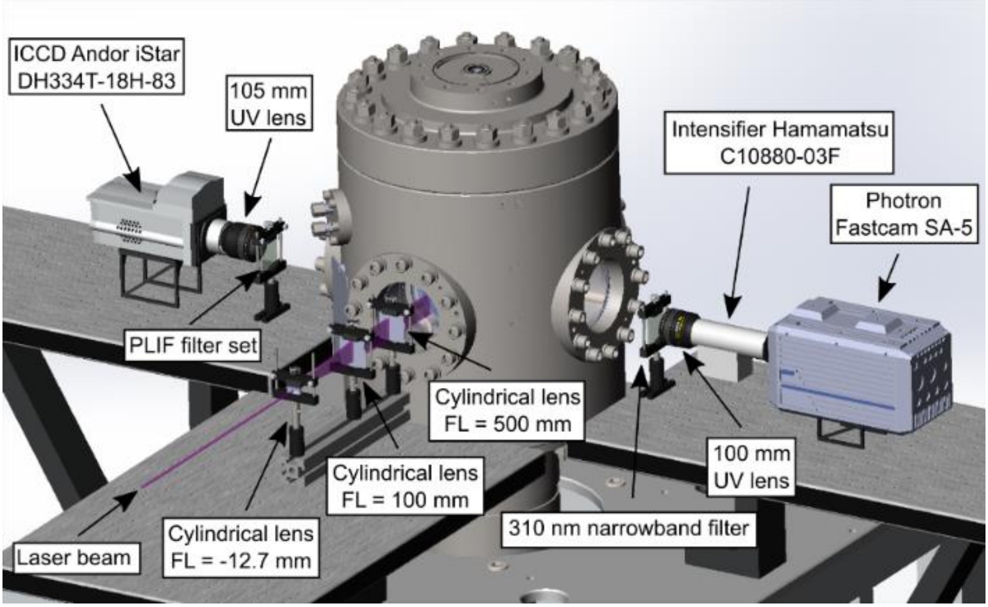

Figure 4-1. Optical setup.

4.3.1 OH* Chemiluminescence

The OH* chemiluminescence images were recorded using a high-speed CMOS camera (Photron Fastcam SA-5) coupled to a high-speed intensifier (Hamamatsu C10880-03F) with a 1:1 relay optic and a multialkali (S-20) intensifier, sensitive from 185 to 900 nm. The intensifier is equipped with a 100 mm focal length, f/2, ultraviolet (UV) lens (Bernhard Halle Nachfl OC 2.5), and a narrowband (10 nm FWHM) filter centered at 310 nm (characteristic OH* emission peak). The set was configured to register chemiluminescence at 25 kHz and 39.75 µs exposure time. The resolution achieved was 6.4 pixels per mm. The gain of the intensifier was set to 75% for Dodecane and 80% for OME_1 and OME_X. The gating mode was set to continuous to avoid the influence of transients on the intensifier response.

During each test, OH* chemiluminescence was recorded for 21 consecutive combustion events when any of the lasers were fired. To prevent potential damage to the intensifier caused by the high intensity of the PLIF signal in comparison with the OH* signal and to avoid crosstalk between the measurements, it was determined that both measurements should not be performed simultaneously.

The OH^* chemiluminescence signal recorded results from integrating radiation emitted by the entire flame volume in the line of sight. On the other hand, PLIF relies on radiation originating from a specific excitation plane, which is the symmetry plane of the flame. To ensure that the two techniques can be compared, the OH^* signal has been deconvoluted to derive the signal corresponding to the flame's symmetry plane, as described in reference [7]. This involved applying the inverse Abel transformation to the line of sight integrated signal (I_{OH^*}) while assuming axisymmetry of the OH^* chemiluminescence about the spray axis. By doing so, the signal at the flame's symmetry plane (I_{Sy}) can be obtained as follows:

$$I_{Sy} = -\frac{1}{\pi} \cdot \int_{r}^{\infty} \frac{dI_{OH^*}}{dy} \cdot \frac{dy}{\sqrt{y^2 - r^2}} \tag{4-1}$$

where r represents the radial distance to the spray axis while y represents the projection of r over the symmetry plane of the flame. The inversion is performed separately for the flame upper and lower parts. Figure 4-2 compares the line of sight integrated OH^* signal and the corresponding Abel-inverted one. In this figure, it is possible to see that the second one shows a distribution of intensity accumulated on the sides of the flame. At the same time, the signal is weak at the center, which is coherent with what could be expected at the symmetry plane of a diffusion flame.

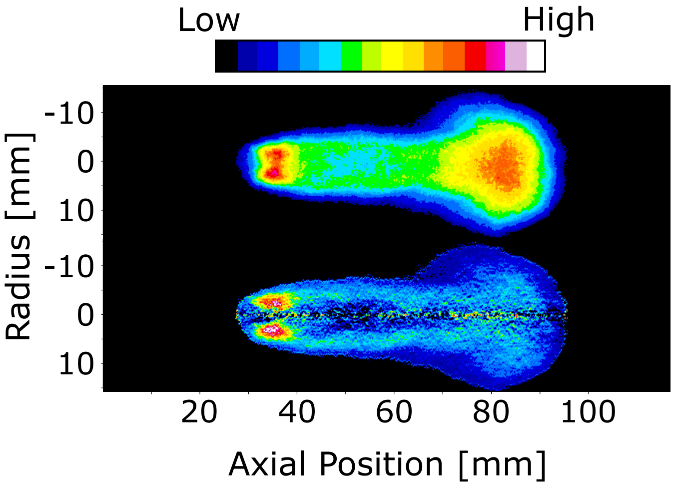

Figure 4-2 The line of sight integrated (top) and deconvoluted (bottom) OH chemiluminescence signal comparison. Data corresponds to OME$_X$-Spray D, at 1536 µs aSOI.*

OH* chemiluminescence signal was also used to describe the evolution of macroscopic flame structure. For this purpose, each image was processed to obtain the flame lift-off length (LOL) and penetration (FL). On the one hand, the LOL was defined as the distance between the nozzle tip and the first point at the flame axis where the intensity of OH* radiation reaches a fixed threshold value of 200 over the background noise level, which was found to be 500 in this work. On the other hand, FL was calculated as the distance between the nozzle tip and the furthest point of the flame located at its axis with an intensity higher than that of the LOL threshold.

4.3.2 Planar Laser Induced Fluorescence (PLIF)

In this work, PLIF was applied to CH_2O molecules in the $\tilde{A}^1A_2 - \tilde{X}^1A_1$ system [8]. For this purpose, the third harmonic (355 nm) of a Nd:YAG laser (Laser Continuum Surelite II) was used. The laser was fired at 10 Hz, obtaining 45 mJ/pulse at this wavelength. This work performed tests with and without laser excitation to account for other radiation sources that could interfere with the measurement, like chemiluminescence or thermal radiation. The optical system was aligned so that the laser sheet excited the vertical symmetry plane of the flame (see more information about the lens system in Chapter 3). An intensified CCD camera (Andor iStar DH334T-18H-83) with a S-20 photocathode (sensitive between 180 and 850 nm) to capture the fluorescence signal was used. It was equipped with a 105 mm, f/4.5 UV lens (Nikon Rayfact), providing a resolution of 9.6 pixels per mm. Besides, a long-pass filter (400 nm cut-off wavelength) combined with a band-pass filter centered at 390 nm (125 nm FWHM) was used to isolate CH_2O fluorescence from other signals.

A similar optical setup was used to perform PLIF on OH radicals in the $A^2\Sigma - X^2\Pi$. In this case, the second harmonic (532 nm) of a Nd:YAG Laser (Powerlite DLS Laser System 8010) was used to pump a Dye Laser (Vista Dye Laser) feed with Rhodamine 590. The system was optimized to emit at around 562 nm, which was later doubled (Vista FX Frequency) to obtain the desired excitation wavelength. On-resonant and off-resonant OH PLIF measurements were performed [6,9] with the laser system tuned at 283.46 nm and 283.38 nm, respectively, as mentioned in Chapter 3. The laser was fired at 10 Hz, and the energy obtained in this case was 28 mJ per pulse for both wavelengths. The same acquisition hardware as for CH_2O fluorescence was used in this case. However, the previous filter set was replaced by a narrowband filter centered at 310 nm (10 nm FWHM) to isolate the fluorescence signal.

OH and CH_2O PLIF were not measured simultaneously. A set of UV laser-line mirrors were placed on a remotely controlled motorized table, allowing to swap between the two different laser sources when desired while keeping the alignment with the lens system previously described. Besides, another motorized table was also used to switch between the corresponding filters set for each species investigated here.

The acquisition frequency of the intensified CCD camera and the lasing frequency of both lasers allowed the recording of only one image per combustion event. Thus, to have time-resolved data, PLIF acquisition was performed at different instants of time after the start of energizing (aSOE) electric pulse of the injectors. Due to the inherent cycle-to-cycle variability of the combustion process, 50 images were acquired per test. The maximum intensifier gain was used for all the tests with a gating duration of 200 ns. This was long enough to register most of the fluorescence radiation while reducing the influence of other radiation events, such as OH^* chemiluminescence or thermal radiation from soot.

When processing the OH fluorescence signal, the ensemble average of the 50 images corresponding to the on-resonant and off-resonant configurations is calculated. Then, the second is subtracted from the first to keep only the fluorescence signal emitted by this radical. Figure 4-3 shows a comparison between on-resonant and off-resonant measured signals for single combustion events and the corresponding ensemble average of the whole set of 50 images. A similar procedure was followed for CH_2O. However, signals with and without laser excitation were subtracted in this case. A comparison of these images is shown in Figure 4-4. In this case, no large differences are observed between them. However, when subtracting both the fluorescence signal remains as it will be shown in the following sections.

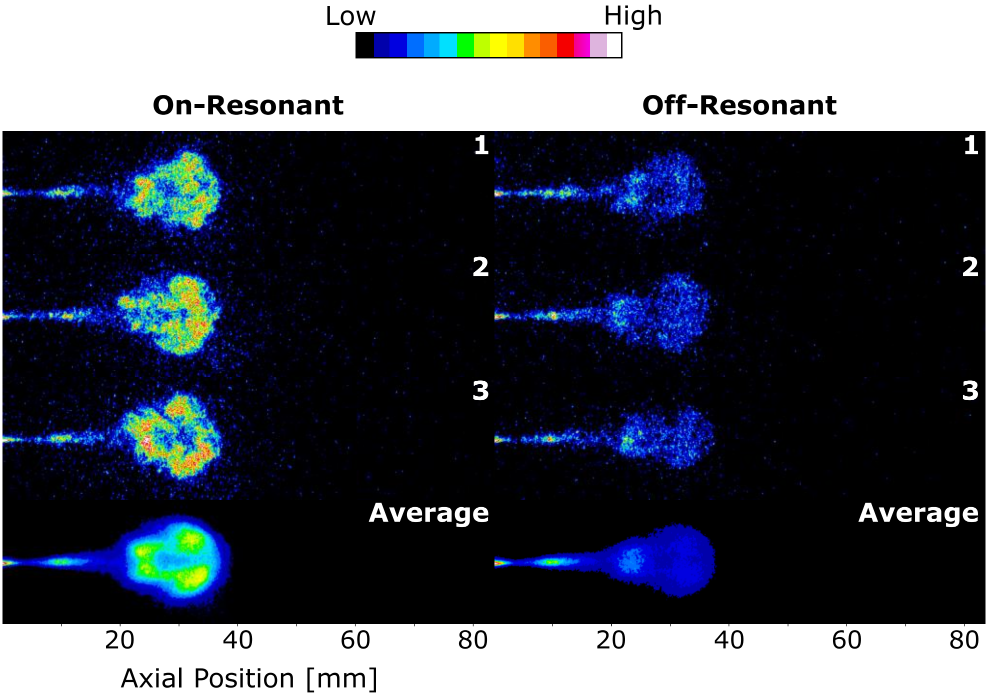

Figure 4-3 Images registered with the on-resonant (left) and off-resonant (right) excitation wavelengths for OH radical detection. The first three rows represent single combustion events, while the last row represents the ensemble average of 50 repetitions. Data correspond to OME_X-Spray A at 735 µs aSOI.

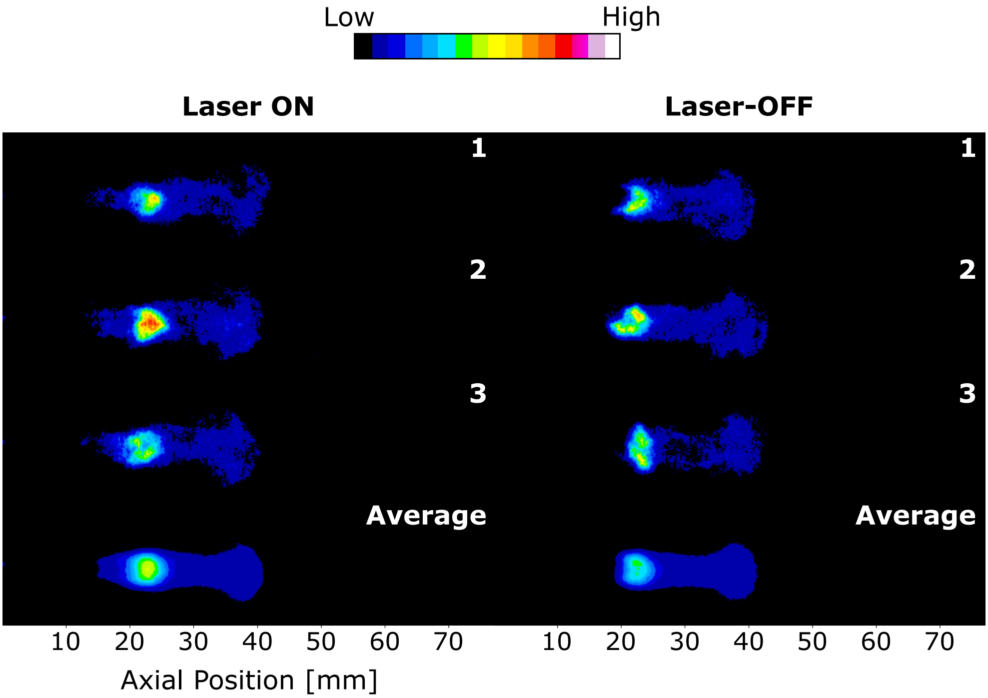

Figure 4-4 Images registered with the laser on (left) and laser off (right) for CH_2O *detection. The first three rows represent single combustion events, while the last row represents the ensemble average of 50 repetitions. Data correspond to* OME_X*-Spray A at 735 µs aSOI.*

4.3.3 Synchronization System

The synchronization between the combustion event and the cameras is crucial. Normally, suppose the optical setup is only based on the detection of flame radiation, as for OH^* radiation used in this study. In that case, synchronizing the electric pulse of the injection system with the cameras is sufficient. However, the case of PLIF is more delicate due to the use of the laser, which is the source that forces the fluorescence of the species to fluoresce between 100 and 200 ns.

In this way, the laser used has two different electrical signals: the flashlamp (Flash) and the Q-Switch. The first one generates the photons inside the laser cavity and, in this case, has to work at 10Hz (laser specifications). The second one is in charge of opening the laser emissions.

The time between both signals (t_1) is critical for the output power of the laser. In this case, the optimum delay is *280 µs 198 µs* for Powerlite DLS Laser System 8010 and Laser Continuum Surelite II, respectively. The camera is synchronized with the Q-Switch signal to register the fluorescence event thanks to the shutter time used, as mentioned previously.

A scheme of these different signals is described in Figure 4-5. The time to observe the event after the start of injection (t) takes into account three temporal events: the specific time that controls the output power of the laser (t_1), the time between the Q-Switch signal and the real output of the laser (t_2) and the parameter τ (time between the Trigger and Flash) allowing to modify the time t aSOI to observe the event. The parameter t_2 can be neglected because it is very small (order of ns) compared with the shutter time used in the camera to record the event (order of hundreds of µs).

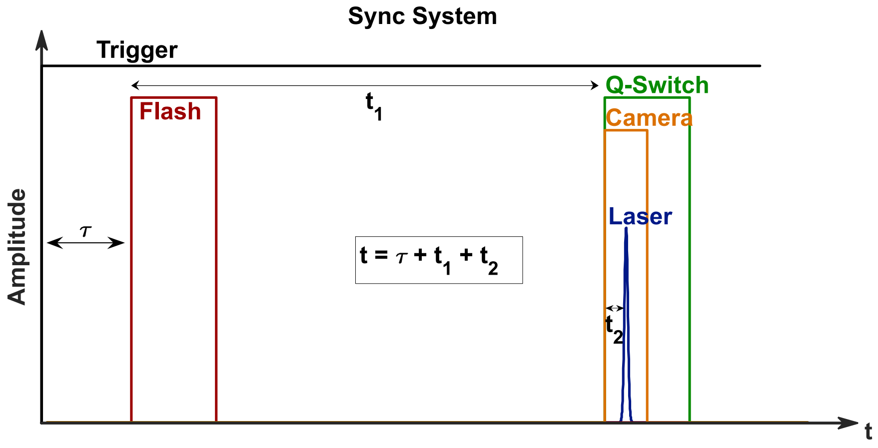

Figure 4-5 Synchronization diagram using the PLIF technique.

4.4 Dodecane Flame Structure

As seen in Chapter 2, the reference condition of the ECN (the framework on which this study is based) is the Spray A condition. Therefore, a first analysis of these conditions was carried out as a reference point for the study, which was later compared with the study proposed in this chapter. As seen previously, OH^* is a good tracer of high-temperature reactions and a good indicator of the locations of the lift-off length position and flame penetration. Given that the chemiluminescence of OH^* is captured using band-pass filters with limited transmission outside their designated spectral range, it becomes crucial to account for the extensive black body radiation emitted by soot particles across the entire spectrum. Despite the diminished efficiency of the intensifier photocathode at longer wavelengths and the low transmission of the filters, the incandescence of soot can be significantly more intense than the emission of OH^* by several magnitudes. Additionally, it may also contribute to emissions near the desired 310 nm collection wavelength [10,11].

The evolution of OH^* under Spray A condition can be observed in Figure 4-6. The left side shows the structure of OH^* at different aSOI instants. In contrast, the right side shows the evolution of the LOL and FL parameters obtained from the images on the left (following the previously explained methodology) and the respective standard deviation as color-shadow. It is expected that the OH^* signal appears at the periphery of the spray, where the high-temperature regions of the flame are located, which is not observed in the OH^* images in Figure 4-6 (left) downstream of 35 mm.

This is consistent with works such as those of Skeen et al. [12] and Cenker et al. [13], conducted under the same ECN conditions. This is because the thermal radiation from soot strongly interferes with the OH* signal, resulting in high intensity in the central zone of the flame. In this case, it has been detected that the LOL stabilizes around $18.7 \pm 0.9\, mm$ and the FL at $88.3 \pm 0.6\, mm$. Several studies conducted under the same ECN conditions reported LOL locations similar to those obtained in this study [14].

Figure 4-7 displays the PLIF images depicting CH_2O and OH. Regarding CH_2O, the images reveal that its signal is strongest during the initial stages of combustion (335 µs), indicating its role as an indicator of low-temperature reactions. As mentioned before, the presence of CH_2O diminishes during high-temperature reactions, evident by the comparatively lower signal at 485 µs compared to the preceding image. This decrease is particularly noticeable at the spray tip, confirming the transition into the high-temperature phase as indicated by the OH^* images in Figure 4-6. Prior research has noted that PLIF images of formaldehyde at 355 nm often include a significant contribution from elastic scattering (primarily originating from the liquid region), soot LII, and PAH fluorescence.

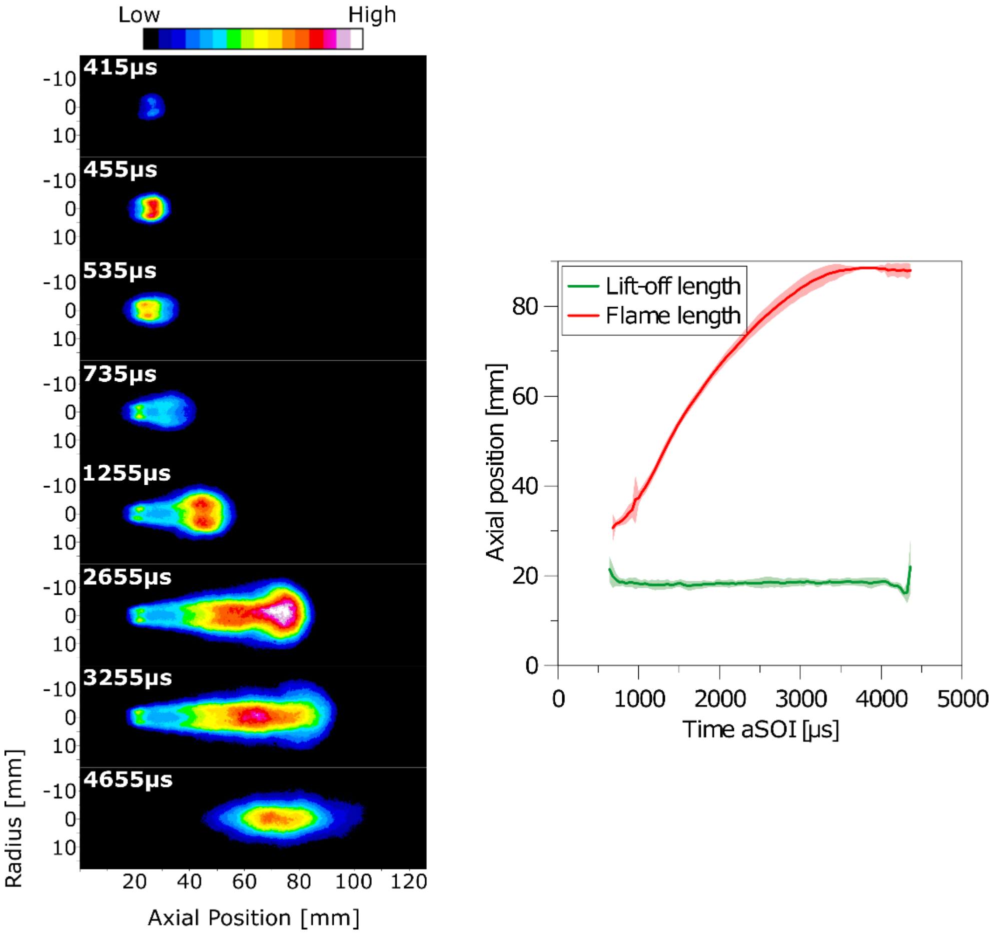

Figure 4-6.OH chemiluminescence evolution images (left), and lift-off length and flame front parameters evolution (right) under Spray A condition.*

The white brackets added in the figure serve to identify the largest axial region displaying fluorescence associated with CH_2O. Upstream of this region, the light observed results from elastic scattering from the liquid fuel, which was not filtered out by the optical filters. This finding aligns with previous studies conducted under similar conditions, which reported an LL of around 10 mm downstream from the tip injector. At the specific moment of 635 µs after the start of injection (aSOI), a high intensity is detected downstream of the CH_2O region, bounded by the white bracket. Notably, this intense region coincides with the occurrence of high-temperature reactions (as seen in Figure 4-6). Therefore, it is clear that this heightened intensity cannot be attributed to CH_2O fluorescence.

Previous research has consistently observed a distinct spatial separation between PAHs and CH_2O in diffusion flames [7,15], reporting that the lower fluorescence intensity region is associated with CH_2O while the higher intensity is mainly due to PAH.

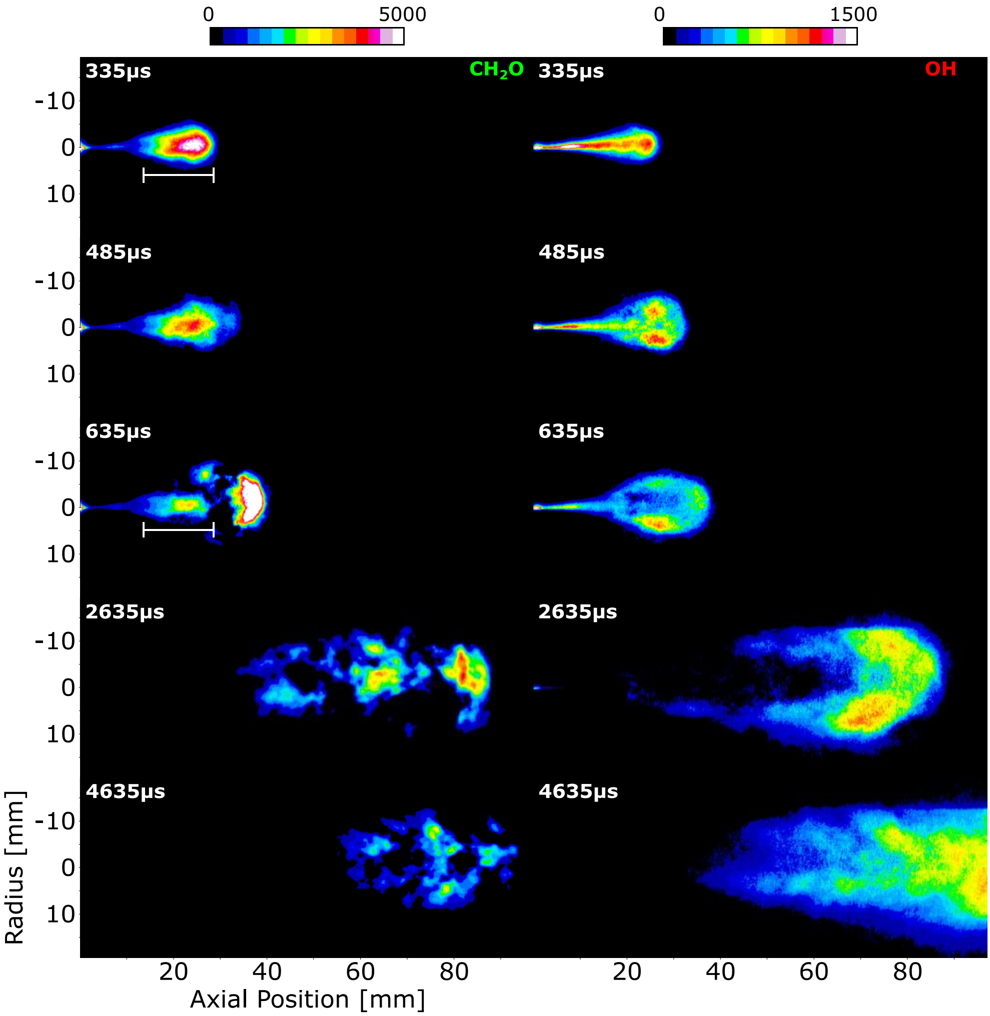

Figure 4-7. Formaldehyde (left) and OH (right) fluorescence evolution under Spray A condition.

Furthermore, this observation aligns entirely with the findings of this study, indicating that the two signals do not appear continuously. As time progresses, the light intensity is reported to be significantly downstream from the spatial location of CH_2O. This signal corresponds to the presence of soot. Furthermore, because the laser sheet illumination is directed through the flame head, it is unable to penetrate the region where CH_2O is located due to high soot absorption. Consequently, it becomes challenging to detect CH_2O species when the flame reaches a fully developed phase with the presence of soot. However, other studies conducted under similar conditions [16], where the laser sheet crosses the flame through its periphery, have shown that CH_2O remains near the lift-off length (LOL) position.

It is presumed that the first image associated with the OH signal (335 us) does not correspond to OH PLIF. The primary argument is that high-temperature reactions have not yet occurred, as evidenced by the OH* images in Figure 4-6. Furthermore, the spatial location of the signal overlaps with that of CH_2O, which is entirely inconsistent with the transition from low- to high-temperature ignition stages. From 485 µs onwards, high-temperature reactions begin to develop, and a broader area corresponding to OH PLIF is observed. As the flame progresses, the highest fluorescence intensity is detected as lateral lobes, corresponding to the flame structure stoichiometric zone [7,17]. In the last images (2635 µs and 4635 µs), the presence of soot in the flame head attenuates the laser sheet intensity, making it challenging to detect OH fluorescence near the LOL position.

Because the laser beam enters the jet head, the flame structure of highly sooty fuels makes it difficult to detect the flame structure at times when the flame is already in the quasi-stationary phase, as was described in Maes thesis [16] discussed in Chapter 2. However, at times earlier than soot formation, the flame structure detected is consistent with the existing literature, as discussed before. This fact serves as a strong basis to continue using the same methodology to analyze the flame structure of OME_1 and OME_X under ECN reference conditions in order to contribute to the further development of the database of these fuels.

4.5 OME_1 and OME_X Flame Structure

As in the case of dodecane, the analysis of the flame structure for the e-fuels studied in this chapter will be performed through the detection of the OH and CH_2O species, together with OH^* images. First, the subsection discusses the spatiotemporal distribution of both OH^* and OH, indicative of the transition to high-temperature reactions. Subsequently, the low-temperature reactions marked by the presence of CH_2O will be analyzed. Finally, the interaction of both CH_2O and OH species in the time instants in which both species coexist will be discussed.

4.5.1 OH^* and OH Distribution

Figure 4-8 presents maps of the OH^* signal along the spray axis to analyze the temporal and spatial evolution of the flame macroscopic structure. The maps for OME_X and OME_1 under Spray A and Spray D conditions are shown. The corresponding image was converted into a single-column array to create each map by summing the OH^* signal in the radial direction at each position along the spray axis. These arrays were then assembled to construct a map where the y-axis represents the distance to the nozzle, and the x-axis represents the time evolution aSOI. Non-dimensional spatial ($\tilde{X}$) and time ($\tilde{T}$) coordinates have been employed for scaling purposes. A scaling law based on momentum-controlled diffusion flames has been applied, utilizing the equivalent diameter (d_{eq}) [18] as a geometrical factor according to equation (4-2):

$$d_{eq} = d_0 \cdot \sqrt{\frac{\rho_f}{\rho_a}} \tag{4-2}$$

where d_0 is the orifice diameter, ρ_f is the fuel density and ρ_a the ambient density.

Additionally, the non-dimensional ensemble average of LOL ($\widetilde{LOL}$) and FL ($\widetilde{FL}$) have been represented. Based on this, the spatial and time coordinates are normalized as follows:

$$\tilde{X} = \frac{X \cdot Z_{st}}{d_{eq}} \tag{4-3}$$

$$\tilde{T} = \frac{T}{d_{eq}} \cdot U_f \tag{4-4}$$

where X represents the distance to the nozzle, Z_{st} is the stoichiometric mixture fraction, T represents the time aSOI and U_f represents the fuel velocity at the nozzle outlet orifice. This velocity can be estimated by applying the Bernoulli principle to the outlet orifice of the nozzle, according to the equation (4-5):

$$U_f = C_v \cdot \sqrt{\frac{\left(P_{inj} - P_{back}\right) \cdot 2}{\rho_f}} \tag{4-5}$$

Where C_v is the velocity coefficient (estimated as 0.9 in this work), P_{inj} is the injection pressure and P_{back} is the test chamber gas pressure.

The maps presented in Figure 4-8 provide information about the macroscopic evolution of flame from the point of view of the OH* radiation. For both fuels, it is possible to see that a highly intense chemiluminescence region appears at the base of the flame at the start of combustion. However, it evolves differently for each fuel. Focusing on the Spray D cases, with OME$_X$, the high-intensity region is located at the jet tip and progresses downstream as the flame develops. Besides, once the combustion event is stabilized ($\tilde{T} > 750$), the OH* radiation is more distributed along the flame axis. Compared with OME$_1$, it is possible to see that the signal at the tip of the developing jet is not so intense, with strong radiation mainly located at the lift-off region. This behavior is observed during the whole combustion process, which leads to large intensity differences along the flame axis even at the stabilized stage ($\tilde{T} > 1000$).

Under Spray A condition, several differences can be observed for both fuels compared to the other nozzle. On the one hand, OME$_X$-Spray A shows a structure more similar to that of OME$_1$-Spray D. The initial downstream propagation is not so intense, and radiation remains mainly at the base of the flame. On the other hand, OME$_1$-Spray A shows intensity within a quite short region. All radiation is located around the lift-off region, and almost no downstream progression is observed.

Using non-dimensional coordinates allows for highlighting several differences between fuels, isolating them from the effect of other boundary conditions, especially that of the nozzle diameter. Figure 4-8 shows that $\widetilde{FL}$ for SA is independent of the fuel, in both cases reaching a similar stabilized value. This behavior suggests that the stabilized flame penetration depends not on fuel reactivity but on mixing formation, which agrees with the results reported by Pastor et al. [19] with non-oxygenated fuels. Even though the same conclusions can be expected for the Spray D condition, the field-of-view limits prevent an experimental confirmation.

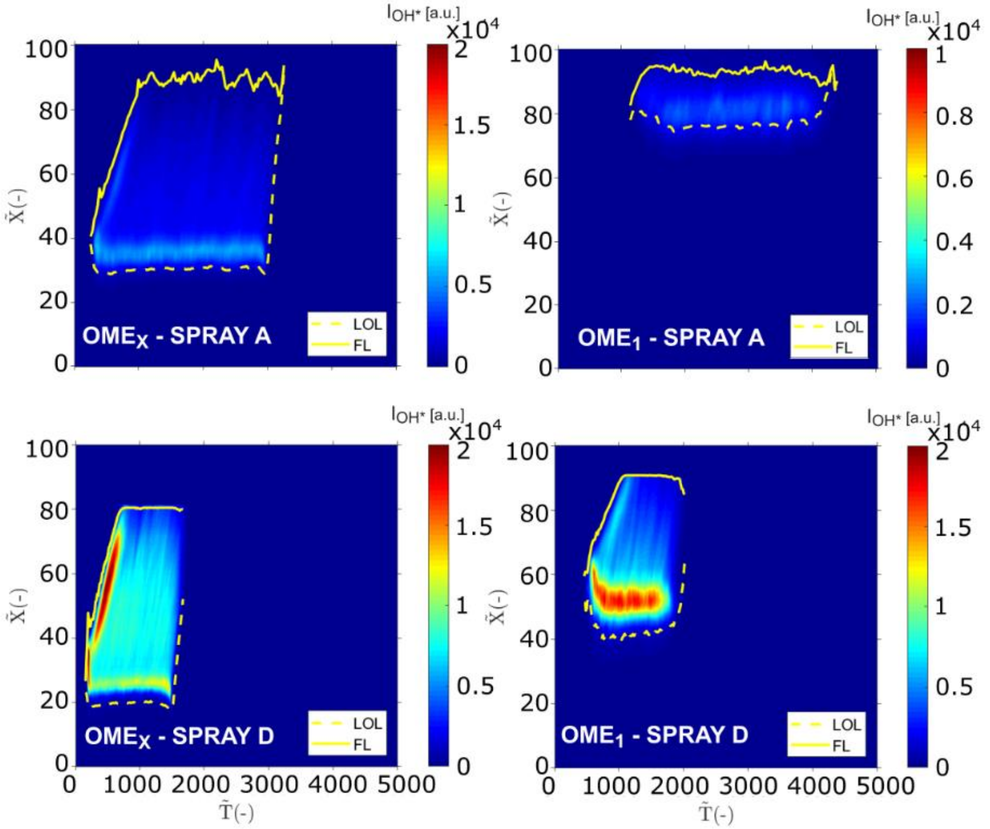

Figure 4-8 Evolution of OH^* chemiluminescence signal with respect to the normalized distance to the nozzle and time aSOI. The continuous and dashed lines represent FL, and LOL normalized according to equation (4-3).

When comparing $\widetilde{LOL}$, differences are visible among fuels and nozzles. The stabilized value for the four cases is sorted so that OME_X-Spray D < OME_X-Spray A < OME_1-Spray D < OME_1-Spray A. The reactivity of the fuels (not considered within the scaling factor) plays a major role, as OME_1, with a lower CN, provides longer LOL values than OME_X. The fact that $\widetilde{LOL}$ increases between the cases suggest that LOL stabilizes under different equivalence ratios (ϕ). Pastor et al. [20] estimated ϕ values at the lift-off region for the same fuels and operating conditions coinciding with those of the current work by the equation (4-6):

$$\phi_{cl,LOL} = \frac{f_{cl,LOL}}{1 - f_{cl,LOL}} \cdot (A/F)_{st} \tag{4-6}$$

where $(A/F)_{st}$ represent the stoichiometric air-fuel ratio of the fuel, and the term $f_{cl,LOL}$ refers to the fuel mixture fraction on the spray center line at the lift-off length location. That term is determined using equation (4-7):

$$f_{cl,LOL} = \frac{C \cdot D_O \cdot \sqrt{\frac{\rho_f}{\rho_a}}}{LOL} = \frac{C}{\widetilde{LOL}} \tag{4-7}$$

where LOL is the lift-off length, C is a constant with a value equal to 7, D_O is the nozzle diameter, and ρ_f and ρ_a represent the fuel and ambient density, respectively. The right-hand side of the equation shows that the equivalence ratio is inversely proportional to the normalized value of the lift-off length.

The equivalence ratio estimated at the lift-off region has been summarized in Table 4-3. The higher reactivity of OME_X under Spray D conditions provides the highest ϕ of all four cases, while OME_1 under Spray A condition provides the lowest.

Table 4-3 Equivalence ratio at lift-off region [21]

	OME_X	**OME_1**
Spray A	2.3	1
Spray D	4	2

Maes et al. [7] described the evolution of OH^* radiation based on a similar representation as the one used in Figure 4-8, corresponding to Spray A operating conditions (dodecane fuel). The authors report the appearance of a first intense region close to LOL that later progresses downstream while increasing its intensity. Besides, a uniform intensity distribution is observed if only the first 20 mm of the flame is considered for Dodecane (to avoid the part of signal contaminated by soot radiation). This behavior matches the one shown by OME_X under Spray D condition in this work, which suggests that conventional diffusion combustion is taking place in this case. This agrees with the high equivalence ratio reported.

When comparing the diffusion flame structure with the other cases, OME_X-Spray A and OME_1-Spray D (with a similar structure) show some differences. As described previously, in both cases, a high-intensity region appears at the LOL position while the radiation emitted from the rest of the flame is much weaker. These discrepancies could be related to the lower equivalence ratio achieved at lift-off length in both cases. This could allow oxidizing a higher percentage of the injected fuel at the base of the flame, reducing the amount of oxidation reactions downstream. For OME_1-Spray A, differences are even more noticeable. In this case, the mixture at LOL is close to stoichiometric, which could be causing the oxidation of most of the fuel when arriving in that region. This would explain the short length of the flame.

To deepen into the differences in flame structure between all cases considered in this work, sequences of deconvoluted OH^* chemiluminescence images are shown in Figure 4-9. The instants represented for each fuel and nozzle were the ones closest to the instants when PLIF was measured. The time indicated in each image corresponds to time aSOI, calculated with the delays from Table 4-2.

The first thing that can be observed for both fuels is that, when looking at the same instants, Spray D generates a larger flame length than Spray A. The bigger diameter of the nozzle allows more fuel to be injected, which takes more time to oxidize completely. However, the OH^* signal distribution for each fuel is different. As stated previously, OME_X-Spray D presents a high radiation intensity at the flame base, and the signal intensity decreases when moving downstream. The deconvoluted signal shows that OH^* radiation comes from the periphery of the flame, where the amount of oxygen is the right one to oxidize the remaining fuel and other partially oxidized species that reach those regions. This structure corresponds to a diffusion-type flame such as the one described by Dec et al. [5].

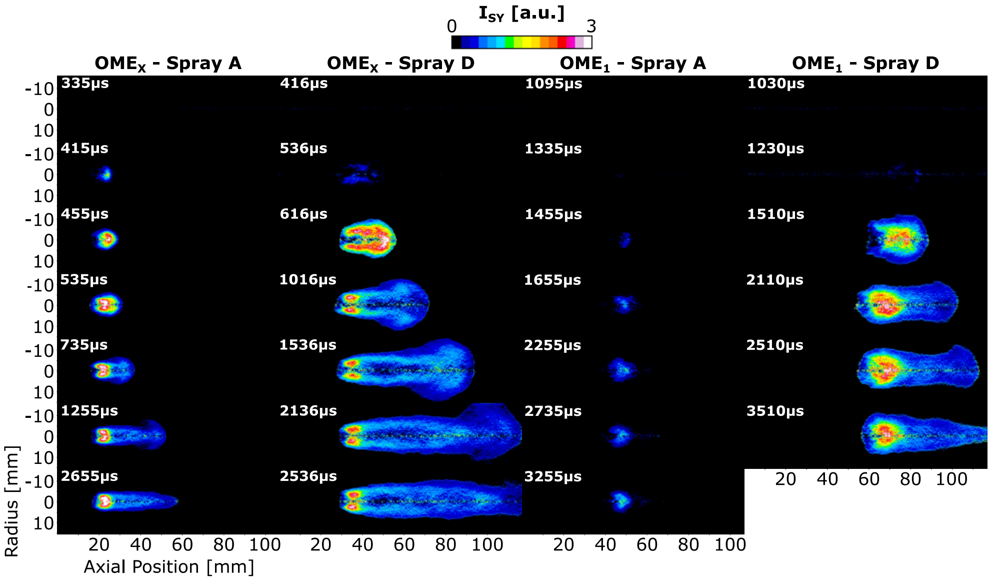

Figure 4-9 OH chemiluminescence deconvoluted signal at the symmetry plane of the flame for* OME_X *and* OME_1*, under Spray A and Spray D conditions.*

The flame obtained for OME_X-Spray A shows some differences. In this case, the signal downstream of the lift-off region seems uniformly distributed and not accumulated at the periphery. Besides, the contrast between the intensity registered at the lift-off region and downstream is higher in agreement with the information shown in Figure 4-8. The leaner air/fuel mixture achieved with this nozzle allows oxidizing of the remaining fuel and other species even at the center of the flame and not only at the periphery. It must be taken into account that the oxygen content of OME_X could play an important role in reaching this behavior with a diffusion flame, which is uncommon for more conventional fuels with the same nozzle and operating conditions [7,21].

The structure shown by OME_1 is more peculiar. A similar behavior to the one described for OME_X-Spray A can be observed in the Spray D case. In this case, OME_1 is less reactive and starts oxidizing further from the nozzle, reaching a similar ϕ value at the lift-off region than in the previous case. However, for OME_1-Spray A, no clear flame structure can be recognized. The OH^* radiation is much weaker, forming a cloud at the lift-off region, not showing any characteristic spatial distribution. At this stage, it is worth mentioning that one of the main assumptions of the deconvolution algorithm is that the flame is axisymmetric. This could be expected for the operating conditions considered in this work. Nevertheless, the information presented in the following paragraphs will allow evaluation of the deconvoluted signal accuracy.

The structure of the OH PLIF signal for the two fuels and the two nozzles is shown in Figure 4-10. Some differences and similarities can be observed when compared with the OH^* deconvoluted chemiluminescence (see Figure 4-9). In general, both experimental techniques reflect similar flame structures. However, the intensity distribution is different, obtaining a high intensity at the flame head for the PLIF technique, while for OH^*, this was obtained at the lift-off location. This difference could be due to an attenuation of the laser that enters the head of the flame, as discussed previously for the reference case. For the case of OME_X and both injectors, the OH PLIF signal indicates that these radicals are mainly located at the periphery of the flame. Even for Spray A condition, it is possible to see a decrease in the signal in its center which, as stated previously, is characteristic of diffusion flames. This is more noticeable for OME_1-Spray D, where the two-lobe structure is clearly identified. However, this was not observable with the OH^* chemiluminescence signal in any of these two cases. Finally, for OME_1-Spray A, the OH PLIF signal shows a shorter flame than the other cases, as observed with the OH^* chemiluminescence. However, the PLIF measurements show a wider OH intensity profile that expands downstream of the OH^* distribution zone. This is because the intensity of OH^* chemiluminescence decreases fast outside the high-temperature reaction zones due to the spontaneous emission of the radical or other phenomena like quenching. Thus, detecting radiation in regions where it is not formed is challenging. In contrast, the PLIF technique excites the ground state OH radicals, which can prevail outside the regions where they are formed (for example, downstream of the LOL region) [22].

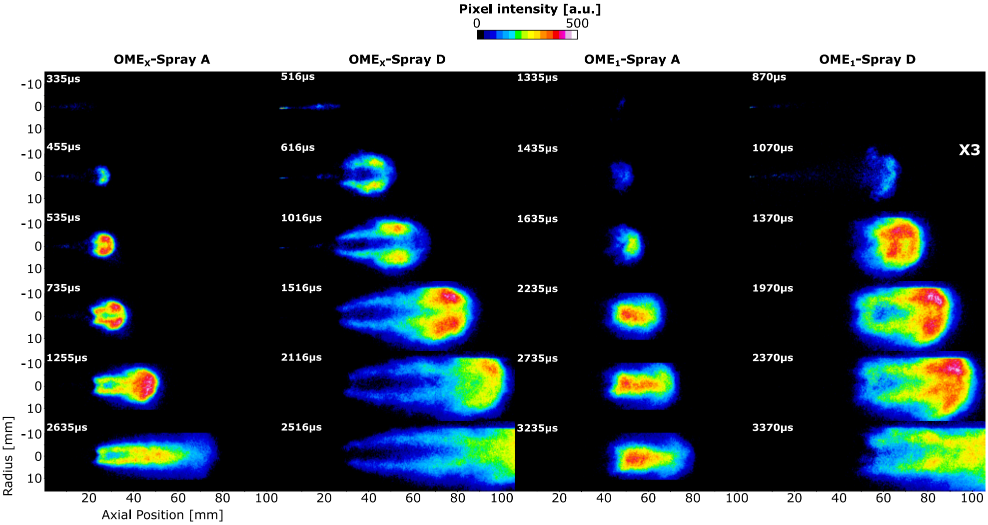

Figure 4-10 OH PLIF signal for OME_X and OME_1, under Spray A and Spray D conditions.

4.5.2 CH_2O Distribution

The first stage of combustion, known as “cool flame”, is characterized by the formation of significant amounts of CH_2O. The formaldehyde is quickly consumed during the second stage, and the formation of OH and CH characterizes the reaction zone. At this stage, a significant part of chemical energy is released. Figure 4-11 shows the CH_2O PLIF signal structure for OME_X and OME_1 under Spray A and Spray D conditions. Following the same methodology used for the reference case with Dodecane, white brackets have been added at the instants with the largest fluorescence region to identify the axial region in which the fluorescence is associated with CH_2O. In general, a contraction of the CH_2O area can be observed as the combustion progresses, with a shorter downstream progression. For all four cases, the first instant, when the CH_2O area is largest, corresponds to the “cool flame” stage (first stage), as no OH signal has been observed yet. In contrast, the last instant represented corresponds to quasi-steady flame instants, where CH_2O intensity decreases in the regions where the mixture transitions to the high-temperature combustion stage. Remember that the intensity visible upstream of the region bounded by the white bracket is caused by the elastic scattering of light from the liquid fuel, which was not suppressed by the optical filters.

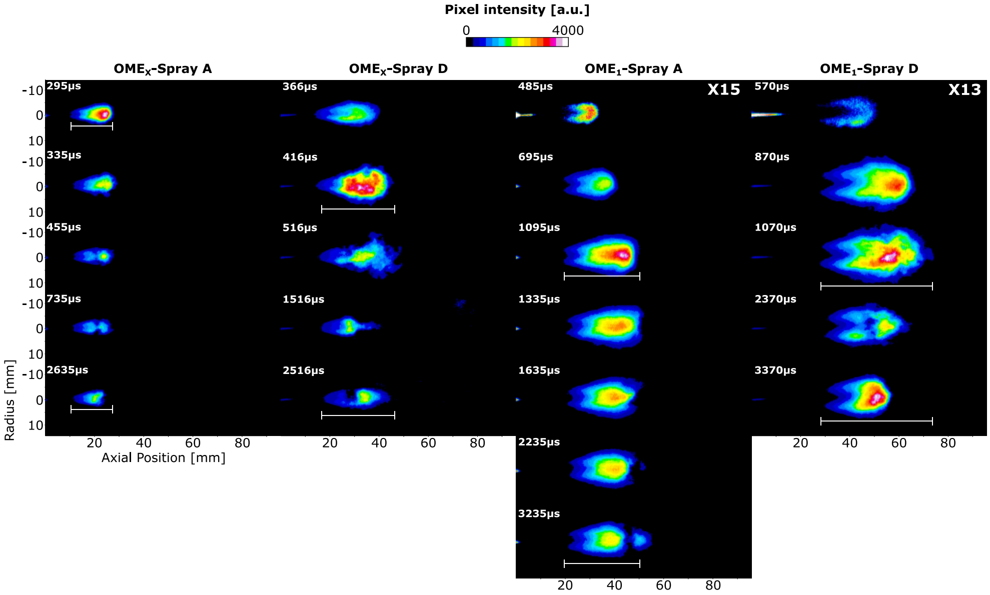

Figure 4-11 CH_2O PLIF signal for OME$_X$ and OME$_1$, under Spray A and Spray D conditions.

Distinct fluorescence lobes of CH_2O, as observed in other studies [15,23], can be identified above and below the spray axis downstream of the first axial position where CH_2O is detected for all test conditions. The PAH structure observed for Dodecane in the reference case is not reported using OME$_X$ and OME$_1$. This fact agrees with the lack of PAH observed in other studies on these fuels [21]. The absence of PAH and soot in this kind of flame allows the detection of CH_2O during the whole combustion event. In this way, CH_2O remains mostly upstream of the LOL location, a region without OH^*, indicating that it is not a high-temperature zone.

When comparing both fuels with the same nozzle, the CH_2O area of OME$_1$ is larger than OME$_X$, indicating that the diffusion process is different for each fuel. The fact that the LOL for OME$_1$ is larger than that of OME$_X$ allows the spray to reach a larger size before reaching the high-temperature reaction zone. Besides, the lower reactivity of the fuel seems to increase the difference between the location where the first CH_2O is detected and the LOL.

4.5.3 OH and CH_2O Interaction

To further dig into the interaction of OH and CH_2O for OME_X and OME_1, the PLIF signal of both species has been combined in Figure 4-12 under Spray A and Spray D conditions. Only the times that both species coexist are taken into account. The green color represents CH_2O, while OH is described in red. The intensity of each fluorescence signal has been normalized with its maximum value at each instant.

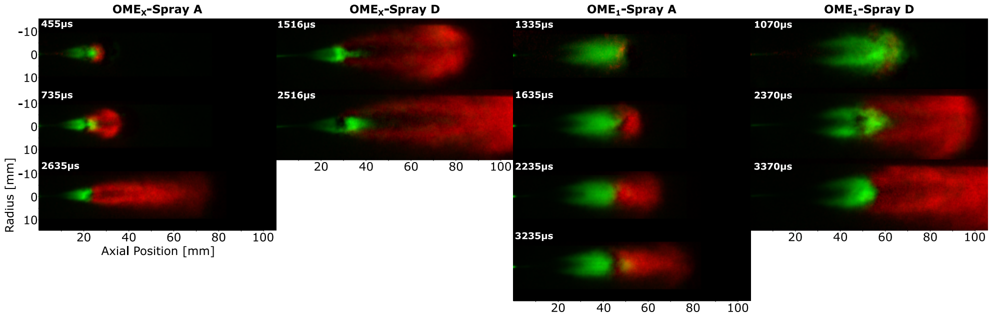

Figure 4-12 CH_2O (green) and OH (red) PLIF signal for OME_X and OME_1, under Spray A and Spray D conditions.

Before reaching the stabilized stage, CH_2O is initially observed to be generated upstream of the lift-off location represented by the OH PLIF frontier (the low-temperature region) and consumed when it enters the high-temperature region (OH). When the flame stabilizes (last instant represented), it is possible to see for OME_X-Spray A, OME_1-Spray A, and OME_1-Spray D conditions, that both CH_2O and OH regions are clearly separated. This agrees with the conclusions reported by Idicheria et al. [15], who observed for non-soot conditions that high-temperature reactions at fuel-rich premixed zones close to the spray center consumed CH_2O. However, for OME_X-Spray D, the frontier between both regions is unclear. In this case, the head of the CH_2O region signal is surrounded by the two lobes of the OH signal and eventually disappears downstream of the lift-off location. For this case, the displacement of the high-temperature reactions to the periphery of the flame could slow down the CH_2O consumption at the inner part of the flame. This could be caused by the high equivalence ratio reached in this case compared to the other three, which displaces the oxidation reactions (and CH_2O consumption) towards the periphery of the flame.

4.6 Summary and Conclusions

The use of e-fuels to replace fossil fuels has great benefits. In particular, the OME_n family is exciting due to its potential to reduce the ICE carbon footprint but also thanks to the soot emission reduction that can be achieved using them as neat fuels or blended with diesel. For this reason, a detailed characterization of the flame structure of OME_X and OME_1 was carried out in a high-pressure and high-temperature vessel under Spray A and Spray D ECN operating conditions. The two characteristic regions of the flame, the low-temperature (identified by the CH_2O) and the high-temperature regions (identified by the OH radicals), were analyzed based on PLIF measurements and high-speed OH^* chemiluminescence visualization.

The results obtained in this study contributed to the first objective described during the first chapter of this thesis regarding the OME_X and OME_1 flame structure description. As discussed at the beginning of this chapter, the use of the Spray A condition has allowed us to fix the basis of this study to use the e-fuels under the reference conditions of the ECN.

Although the flame structure of the Spray A condition could not be evaluated during the quasistationary period because the laser was introduced through the flame head, times prior to soot formation have clearly shown a flame structure for this condition consistent with the literature. Furthermore, the no-soot formation characteristic of these e-fuels allows the detection of the flame structure during the whole combustion period.

In this way, the main results using OME_X and OME_1 under Spray A and Spray D conditions are summarized below:

- Flame penetration using OME_X and OME_1 under Spray A condition seems not to depend on fuel reactivity but on mixing formation, which agrees with the results of other studies with non-oxygenated fuels. Even though the same conclusions can be expected for the Spray D condition, the field-of-view limits prevent an experimental confirmation.

- Non-dimensional LOL stabilized closer to the tip injector for OME_X than $OME_{1,}$ indicating that the reactivity of the fuel plays a significant role. This fact suggests that LOL stabilizes under different equivalence ratios for each fuel.

• Two typical lobes of CH_2O can be identified above and below the spray axis for all cases. The presence of this intermediate species is much more intense during the cool flame stages and is later reduced when a high-temperature reaction arises. No PAH radiation appears downstream of the LOL, corroborating the free-soot characteristics of these fuels. Finally, a larger CH_2O area is observed for OME_1 compared to OME_X, which has been related to the lower reactivity of the first fuel, displacing reactions downstream where the spray is wider.

• OH^* deconvolution shows the high-temperature reaction zones of the flame for all cases. A similar structure between OH^* deconvolution and OH PLIF was obtained. However, for OME_1-Spray A, OH PLIF shows a wider distribution than OH^* deconvolution, indicating that part of OH appears outside the high-temperature reaction zones.

• Before the stabilized stage, a high-intensity CH_2O associated with the cool flame stage was observed. The appearance of OH, indicating that the high-temperature phase starts, entails the consumption of CH_2O, avoiding the downstream progression of this species and generating a visible frontier between both structures. This was not observed for OME_X-Spray D, which showed that a certain amount of CH_2O progressed downstream the LOL position in the central region of the flame within the two OH lobes. The higher equivalence ratio reached in this case could hinder the CH_2O consumption at the spray axis compared to the other cases.

These findings serve as an important contribution to the characterization of these e-fuels initiated in García-Carrero thesis [1] to increase their database in the Engine Combustion Network (ECN).

These results lead to continuing to study these fuels in engine-like conditions, where the dynamics of the engine directly affect the behavior of the combustion process. This topic is addressed in the following chapters.

Bibliography

[1] García Carrero AA. Experimental Study of the Fuel Effect on Diffusion Combustion and Soot Formation under Diesel Engine-Like Conditions. Universitat Politècnica de València, 2022. https://doi.org/10.4995/THESIS/10251/179997.

[2] CMT - Motores Térmicos website n.d. https://www.cmt.upv.es/#/ecn/Principal (accessed August 26, 2023).

[3] Pastor J V., Garcia-Oliver JM, Micó C, Tejada FJ. Comparison of the Diffusive Flame Structure for Dodecane and OMEX Fuels for Conditions of Spray A of the ECN. SAE Technical Papers 2020:1–10. https://doi.org/10.4271/2020-01-2120.

[4] Pastor J V, García-Oliver JM, Micó C, Tejada FJ. Characterization of the oxymethylene ether fuels flame structure for ECN Spray A and Spray D nozzles. Appl Energy 2023;332:120475. https://doi.org/10.1016/j.apenergy.2022.120475.

[5] Dec JE, Coy EB. OH radical imaging in a di diesel engine and the structure of the early diffusion flame. SAE Technical Papers 1996. https://doi.org/10.4271/960831.

[6] Donkerbroek AJ, van Vliet AP, Somers LMT, Dam NJ, ter Meulen JJ. Relation between hydroxyl and formaldehyde in a direct-injection heavy-duty diesel engine. Combust Flame 2011;158:564–72. https://doi.org/https://doi.org/10.1016/j.combustflame.2010.09.024.

[7] Maes N, Meijer M, Dam N, Somers B, Baya Toda H, Bruneaux G, et al. Characterization of Spray A flame structure for parametric variations in ECN constant-volume vessels using chemiluminescence and laser-induced fluorescence. Combust Flame 2016;174:138–51. https://doi.org/10.1016/j.combustflame.2016.09.005.

[8] Donkerbroek AJ, Van Vliet AP, Somers LMT, Frijters PJM, Klein-Douwel RJH, Dam NJ, et al. Time-and space-resolved quantitative LIF measurements of formaldehyde in a heavy-duty diesel engine. Combust Flame 2010;157:155–66.

[9] Bakker PC, Maes N, Dam N. The potential of on- and off-resonant formaldehyde imaging combined with bootstrapping in diesel sprays.

Combust Flame 2017;182:20–7. https://doi.org/10.1016/j.combustflame.2017.03.032.

[10] Dec JE, Espey C. Chemiluminescence Imaging of Autoignition in a DI Diesel Engine. SAE Technical Paper 982685, 1998. https://doi.org/10.4271/982685.

[11] Klein-Douwel RJH, Donkerbroek AJ, van Vliet AP, Boot MD, Somers LMT, Baert RSG, et al. Soot and chemiluminescence in diesel combustion of bio-derived, oxygenated and reference fuels. Proceedings of the Combustion Institute 2009;32:2817–25. https://doi.org/10.1016/j.proci.2008.06.140.

[12] Skeen SA, Manin J, Pickett LM, Cenker E, Bruneaux G, Kondo K, et al. A Progress Review on Soot Experiments and Modeling in the Engine Combustion Network (ECN). SAE Int J Engines 2016;9:2016-01–0734. https://doi.org/10.4271/2016-01-0734.

[13] Cenker E, Bruneaux G, Pickett L, Schulz C. Study of Soot Formation and Oxidation in the Engine Combustion Network (ECN), Spray A: Effects of Ambient Temperature and Oxygen Concentration. SAE Int J Engines 2013;6:2013-01–0901. https://doi.org/10.4271/2013-01-0901.

[14] Bardi M, Payri R, Malbec LM, Bruneaux G, Pickett LM, Manin J, et al. ENGINE COMBUSTION NETWORK: COMPARISON OF SPRAY DEVELOPMENT, VAPORIZATION, AND COMBUSTION IN DIFFERENT COMBUSTION VESSELS. Atomization and Sprays 2012;22:807–42. https://doi.org/10.1615/AtomizSpr.2013005837.

[15] Idicheria CA, Pickett LM. Formaldehyde visualization near lift-off location in a diesel jet. SAE Technical Papers 2006. https://doi.org/10.4271/2006-01-3434.

[16] Maes N. The life of a spray. Technische Universiteit Eindhoven, 2019.

[17] Pickett LM, Manin J, Genzale CL, Siebers DL, Musculus MPB, Idicheria CA. Relationship Between Diesel Fuel Spray Vapor Penetration/Dispersion and Local Fuel Mixture Fraction. SAE Int J Engines 2011;4:2011-01–0686. https://doi.org/10.4271/2011-01-0686.

[18] Thring MW, Newby MP. Combustion length of enclosed turbulent jet flames. Symposium (International) on Combustion 1953;4:789–96. https://doi.org/10.1016/S0082-0784(53)80103-7.

[19] Pastor JV, García-Oliver JM, López JJ, Vera-Tudela W. An experimental study of the effects of fuel properties on reactive spray evolution using Primary Reference Fuels. Fuel 2016;163:260–70. https://doi.org/10.1016/j.fuel.2015.09.064.

[20] Pastor J V., García-Oliver JM, Micó C, García-Carrero AA. An experimental study with renewable fuels using ECN Spray A and D nozzles. International Journal of Engine Research 2021. https://doi.org/10.1177/14680874211031200.

[21] Pastor J V., García-Oliver JM, Micó C, García-Carrero AA, Gómez A. Experimental study of the effect of hydrotreated vegetable oil and oxymethylene ethers on main spray and combustion characteristics under engine combustion network spray A conditions. Applied Sciences (Switzerland) 2020;10. https://doi.org/10.3390/APP10165460.

[22] Hardalupas Y, Orain M, Panoutsos CS, Taylor AMKP, Olofsson J, Seyfried H, et al. Chemiluminescence sensor for local equivalence ratio of reacting mixtures of fuel and air (FLAMESEEK). Appl Therm Eng 2004;24:1619–32. https://doi.org/10.1016/J.APPLTHERMALENG.2003.10.028.

[23] Skeen SA, Manin J, Pickett LM. Simultaneous formaldehyde PLIF and high-speed schlieren imaging for ignition visualization in high-pressure spray flames. Proceedings of the Combustion Institute 2015;35:3167–74. https://doi.org/10.1016/j.proci.2014.06.040.

Chapter 5

Piston geometry effects on air-fuel mixing

Content

5.1 Introduction

The second objective of the thesis is to identify the relevance of some particular aspects of piston geometry on mixture formation, combustion development, and soot formation under engine conditions. Several studies appear in the literature analyzing this phenomenon in light-duty engines, showing a great potential to reduce pollutant emissions.

The effect of radial lips geometry, as the more recent innovative geometry, was analyzed by several authors, as mentioned in Chapter 2. Lewiski [1] studied the effect of this geometry in a light-duty optical engine, indicating that this geometry could improve the in-cylinder soot reduction compared to conventional geometries. However, it is necessary to carry out this type of study on larger engines, where the literature shows a clear lack of studies. Therefore, this study was conducted in a medium-duty optical engine with access through the piston, allowing the visualization inside the combustion chamber. Two pistons were used, each featuring the radial-lips geometry with certain modifications. In addition, the same fuel (conventional Diesel) was used in all these tests, so the differences observed in the combustion process must be due only to piston geometry. For the study, two optical techniques were implemented simultaneously: Two Color Pyrometry as an indicator of soot concentration and OH* chemiluminescence as a high-temperature tracer indicating areas of the combustion chamber where soot oxidation occurs.

In this way, this study uses two reference points: one at low engine load and the second at high engine load. This chapter starts analyzing parametric variations in the reference case at low engine load. These variations include the injection system (injection pressure and SOE) and the oxygen percentage inside the combustion chamber in order to simulate EGR conditions. Then, the analysis goes on to study the behavior in high soot conditions under high engine load and reducing the oxygen percentage inside the combustion chamber. The results obtained in this study were published in two scientific publications and summarized in this thesis chapter [2,3].

5.2 Operating Conditions

This study was conducted using a conventional diesel on a medium-duty single-cylinder optical engine. The analysis compares CS1 and CS2 pistons using STD and CDS injectors. For more information about the fuel, pistons, and injectors, see Chapter 3.

In summary, CS2 piston has a smoother bowl pip. In addition, CS2-Lips has a radial lips geometry slightly more pronounced than CS1. *PUNCH Torino* company contributed to this study, providing CFD simulations of these pistons. The company justifies the implementation of this variation in CS2 to achieve a balance between increasing the influence of the bowl on the air/fuel mixing process without penalizing other aspects, such as thermal efficiency [4,5]. For more details, see piston sketches in Chapter 3.

The STD injector was used for the study at low and high engine loads. However, the CDS injector was used only to compare both injectors at high engine load. As discussed in Chapter 3, the CDS injector provides a combustion closer to the center of the piston bowl, improving the air-fuel mixing [6–8]. In this way, the comparison of both injectors at a high engine load, as a high soot condition, combined with the radial lips geometry, is done.

This study evaluated the influence of different operating conditions on the piston performance. Two different engine loads were tested, corresponding to 2.7 and 6.7 bar of indicated mean effective pressure (IMEP). The combination of operating conditions defined for each was chosen to represent a realistic configuration of the type of engine on which the optical one is based. The baseline condition for each IMEP is highlighted in Table 5-1, where the cases of 2.7 bar and 6.7 bar are used as low engine load (LEL) and high engine load (HEL) reference conditions.

Table 5-1. Baseline operating conditions for the two engine loads.

Test	**IMEP (bar)**	**Engine Speed (rpm)**	**P_{int} (bar)**	**P_{exh} (bar)**	**T_{int} (°C)**	**P_{inj} (bar)**	**SOE (°aTDC)**	**O_2 (%)**	**Injector**
LEL	2.7	1200	1.04	1.24	102	731	-20.4	21	STD
HEL	6.7	1400	1.34	1.54	55	1182	-33.7	21	STD

Additionally, a parametric variation is carried out for each engine load baseline condition. For the low engine load baseline condition (2.7 bar IMEP), the injection pressure (P_{inj}) was modified ± 100 bar, the start of energizing (SOE) of the nozzle was increased by 4° and 8° and oxygen concentration (% O_2) was reduced to 18% and 15% to simulate exhaust gas recirculation (EGR). For the high engine load baseline condition (6.7 bar IMEP), the variation of oxygen concentration (18% and 15%) and the injector model (CDS) is analyzed. All of these operating conditions variations can be seen in Table 5-2. In order to avoid the influence of cycle-to-cycle engine variability on the analysis, 10 combustion cycles were registered per operating condition, and data were averaged.

Table 5-2 Operating variation conditions for the two engine loads.

Baseline operating condition reference	**Pinj (bar)**	**SOE (°aTDC)**	**O_2 (%)**	**Injector**
Low engine load (LEL)	631/831	-16.4/-12.4	18/15	-
High engine load (HEL)	-	-	18/15	CDS

A realistic injection strategy was adjusted to mimic the RoHR of the metal engine at the same IMEP values used in this study. Dwels (D) and durations (ET), as well as other engine settings, were adapted to compensate the differences in heat transfer and compression ratio between the optical single-cylinder engine and the metal engine. These injection strategies are represented in Figure 5-1, which include two pilot injections (Pil1 and Pil2), one main injection (M), and one post injection (Post). The values of each electric pulse for both engine loads are shown in Table 5-3.

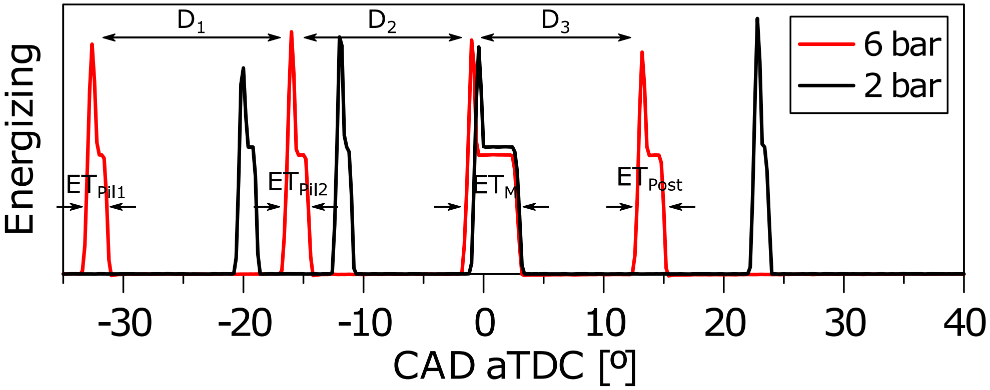

Figure 5-1. Graph of injection strategy for each engine load. The marks of different times that define the injection strategy are only highlighted for 6 bar.

Table 5-3 Injection strategy timings for both engine loads.

IMEP (bar)	D_1 (µs)	D_2 (µs)	D_3 (µs)	ET_{Pil1} (µs)	ET_{Pil2} (µs)	ET_M (µs)	ET_{Post} (µs)	SOI_M (°aTDC)
2.7	894	1394	2661	226.4	192.5	379.9	197.3	-1
6.7	1360	1203	891	174.6	189.3	450	225.7	-2

5.3 Optical Arrangement

Two simultaneous optical techniques: 2-Color Pyrometry and OH^* chemiluminescence high-speed imaging, were applied in order to analyze the soot formation and the oxidation process during combustion. The optical setup is shown in Figure 5-2.

With this setup, flame radiation goes through the quartz piston bowl and gets reflected by the 45° elliptical mirror. This element has an enhanced aluminium coating to obtain a good reflection efficiency in the UV and visible spectrum (above 85% between 250 and 700 nm). Then, radiation reaches a dichroic mirror (DMSP805L-Thorlabs) that transmits the visible spectrum and reflects UV radiation in a small range of around 310 nm, coinciding with one of the most intense emission bands of the OH^* radical. According to the specifications of this dichroic mirror [9], this is a short pass with a cutoff wavelength at 850 nm, transmitting radiation between 400 nm and 799 nm (VIS) and reflecting between 823 nm and 1300 nm (IR). However, this element has an additional reflection band at 310 nm which coincides with the OH* emission. A high-speed camera equipped with a high-speed intensifier and a narrowband interference filter is used to register it.

At the same time, the light transmitted through the dichroic mirror (VIS) reaches a beam splitter that reflects 50% of it and transmits the other 50%. All this radiation is directed toward two high-speed cameras equipped with specific narrowband interference filters to register only specific wavelengths, which is required to apply the 2-Color Pyrometry algorithm. The three high-speed cameras were triggered simultaneously with the SOE and synchronized on a frame basis. Thus, the image-by-image correlation between them was ensured.

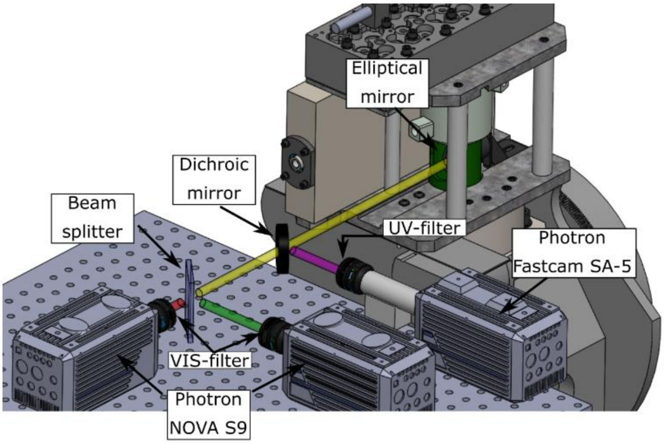

Figure 5-2. Optical setup.

5.3.1 OH* chemiluminescence imaging

High-speed OH* chemiluminescence images were used to trace the piston bowl oxidation reactions. It is important to remember that the signal obtained is line-of-sight integrated, limiting the results spatial resolution.

A Photron SA5 (high-speed CMOS) equipped with a Hamamatsu C10880-03F high-speed intensifier was used. The intensifier photocathode is a multialkali (S-20), which allows detection from UV to near IR (spectral response: 185-900 nm). The intensifier was coupled to the camera with 1:1 relay optics. A UV-Nikor Rayfact 105 mm f 4.5 was used as the system lens. A narrowband interference filter with central wavelength at 310 nm and 10 nm full-width half maximum (FWHM) was set in front of the camera lens to register only the radiation corresponding to the OH* emission peak and reject the rest. The gating of the intensifier was the same as the exposure time of the high-speed camera, which was set at 39.75 µs. Its gain was adjusted to maximize the dynamic range under each engine load. The acquisition speed was 25 kfps, and the resolution was 4.4 pixels/mm.

5.3.2 2-Color pyrometry

Two high-speed cameras, Photron NOVA S9, were used in order to collect the radiation emitted by the soot within the flame at two specific wavelengths. For both cameras, the frame rate was set to 25 kfps, and a 100 mm f 2 Karl-Zeiss Makroplanar camera lens was used. One of the cameras was equipped with a narrowband interference filter with the transmission peak centered at 660 nm and 10 nm FWHM, while the other, a filter centered at 560 nm and 10 nm FWHM, was utilized. A specific exposure time was set for each camera due to the different intensity levels of radiation at each wavelength and each operating condition to make the most of the camera dynamic range.

5.4 Image Processing

For discussion in this study, the average OH* radiation and KL collected from the 10 combustion cycles have been analyzed. OH* and KL data were averaged for each recorded instant for the 10 combustion cycles to get matrices representing both parameters spatial distribution and average value. These matrices were used later to calculate the temporal evolution of the in-cylinder average OH* chemiluminescence and KL. It is important to remark that for the CS2 analysis, these average values were obtained using only the area of interest corresponding to the geometry analyzed, named as CS2-Lips or CS2-NoLips as described in Chapter 3. However, the whole piston area for CS1 was considered. This approach provides a clear way to present an analysis of the temporal evolution of the combustion process for both pistons. Still, it requires integrating all the information within the cylinder into one value. Therefore, it would not provide spatial distribution information.

For this reason, an additional approach was followed to present KL and OH* data with spatial and temporal resolution. It divides the combustion chamber into concentrical rings (0.5 mm thickness centered at the nozzle location), for which the average KL or OH* intensity value is calculated according to (5-1). It was calculated with the ring area (A_a) and the sum of all pixels contained in the ring ($KL_{cummul,a}$). This procedure is carried out for each frame, corresponding to a different crank angle degree (CAD). The result is a 2D matrix where each column represents a different CAD while the row is the radial distance to the center of the piston. An example of the result from this methodology is represented in Figure 5-3. The green and red circles indicate the minimum and maximum radial distances used for the analysis. In this study, the analysis does not consider the squish zone (the area between red and white circles in the left image). The average KL values of the different rings at a specific CAD are represented between the two white lines in the right image. The value of a specific ring, represented in purple in the left image, has been highlighted with the same color in the 2D map. The same methodology is followed for OH* chemiluminescence.

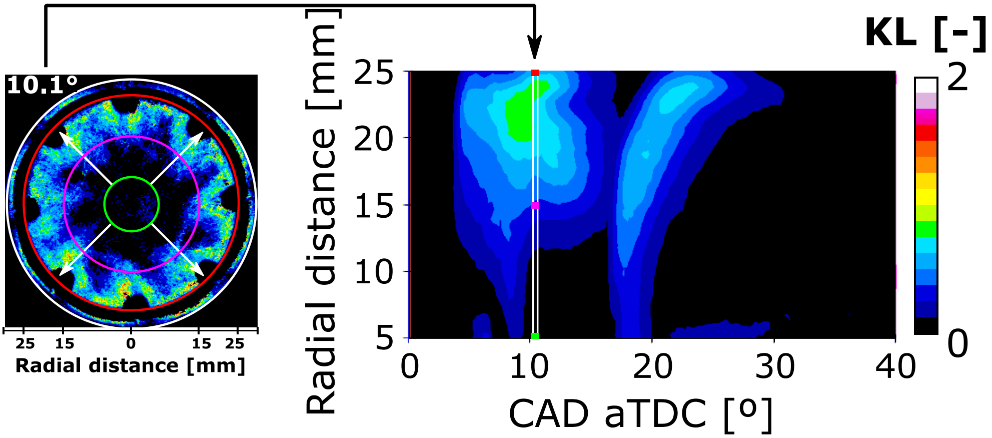

Figure 5-3 A sketch of the methodology used to represent KL evolution maps.

$$KL_{mean} = KL_{cummul,a}/A_a \qquad (5\text{-}1)$$

From now on, the graphic representation of these matrices will be identified as "radial maps". These radial maps will be used only for the radial lips geometries (CS1 and CS2-Lips) to deep in the flame dynamic changes due to them.

To highlight the differences when comparing both pistons, relative difference radial maps were calculated for both KL and OH*. They were obtained by subtracting the information contained in the radial map of CS1 to CS2-Lips. Then, the resulting matrix is divided by the values of CS1 as per (5-2). Therefore, the positive values of the relative difference radial maps show a higher contribution from CS2-Lips, represented by green to red in the color pallet. In contrast, the negative ones correspond to a higher contribution from CS1, represented by green to blue. An example of these relative difference maps is shown in Figure 5-4. It is important to highlight that the aim of these maps is not to quantify the parameter shown but to identify the region and time where differences between both pistons arise.

$$Relative\ radial\ map = \frac{\left(Map_{CS2-Lips} - Map_{CS1}\right)}{Map_{CS1}} \qquad (5\text{-}2)$$

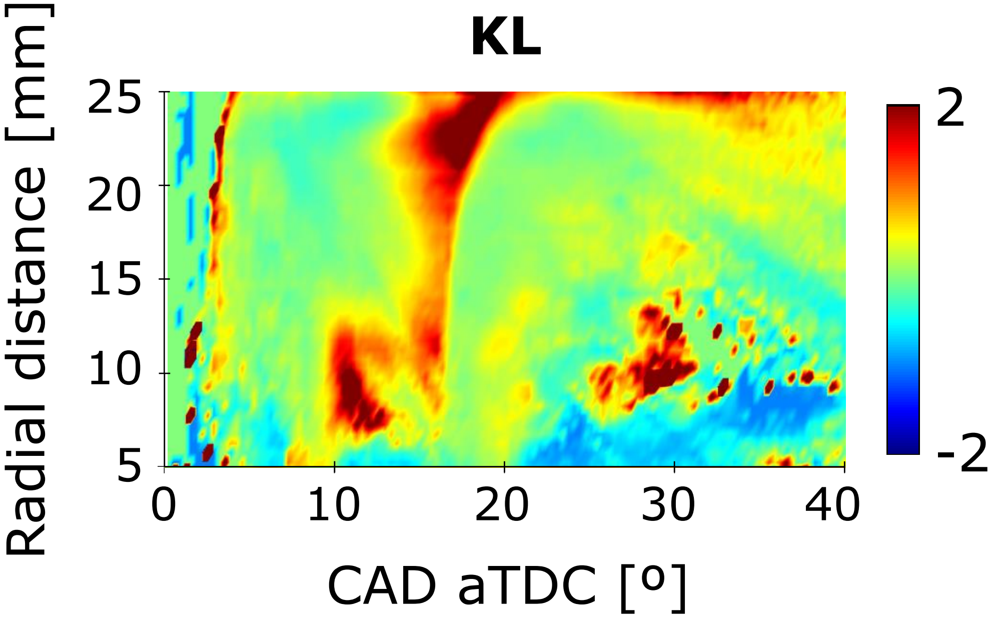

Figure 5-4 Example of KL relative radial maps: Positive values (green to red color) indicate a higher KL for CS2-Lips, while negative values (green to blue) indicate a higher KL for CS1. The same discussion can be done for OH* relative radial maps.

5.5 Effect of Radial Lips Geometry at Different Operating Conditions under Low Engine Load

As stated previously, CS2-Lips geometry was proposed to increase the influence of radial lips over in-cylinder flow dynamics. This can be analyzed based on the flame movement inside each combustion system. Figure 5-5 shows a KL and OH* chemiluminescence distribution sequence for CS1 and CS2 at 2.7 bar IMEP and baseline operating conditions. At 6.1° aTDC, the flame reaches the bowl wall and starts spreading tangentially, guided by the periphery of the bowl. At this instant, where the injection event still occurs, no significant differences are observed among the three geometries (CS1, CS2-Lips, and CS2-NoLips) regarding KL distribution. When looking at OH* chemiluminescence, it is possible to see no differences between the three geometries either. Most oxidation reactions are located upstream of the bowl periphery (even separated several millimeters).

Once the flame front reaches the radial lips, differences start to appear. At 10.1° aTDC, the radial lips (CS1 and CS2-Lips) stop the tangential spreading and redirect the flame toward the bowl center. This is not observed for the CS2-NoLips side, which concentrates the flame at the bowl periphery. The flame-to-flame collision is stronger for this geometry, forming more soot than the CS1 and CS2-Lips, as the higher KL indicates. The OH* chemiluminescence signal also shows that most of the oxidation reactions on this side occur close to the bowl periphery.

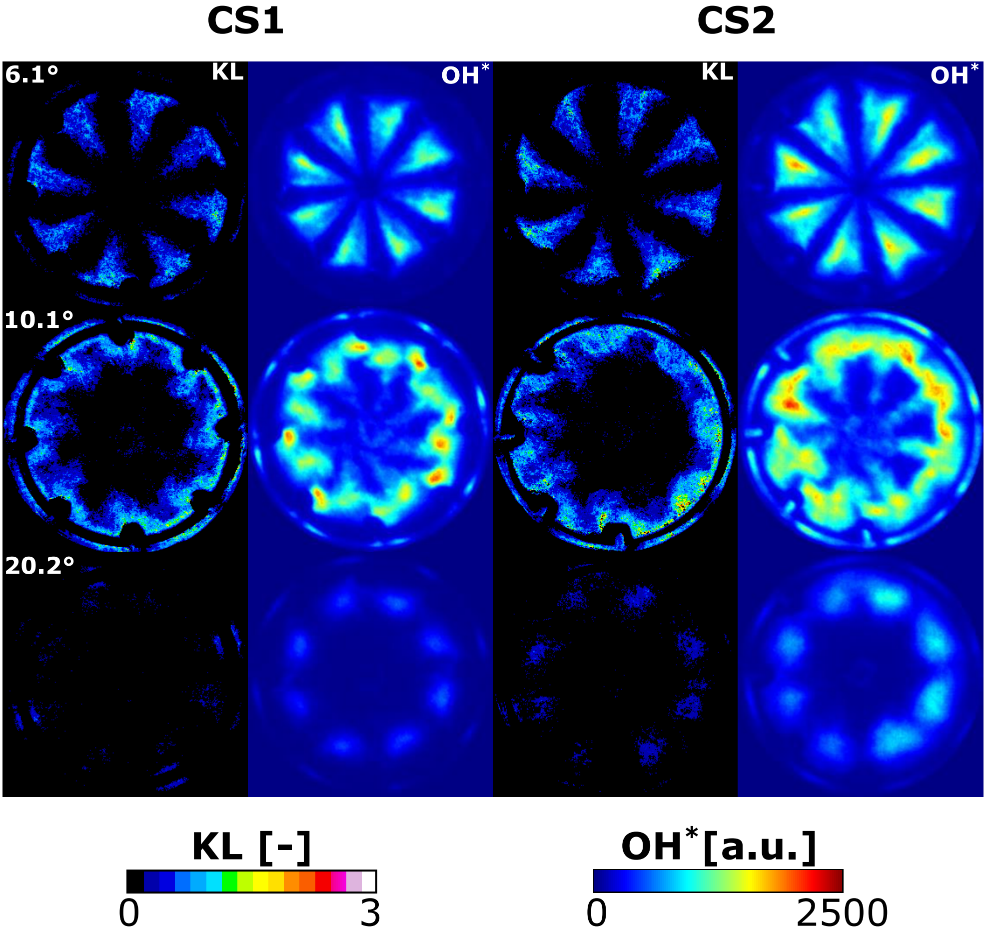

Figure 5-5 KL and OH* chemiluminescence for CS1 and CS2 at 2.7 bar IMEP and baseline conditions.

In contrast, the oxidation reactions spread towards the bowl center for the geometries with the radial lips. Besides that, slight differences between both radial lip designs can also be highlighted at this instant. The CS2-Lips (more pronounced) conduct the flame closer to the bowl center than the CS1, which can improve the use of in-cylinder oxygen. This statement is also supported by OH^* radiation, which shows larger clouds closer to the center for the CS2-Lips than CS1. Going forward on the combustion process, at 20.2° aTDC, CS1 and CS2-Lips are much more similar during the late oxidation phase. Both geometries show very low KL and OH^* chemiluminescence levels, which indicates that combustion has almost finished. However, for the CS2-NoLips, relatively intense OH^* radiation is visible, showing that oxidation reactions are still occurring. This confirms that the radial lips can also accelerate the reaction.

The combustion process described in the previous paragraph is represented in Figure 5-6 in terms of aRoHR (left) and the evolution of average KL (right) for both combustion systems. Regarding the aRoHR curves, it is important to remark that this allows to compare both pistons, but it is not possible to isolate the effect of each side of the CS2. However, this data identifies if the combustion develops similarly from a macroscopic point of view. On the one hand, it is possible to see that both designs provide very similar aRoHR, although CS2 reaches a slightly higher peak. On the other hand, the KL evolution shows a lower soot formation by the radial lips geometries in comparison with CS2-NoLips, as was observed previously. However, it is also possible to see that CS2-Lips provides lower KL than CS1. This indicates that the more intense reentrant movement achieved by the more pronounced radial lip profile can improve the effectiveness of this concept on soot reduction.

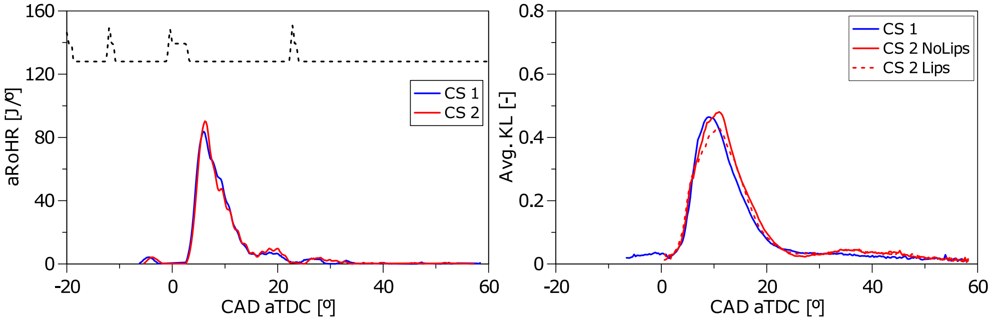

Figure 5-6 aRoHR (a) for CS1 and CS2 and average KL evolution (b) for CS1, CS2-Lips, and CS2-NoLips at 2.7 bar IMEP and baseline conditions. The dashed line on top of the aRoHR represents the injection strategy for reference.

The previous description was based on a single operating point. Therefore, it is interesting to extend the analysis to different experimental conditions. Therefore, a sweep of operating conditions was performed as described in previous sections. Figure 5-7 shows the aRoHR (a) and average KL evolution (b) when SOE is increased, delaying injection by 4° and 8°. In this way, the late oxidation stages will occur later in the cycle with lower in-cylinder pressure and temperature. The aRoHR curves confirm that the pistons operate under the same in-cylinder conditions and that a similar IMEP is achieved despite the modifications. As SOE is increased, the combustion of the main injection event is delayed. Until 4° increase, the aRoHR is very similar to the baseline case. However, when the injection is delayed by 8°, a more intense peak is achieved, suggesting more premixed combustion. This effect can be related to the fact the main injection event starts later during the expansion stroke (lower pressure and temperature), leading to a longer ignition delay. For the three cases, differences in terms of average KL are observed between CS1 and CS2-Lips. For the first one, a slight increase is observed for 4°, while a slight decrease is achieved at 8°. In contrast, for the CS2-Lips, a higher increase is observed in the first case, but also a larger decrease is achieved when moving to 8°. These results show that CS2-Lips is more effective in reducing the soot formation when combustion conditions are worsened, but more mixing time is allowed.

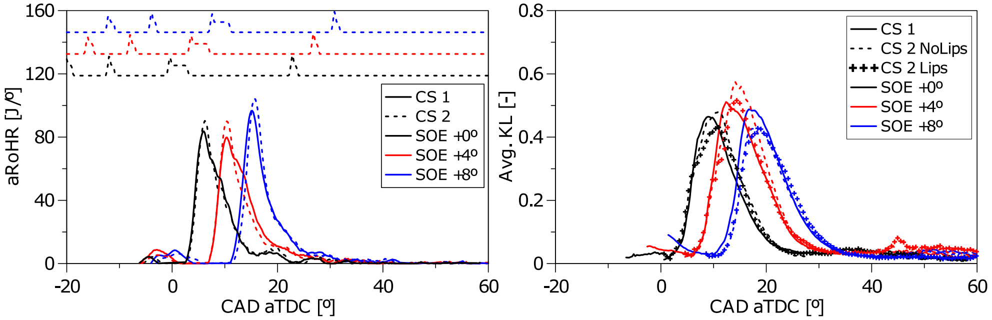

Figure 5-7 aRoHR (a) for CS1 and CS2 and average KL evolution (b) for CS1, CS2-Lips, and CS2-NoLips at 2.7 bar IMEP and different SOE configurations. The dashed line on top of the aRoHR represents the injection strategy for reference.

The performance of the different geometries at different injection pressures is shown in Figure 5-8. When the pressure is increased by 100 bar, even if the atomization process improves, more fuel is injected into the cylinder. In this case, both combustion systems have a similar aRoHR. However, again less KL values were obtained for CS2-Lips compared to CS1. The difference is even more prominent when the injection pressure is reduced by 100 bar from the nominal one. However, in this case, a slight delay is observed in the aRoHR, which could lead to a better air/fuel mixture and a consequent reduction of soot formation in addition to the influence of the CS2-Lips geometry.

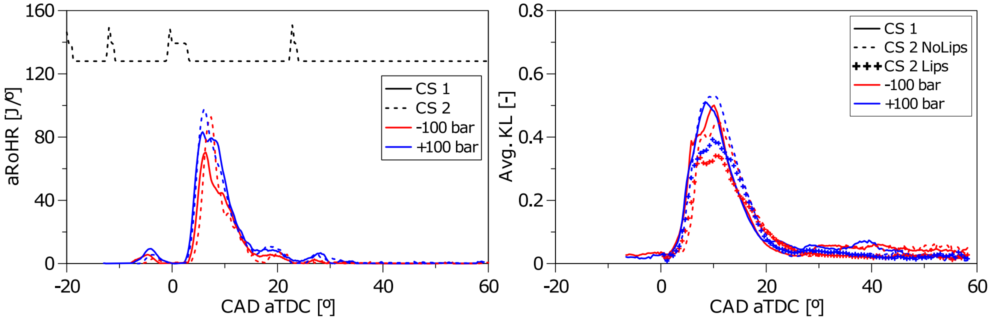

Figure 5-8 aRoHR (a) for CS1 and CS2 and average KL evolution (b) for CS1, CS2-Lips, and CS2-NoLips at 2.6 bar IMEP and different P_{inj}. The dashed line on top of the aRoHR represents the injection strategy for reference.

Under EGR conditions, combustion systems are forced to work under low oxygen concentrations. Therefore, the benefits of redirecting flames toward the center region of the bowl could be affected. Figure 5-9 shows aRoHR (left) and average KL evolution (right) for 18% and 15% O2 concentration, simulating different EGR rates. At 15% O_2, the aRoHR curves indicate that combustion starts much later than the baseline case for both combustion systems. When looking at the evolution of average KL for this case, a significant reduction is observed for both CS1 and CS2, challenging the analysis. This behavior can be related to more premixed combustion due to the longer ignition delay. It is in agreement with the higher peak of the aRoHR.

In contrast, at 18% O_2, the benefits of CS2-Lips are more visible. A more intense peak of CS2 aRoHR compared to CS1 could suggest more premixed combustion. However, no delay is observed for this condition between both geometries. Thus, all the differences observed for this operating condition can be related to the radial lip geometry. First, a faster oxidation process occurs for CS2, as the higher aRoHR peak indicates. In addition, it is possible to see that CS2-Lips can keep KL values even when decreasing from 21% to 18% O_2, which is not observed for CS1.

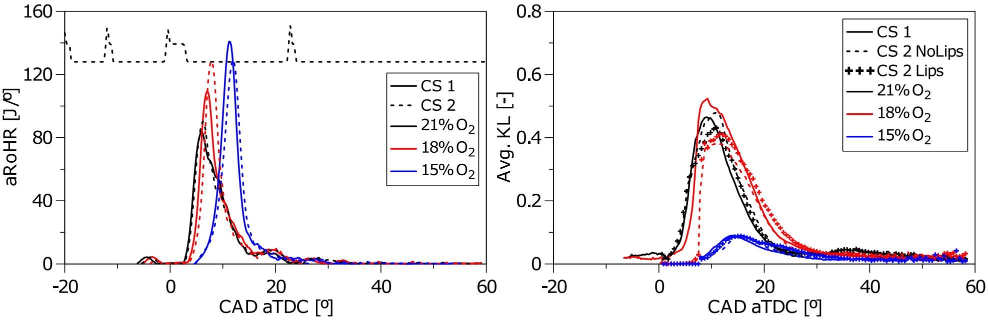

Figure 5-9 aRoHR (a) for CS1 and CS2 and average KL evolution (b) for CS1, CS2-Lips and CS2-NoLips at 2.7 bar IMEP and different oxygen concentrations. The dashed line on top of the aRoHR represents the injection strategy for reference.

5.6 Effect of Radial Lips Geometry under High Soot Operating Conditions: Low Oxygen Concentration and High Engine Load

In the previous section, a sweep of operating conditions was carried out to study the effect of piston geometry on the evolution of the combustion process by analyzing the aRoHR and the in-cylinder soot formation. The results show that the geometry with a more pronounced radial lip (CS2-Lips) exhibits more significant reductions in soot compared to the CS1 geometry when subjected to high soot formation conditions. Therefore, this section focuses on analyzing both geometries under these types of conditions. In this section, the tests are conducted at a high engine load of 6.7 bar IMEP, with the same sweep of oxygen percentages within the cylinder (18% and 15% O_2), simulating conditions similar to using EGR strategies. From now on, the baseline condition will be considered for the high-load cases shown in the *Operating Conditions* section.

Figure 5-10 shows both aRoHR and average KL for CS1 and CS2 under baseline operating conditions. The evolution of the aRoHR from both pistons is similar, indicating that the different bowl geometry does not significantly impact the combustion progress and energy released during the combustion process. This is consistent with the IMEP values obtained with CS1 and CS2: 6.8 bar and 6.7 bar, respectively. Focusing on the soot evolution, comparing both pistons, less KL was measured for CS2-Lips (red line) compared with CS1 during the main-injection combustion event (from 3 to 18° aTDC). However, before the post-injection combustion event (around 18° aTDC), the KL values do not decrease with CS2-Lips as is observed with the other geometry, indicating poorer soot oxidation at this stage. This causes the KL peak reached with the CS2-Lips to be close to the one measured with CS1 at 20° aTDC. At the late stage of the combustion process (after 20° aTDC), no differences are observable between CS2-Lips and CS1.

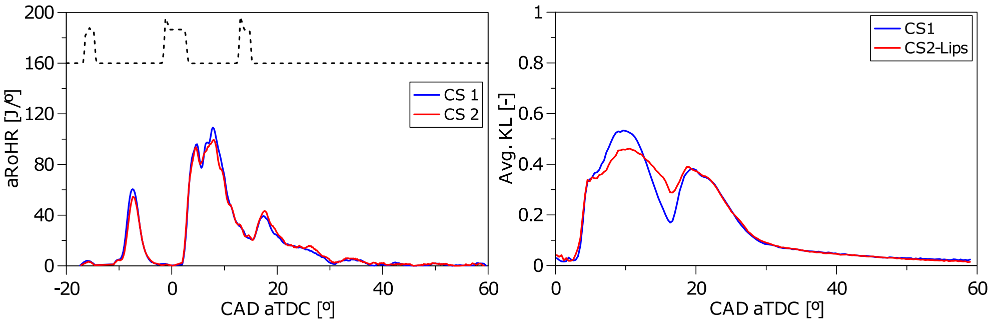

Figure 5-10 aRoHR (left) for CS1 and CS2 and average KL evolution (right) for CS1, CS2-Lips at 6.7 bar IMEP and baseline conditions. The dashed line on top of the aRoHR represents the injection strategy for reference.

To provide more insight into the soot evolution, radial maps for the CS2-Lips piston geometry are shown in Figure 5-11 for KL (left) and OH* chemiluminescence (right). In addition, white arrows indicating the end of the main injection (EOI_{Main}) and the start of post-injection (SOI_{Post}) were added at the top of both radial maps. At the first stages of combustion, KL appears between 12 mm and the bowl periphery. Then, it progresses toward the center of the bowl until 10° aTDC. A first white arrow has been added to the radial map to highlight this movement. These instants correspond with the first soot peak observed in Figure 5-10, related to the main injection combustion event. Between the main and the post-injection combustion events (between 10° and 18° aTDC), the soot closer to the center of the bowl (below 10 mm radius) seems to oxidize faster, generating a retraction of the KL cloud towards positions far from the center. This has been highlighted with a second white arrow on the KL map. The signal observed in the OH* chemiluminescence map during the same time interval and the region close to the bowl center confirms the appearance of oxidation reactions. They would be responsible for retracting the KL cloud between the main and post-injection combustion discussed before. This can be related to the fact that the flame is redirected towards the piston center, which has more oxygen available in this region, leading to leaner combustion than the one at the periphery of the bowl. Besides, this behavior is related to the decrease observed in the average KL curve (see Figure 5-10) during the same stage of the combustion process.

In contrast, above 12 mm, the OH* chemiluminescence also shows the existence of oxidation reactions, which does not result in the complete disappearance of the related KL. In this region, the mixture is expected to be richer as the fuel trends accumulate there (despite the effect of the radial lips). In that region, there is not enough oxygen to oxidize all the soot formed. With the post-injection (after 18° aTDC), soot is observed close to the center of the bowl and evolves toward the periphery of the piston. The high temperature inside the combustion chamber allows the fuel to ignite fast, resulting in a short lift-off length while the post-injection event lasts. After this, the oxidation of the soot is faster, close to the center, and the soot remaining is located closer to the periphery of the bowl.

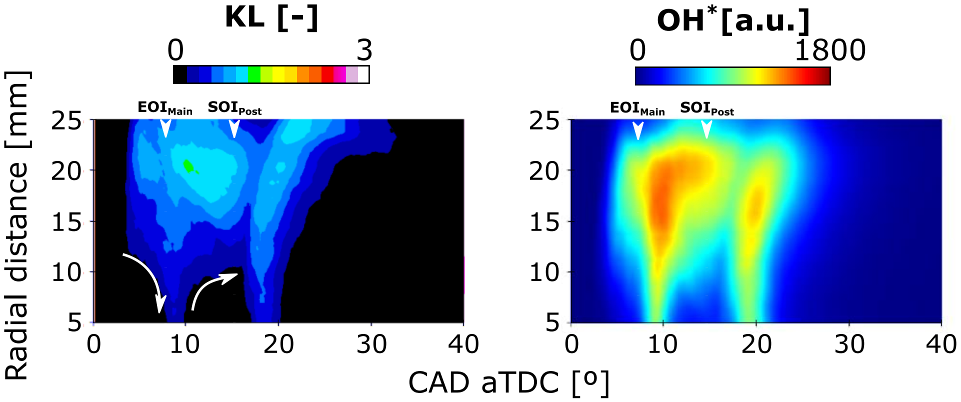

Figure 5-11 KL factor (left) and OH* chemiluminescence (right) radial maps for CS2-Lips.

The differences between CS1 and CS2-Lips can be analyzed thanks to the relative radial maps, explained in the methodology section of this chapter, for KL (left) and OH* chemiluminescence (right) presented in Figure 5-12. During the main injection combustion event, a higher soot cloud close to the center of the bowl is observed for CS2-Lips, indicating that this geometry displaces more soot to the bowl's center than CS1. A higher soot cloud is observed for the CS2-Lips between the main and post-injection combustion, consistent with the higher KL values discussed in Figure 5-10. Furthermore, during the post-injection combustion event (after 20° aTDC), a higher KL cloud remains at the bowl periphery for CS2-Lips. The oxidation reactions observed in OH* images (right) are insufficient to oxidize it. The result suggests that this geometry has difficulties oxidizing soot in this zone compared to CS1, which can be related to the fact that CS2-Lips accumulates a richer mixture in this region, as already discussed in Figure 5-11. At the late stages of combustion, some differences can still be observed between both pistons. From 25° to 30° aTDC, the CS2-Lips present higher values of KL below a 15 mm radius. However, after 30°, the soot at this region increases for CS1. This can be caused by the different movements promoted by each geometry. As suggested previously, CS2-Lips allows the flame to reach regions closer to the nozzle faster than CS1. Besides, this gives some time for the first geometry for additional oxidation with the oxygen still available there. Therefore, that soot cloud in CS2-Lips reaches the center of the piston before and has some time to oxidize and decrease before a similar displacement is completed with the CS1.

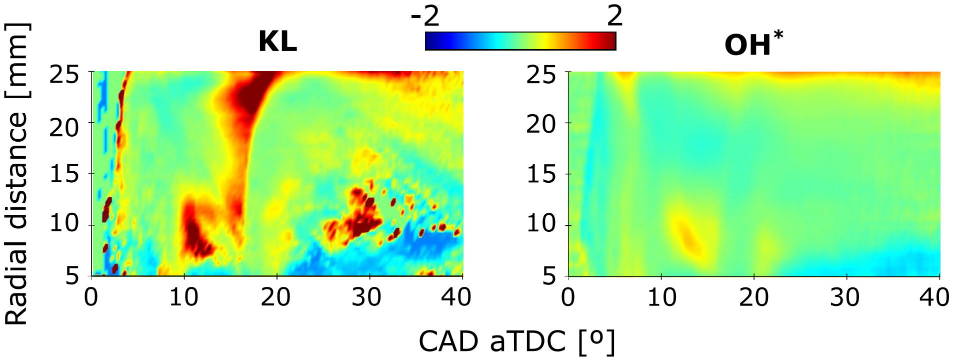

Figure 5-12 KL factor (left) and OH* (right) relative radial maps comparing CS2-Lips and CS1. Positive values (green to red color) indicate higher values for CS2-Lips, while negative values (green to blue color) indicate higher values for CS1.

In this study, the performance of CS1 and CS2 have also been evaluated for 18% and 15% of O_2 (in volume) concentration. In this way, the behavior of the piston under more unfavorable oxidation conditions can be evaluated. In Figure 5-13, the aRoHR (left) and average KL (right) for 21% (green), 18% (red), and 15% (blue) O_2 concentration for CS1 (solid line) and CS2 (dashed line) are shown. Regarding the aRoHR, less energy was obtained for CS2 during the second pilot injection combustion event (around -3° aTDC) at 18% O2. Then, a slightly higher and delayed main combustion peak is obtained for CS2 during the main injection combustion event. This suggests more premixed combustion caused by the lower energy released during the previous phase. When looking at 15% O_2, almost no differences can be observed between both pistons.

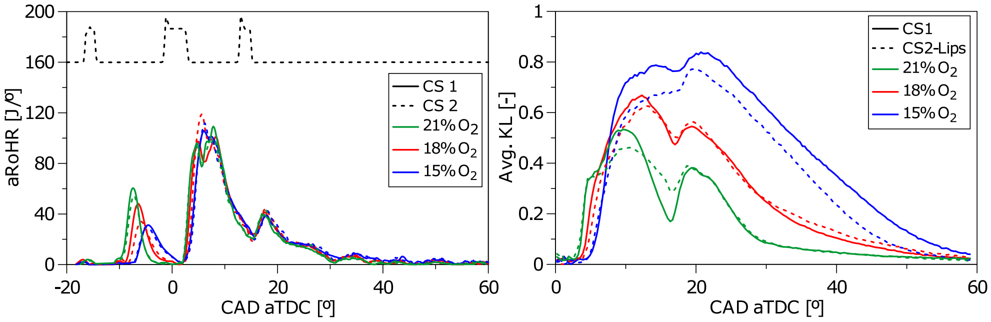

Figure 5-13 aRoHR (left) for CS1 and CS2 and average KL evolution (right) for CS1(solid-line), CS2-Lips (dashed line) at 6.7 bar IMEP and with 21% O_2 (green), 18% O_2 (red), and 15% O_2 (blue) conditions. The dashed line on top of the aRoHR represents the injection strategy for reference.

In addition, the IMEP values obtained for all these tests have been summarized in Table 5-4 where, despite the difference mentioned, a similar performance was obtained with both pistons for the two additional operating conditions.

Table 5-4. IMEP at different O2 concentration test conditions.

Piston	**%O_2 (vol.)**	**IMEP (bar)**
CS1	18/15	6.9/6.7
CS2	18/15	6.7/6.6

Regarding the average KL curves in Figure 5-13, the decrease of oxygen provides a clear KL increasing trend (for both pistons), as expected. With 18% O_2 (red), similar behavior of CS2-Lips with reference to CS1 as with the baseline case is observed. Less soot is formed during the main injection event, while a shy soot reduction is obtained between the main and post-injection combustion. However, the oxygen reduction harms the CS1 geometry during this stage, and the difference with CS2-Lips is clearly reduced. No differences are observed between the geometries during the post-injection combustion (between 18° and 30° aTDC). At the late stages of combustion (after 30° aTDC), higher KL values are reported for CS2-Lips, indicating better late oxidation with CS1.

Nevertheless, this behavior was not observed with 21% O_2. With 15% O_2 (blue), a clear KL reduction is achieved with CS2-Lips compared to the other geometry along the combustion process. More soot is formed in this condition, as shown by the higher KL values reached. Besides, oxidation is slower as the absence of a gap in the KL curve between the main and post-injection combustion events in contrast with higher oxygen concentration operating conditions suggests it. In this scenario, KL values achieved by CS1 are much higher than those of CS2-Lips, which suggests a greater improvement in comparison with CS1 than that observed with more oxygen availability. This indicates that the radial lips of the CS2 form less soot at high EGR conditions, indicating a better use of oxygen inside the combustion chamber. After 25° aTDC, the KL reduction velocity is equivalent for both geometries, indicating that the late oxidation process is similar. This is coherent with the fact that no clear dependences between the geometry and the late oxidation were identified in any of the other operating conditions analyzed.

The radial maps of KL and OH^* chemiluminescence presented in Figure 5-14 allows to identify the differences between 18% and 15% O_2. Regarding KL distribution, the decrease observed at baseline condition between the main and the post-injection combustion events is not visible for the other oxygen concentration conditions, especially for 15% O_2. This is consistent with the average KL evolution shown in Figure 5-14. At the late stages of combustion, the 15% O_2 case shows KL values between 10 mm radius and the periphery of the bowl, indicating a much larger area where soot remains compared to the other two cases with higher oxygen content. The OH^* chemiluminescence decreases with the oxygen content due to the lower oxygen availability to oxidize hydrocarbons and soot during combustion. Therefore, the scale from OH^* maps was reduced by almost an order of magnitude for each concentration evaluated.

Additionally, the spatial distribution of the OH^* signal moves from the bowl periphery to the center of the piston as the oxygen concentration is decreased. This could be related to the fact that a much richer mixture is achieved close to the periphery of the bowl, reducing the reactivity in this region. In the case of 21% O_2, the maximum distance where the oxidation activity appears is around 25 mm of radial distance, while 18% and 15% of

O_2 are 23 mm and 20 mm, respectively. For this reason, the soot that remains at the bowl periphery is not oxidized, which could explain the weaker oxidation reported in Figure 5-13.

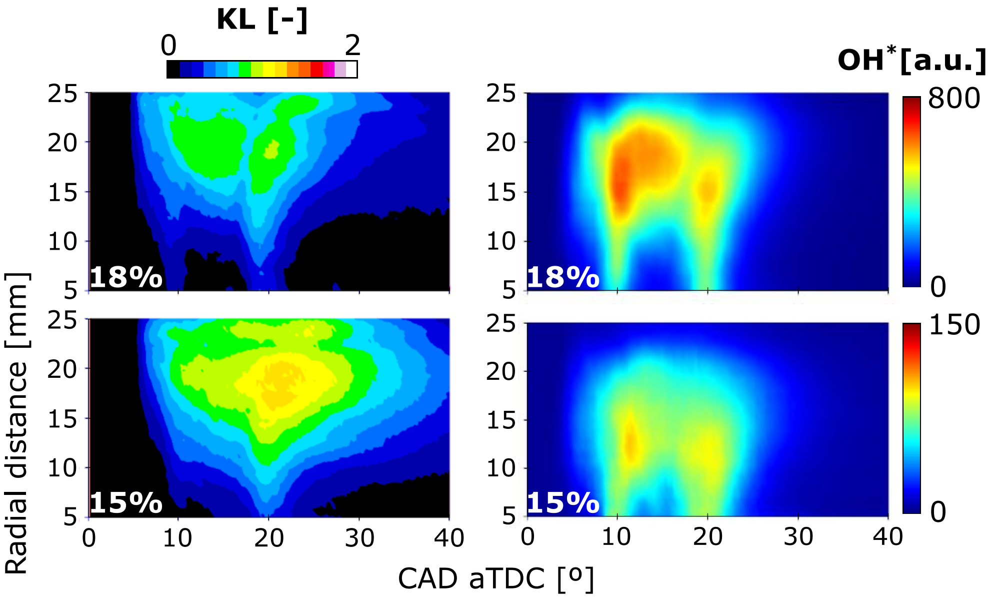

Figure 5-14 KL factor (left) and OH* chemiluminescence (right) radial maps for CS2-Lips at 18% (top) and 15% (bottom) O_2 conditions.

Relative radial maps between CS1 and CS2-Lips are shown in Figure 5-15. At 18% O_2, slight differences between pistons are reported, especially compared to the baseline condition. In this case, CS1 and CS2-Lips are quite similar between the main and post injection combustion events, as no blue or red regions are visible. This is consistent with the gap reduction in KL curves reported in Figure 5-13. In addition, during the late combustion stage (after 25° aTDC), a higher KL cloud for CS2-Lips between 7 mm and 20 mm radius is detected. This is consistent with the higher values in KL curves (red dashed line) reported in Figure 5-13 for this piston. However, this has not been observed in any other operating conditions tested and has not been successfully related to the effect of the different geometry. Furthermore, the difference is even lower than the variability of the measurement at that stage of the combustion process, and, therefore, it is not conclusive.

Remarkable differences are obtained at the lowest oxygen concentration condition compared with others reported in this study. At 15% O_2, a higher KL cloud is detected for CS2-Lips below 20 mm radius during the main injection combustion event and evolves towards the center of the bowl until the start of the post injection combustion. This is represented by the red cloud visible in the relative difference radial map. This behavior confirms that CS2-Lips displaces a higher soot quantity toward the bowl center than CS1. However, according to the results presented in Figure 5-13, considering the whole region, KL values are lower than those of CS1. The higher oxidation activity (OH^* signal) provided by CS2-Lips in this region and the later disappearance of KL confirms the capability of this geometry to improve oxygen usage close to the bowl center and the benefits of using it under very low oxygen concentration. After 20°, the combustion process and soot formation evolve similarly for both pistons. However, the KL spatial distribution is different. While CS1 is mainly located at the periphery of the bowl, CS2-Lips is found between 10 and 20 mm.

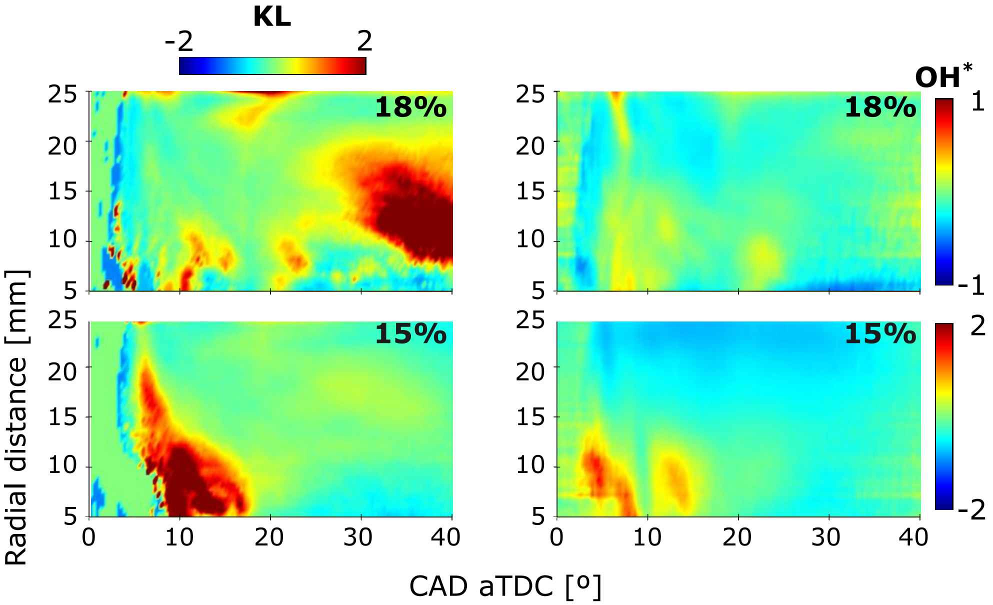

Figure 5-15 KL factor (left) and OH^* (right) relative radial maps at 18% (top) and 15% (bottom) O_2 conditions. Positive values (green to red color) indicate higher values for CS2-Lips, while negative values (green to blue color) indicate higher values for CS1.

5.7 CDS Injector and Radial-Lip Design Interaction

When using the same injection strategy for the STD and the CDS injectors, their different geometry leads to a different amount of fuel injected, resulting in a higher IMEP for the second one. For this reason, the main injection electric pulse (ET_M) was reduced 90 μs for the CDS injector to maintain the same IMEP as the reference for comparing both injectors. However, the dwell time between the main and post-injection (D_3) was kept constant to not increase the time available for soot oxidation between both events, as it was observed that it was a critical process when comparing CS1 and CS2-Lips. At baseline condition (21% O_2), the use of CDS injector has a certain influence on the combustion behavior compared with STD injector. An earlier decrease of aRoHR corresponding to the main injection combustion can be seen in Figure 5-16. Although the injection duration is slightly shorter for the CDS injector, it cannot explain the difference observed. Therefore, other effects related to the CDS concept, like better atomization and air-fuel mixture, are effective. The post-injection combustion event is slightly advanced for the same reason. Despite this, the same IMEP was reached with both injectors, as reported in Table 5-5.

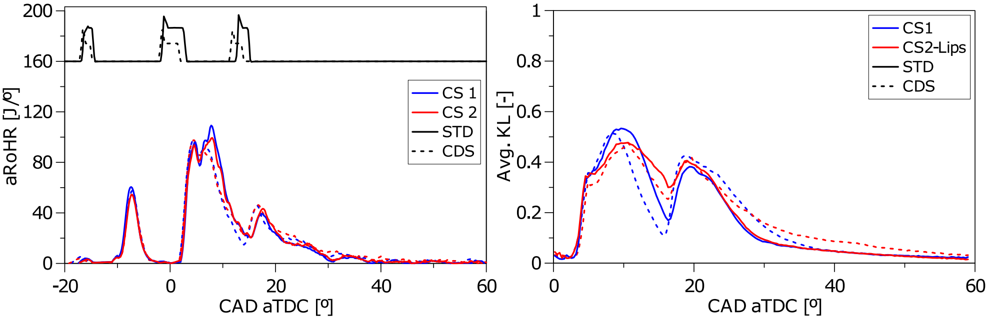

Figure 5-16 Apparent Heat Release Rate (left) and average KL evolution (right) at baseline condition using STD (solid-line) and CDS (dashed-line) injectors for CS1 (blue line) and CS2 (red line). The injection strategy has been included in the upper part of the plot as a reference.

Table 5-5 IMEP at the baseline condition for STD and CDS injectors.

Piston	**Injector**	**%O_2 (vol.)**	**IMEP (bar)**
CS1	STD	21	6.8
	CDS		6.7
CS2	STD	21	6.7
	CDS		6.7

In Figure 5-16, average KL evolution curves are reported using CDS injector at baseline conditions. These results are compared with the previous ones where the STD injector was used. For both combustion systems (CS1 and CS2-Lips), no differences can be appreciated during the main injection combustion between the CDS and STD injectors. When the soot formation slows down (peak of the curve) and the soot oxidation starts to dominate the soot evolution, a different trend is observed for the CDS injector, regardless of the piston used. The KL values decrease earlier with CDS, achieving lower values when compared to the STD (minimum KL). In addition, for CS1 and CS2-Lips, the CDS seems to be also promoting faster soot oxidation since the curve slope is steeper.

In this way, the combination of CDS and radial lips provides lower maximum KL values and earlier and faster soot oxidation during the main combustion event. This is coherent with the aRoHR curves discussed previously, evidencing that the CDS favors the mixing process. Moving forward, an opposite trend can be observed when the post-injection occurs. The CDS injector starts the post-injection combustion from lower KL values than STD, but it reaches slightly higher values when the curve achieves the maximum KL. In addition, the oxidation phase of the post-injection combustion is also slowed down when using the CDS, a completely different behavior compared with the main combustion. This is mainly because the post-injection duration was kept the same for both injectors, not being corrected for the CDS as was done during the main injection. It means more fuel mass is injected with this hardware during the post-injection, promoting higher soot formation in this phase. As this extra soot mass is formed when in-cylinder pressure and temperature decrease (late combustion phase), its oxidation process is also more difficult and slower. This is also observed in the aRoHR, which at the late stages shows slightly higher values than those of STD, corresponding with a longer oxidation activity.

5.8 Summary and Conclusions

The current study aimed to analyze two pistons with different radial-lip geometries, trying to identify the differences in terms of the combustion process and soot formation by employing an optical engine based on a compression ignition engine. Different operating conditions (P_{inj}, SOE, % O_2) and engine loads were evaluated. Furthermore, two different injector systems were used to study the combined effect. To achieve this, in-cylinder soot formation was analyzed through the 2C-pyrometry KL factor and high-speed OH* chemiluminescence images as a tracer of the oxidation reactions inside the piston. The main results are summarized below:

- The results showed that both combustion systems tested (CS1 and CS2-Lips) can promote the flame movement from the periphery towards the bowl center, allowing the flame to achieve regions where fresh oxygen is available. However, the analysis confirmed the CS2-Lips, which has a more pronounced radial lip profile, drives the flames closer to the bowl center than the CS1 design. This factor makes the oxidation process faster and reduces soot formation.

- At lower engine loads, the in-cylinder soot formation was reduced in CS2-Lips compared to CS1. It was a common behavior observed at all the operating conditions evaluated, which confirms that the radial lips of CS2 are more effective in reducing soot formation. This is coherent with the higher flame redirecting effect that was also reported.

- At higher engine load, the effect of the CS2-Lips is more noticeable, especially under unfavorable operating conditions such as low oxygen concentration. At baseline conditions (21% O_2), clear differences were observed during the main injection combustion and before the post-injection combustion. CS2-Lips forms less soot than CS1 during the main injection combustion. However, this geometry oxidation between main and post-injection combustion is poorer. After the post-injection combustion event, no differences arise between these two pistons indicating that the geometry of the radial lips does not seem to affect the late oxidation process. When increasing the EGR ratio from 21% O_2 (no-EGR) to 15% O_2, the differences between CS1 and CS2-Lips are more prominent. The CS2-Lips proved to work better than CS1 under deficient oxygen concentration (15% O_2), providing much lower soot formation.

- Regarding the injector nozzles, certain differences were observed between CDS and STD injectors regarding combustion behavior. The aRoHR showed faster combustion during the main injection for the CDS with respect to the STD. This impacted soot formation and oxidation, similar to both piston geometries. Besides, at the late stages of combustion, the injection strategy leads to longer combustion and slower final oxidation for both pistons. Therefore, a relation between the CDS injector and the radial-lip design was not identified.

In summary, the effectiveness of the radial-lip concept was confirmed by the results obtained under different engine conditions. The more pronounced lips provide an improvement of the recirculation effect as well as the reduction of the flame-to-flame interaction while promoting the use of in-cylinder oxygen. However, its effect on soot formation was more appreciable at operating conditions under low oxygen scenarios, higher loads or during the main injection combustion event, where the need of oxygen is higher.

The results obtained in this Thesis Chapter allowed to *identify the relevance of some particular aspects of piston geometry on mixture formation, combustion development, and soot formation under engine conditions*, as the second thesis objective mentioned in Chapter 1. These results could help characterize and better understand how unconventional piston geometry affects the combustion behavior in larger engines, thus filling in gaps in the literature.

These benefits are clear when using conventional diesel fuel, but how does this piston geometry affect when diesel is replaced by other fuel such as OME_X? The literature and the results discussed in Chapter 4 push the use of OME_X as a good candidate for use in CI engines. The OME_X is blended with diesel as a friendly method to use inside the current engine infrastructure. However, these blends make to consider the soot formation contribution due to the presence of diesel, as discussed in Lewiski thesis [1] in a light-duty optical engine. In this way, the results obtained in this chapter open the door to reducing the soot formation using these blends using unconventional piston geometries in a medium-duty engine. This will be discussed in the following Chapter.

Bibliography

[1] Lewiski F. Analysis of the combustion process and soot formation in a single cylinder optical engine fueled with e-fuels and using different piston geometries. Universitat Politècnica de València, 2021. https://doi.org/10.4995/Thesis/10251/180351.

[2] Pastor J V, Micó C, Lewiski F, Tejada FJ, Vassallo A. Innovative diesel piston geometries for soot emissions reduction and cleaner combustion : An optical investigation. Thiesel 2022 Conference on Thermo-and Fluid Dynamics of Clean Propulsion Powerplants 2022.

[3] Pastor J V., Micó C, Lewiski F, Tejada FJ, Vassallo A, Pesce FC, et al. Influence of the radial-lip concept design to achieve ultra-low soot emission reductions: An optical analysis. Fuel 2023;345:128161. https://doi.org/10.1016/J.FUEL.2023.128161.

[4] Di Blasio G, Ianniello R, Beatrice C, Pesce FC, Vassallo A, Belgiorno G. Experimental Investigation on an Innovative Additive ManufacturingEnabled Diesel Piston Design to improve Engine-out Emissions and Thermal Efficiency beyond Euro6. THIESEL 2020 Conference on Thermo- and Fluid Dynamic Processes in Direct Injection Engines 2020.

[5] Millo F, Piano A, Roggio S, Bianco A, Pesce FC, Vassallo AL. Numerical Assessment of Additive Manufacturing-Enabled Innovative Piston Bowl Design for a Light-Duty Diesel Engine Achieving Ultra-Low Engine-Out Soot Emissions. SAE Int J Engines 2021;15:3–15. https://doi.org/10.4271/03-15-03-0022.

[6] Serizawa K, Ueda D, Mikami N, Tomida Y, Weber J. Realizing Robust Combustion with High Response Diesel Injector with Controlled Diffusive Spray Nozzle and Closed Loop Injection Control. SAE Technical Papers 2017;2017-March. https://doi.org/10.4271/2017-01-0845.

[7] Payri R, De La Morena J, Monsalve-Serrano J, Pesce FC, Vassallo A. Impact of counter-bore nozzle on the combustion process and exhaust emissions for light-duty diesel engine application. International Journal of Engine Research 2018;20:46–57. https://doi.org/10.1177/1468087418819250.

[8] Payri R, Hardy G, Gimeno J, Bautista A. Analysis of counterbore effect in five diesel common rail injectors. Exp Therm Fluid Sci 2019;107:69–78. https://doi.org/10.1016/J.EXPTHERMFLUSCI.2019.05.008.

[9] Thorlabs, Inc. - Your Source for Fiber Optics, Laser Diodes, Optical Instrumentation and Polarization Measurement & Control n.d. https://www.thorlabs.com/ (accessed August 31, 2023).

Chapter 6

Synergy of OME$_X$ and Piston Geometry to achieve Low Soot Formation

Content

6.1 Introduction

In Chapter 4, the flame structure of two e-fuels, OME_X and OME_1, has been studied under Spray A and Spray D ECN reference conditions in a HPHT facility. The Spray A condition, as a light-duty engine reference due to the nozzle orifice size, is considered the most robust condition within the ECN due to the large amount of information it contains. However, the Spray D condition needs to enlarge its database as a medium and heavy-duty engine reference. The results showed the absence of soot precursors, consistent with the literature discussed in Chapter 2, making them very interesting as a replacement for conventional diesel.

Chapter 5 analyzed the effect of an unconventional piston geometry on the formation of soot inside the cylinder using diesel in a medium-duty optical engine. The radial lips geometry at the edges of the bowl plays a very important role in the movement of the flame once it impacts the bowl wall, avoiding direct flame-to-flame interaction while directing the flame towards the center of the bowl where fresh oxygen is available to oxidize the soot. Therefore, two different radial lips geometries were analyzed to characterize this geometry further. The study included a range of operating conditions, but the benefit of the radial lip was most notable under conditions of high soot formation (high engine load and low oxygen percentage in the cylinder).

Despite these results, it is necessary to continue delving into the characterization of these fuels and piston geometry. As mentioned in this thesis, the fuels studied in Chapter 4 show certain incompatibilities with the engine infrastructure, so the literature suggests using blends with diesel to address these issues. Using these blends means that, although these e-fuel potential remains visible, the presence of diesel involves soot formation.

In this way, the piston geometry can significantly help reduce soot formation. However, no studies have analyzed how is the interaction between the piston geometry and OME_X. Therefore, this final chapter of the thesis evaluates soot formation in the same optical engine as in Chapter 5, using a conventional piston geometry with several OME_X/diesel blends. Subsequently, the results will be compared using a radial lips geometry (CS1) for the same fuels.

The results explored in this chapter have been published in a scientific journal [1].

6.2 Operating Conditions

Two different bowl designs were employed in this investigation: a conventional piston and radial-lips piston, named CS3 and CS1, respectively, in this thesis. Both pistons provide the same compression ratio, guaranteeing the same in-cylinder ambient conditions, allowing a direct comparison between them. Regarding the injection system, the injector used is the CDS injector.

All the tests were performed at an engine speed of 1400 rpm, reaching 6.7 bar of IMEP. For each piston geometry, three fuels were investigated: pure diesel (0 Ox), a blend of 70% diesel and 30% OME_X by mass (30 Ox), and a mixture of 50% diesel and 50% OME_X by mass (50 Ox). The different percentages used in this study have shown good miscibility in previous studies [2]. Two different oxygen concentrations in the combustion chamber were tested for each fuel: 21% and 15%. The 15% of oxygen simulated the optical engine operating under EGR conditions. A total of 12 different operating points were investigated. The engine operating conditions selected correspond to the high engine load (HEL) baseline operating condition used in Chapter 5 but using the CDS injector. All operating points are summarized in Table 6-1.

All information about pistons, CDS injector, and fuels used in this Chapter is explained in Chapter 3.

Table 6-1 Engine operating conditions.

Fuel	**IMEP (bar)**	**Engine Speed (rpm)**	**P_{int} (bar)**	**P_{exh} (bar)**	**T_{int} (°C)**	**P_{inj} (bar)**	**SOE (°aTDC)**	**O_2 (%)**	**Injector**
0Ox	6.7	1400	1.34	1.54	55	1182	-33.7	21/15	CDS
30Ox	6.7	1400	1.34	1.54	55	1182	-33.7	21/15	CDS
50Ox	6.7	1400	1.34	1.54	55	1182	-33.7	21/15	CDS

The injection strategy is the same used in Chapter 5 for the case of 6.7 bar IMEP. However, the additions of OME_X, make it necessary to adjust the main injection pulse in order to keep the same energy released between fuels (@21% O_2), compensating the lower OME_X lower heating value (LHV). The dwell time between the end of the main injection and the start of the post injection was kept constant by appropriately shifting the start of the post injection. Figure 6-1 shows the electric injection signals adopted for each fuel and the duration in µs of the main injection.

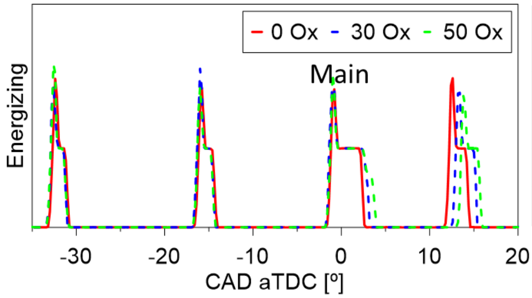

Adjust injection strategy	
Fuel	**t_{main} [us]**
0 Ox	450
30 Ox	560
50 Ox	620

Figure 6-1 Details on fuel injection strategy.

6.3 Optical Arrangement

This study used 2-color pyrometry (2C) and OH^* high-speed imaging to analyze the evolution of soot formation and oxidation processes in the combustion chamber, as in Chapter 5. In this way, the same optical setup described in the previous chapter was used in this study (for more information, see Chapter 5). It is important to remember that the same start of energizing (SOE) electric pulse used for the injector serves as a trigger for all the cameras. Thus, time-synchronized images from all cameras are obtained. This allows a direct comparison between the frames of each camera.

6.3.1 OH^* chemiluminescence imaging

It comprises a high-speed CMOS camera (Photron SA5) coupled with a high-speed intensifier (Hamamatsu C10880-03F) with 1:1 relay optics. The intensifier photocathode is a multialkali (S-20), which allows detection from UV to near infrared radiation (spectral response: 185-900 nm). An UV-Nikor Rayfact is used as a lens with a focal length of 105 mm and a maximum f-aperture of 4.5. In addition, a narrowband interference filter with a central wavelength at 310 nm with a full width at half maximum (FWHM) of 10 nm was coupled with the camera lens to collect the radiation from the OH^* peak emission and avoid other radiation sources. The acquisition rate was set at 25 kfps with a resolution of 4.4 pixels/mm. The gating of the intensifier was set to the same exposure time value as the high-speed camera, which is 39.75 µs. The intensifier gain ranges from 600 (minimum gain) to 999 (maximum gain). In this study, the gain used was 900.

6.3.2 2-Color pyrometry

The setup is composed of two identical high-speed cameras (Photron NOVA S9) coupled with different bandpass color filters. One of the cameras is equipped with a filter centered at 660 nm (10 nm FWHM), while the other has a filter centered at 560 nm (10 nm FWHM). The exposure time for each camera, and also for each operating condition, was chosen in order to make the most of the dynamic range of the camera: 0.5 µs (660 nm camera) and 5 µs (560 nm camera) at 21% O_2, and 0.7 µs (660 nm camera) and 20 µs (560 nm camera) at 15% O_2. Furthermore, both cameras were coupled with a Karl-Zeiss Makroplanar lens with a 100 mm focal length and a maximum f-aperture of 2. The frame rate was fixed at 25 kfps, corresponding to the same frame rate used for the OH^* chemiluminescence imaging, with a resolution of 4.6 pixels/mm.

6.4 Image Processing

The methodology used in processing and presenting the images in this thesis chapter is the same as in the previous chapter. An average of the OH^* radiation and KL values from 10 combustion cycles has been taken. The analysis will be conducted through spatial distribution images within the combustion chamber and with temporal evolution curves of KL. Additionally, the radial map will analyze the spatial and temporal evolution of KL and OH^*. The pistons used are symmetrical, without presenting two different geometries in the bowl (see Chapter 3), so the analysis will be carried out for the entire bowl without differentiating two zones within it, as was done in the previous chapter with the CS2.

6.5 Combustion evolution of OME_X/diesel blends

As reported in the scientific literature [3], using OME_X improves the reduction of in-cylinder soot formation during the combustion process. Furthermore, the velocity of the combustion event increases, reducing its duration when using this fuel [4]. OME_X/diesel blends are considered to be used in the current vehicle fleet to overcome incompatibilities of OME_X with the engine infrastructure and its low LHV. However, using diesel in the blend promotes soot formation, especially when using EGR strategies necessary for NO_X reduction. The study carried out in the previous chapter has shown the benefits of using non-conventional piston geometries to reduce soot formation. This way, it is important to identify the behavior using OME_X/diesel blends to deepen their characterization. For this purpose, this results section analyses the combustion behavior and soot evolution using two piston geometries: Conventional (CS3) and Radial-Lips (CS1) pistons.

6.5.1 Conventional Piston (CS3)

The first part of the analysis aims to describe the behavior of the different blends and the benefits of increasing OME_X content with the convention piston (CS3). The upper part of Figure 6-2 shows the distribution of KL values at different CADs for three different OME_X percentages in the fuel: 0 Ox (top), 30 Ox (middle), and 50 Ox (bottom), at 21% O_2 to illustrate the temporal evolution during the combustion process inside the combustion chamber. The bottom part of the figure shows the aRoHR profiles and the average KL curves for the selected fuels from the top dead center (TDC) to 28 CAD aTDC. As color rectangles, the aRoHR plots highlight the duration of the main and post injections (retrieved from high-speed images).

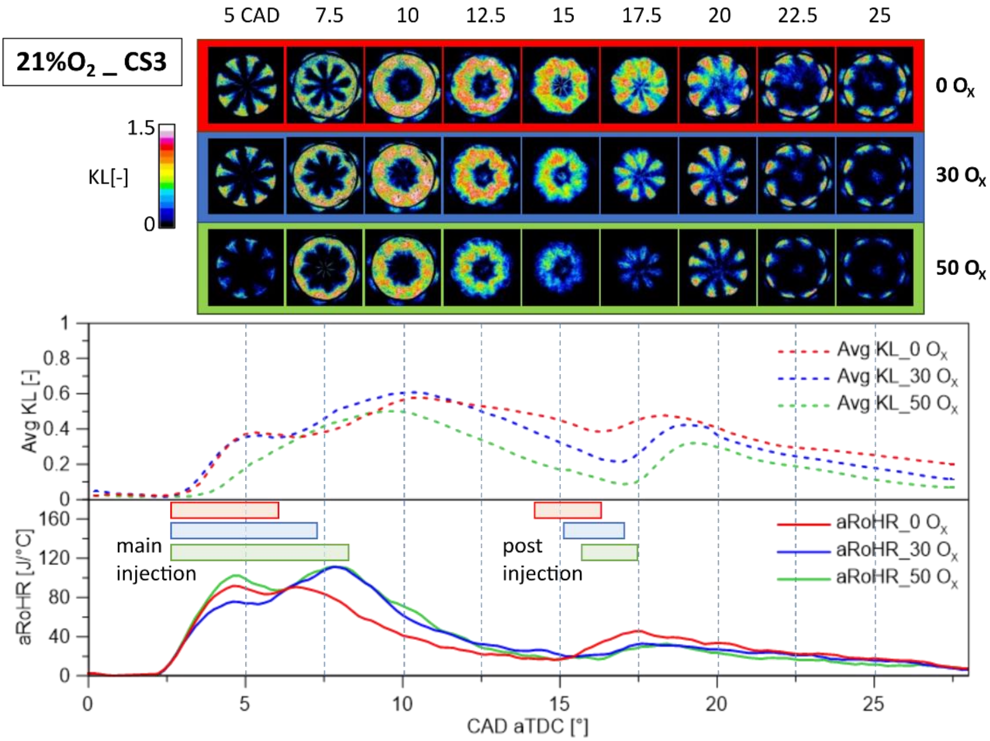

Figure 6-2 KL factor imaging evolution, average KL and aRoHR for 0 Ox, 30 Ox, and 50 Ox at 21% O_2. The results correspond to the average of 10 combustion cycles.

The main injection starts at ~2.5 CAD aTDC, and, as stated previously, its duration depends on the OME_X percentage in the blend (see Figure 6-1). During the main injection (frame@5 CAD), producing soot for identifying a diffusive flame's characteristic structure. A few CADs later, the sprays impinge on the piston bowl wall, and the burning jets start to expand tangentially, interacting between them and merging, forming a crown. For 50 Ox the liquid fuel sprays are still visible around the nozzle at 7.5 CAD aTDC, because of the longer injection duration than 0 Ox and 30 Ox. For all mixtures, at this stage, the soot production is more relevant than the oxidation process (increase in area and intensity) until around 10 CAD aTDC. After this instant, the reduction in intensity and area of the KL distribution indicates that the soot oxidation processes dominate overproduction.

The peak of aRoHR corresponding to the main injection shows a clearer staged combustion when increasing the OME_X percentage in the blend. The first stage, which corresponds to the first peak, is the premixed combustion phase. The second stage, which corresponds to the diffusive combustion stage, is more intense for 30 Ox and 50 Ox due to the longer duration of the main injection when increasing OME_X content. When the post injection starts, the KL curve for 30 Ox and 50 Ox suggest that a big part of the soot produced has already been oxidized. Therefore, the expected benefits of post injection (increasing late oxidation) [5] are not so evident.

In contrast, a significant increase of soot is observed. However, with Diesel, the KL curve suggests higher levels of soot at this stage. In this scenario, the contribution of pilot injection has more potential to improve oxidation, and it causes a smaller increase in the KL curve. However, the soot remaining from the main injection combustion event is added to the soot produced during the post injection combustion event, resulting in higher soot levels than the other blends. The fact that the post injection peak of aRoHR is reduced when increasing OME_X percentage in the blend indicates that the oxygenated fuel allowed a complete main injection combustion resulting in less fuel partially or not oxidized.

With all discussed above, a clear in-cylinder soot reduction and faster combustion event are reported when increasing the quantity of OME_X in the fuel, consistent with what can be found in the literature. Thanks to this, the use of OME_X seems promising to maintain low levels of soot formation when applying other strategies to reduce the temperature chamber (like EGR), with the aim of reducing the NO_X formation. It is essential to consider that this strategy increases the soot formation due to the reduction of fresh oxygen inside the cylinder, leading to the well-known soot-NO_X trade-off.

To evaluate this, EGR was simulated by reducing the oxygen concentration at the intake up to 15%. A comparison of KL distribution inside the combustion chamber, the KL evolution curves, and the aRoHR for 50 Ox at 21% O_2 and 15% O_2 are shown in Figure 6-3. At the first CAD represented in this figure, for 15% O_2, no KL values can be observed due to the later start of combustion typical of EGR conditions [6]. This is consistent with the aRoHR shown. Until 10 CAD, approximately, lower KL values and a smaller area can be observed for 15% compared to 21% O_2. After that, the trend is reversed. When the post injection takes place (~15 CAD), the 21% O_2 case shows much lower KL values with respect to the 15% O_2 case. This highlights the difficulty of this operating condition to oxidize soot. Besides, it confirms that ambient oxygen is important for the oxidation and the reduction of soot levels inside the cylinder, even using 50% OME_X in the fuel.

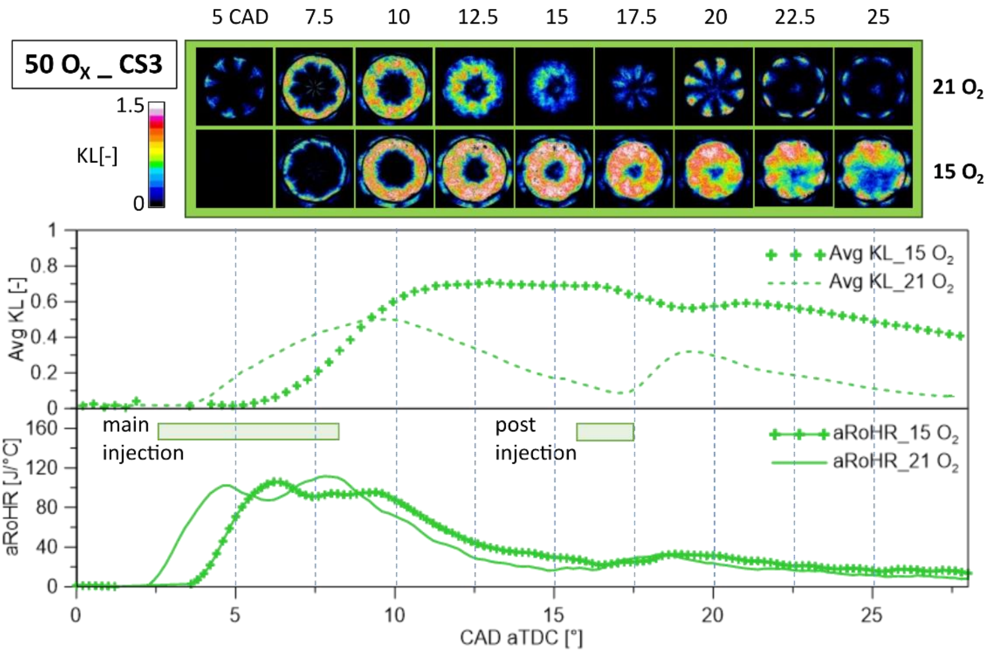

Figure 6-3 KL factor imaging evolution, KL evolution curves, and aRoHR for 50% Ox in fuel at 21% O_2 and 15% O_2. The results correspond to the average of 10 combustion cycles.

The reduction of oxygen concentration has a similar effect over all the fuels considered in this study. In summary, the KL evolution curves for all fuels are reported in Figure 6-4 for 21% and 15% O_2. The different curves show that even 50 Ox at 15% O_2 forms more soot than any other blends at 21% O_2.

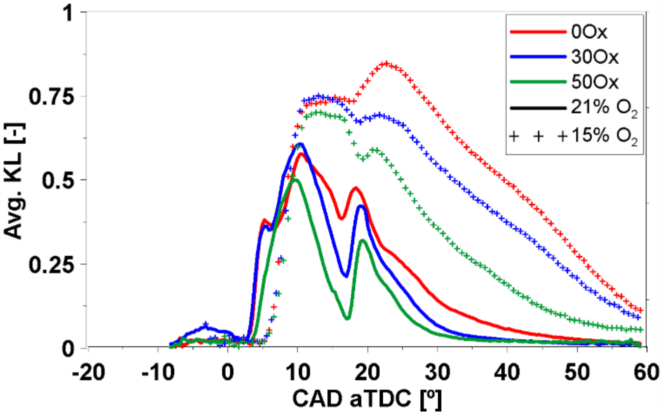

Figure 6-4 KL evolution curves using 0 Ox, 30 Ox, and 50 Ox in the fuel at 21% O_2 and 15% O_2.

The results show that the O_2 contained in the molecule of OME_X is insufficient at high EGR conditions to keep the same soot levels as without EGR. The use of neat OME_X would indeed be able to improve the soot reduction further. However, the incompatibility with elements of the injection system [7] and the increased fuel injected to achieve the same energy released by the fuel make that not a good option to consider. For these reasons, it is necessary to implement additional strategies to improve soot reduction without increasing OME_X content in the fuel.

6.5.2 Radial-Lips Piston (CS1)

As previously discussed, this study tested a second bowl geometry (CS1) containing a stepped lip and radial lips at the bowl edge.

KL distribution and the KL/OH^* radial maps are presented in Figure 6-5 and Figure 6-6, respectively, to show the temporal and spatial evolution for both pistons using 50 Ox at 15% O_2. The first thing that can be observed is a different aRoHR evolution. The CS1 provides a faster ignition and a much more intense heat release than the CS3. This is relevant as it compensates the delay caused by the oxygen reduction that was previously mentioned. Regarding soot production, it can be clearly seen that higher KL values are reported for the CS3 during the whole combustion event. The first KL values appear close to the bowl periphery at 7.5 CAD, probably due to the flame-to-flame interaction after impacting the bowl wall, as seen in Figure 6-7. After this, the high KL cloud evolves toward the center of the bowl until 20 CAD (before the post injection combustion). The movement of the KL cloud and OH^* reactions can be seen clearly in radial maps (left images from Figure 6-6). During the same interval, the low values of OH^* in the radial map confirm the soot is hardly oxidized, resulting in the high KL cloud mentioned previously. The lack of oxygen available due to its low concentration difficulties the soot cloud oxidation, even for this blend.

In contrast, the CS1 shows several differences, which lead to lower KL values. The first KL values also appear at the bowl periphery and evolve toward the center of the bowl, as in the CS3 case. However, the intensity of KL values is significantly lower for this piston, and the OH^* radial map (see the right image from Figure 6-6) confirms a higher oxidation activity from the periphery to a 15 mm radius during the main injection combustion event. This suggests that less soot is formed, but it is also significantly oxidized before the beginning of the post injection combustion event, as seen in Figure 6-5 at 17.5 CAD. This fact is also visible in the KL radial map of Figure 6-6. Here, two different KL clouds separated by a dark gap around 20 CAD can be observed, indicating that the oxidation process during the main injection combustion event is sufficient to oxidize a big part of the soot formed. The results show that radial lip geometry improves the use of low oxygen concentration inside the combustion chamber to oxidize the in-cylinder soot formation compared to the conventional piston.

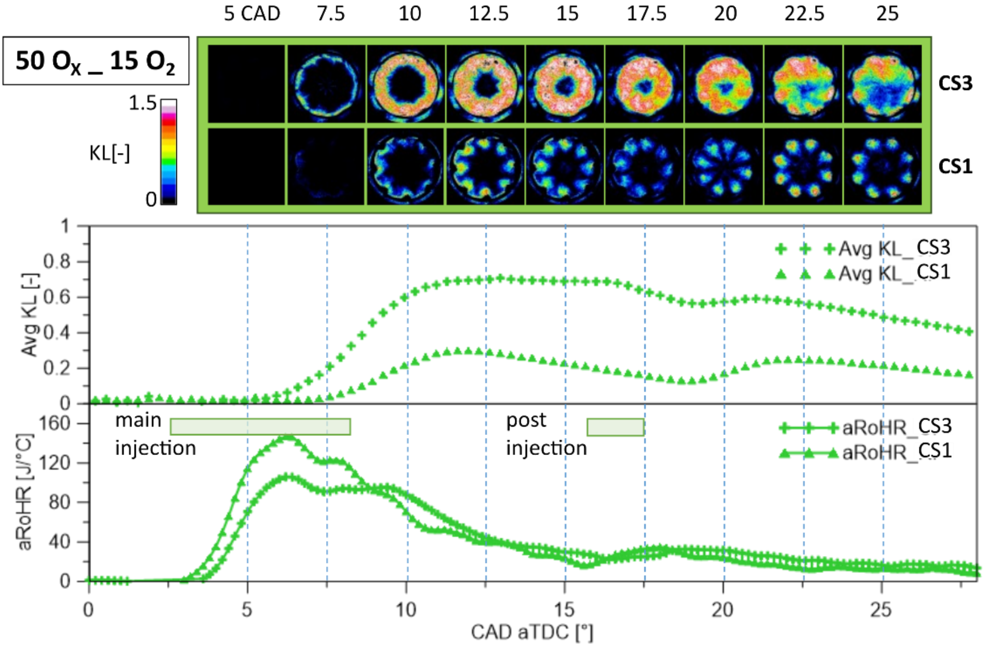

Figure 6-5 KL factor imaging evolution, KL evolution curves, and aRoHR for 50 Ox at 15% O_2 using conventional (CS3) and radial lips (CS1) pistons. The results correspond to the average of 10 combustion cycles.

From the sequence of images shown in Figure 6-5, it is possible to see that, in contrast with CS3, the CS1 geometry reduces the interaction between flames at the periphery of the flame. As represented in Figure 6-7, the presence of radial lips prevents the flames from spreading tangentially, creating a backward movement instead. This reduces the flame-to-flame interaction, reducing the formation of high equivalence ratio regions and promoting the use of fresh oxygen close to the center of the bowl, as described in Chapter 5 and in agreement with Lewiski [8]. In addition, the stepped lip improves the oxidation of part of the fuel at the squish region compared to the CS3 geometry [9].

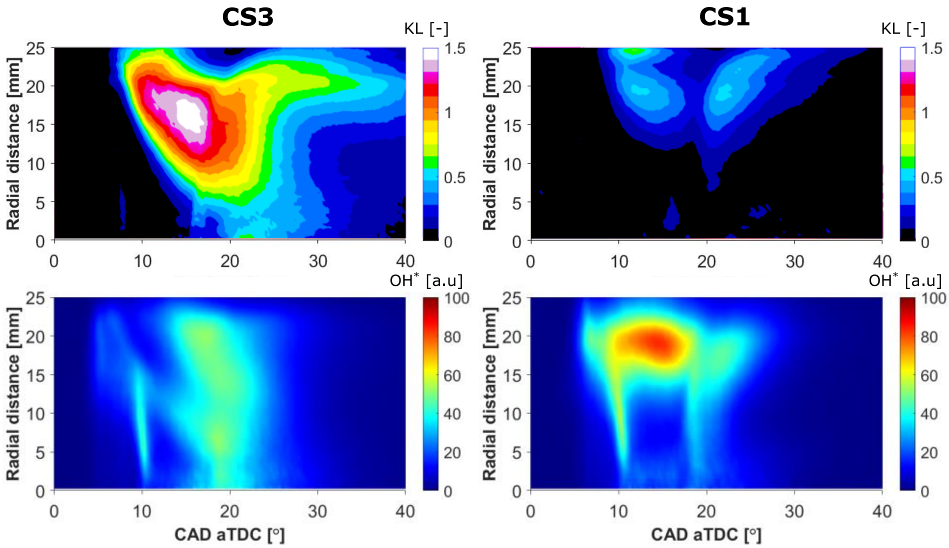

Figure 6-6 KL (top) and OH* (bottom) radial maps using conventional (left) and radial (right) pistons at 50 Ox and 15% O_2.

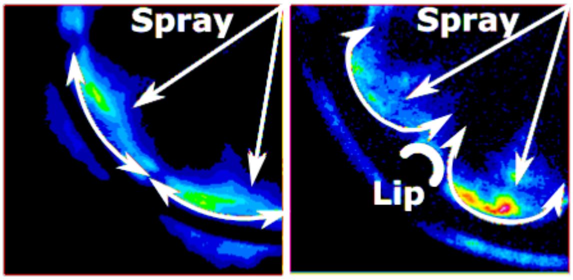

Figure 6-7 Flame distribution due to CS3 (left) and CS1 (right) pistons.

To summarize the performance of the CS1 in combination with the fuel, KL evolution curves for all fuels tested in this study at two oxygen concentrations (21% and 15%) are reported in Figure 6-8. The results show the same behavior discussed previously for all the cases. The CS1 reduces soot formation and improves its oxidation during the whole combustion event, independently of the oxygen concentration. However, its effect is more prominent at 15% O_2. This indicates that CS1 is more effective than CS3 under low oxygen concentrations, which agrees with the previous study in Chapter 5. To quantify the reduction in terms of KL achieved with CS1 for each fuel, the relative decrease of KL values at 15% O2 has been calculated according to equation (6-1):

$$Rel.\ KL = \frac{Avg.KL_{CS3} - Avg.KL_{CS1}}{Avg.KL_{CS3}} \quad (6\text{-}1)$$

The Rel. KL evolution for the three fuels considered in this study is shown in Figure 6-9. Between 0 and 20 CAD aTDC, the KL reduction achieved with the CS1 with 0 Ox varies from 10% to 45%. In the same interval, a much higher reduction is achieved when increased the OME_X content in the blend. For 30 Ox, it varies between 40% and 75%, while for 50 Ox, it reaches from 30% to 80%, depending on the combustion stage. During the late stages of combustion, the KL reduction using the CS1 is 17%, 70%, and 70% for 0 Ox, 30 Ox, and 50 Ox, respectively. Therefore, the trend shows a clear improvement in terms of soot reduction when combining the radial-lips design with OME_X content in the fuel, especially at low ambient oxygen concentrations, which are representative of low NO_X operating conditions. When comparing 21% and 15% O_2, it is possible to see that the CS1 is able to keep the same KL values with 30 Ox and 50 Ox. The level reached with both oxygen concentrations is similar when looking at the two peaks. However, when looking at the interval between peaks and the late oxidation stage, it is possible to see that KL decreases much faster with 21% O_2. This behavior suggests that with CS1, the fuel's oxygen substantially impacts the soot formation (and the maximum KL reached). In contrast, the ambient oxygen controls the oxidation (and the velocity with which the KL decreases). However, this is not observable with 0 Ox.

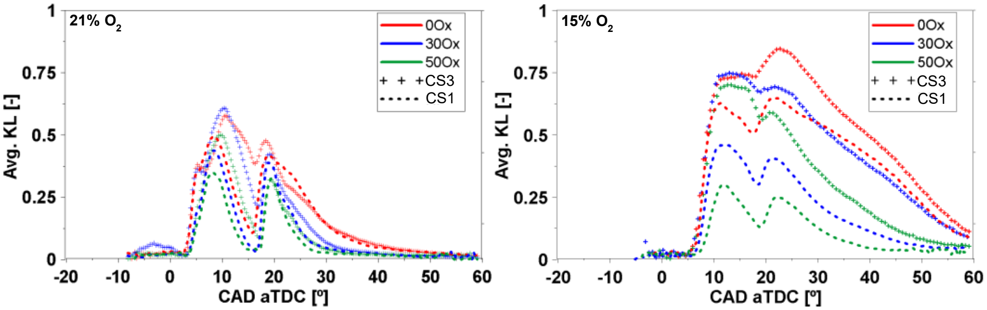

Figure 6-8 KL evolution curves using 0 Ox, 30 Ox, and 50 Ox in the fuel at 21% O_2 (left) and 15% O_2 (right) for CS3 and CS1 pistons.

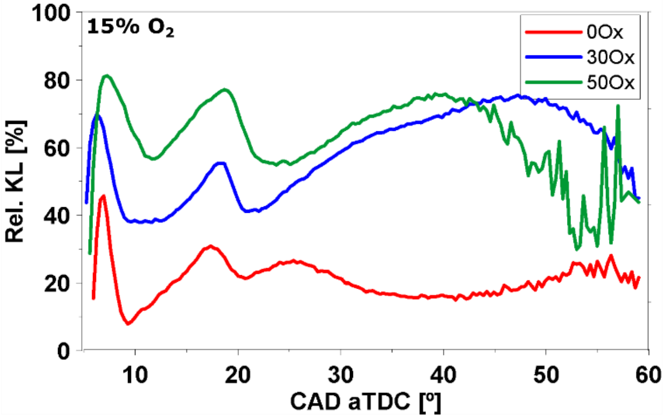

Figure 6-9 KL values reduction percentage using CS1 piston compared to CS3 piston for all fuels at 15% O_2.

To summarize the differences between both piston geometries in combination with all fuels tested, the area below the KL evolution curves from Figure 6-8 is plotted in Figure 6-10. The aim is to represent the accumulation of KL reached along the combustion process. The curves corresponding to CS3 at 21% O_2 for all fuels are plotted with solid lines for reference. The 15% O_2 cases show a higher accumulation of KL when using CS3 compared to the CS1 one. The use of this piston achieves a reduction of 37%, 70%, and 78% using 0%, 30%, and 50% of OME_X in the fuel, respectively. It is true that without OME_X in the fuel (0 Ox), the CS3 (red-solid line) reaches a 48% lower value for 21% O_2 than CS1 at the lowest oxygen concentration condition using the same fuel (red-dashed line). However, when combined with OME_X in the blend, the CS1 achieves similar values as the cases using the CS3 at 21% O_2. Even with 50 Ox, the values reported are below the ones corresponding to the reference case. On the one hand, this indicates that using only the piston geometry with low oxygen concentration conditions inside the combustion chamber is insufficient to achieve or improve the soot levels significantly compared to using a CS3 geometry with no EGR. On the other hand, it confirms a synergy when combining oxygenated fuels (blended with diesel) with the CS1 geometry, as the effect of reducing ambient oxygen concentration over soot is almost negligible.

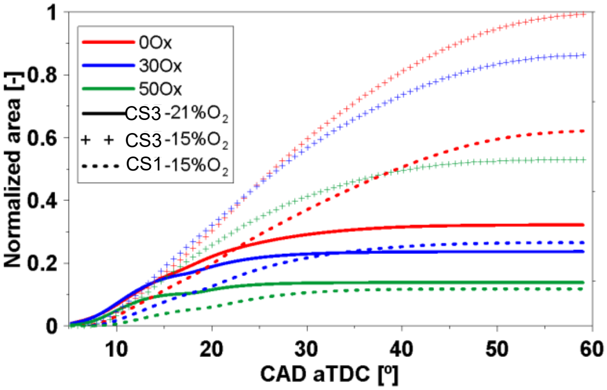

Figure 6-10 Normalized average KL closed curves area.

6.6 Summary and Conclusions

The main results of this study are summarized below in bullet points.

Regarding the conventional piston:

- At no-EGR condition (21% O_2), the reduction of KL is more prominent when increasing the OMEX quantity in the blend, which agrees with what can be found in the literature.

- The OME_X content in the blend reduces the amount of soot formed, even at 15% O_2. However, results confirm that only OME_X (up to 50%) is insufficient to avoid the increase because of the reduction of ambient oxygen.

Regarding the radial-lips piston:

- The avoidance of flame-to-flame interaction achieved by the radial-lips feature results in lower soot formation close to the bowl wall. In addition, the redirection of flames toward the center of the piston takes advantage of the oxygen available and significantly improves soot oxidation.

- The addition of OME_X improves the radial-lips piston geometry benefits. In the most unfavorable condition (15% O_2), the addition of OME_X can extend the KL reduction achieved by the novel piston geometry from 17% (0 Ox) up to 70% (50 Ox) during the late stage of combustion.

- Results show that 30% and 50% OME_X in the blend, in combination with the radial-lips piston, can provide similar soot levels with 15% and 21% O_2. This confirms the potential of this combined solution to reduce soot levels when using EGR significantly.

The reported synergy between OME_X and the radial-lips concept represents a promising solution to mitigate the existing soot-NO_X trade-off-. It opens a path to using temperature reduction strategies like EGR to minimize NO_X formation without compromising soot emissions.

These findings address the third main objective of this thesis, mentioned in Chapter 1, through the analyses of the combustion behavior using OME_X-diesel blends (0%, 30%, and 50%) in combination with a novel radial-lips piston geometry under high EGR rate condition (15% O_2). These results have deepened the understanding of the combustion process of OME_X/diesel blends in larger engines, filling some of the gaps in the literature.

Bibliography

[1] Pastor J V., Micó C, Lewiski F, Tejada FJ, Tornatore C. A Synergic Application of High-Oxygenated E-Fuels and New Bowl Designs for Low Soot Emissions: An Optical Analysis. Applied Sciences 2023;13:8560. https://doi.org/10.3390/app13148560.

[2] García A, Gil A, Monsalve-Serrano J, Lago Sari R. OMEx-diesel blends as high reactivity fuel for ultra-low NOx and soot emissions in the dual-mode dual-fuel combustion strategy. Fuel 2020;275:117898. https://doi.org/10.1016/j.fuel.2020.117898.

[3] Pastor J V., García A, Micó C, Lewiski F. Simultaneous high-speed spectroscopy and 2-color pyrometry analysis in an optical compression ignition engine fueled with OMEX-diesel blends. Combust Flame 2021;230:111437. https://doi.org/10.1016/j.combustflame.2021.111437.

[4] García-Oliver JM, Novella R, Micó C, De Leon-Ceriani D. Numerical analysis of the combustion process of oxymethylene ethers as low-carbon fuels for compression ignition engines. International Journal of Engine Research 2022. https://doi.org/10.1177/14680874221113749/ASSET/IMAGES/LARGE/10.1177_14680874221113749-FIG13.JPEG.

[5] Farhan SM, Wang P. Post-injection strategies for performance improvement and emissions reduction in DI diesel engines—A review. Fuel Processing Technology 2022;228. https://doi.org/10.1016/j.fuproc.2021.107145.

[6] Idicheria CA, Pickett LM. Ignition, soot formation, and end-of-combustion transients in diesel combustion under high-EGR conditions. International Journal of Engine Research 2011;12:376–92. https://doi.org/10.1177/1468087411399505.

[7] Bhatelia T, Lee WJ, Samanta C, Patel J, Bordoloi A. Processes for the production of oxymethylene ethers: promising synthetic diesel additives. Asia-Pacific Journal of Chemical Engineering 2017;12:827–37. https://doi.org/10.1002/apj.2119.

[8] Pastor J V., García A, Micó C, Lewiski F, Vassallo A, Pesce FC. Effect of a novel piston geometry on the combustion process of a light-duty

compression ignition engine: An optical analysis. Energy 2021;221:119764. https://doi.org/10.1016/j.energy.2021.119764.

[9] Leach F, Ismail R, Davy M, Weall A, Cooper B. The effect of a stepped lip piston design on performance and emissions from a high-speed diesel engine. Appl Energy 2018;215:679–89. https://doi.org/10.1016/j.apenergy.2018.02.076.

Chapter 7

Conclusions and Future Works

Content

7.1 Introduction

The objective of this chapter is to compile the main results obtained in the results chapters of this thesis. Therefore, the conclusion section has been divided into three subsections corresponding to the studies focused on in this work: Flame characterization for OME_X and OME_1 (Chapter 4), Piston geometry effects on air-fuel mixing (Chapter 5), and Synergy of OME_X and Piston Geometry to achieve Low Soot Formation (Chapter 6). The end of the chapter focuses on possible future work that could be carried out based on the studies conducted in this thesis. These works arise from the gaps that this thesis has not been able to cover due to time or resources, thus contributing to improving the knowledge of the combustion process of a series of fuels with high potential for use in applications in the transportation sector.

7.2 Conclusions

As mentioned at the beginning of the thesis, the main objective is the characterization of fuels belonging to E-fuels, which have great potential as a substitute for conventional fossil fuels in Internal Combustion Engines (ICE). These fuels, specifically OME_n, can be obtained from renewable energy sources (renewable electricity), thus reducing the use of non-renewable energy and directly reducing carbon footprint. Furthermore, due to their molecular structure composition, the fuels studied in this thesis are known as oxygenated fuels, which have proven to be very interesting in reducing soot formation. The effect on reducing soot is also notable due to the absence of C-C bonds, which are directly responsible for forming Polycyclic Aromatic Hydrocarbons (PAHs) that subsequently lead to soot formation. Using single components (for a fixed n) is of great interest in characterizing this family of fuels. However, it has been shown that the combination of several single components, known in the literature as OME_X (where X represents the combination of these single components), solves certain problems that single components present, such as their lower low heating value (LHV) compared to conventional diesel. This is of great importance for further research on these fuels because the LHV of single components could make their use in ICE impractical due to the large amount of fuel that would need to be injected to obtain the same energy as currently obtained from fossil fuels. Despite the potential of these fuels, especially OME_X, they have very low lubricity, which hinders their use with current engine materials. A promising solution is the blending of these fuels with conventional Diesel. This blend resolves compatibility issues with the infrastructure and avoids miscibility problems among these E-fuels. As expected, the use of diesel in the fuel makes the overall fuel less clean. The presence of diesel necessitates careful consideration of soot formation. Indeed, the potential of OME_X is still evident, as it achieves reductions in soot formation and faster combustion compared to pure diesel. Nevertheless, the presence of soot formed during the combustion process of this fuel is evident and must be taken into account, especially under conditions of high soot formation.

For diesel combustion, over the years, many strategies for reducing soot have been studied (and are still used today), such as aftertreatment systems, combustion modes, and combustion chamber geometries. The latter is particularly attractive because it has been shown that by modifying the piston bowl geometry, the flame dynamics can be "controlled," making combustion more efficient, directly impacting pollutant formation. Recently, a geometry that includes protrusions on the edges of the bowl (referred to as radial-lips in this thesis) has been developed. This design allows for the displacement of the flame once it impacts the bowl edge towards the center of the piston, where fresh oxygen is present to oxidize the soot within the flame.

With the information mentioned above, using oxygenated fuel and modifying the combustion chamber geometry could be ideal for reducing soot formation in the cylinder when using fossil fuel, such as Diesel, in ICE applications.

In order to fulfill the main objective of this thesis, **to Improve the understanding of the combustion process of OME_X and OME_X/diesel blends under engine conditions and to identify the relevance of constructive and operational conditions on the mixing/combustion process and pollutant formation**, the present thesis was divided into three parts, distributed across three results chapters. The first part was based on the characterization of the flame structure of OME_1 and OME_X under reference conditions of the Engine Combustion Network (ECN). The second part focused on analyzing the modification of the radial-lips geometry in the bowl and its impact on soot formation. Finally, the third part focused on the combined effect of using OME_X-diesel blends with a piston featuring radial-lips geometry. The most significant conclusions from each study are summarized in the following subsections.

- **Flame Structure Characterization for OME_X and OME_1**

In the first results chapter (Chapter 4), the characterization of the flame structure was conducted for two oxygenated fuels: a single-component fuel (OME_1) and a combination of different single components (OME_X) belonging to the OME_n family. A High-Pressure High Temperature (HPHT) facility was used for this study, which allows for controlled conditions without piston dynamics or spray-wall interactions (free jet conditions). The study was conducted under the Spray A and Spray D ECN reference conditions. The main difference between both conditions is the size of the nozzle orifice, where for the Spray A is considered for light-duty engines, while the Spray D is considered for medium-heavy duty engines.

The flame structure was identified using the Planar Laser-Induced Fluorescence (PLIF) technique, which enabled the identification of the low-temperature flame zone (associated with the presence of CH_2O) and the high-temperature flame zone (associated with OH detection). The application of the PLIF technique for OH radical detection was performed for the first time in the facilities of I.U.I. CMT-Motores Térmicos, where this doctoral thesis was conducted.

This information was combined with the analysis of chemiluminescent radiation from OH^* radicals, which serve as tracers for high-temperature reactions in the flame. Dodecane was used because ECN fixed it as a reference for Diesel due to its simple molecular composition (maintaining physicochemical characteristics very similar to diesel), making it easier to implement in CFD models. The main results showed that the oxygenated fuels, regardless of the nozzle used, did not exhibit the presence of Polycyclic Aromatic Hydrocarbons (PAHs), which are the main precursors for soot formation. However, PAHs were detected in the case of dodecane.

Different behaviors arose between both oxygenated fuels. On the one hand, the fuel reactivity did not seem influential in flame penetration. However, the mixture formation was found to be influential, which aligns with previous studies on non-oxygenated fuels. On the other hand, the Lift-Off Length (LOL) position was directly affected by the fuel reactivity, with it being closer to the injector tip for OME_X than OME_1. This result suggests that the fuel equivalence ratio influences the stabilization of the LOL.

Certain differences were also detected between the cases regarding the low-temperature and high-temperature flame structures. The typical lobes characteristic of CH_2O were observed for all cases. However, the area of CH_2O detection was influenced by the fuel reactivity, with OME_1 exhibiting a larger area than OME_X. As for the high-temperature reactions marked by the presence of OH, a clear spatial boundary was detected between CH_2O and OH (with the LOL position being the boundary between both species) for all cases except for OME_X-Spray D. In the latter case, CH_2O was detected downstream of the LOL position, being encompassed by the characteristic lobes of OH. This effect could be attributed to the high equivalence ratio in this case, which would hinder the consumption of CH_2O in the spray axis. Thanks to these results, contributions have been made to the ECN database for these oxygenated fuels.

• Piston geometry effects on air-fuel mixing

In the second results chapter (Chapter 5), a study was conducted on the effect of the combustion chamber geometry on the soot formation process in the cylinder. The study was carried out using a medium-duty single-cylinder optical engine. Three different bowl geometries were analyzed using two pistons. The first piston (CS1) has a symmetrical geometry combining stepped lip and radial lip geometries. The second piston (CS2) was a hybrid piston that featured a portion with a stepped lip combined with radial lip geometry (CS2-Lips), while the other side had a stepped lip combined with reentrant geometry (CS2-NoLips). The hybrid geometry of the CS2 piston allowed for a direct comparison (with the same combustion) between a non-conventional geometry (CS2-Lips) and a conventional geometry (CS2-NoLips). It is important to note that, in order to delve deeper into the characterization of the radial-lips geometry, the radial lip geometry in both pistons was different. The main difference between these radial lips was that the CS2-Lips had a more pronounced shape than that of CS1. This study was conducted with a range of operating conditions, including modifications in injection strategy, engine load, and oxygen concentration inside the combustion chamber. The fuel used in this study was conventional Diesel. Due to its size, the low swirl in the engine made it suitable for analyzing the potential of piston geometry in flame dynamics and the consequent in-cylinder soot formation. For the analysis of the soot formation evolution, the 2-color pyrometry (2C) and OH^* chemiluminescence techniques were implemented simultaneously to obtain the KL concentration (associated with soot concentration) and high-reactivity oxidation zones, respectively.

The main observation was that both radial-lips geometries directly influenced the displacement of the flame towards the center of the bowl once it impacted the edge, reaching high oxygen concentration zones that facilitated the oxidation of soot within the flame. However, it was found that a more pronounced radial-lip geometry (CS2-Lips) resulted in the flame reaching areas closer to the center of the piston compared to CS1. This effect led to reduced soot formation and faster combustion. Overall, CS2-Lips exhibited lower soot formation for all studied operating conditions compared to CS1. Additionally, it was observed that this more pronounced geometry had a more significant impact under conditions of high soot formation, such as low oxygen concentration in the combustion chamber and high engine load.

- **Synergy of OME_X and Piston Geometry to achieve Low Soot Formation**

Finally, the last experimental study of the thesis (Chapter 6) was the use of unconventional piston geometry combined with OME_X-Diesel blends. The previous results in Chapters 4 and 5 showed the potential of using these oxygenated fuels and unconventional piston geometries in reducing soot formation inside the cylinder. Visualization techniques for diagnosing the combustion process and soot formation were carried out using the same techniques as in the previous study: 2C pyrometry and OH^* chemiluminescence. The pistons used for the study were the CS1, used in the previous study as the unconventional piston geometry, and a piston with real geometry, the same as the original piston corresponding to this engine, as the conventional geometry (CS3). The operating conditions in this study favored soot formation, including high engine load and low oxygen levels. The low oxygen condition, aimed at simulating exhaust gas recirculation (EGR) conditions, showed a significant increase in the registered soot compared to the nominal oxygen condition (21% O_2 - non-EGR). It was observed that increasing the amount of OME_X in the blend directly affected the reduction of soot formation during the combustion process. However, when OME_X was used in the fuel, a higher amount of soot was detected under low oxygen conditions than pure Diesel under non-EGR conditions. In order to enhance the reduction of soot, which OME_X cannot achieve under those conditions, the CS1 was used to improve the mixing process, as observed in the previous study using conventional Diesel (Chapter 5).

The main results showed that in the presence of OME_X, the CS1 piston reduces the direct flame-to-flame impact and redirects the flame toward the center of the bowl, taking advantage of the available oxygen in that region, as observed in the previous study with diesel. It was also observed that the higher the proportion of OME_X in the blend, the greater the reduction in soot when comparing both pistons, reaching up to a 70% reduction for the case with the highest OME_X content in this study. Finally, it was reported that the combination of both technologies, the use of an oxygenated fuel (OME_X) along with the unconventional piston geometry (radial-lips), under conditions of high soot formation (EGR usage and high engine load), allows for much lower soot levels compared to using only one of these strategies. In fact, combining both technologies can achieve similar soot levels in cases without simulating EGR. This finding confirmed the potential of combining both technologies to reduce the existing trade-off between soot and NO_X emissions.

7.3 Future Works

The results obtained in the studies carried out in this thesis have allowed for a deeper understanding of the combustion process and flame structure of synthetic fuels with high potential for use in Internal Combustion Engines (ICE) applications. Furthermore, the results obtained in the study of piston geometry as a strategy for reducing in-cylinder soot formation are in line with previous studies and contribute to increasing knowledge when operating under conditions of low swirl and high soot formation. The use of this geometry is greatly enhanced when an oxygenated fuel is used, as analyzed in this thesis. However, it is necessary to continue furthering this study with the aim of covering aspects not considered in the present doctoral thesis, which are presented in the following subsections.

• CFD models based on OME_n Fuels

The entire study conducted in this thesis is experimental. Therefore, it is necessary to study CFD modeling of these oxygenated fuels based on their physicochemical properties and the chemical mechanism governing this fuel type. The results of this thesis can serve as an experimental database for adjusting the computational model.

Furthermore, advancing with modeling the behavior and evolution of combustion of these oxygenated fuels under engine conditions, thus getting closer to real-world behavior, is crucial for improving engine hardware, such as enhancing piston geometry.

- ## Flame Structure in an Optical Engine

This thesis has studied the flame structure of OME_X and OME_1 through the identification of low and high-temperature structures under controlled conditions. As demonstrated in the thesis, this is highly important for characterizing the fuels in an environment that is typically challenging for optical studies. Additionally, it serves as an experimental database and aids in adjusting CFD models for the Engine Combustion Network (ECN). However, further research is needed to deepen our understanding of the behavior of these fuels under more realistic engine conditions, where the flame is influenced by the dynamics of the air generated by piston movement, flame-wall interactions, and even spray-spray interactions. Despite the challenges associated with applying the technique, it is encouraged to characterize the flame structure using the PLIF technique in an optical engine with sufficient optical access to carry out such investigations.

- ## Optimization on Engine Conditions

The analysis in Chapter 6, shows a good synergy combining the use of OME_X/diesel blends with radial-lips piston geometry in terms of in-cylinder soot formation reduction. However, only the duration of the main injection was modified to compensate for the lower LHV of OME_X to reach the same engine load for all cases. Future studies should explore further improvement and optimization of the injection strategy for the blends by modifying other parameters, such as the number of injections, the injection pressure, or the delay between pulses.

In addition, the study analyzed the combustion behavior in an optical engine, which has certain limitations in terms of operating conditions compared to more conventional engines. Therefore, to extend the application of the results presented here, a similar study in a full-metal version of a single-cylinder engine would be beneficial to analyze the exhaust emissions and corroborate what has been observed inside the cylinder and has been reported in this work.

Global Bibliography

AECC website n.d. https://www.aecc.eu/ (accessed September 12, 2023).

Air pollution — European Environment Agency n.d. https://www.eea.europa.eu/themes/air (accessed December 13, 2022).

Arellano-Treviño MA, Bartholet D, To AT, Bartling AW, Baddour FG, Alleman TL, et al. Synthesis of Butyl-Exchanged Polyoxymethylene Ethers as Renewable Diesel Blendstocks with Improved Fuel Properties. ACS Sustain Chem Eng 2021;9:6266–73. https://doi.org/10.1021/acssuschemeng.0c09216.

Arrègle J. Análisis de la estructura y dinámica interna de chorros Diesel. Universitat Politècnica de València, 1998.

Badami M, Mallamo F, Millo F, Rossi EE. Influence of Multiple Injection Strategies on Emissions, Combustion Noise and BSFC of a DI Common Rail Diesel Engine. SAE Technical Paper, 2002. https://doi.org/10.4271/2002-01-0503.

Bakker PC, Maes N, Dam N. The potential of on- and off-resonant formaldehyde imaging combined with bootstrapping in diesel sprays. Combust Flame 2017;182:20–7. https://doi.org/10.1016/j.combustflame.2017.03.032.

Bardi M, Payri R, Malbec LM, Bruneaux G, Pickett LM, Manin J, et al. Engine Combustion Network: Comparison of Spray Development, Vaporization, and Combustion in Different Combustion Vessels. Atomization and Sprays 2012;22:807–42. https://doi.org/10.1615/ATOMIZSPR.2013005837.

Bardi M, Payri R, Malbec LM, Bruneaux G, Pickett LM, Manin J, et al. ENGINE COMBUSTION NETWORK: COMPARISON OF SPRAY DEVELOPMENT, VAPORIZATION, AND COMBUSTION IN DIFFERENT COMBUSTION VESSELS. Atomization and Sprays 2012;22:807–42. https://doi.org/10.1615/AtomizSpr.2013005837.

Barro C, Parravicini M, Boulouchos K, Liati A. Neat polyoxymethylene dimethyl ether in a diesel engine; part 2: Exhaust emission analysis. Fuel 2018;234:1414–21. https://doi.org/10.1016/j.fuel.2018.07.108.

Barro C, Parravicini M, Boulouchos K. Neat polyoxymethylene dimethyl ether in a diesel engine; part 1: Detailed combustion analysis. Fuel 2019;256:115892. https://doi.org/10.1016/j.fuel.2019.115892.

Bartholet DL, Arellano-Treviño MA, Chan FL, Lucas S, Zhu J, St. John PC, et al. Property predictions demonstrate that structural diversity can improve the performance of polyoxymethylene ethers as potential bio-based diesel fuels. Fuel 2021;295:120509. https://doi.org/10.1016/j.fuel.2021.120509.

Beatrice C, Bertoli C, Del Giacomo N, Migliaccio M na. Experimental Investigation on High-Quality Diesel Fuels Effects in a Light Duty CR Diesel Engine. SAE Transactions, 2000, p. 1517–24. https://doi.org/10.4271/2000-01-1911.

Benajes J, García A, Monsalve-Serrano J, Martínez-Boggio S. Potential of using OMEx as substitute of diesel in the dual-fuel combustion mode to reduce the global CO2 emissions. Transportation Engineering 2020;1:100001. https://doi.org/10.1016/j.treng.2020.01.001.

Bhatelia T, Lee WJ, Samanta C, Patel J, Bordoloi A. Processes for the production of oxymethylene ethers: promising synthetic diesel additives. Asia-Pacific Journal of Chemical Engineering 2017;12:827–37. https://doi.org/10.1002/apj.2119.

Bianchi GM, Pelloni P, Corcione FE, Mattarelli E, Bertoni FL. Numerical Study of the Combustion Chamber Shape for Common Rail H.S.D.I. Diesel Engines. SAE Technical Paper, 2000. https://doi.org/10.4271/2000-01-1179.

Bruneaux G. Combustion structure of free and wall-impinging diesel jets by simultaneous laser-induced fluorescence of formaldehyde, poly-aromatic hydrocarbons, and hydroxides. International Journal of Engine Research 2008;9:249–65. https://doi.org/10.1243/14680874JER00108.

Bruneaux G. Mixing Process in High Pressure Diesel Jets by Normalized Laser Induced Exciplex Fluorescence Part II: Wall Impinging Versus Free Jet. SAE Technical Paper, 2005. https://doi.org/10.4271/2005-01-2097.

Burger J, Siegert M, Ströfer E, Hasse H. Poly(oxymethylene) dimethyl ethers as components of tailored diesel fuel: Properties, synthesis and purification concepts. Fuel 2010;89:3315–9. https://doi.org/10.1016/j.fuel.2010.05.014.

Busch S, Zha K, Kurtz E, Warey A, Peterson R. Experimental and Numerical Studies of Bowl Geometry Impacts on Thermal Efficiency in a Light-Duty Diesel Engine. SAE Technical Papers, 2018, p. 1–12. https://doi.org/10.4271/2018-01-0228.

Busch S, Zha K, Perini F, Reitz R, Kurtz E, Warey A, et al. Bowl Geometry Effects on Turbulent Flow Structure in a Direct Injection Diesel Engine. SAE Technical Paper, 2018. https://doi.org/10.4271/2018-01-1794.

Busch S, Zha K, Perini F, Reitz R. Piston Bowl Geometry Impacts on Late-Cycle Flow and Mixing in a Small-Bore Diesel Engine. 2017.

Cartellieri WP, Herzog PL. Swirl Supported or Quiescent Combustion for 1990's Heavy-Duty DI Diesel Engines - An Analysis. SAE Technical Papers, 1988. https://doi.org/10.4271/880342.

Cenker E, Bruneaux G, Pickett L, Schulz C. Study of Soot Formation and Oxidation in the Engine Combustion Network (ECN), Spray A: Effects of Ambient Temperature and Oxygen Concentration. SAE Int J Engines 2013;6:2013-01–0901. https://doi.org/10.4271/2013-01-0901.

Chen Y, Li X, Li X, Zhao W, Liu F. The wall-flow-guided and interferential interactions of the lateral swirl combustion system for improving the fuel/air mixing and combustion performance in DI diesel engines. Energy 2019;166:690–700. https://doi.org/10.1016/j.energy.2018.10.107.

Chen Y, Ma J, Han B, Zhang P, Hua H, Chen H, et al. Emissions of automobiles fueled with alternative fuels based on engine technology: A review. Journal of Traffic and Transportation Engineering (English Edition) 2018;5:318–34. https://doi.org/10.1016/j.jtte.2018.05.001.

Cheng AS, Dibble RW. Emissions Performance of Oxygenate-in-Diesel Blends and Fischer-Tropsch Diesel in a Compression Ignition Engine, 1999. https://doi.org/10.4271/1999-01-3606.

Climate European Comission. An Official Website of the European Union n.d. https://climate.ec.europa.eu/index_en (accessed July 10, 2023).

CMT - Motores Térmicos website n.d. https://www.cmt.upv.es/#/ecn/Principal (accessed August 26, 2023).

Cornwell R, Conicella F. Direct injection diesel engines. US 8,770,168 B2, 2014.

Correas Jiménez D. Estudio teorico-experimental del chorro libre diesel isotermo. Universitat Politècnica de Valencia, 1998.

Dahlstrom J, Andersson O, Tuner M, Persson H. Experimental Comparison of Heat Losses in Stepped-Bowl and Re-Entrant Combustion Chambers in a Light Duty Diesel Engine. SAE Technical Papers, 2016. https://doi.org/10.4271/2016-01-0732.

Dec JE, Canaan RE. PLIF Imaging of NO Formation in a DI Diesel Engine. SAE Technical Paper 980147, 1998. https://doi.org/10.4271/980147.

Dec JE, Coy EB. OH radical imaging in a di diesel engine and the structure of the early diffusion flame. SAE Technical Papers 1996. https://doi.org/10.4271/960831.

Dec JE, Espey C. Chemiluminescence Imaging of Autoignition in a DI Diesel Engine. SAE Technical Paper 982685, 1998. https://doi.org/10.4271/982685.

Dec JE, Kelly-Zion PL. The Effects of Injection Timing and Diluent Addition on Late-Combustion Soot Burnout in a DI Diesel Engine Based on Simultaneous 2-D Imaging of OH and Soot. SAE Technical Papers, SAE International; 2000. https://doi.org/10.4271/2000-01-0238.

Dec JE. A conceptual model of DL diesel combustion based on laser-sheet imaging. SAE Transactions 1997:1319–48.

DewesoftX 2020.

Di Blasio G, Ianniello R, Beatrice C, Pesce FC, Vassallo A, Belgiorno G. Experimental Investigation on an Innovative Additive ManufacturingEnabled Diesel Piston Design to improve Engine-out Emissions and Thermal Efficiency beyond Euro6. THIESEL 2020 Conference on Thermo- and Fluid Dynamic Processes in Direct Injection Engines 2020.

Dolak JG, Shi Y, Reitz RD. A Computational Investigation of Stepped-Bowl Piston Geometry for a Light Duty Engine Operating at Low Load. SAE Technical Papers, 2010. https://doi.org/10.4271/2010-01-1263.

Donkerbroek AJ, van Vliet AP, Somers LMT, Dam NJ, ter Meulen JJ. Relation between hydroxyl and formaldehyde in a direct-injection heavy-duty diesel engine. Combust Flame 2011;158:564–72. https://doi.org/https://doi.org/10.1016/j.combustflame.2010.09.024.

Donkerbroek AJ, van Vliet AP, Somers LMT, Frijters PJM, Klein-Douwel RJH, Dam NJ, et al. Time- and space-resolved quantitative LIF measurements of formaldehyde in a heavy-duty diesel engine. Combust Flame 2010;157:155–66. https://doi.org/10.1016/j.combustflame.2009.07.004.

Dreizler A, Böhm B. Advanced laser diagnostics for an improved understanding of premixed flame-wall interactions. Proceedings of the Combustion Institute 2015;35:37–64. https://doi.org/10.1016/j.proci.2014.08.014.

Dworschak P, Berger V, Härtl M, Wachtmeister G. Neat Oxymethylene Ethers: Combustion Performance and Emissions of OME2, OME3, OME4 and OME5 in a Single-Cylinder Diesel Engine, 2020. https://doi.org/10.4271/2020-01-0805.

Eckbreth AC. Laser diagnostics for combustion temperature and species. vol. 3. Second. Great Britain: Taylor & Francis Books; 1996.

eFuel Alliance e.V. 2022 n.d. https://www.efuel-alliance.eu/ (accessed July 14, 2023).

Eismark J, Andersson M, Christensen M, Karlsson A, Denbratt I. Role of Piston Bowl Shape to Enhance Late-Cycle Soot Oxidation in Low-Swirl Diesel Combustion. SAE Int J Engines 2019;12:233–49. https://doi.org/10.4271/03-12-03-0017.

Eismark J, Balthasar M. Device for Reducing Emissions in a Vehicle Combustion Engine. US 8,499,735 B2, 2013.

Eismark J, Christensen M, Andersson M, Karlsson A, Denbratt I. Role of fuel properties and piston shape in influencing soot oxidation in heavy-duty low swirl diesel engine combustion. Fuel 2019;254:115568. https://doi.org/10.1016/j.fuel.2019.05.151.

Enerdata n.d. https://www.enerdata.net/ (accessed September 14, 2023).

Engine Combustion Network n.d. https://ecn.sandia.gov/ (accessed February 22, 2023).

Escofet Martin D. Laser diagnostics for high pressure combustion. University of California, 2017.

Faiz A, Weaver CS, Walsh MP. Air Pollution from Motor Vehicles: Standards and Technologies for Controlling Emissions. World Bank Publications; 1996.

Farhan SM, Wang P. Post-injection strategies for performance improvement and emissions reduction in DI diesel engines—A review. Fuel Processing Technology 2022;228. https://doi.org/10.1016/j.fuproc.2021.107145.

Flynn PF, Durrett RP, Hunter GL, Zur Loye AO, Akinyemi OC, Dec JE, et al. Diesel combustion: An integrated view combining laser diagnostics, chemical kinetics, and empirical validation. SAE Technical Paper 1999-01-0509, 1999. https://doi.org/10.4271/1999-01-0509.

Gao J, Moon S, Zhang Y, Nishida K, Matsumoto Y. Flame structure of wall-impinging diesel fuel sprays injected by group-hole nozzles. Combust Flame 2009;156:1263–77. https://doi.org/10.1016/j.combustflame.2009.01.014.

García A, Gil A, Monsalve-Serrano J, Lago Sari R. OMEx-diesel blends as high reactivity fuel for ultra-low NOx and soot emissions in the dual-mode dual-fuel combustion strategy. Fuel 2020;275:117898. https://doi.org/10.1016/j.fuel.2020.117898.

García A, Monsalve-Serrano J, José Sanchís E, Fogué-Robles Á. Exploration of suitable injector configuration for dual-mode dual-fuel engine with diesel and OMEx as high reactivity fuels. Fuel 2020;280:118670. https://doi.org/10.1016/j.fuel.2020.118670.

García A, Monsalve-Serrano J, Villalta D, Fogué-Robles Á. Evaluating OMEx combustion towards stoichiometric conditions in a compression ignition engine. Fuel 2021;303:121273. https://doi.org/10.1016/J.FUEL.2021.121273.

García Carrero AA. Experimental Study of the Fuel Effect on Diffusion Combustion and Soot Formation under Diesel Engine-Like Conditions. Universitat Politècnica de València, 2022. https://doi.org/10.4995/THESIS/10251/179997.

García Oliver JM. Aportaciones al estudio del proceso de combustión turbulenta de chorros en motores diesel de inyección directa. Universitat Politècnica de València, 2004. https://doi.org/10.4995/Thesis/10251/55164.

García-Oliver JM, Novella R, Micó C, De Leon-Ceriani D. Numerical analysis of the combustion process of oxymethylene ethers as low-carbon fuels for compression ignition engines. International Journal of Engine Research 2022. https://doi.org/10.1177/14680874221113749/ASSET/IMAGES/LARGE/10.1177_14680874221113749-FIG13.JPEG.

Gardner TP, Low SS, Kenney TE. Evaluation of Some Alternative Diesel Fuels for Low Emissions and Improved Fuel Economy. SAE Transactions, 2001, p. 24–78. https://doi.org/10.4271/2001-01-0149.

Gaydon AG. The Spectroscopy of Flames. Dordrecht: Springer Netherlands; 1974. https://doi.org/10.1007/978-94-009-5720-6.

Genzale CL, Reitz RD, Musculus MPB. Effects of Piston Bowl Geometry on Mixture Development and Late-Injection Low-Temperature Combustion in a Heavy-Duty Diesel Engine. SAE Int J Engines 2008;1:2008-01–1330. https://doi.org/10.4271/2008-01-1330.

Glassman Irvin. Combustion. 3rd ed. San Diego: Academic Press; 1996.

Han Z, Uludogan A, Hampson GJ, Reitz RD. Mechanism of Soot and NOx Emission Reduction Using Multiple-injection in a Diesel Engine. SAE Technical Paper, 1996. https://doi.org/10.4271/960633.

Hardalupas Y, Orain M, Panoutsos CS, Taylor AMKP, Olofsson J, Seyfried H, et al. Chemiluminescence sensor for local equivalence ratio of reacting mixtures of fuel and air (FLAMESEEK). Appl Therm Eng 2004;24:1619–32. https://doi.org/10.1016/J.APPLTHERMALENG.2003.10.028.

Härtl M, Seidenspinner P, Jacob E, Wachtmeister G. Oxygenate screening on a heavy-duty diesel engine and emission characteristics of highly oxygenated oxymethylene ether fuel OME1. Fuel 2015;153:328–35. https://doi.org/10.1016/j.fuel.2015.03.012.

Heywood J. Internal Combustion Engine Fundamentals. 2nd ed. New York: McGraw-Hill Education; 2018.

Higgins B, Siebers DL. Measurement of the Flame Lift-Off Location on DI Diesel Sprays Using OH Chemiluminescence. SAE Technical Papers, 2001. https://doi.org/10.4271/2001-01-0918.

Hobohm J, Auf Der Maur A, Dambeck H, Kemmler A, Koziel S, Kreidelmeyer S, et al. STATUS AND PERSPECTIVES OF LIQUID ENERGY SOURCES IN THE ENERGY TRANSITION. 2018.

Honecker C, Neumann M, Glueck S, Schoenen M, Pischinger S. Optical Spray Investigations on OME3-5 in a Constant Volume High Pressure Chamber, 2019. https://doi.org/10.4271/2019-24-0234.

Hottel HC, Broughton FP. Determination of True Temperature and Total Radiation from Luminous Gas Flames. Industrial & Engineering Chemistry Analytical Edition 1932;4:166–75. https://doi.org/10.1021/ac50078a004.

Hua Y, Liu S, Li R, Mei L. Experimental study of regulated and unregulated emissions from a diesel engine using coal-based fuels. Fuel 2020. https://doi.org/10.1016/j.fuel.2020.118658.

Huang H, Teng W, Li Z, Liu Q, Wang Q, Pan M. Improvement of emission characteristics and maximum pressure rise rate of diesel engines fueled with n-butanol/PODE3-4/diesel blends at high injection pressure. Energy Convers Manag 2017;152:45–56. https://doi.org/10.1016/j.enconman.2017.09.038.

Iannuzzi SE, Barro C, Boulouchos K, Burger J. Combustion behavior and soot formation/oxidation of oxygenated fuels in a cylindrical constant volume chamber. Fuel 2016;167:49–59. https://doi.org/10.1016/j.fuel.2015.11.060.

Iannuzzi SE, Barro C, Boulouchos K, Burger J. POMDME-diesel blends: Evaluation of performance and exhaust emissions in a single cylinder heavy-duty diesel engine. Fuel 2017;203:57–67. https://doi.org/10.1016/j.fuel.2017.04.089.

Idicheria CA, Pickett LM. Formaldehyde visualization near lift-off location in a diesel jet. SAE Technical Papers 2006. https://doi.org/10.4271/2006-01-3434.

Idicheria CA, Pickett LM. Ignition, soot formation, and end-of-combustion transients in diesel combustion under high-EGR conditions. International Journal of Engine Research 2011;12:376–92. https://doi.org/10.1177/1468087411399505.

Jing W, Roberts WL, Fang T. Spray combustion of Jet-A and diesel fuels in a constant volume combustion chamber. Energy Convers Manag 2015;89:525–40. https://doi.org/10.1016/j.enconman.2014.10.010.

Kastengren AL, Tilocco FZ, Powell CF, Manin J, Pickett LM, Payri R, et al. Engine Combustion Network (ECN): Measurements of Nozzle Geometry and Hydraulic Behavior. Atomization and Sprays 2012;22:1011–52. https://doi.org/10.1615/ATOMIZSPR.2013006309.

Klein-Douwel RJH, Donkerbroek AJ, van Vliet AP, Boot MD, Somers LMT, Baert RSG, et al. Soot and chemiluminescence in diesel combustion of bio-derived, oxygenated and reference fuels. Proceedings of the Combustion Institute 2009;32:2817–25. https://doi.org/10.1016/j.proci.2008.06.140.

Kosaka H, Aizawa T, Kamimoto T. Two-dimensional imaging of ignition and soot formation processes in a diesel flame. International Journal of Engine Research 2005;6:21–42. https://doi.org/10.1243/146808705X7347.

Kosaka H, Drewes VH, Catalfamo L, Aradi AA, Iida N, Kamimoto T. Two-dimensional imaging of formaldehyde formed during the ignition process of a diesel fuel spray. SAE Technical Papers 2000. https://doi.org/10.4271/2000-01-0236.

Kosaka H, Nishigaki T, Kamimoto T, Sano T, Matsutani A, Harada S. Simultaneous 2-D Imaging of OH Radicals and Soot in a Diesel Flame by Laser Sheet Techniques. SAE transactions, 1996, p. 1184–95. https://doi.org/10.4271/960834.

Kühn E, Ates A, Perner J, Steinfort T. THE OVERALL CO2 IMPACT FOR DRIVE TECHNOLOGIES IN INDIVIDUAL TRANSPORT TODAY AND IN THE FUTURE. Berlin: 2019.

Kurtz EM, Styron J. An Assessment of Two Piston Bowl Concepts in a Medium-Duty Diesel Engine. SAE Int J Engines 2012;5:2012-01–0423. https://doi.org/10.4271/2012-01-0423.

Leach F, Ismail R, Davy M, Weall A, Cooper B. The effect of a stepped lip piston design on performance and emissions from a high-speed diesel engine. Appl Energy 2018;215:679–89. https://doi.org/10.1016/j.apenergy.2018.02.076.

Lee J, Lee S, Kim J, Kim D. Bowl Shape Design Optimization for Engine-Out PM Reduction in Heavy Duty Diesel Engine. SAE Technical Papers, 2015. https://doi.org/10.4271/2015-01-0789.

Lewiski F. Analysis of the combustion process and soot formation in a single cylinder optical engine fueled with e-fuels and using different piston geometries. Universitat Politècnica de València, 2021. https://doi.org/10.4995/Thesis/10251/180351.

Li D, Gao Y, Liu S, Ma Z, Wei Y. Effect of polyoxymethylene dimethyl ethers addition on spray and atomization characteristics using a common rail diesel injection system. Fuel 2016;186:235–47. https://doi.org/10.1016/j.fuel.2016.08.082.

Li T, Okabe Y, Izumi H, Shudo T, Ogawa H. Dependence of Ultra-High EGR Low Temperature Diesel Combustion on Fuel Properties, 2006. https://doi.org/10.4271/2006-01-3387.

Liu H, Wang Z, Li Y, Zheng Y, He T, Wang J. Recent progress in the application in compression ignition engines and the synthesis technologies of polyoxymethylene dimethyl ethers. Appl Energy 2019;233–234:599–611. https://doi.org/10.1016/j.apenergy.2018.10.064.

Liu H, Wang Z, Zhang J, Wang J, Shuai S. Study on combustion and emission characteristics of Polyoxymethylene Dimethyl Ethers/diesel blends in light-duty and heavy-duty diesel engines. Appl Energy 2017;185:1393–402. https://doi.org/10.1016/j.apenergy.2015.10.183.

Liu J, Feng L, Wang H, Zheng Z, Chen B, Zhang D, et al. Spray characteristics of gasoline/PODE and diesel/PODE blends in a constant volume chamber. Appl Therm Eng 2019;159:113850. https://doi.org/10.1016/j.applthermaleng.2019.113850.

Liu J, Sun P, Huang H, Meng J, Yao X. Experimental investigation on performance, combustion and emission characteristics of a common-rail diesel engine fueled with polyoxymethylene dimethyl ethers-diesel blends. Appl Energy 2017;202:527–36. https://doi.org/10.1016/j.apenergy.2017.05.166.

Liu J, Wang H, Li Y, Zheng Z, Xue Z, Shang H, et al. Effects of diesel/PODE (polyoxymethylene dimethyl ethers) blends on combustion and emission characteristics in a heavy duty diesel engine. Fuel 2016;177:206–16. https://doi.org/10.1016/j.fuel.2016.03.019.

Liu J, Wang L, Wang P, Sun P, Liu H, Meng Z, et al. An overview of polyoxymethylene dimethyl ethers as alternative fuel for compression ignition engines. Fuel 2022;318:123582. https://doi.org/10.1016/j.fuel.2022.123582.

Liu Y, Tan J, Wan M, Zhang L, Yao X. Quantitative Measurement of OH* and CH* Chemiluminescence in Jet Diffusion Flames. ACS Omega 2020. https://doi.org/10.1021/acsomega.0c01093.

Luque J, Crosley DR. LIFBASE: Database and Spectral Simulation Program 1999.

Ma X, Ma Y, Sun S, Shuai S-J, Wang Z, Wang J-X. PLII-LEM and OH* Chemiluminescence Study on Soot Formation in Spray Combustion of PODEn-Diesel Blend Fuels in a Constant Volume Vessel, 2017. https://doi.org/10.4271/2017-01-2329.

Maes N, Meijer M, Dam N, Somers B, Baya Toda H, Bruneaux G, et al. Characterization of Spray A flame structure for parametric variations in ECN constant-volume vessels using chemiluminescence and laser-induced fluorescence. Combust Flame 2016;174:138–51. https://doi.org/10.1016/j.combustflame.2016.09.005.

Maes N. The life of a spray. Technische Universiteit Eindhoven, 2019.

Magnusson A, Andersson S, Jedrzejowski S. Spray-Wall Interaction: Diesel Fuels Impinging on a Tempered Wall. SAE Technical Paper, 2006. https://doi.org/10.4271/2006-01-1116.

Meijer M, Somers B, Johnson J, Naber J, Lee S-Y, Malbec LM, et al. ENGINE COMBUSTION NETWORK (ECN): CHARACTERIZATION AND COMPARISON OF BOUNDARY CONDITIONS FOR DIFFERENT COMBUSTION VESSELS. Atomization and Sprays 2012;22:777–806. https://doi.org/10.1615/AtomizSpr.2012006083.

Meingast U, Staudt M, Reichelt L, Renz U, Sommerhoff F-A. Analysis of Spray/Wall Interaction Under Diesel Engine Conditions. SAE Technical Paper, 2000. https://doi.org/10.4271/2000-01-0272.

Micó Reche C. DEVELOPMENT OF MEASUREMENT AND VISUALIZATION TECHNIQUES FOR CHARACTERIZATION OF MIXING AND COMBUSTION PROCESSES WITH SURROGATE FUELS. Universitat Politècnica de València, 2015. https://doi.org/10.4995/Thesis/10251/58991.

Millo F, Piano A, Roggio S, Bianco A, Pesce FC, Vassallo AL. Numerical Assessment of Additive Manufacturing-Enabled Innovative Piston Bowl Design for a Light-Duty Diesel Engine Achieving Ultra-Low Engine-Out Soot

Emissions. SAE Int J Engines 2021;15:3–15. https://doi.org/10.4271/03-15-03-0022.

Mollenhauer K, Tschöke H. Handbook of Diesel Engines. Berlin, Heidelberg: Springer Berlin Heidelberg; 2010. https://doi.org/10.1007/978-3-540-89083-6.

Montgomery MJ, Das DD, McEnally CS, Pfefferle LD. Analyzing the robustness of the yield sooting index as a measure of sooting tendency. Proceedings of the Combustion Institute 2019;37:911–8. https://doi.org/10.1016/j.proci.2018.06.105.

Musculus MP, Dec JE, Tree DR. Effects of Fuel Parameters and Diffusion Flame Lift-Off on Soot Formation in a Heavy-Duty DI Diesel Engine. SAE transactions, 2002, p. 1467–89. https://doi.org/10.4271/2002-01-0889.

Musculus MPB, Kattke K. Entrainment Waves in Diesel Jets. SAE Int J Engines 2009;2:2009-01–1355. https://doi.org/10.4271/2009-01-1355.

Musculus MPB, Miles PC, Pickett LM. Conceptual models for partially premixed low-temperature diesel combustion. Prog Energy Combust Sci 2013;39:246–83. https://doi.org/10.1016/j.pecs.2012.09.001.

Musculus MPB, Singh S, Reitz RD. Gradient effects on two-color soot optical pyrometry in a heavy-duty DI diesel engine. Combust Flame 2008;153:216–27. https://doi.org/10.1016/j.combustflame.2007.10.023.

Musculus MPB. Multiple Simultaneous Optical Diagnostic Imaging of Early-Injection Low-Temperature Combustion in a Heavy-Duty Diesel Engine, 2006. https://doi.org/10.4271/2006-01-0079.

Neely GD, Sasaki S, Sono H. Investigation of Alternative Combustion Crossing Stoichiometric Air Fuel Ratio for Clean Diesels. SAE Technical Paper, 2007. https://doi.org/10.4271/2007-01-1840.

Nour M, Attia AMA, Nada SA. Improvement of CI engine combustion and performance running on ternary blends of higher alcohol (Pentanol and Octanol)/hydrous ethanol/diesel. Fuel 2019;251:10–22. https://doi.org/10.1016/j.fuel.2019.04.026.

O’Connor J, Musculus M. Post Injections for Soot Reduction in Diesel Engines: A Review of Current Understanding. SAE International Journal Engines 2013:400–21. https://doi.org/10.4271/2013-01-0917.

Ogawa H, Nabi N, Minami M, Miyamoto N, Bong-Seock K. Ultra Low Emissions and High Performance Diesel Combustion with a Combination of High EGR, Three-Way Catalyst, and a Highly Oxygenated Fuel, Dimethoxy Methane (DMM). SAE transactions, 2000, p. 1019–27. https://doi.org/10.4271/2000-01-1819.

Omari A, Heuser B, Pischinger S, Rüdinger C. Potential of long-chain oxymethylene ether and oxymethylene ether-diesel blends for ultra-low emission engines. Appl Energy 2019;239:1242–9. https://doi.org/10.1016/j.apenergy.2019.02.035.

Ottenwaelder T, Pischinger S. Effects of Biofuels on the Mixture Formation and Ignition Process in Diesel-Like Jets, 2017. https://doi.org/10.4271/2017-01-2332.

Pastor J V, García-Oliver JM, Micó C, Tejada FJ. Characterization of the oxymethylene ether fuels flame structure for ECN Spray A and Spray D nozzles. Appl Energy 2023;332:120475. https://doi.org/10.1016/j.apenergy.2022.120475.

Pastor J V, Micó C, Lewiski F, Tejada FJ, Vassallo A. Innovative diesel piston geometries for soot emissions reduction and cleaner combustion : An optical investigation. Thiesel 2022 Conference on Thermo-and Fluid Dynamics of Clean Propulsion Powerplants 2022.

Pastor J V., García A, Micó C, Lewiski F, Vassallo A, Pesce FC. Effect of a novel piston geometry on the combustion process of a light-duty compression ignition engine: An optical analysis. Energy 2021;221:119764. https://doi.org/10.1016/j.energy.2021.119764.

Pastor J V., García A, Micó C, Lewiski F. Simultaneous high-speed spectroscopy and 2-color pyrometry analysis in an optical compression ignition engine fueled with OMEX-diesel blends. Combust Flame 2021;230:111437. https://doi.org/10.1016/J.COMBUSTFLAME.2021.111437.

Pastor J V., García-Oliver JM, García A, Micó C, Möller S. Application of optical diagnostics to the quantification of soot in n-alkane flames under diesel conditions. Combust Flame 2016;164:212–23. https://doi.org/10.1016/j.combustflame.2015.11.018.

Pastor J V., García-Oliver JM, Micó C, García-Carrero AA, Gómez A. Experimental Study of the Effect of Hydrotreated Vegetable Oil and Oxymethylene Ethers on Main Spray and Combustion Characteristics under Engine Combustion Network Spray A Conditions. Applied Sciences 2020;10:5460. https://doi.org/10.3390/app10165460.

Pastor J V., García-Oliver JM, Micó C, García-Carrero AA. An experimental study with renewable fuels using ECN Spray A and D nozzles. International Journal of Engine Research 2021. https://doi.org/10.1177/14680874211031200.

Pastor J V., Garcia-Oliver JM, Micó C, Tejada FJ. Comparison of the Diffusive Flame Structure for Dodecane and OMEX Fuels for Conditions of Spray A of the ECN. SAE Technical Papers 2020:1–10. https://doi.org/10.4271/2020-01-2120.

Pastor J V., Micó C, Lewiski F, Tejada FJ, Tornatore C. A Synergic Application of High-Oxygenated E-Fuels and New Bowl Designs for Low Soot Emissions: An Optical Analysis. Applied Sciences 2023;13:8560. https://doi.org/10.3390/app13148560.

Pastor J V., Micó C, Lewiski F, Tejada FJ, Vassallo A, Pesce FC, et al. Influence of the radial-lip concept design to achieve ultra-low soot emission reductions: An optical analysis. Fuel 2023;345:128161. https://doi.org/10.1016/J.FUEL.2023.128161.

Pastor JV, García-Oliver JM, López JJ, Vera-Tudela W. An experimental study of the effects of fuel properties on reactive spray evolution using Primary Reference Fuels. Fuel 2016;163:260–70. https://doi.org/10.1016/j.fuel.2015.09.064.

Payri R, De La Morena J, Monsalve-Serrano J, Pesce FC, Vassallo A. Impact of counter-bore nozzle on the combustion process and exhaust emissions for light-duty diesel engine application. International Journal of Engine Research 2018;20:46–57. https://doi.org/10.1177/1468087418819250.

Payri R, García-Oliver JM, Bardi M, Manin J. Fuel temperature influence on diesel sprays in inert and reacting conditions. Appl Therm Eng 2012;35:185–95. https://doi.org/10.1016/j.applthermaleng.2011.10.027.

Payri R, Gimeno J, Cardona S, Ayyapureddi S. Experimental study of the influence of the fuel and boundary conditions over the soot formation in multi-hole diesel injectors using high-speed color diffused back-illumination technique. Appl Therm Eng 2019;158:113746. https://doi.org/10.1016/j.applthermaleng.2019.113746.

Payri R, Hardy G, Gimeno J, Bautista A. Analysis of counterbore effect in five diesel common rail injectors. Exp Therm Fluid Sci 2019;107:69–78. https://doi.org/10.1016/J.EXPTHERMFLUSCI.2019.05.008.

Pélerin D, Gaukel K, Härtl M, Jacob E, Wachtmeister G. Potentials to simplify the engine system using the alternative diesel fuels oxymethylene ether OME1 and OME3−6 on a heavy-duty engine. Fuel 2020;259:116231. https://doi.org/10.1016/j.fuel.2019.116231.

Pellegrini L, Marchionna M, Patrini R, Beatrice C, Del Giacomo N, Guido C. Combustion Behaviour and Emission Performance of Neat and Blended Polyoxymethylene Dimethyl Ethers in a Light-Duty Diesel Engine, 2012. https://doi.org/10.4271/2012-01-1053.

Pellegrini L, Marchionna M, Patrini R, Florio S. Emission Performance of Neat and Blended Polyoxymethylene Dimethyl Ethers in an Old Light-Duty Diesel Car, 2013. https://doi.org/10.4271/2013-01-1035.

Pellegrini L, Patrini R, Marchionna M. Effect of POMDME Blend on PAH Emissions and Particulate Size Distribution from an In-Use Light-Duty Diesel Engine, 2014. https://doi.org/10.4271/2014-01-1951.

Perini F, Zha K, Busch S, Kurtz E, Peterson RC, Warey A, et al. Piston geometry effects in a light-duty, swirl-supported diesel engine: Flow structure characterization. International Journal Engine Research 2018;19:1079–98. https://doi.org/10.1177/1468087417742572.

Pickett LM, Genzale CL, Bruneaux G, Malbec L-M, Hermant L, Christiansen C, et al. Comparison of Diesel Spray Combustion in Different High-Temperature, High-Pressure Facilities. SAE Int J Engines 2010;3:2010-01–2106. https://doi.org/10.4271/2010-01-2106.

Pickett LM, López JJ. Jet-Wall Interaction Effects on Diesel Combustion and Soot Formation. SAE Technical Paper, 2005. https://doi.org/10.4271/2005-01-0921.

Pickett LM, Manin J, Genzale CL, Siebers DL, Musculus MPB, Idicheria CA. Relationship Between Diesel Fuel Spray Vapor Penetration/Dispersion and Local Fuel Mixture Fraction. SAE Int J Engines 2011;4:2011-01–0686. https://doi.org/10.4271/2011-01-0686.

Pickett LM, Siebers DL, Idicheria CA. Relationship Between Ignition Processes and the Lift-Off Length of Diesel Fuel Jets. JSTOR, 2005. https://doi.org/10.4271/2005-01-3843.

Ren Y, Huang ZH, Jiang DM, Liu LX, Zeng K, Liu B, et al. Engine performance and emission characteristics of a compression ignition engine fuelled with diesel/dimethoxymethane blends. Proceedings of the Institution of Mechanical Engineers, Part D: Journal of Automobile Engineering 2005;219:905–14. https://doi.org/10.1243/095440705X28367.

Ruth D, O'Connor J. Development and Verification of Reduced-Order Model for Diesel Spray Penetration and Spreading during Wall Impingement. SAE Technical Paper, 2017. https://doi.org/10.4271/2017-01-0814.

Serizawa K, Ueda D, Mikami N, Tomida Y, Weber J. Realizing Robust Combustion with High Response Diesel Injector with Controlled Diffusive Spray Nozzle and Closed Loop Injection Control. SAE Technical Papers 2017;2017-March. https://doi.org/10.4271/2017-01-0845.

Shiwaku T, Yasaki S, Nishida K, Ogata Y, Suzuki M, Umehara T. Split Injection Spray Development, Mixture Formation, and Combustion Processes in a Diesel Engine Piston Cavity: Rig Test and Real Engine Results. SAE Technical Paper, 2018. https://doi.org/10.4271/2018-01-1698.

Siebers DL, Higgins B, Pickett L. Flame Lift-Off on Direct-Injection Diesel Fuel Jets: Oxygen Concentration Effects. SAE transactions, 2002, p. 1490–509. https://doi.org/10.4271/2002-01-0890.

Siebers DL, Higgins B. Flame Lift-Off on Direct-Injection Diesel Sprays Under Quiescent Conditions. SAE transactions, 2001, p. 400–21. https://doi.org/10.4271/2001-01-0530.

Siebers DL, Hyggins BS. Effects of Injector Conditions on the Flame Lift-off Length of DI Diesel Spray. Springer-Verlag; 2002.

Skeen SA, Manin J, Pickett LM, Cenker E, Bruneaux G, Kondo K, et al. A Progress Review on Soot Experiments and Modeling in the Engine Combustion

Network (ECN). SAE Int J Engines 2016;9:2016-01–0734. https://doi.org/10.4271/2016-01-0734.

Skeen SA, Manin J, Pickett LM. Simultaneous formaldehyde PLIF and high-speed schlieren imaging for ignition visualization in high-pressure spray flames. Proceedings of the Combustion Institute 2015;35:3167–74. https://doi.org/10.1016/j.proci.2014.06.040.

Smith A. Ricardo low emissions combustion technology helps JCB create the off-highway industry's cleanest engine. Ricardo Press Release 2010:4–6.

Srna A, Barro C, Herrmann K, Möri F, Hutter R, Boulouchos K. POMDME as an Alternative Pilot Fuel for Dual-Fuel Engines: Optical Study in a RCEM and Application in an Automotive Size Dual-Fuel Diesel Engine, 2018. https://doi.org/10.4271/2018-01-1734.

Tan YR, Botero ML, Sheng Y, Dreyer JAH, Xu R, Yang W, et al. Sooting characteristics of polyoxymethylene dimethyl ether blends with diesel in a diffusion flame. Fuel 2018;224:499–506. https://doi.org/10.1016/j.fuel.2018.03.051.

Theinnoi K, Suksompong P, Temwutthikun W. Engine Performance of Dual Fuel Operation with In-cylinder Injected Diesel Fuels and In-Port Injected DME. Energy Procedia 2017;142:461–7. https://doi.org/10.1016/j.egypro.2017.12.072.

Thorlabs, Inc. - Your Source for Fiber Optics, Laser Diodes, Optical Instrumentation and Polarization Measurement & Control n.d. https://www.thorlabs.com/ (accessed August 31, 2023).

Thring MW, Newby MP. Combustion length of enclosed turbulent jet flames. Symposium (International) on Combustion 1953;4:789–96. https://doi.org/10.1016/S0082-0784(53)80103-7.

Tu PW, Xu H, Srivastava DK, Dean K, Jing D, Cao L, et al. Numerical Investigation of GDI Injector Nozzle Geometry on Spray Characteristics. SAE Technical Papers 2015;2015-Septe. https://doi.org/10.4271/2015-01-1906.

Vertin KD, Ohi JM, Naegeli DW, Childress KH, Hagen GP, McCarthy CI, et al. Methylal and Methylal-Diesel Blended Fuels for Use in Compression-Ignition Engines, 1999. https://doi.org/10.4271/1999-01-1508.

Viera Sotillo AA. Effect of multiple injection strategies on the Diesel spray formation and combustion using optical diagnostics. Universitat Politècnica de València, 2019. https://doi.org/10.4995/Thesis/10251/123954.

Wang X, Huang Z, Zhang W, Kuti OA, Nishida K. Effects of ultra-high injection pressure and micro-hole nozzle on flame structure and soot formation of impinging diesel spray. Appl Energy 2011;88:1620–8. https://doi.org/10.1016/j.apenergy.2010.11.035.

Wei J, Zeng Y, Pan M, Zhuang Y, Qiu L, Zhou T, et al. Morphology analysis of soot particles from a modern diesel engine fueled with different types of oxygenated fuels. Fuel 2020;267:117248. https://doi.org/10.1016/j.fuel.2020.117248.

Wickman DD, Senecal PK, Reitz RD. Diesel Engine Combustion Chamber Geometry Optimization Using Genetic Algorithms and Multi-Dimensional Spray and Combustion Modeling. SAE Technical Papers, 2001. https://doi.org/10.4271/2001-01-0547.

Xuan T, Pastor J V., García-Oliver JM, García A, He Z, Wang Q, et al. In-flame soot quantification of diesel sprays under sooting/non-sooting critical conditions in an optical engine. Appl Therm Eng 2019;149:1–10. https://doi.org/10.1016/j.applthermaleng.2018.11.112.

Yoo D, Kim D, Jung W, Kim N, Lee D. Optimization of Diesel Combustion System for Reducing PM to Meet Tier4-Final Emission Regulation without Diesel Particulate Filter. SAE Technical Papers, 2013. https://doi.org/10.4271/2013-01-2538.

Zha K, Busch S, Warey A, Peterson RC, Kurtz E. A Study of Piston Geometry Effects on Late-Stage Combustion in a Light-Duty Optical Diesel Engine Using Combustion Image Velocimetry. SAE Int J Engines 2018;11:2018-01–0230. https://doi.org/10.4271/2018-01-0230.

Zhang T, Yu G, Guo Q, Wang F. Experimental Study on the Characteristics of Impinging Reaction Region with OH* Chemiluminescence in Opposed Impinging Diffusion Flames. Energy & Fuels 2013. https://doi.org/10.1021/ef401204g.

Zhao H, Ladommatos N. Optical diagnostics for soot and temperature measurement in diesel engines. Prog Energy Combust Sci 1998;24:221–55. https://doi.org/10.1016/S0360-1285(97)00033-6.

Zhao H. Laser Diagnostics and Optical Measurement Techniques in Internal Combustion Engines. Warrendale, PA: SAE International; 2012. https://doi.org/10.4271/R-406.

Zhao Q, Wang H, Qin Z, Wu Z, Wu J, Fan W, et al. Synthesis of polyoxymethylene dimethyl ethers from methanol and trioxymethylene with molecular sieves as catalysts. Journal of Fuel Chemistry and Technology 2011;39:918–23. https://doi.org/10.1016/S1872-5813(12)60003-6.

Zheng Z, Wang X, Zhong X, Hu B, Liu H, Yao M. Experimental study on the combustion and emissions fueling biodiesel/n-butanol, biodiesel/ethanol and biodiesel/2,5-dimethylfuran on a diesel engine. Energy 2016;115:539–49. https://doi.org/10.1016/j.energy.2016.09.054.

Zhu R, Miao H, Wang X, Huang Z. Effects of fuel constituents and injection timing on combustion and emission characteristics of a compression-ignition engine fueled with diesel-DMM blends. Proceedings of the Combustion Institute 2013;34:3013–20. https://doi.org/10.1016/j.proci.2012.06.174.

Zhu Y, Zhao H, Melas DA, Ladommatos N. Computational Study of the Effects of the Re-entrant Lip Shape and Toroidal Radii of Piston Bowl on a HSDI Diesel Engine’s Performance and Emissions. SAE Technical Papers, 2004. https://doi.org/10.4271/2004-01-0118.